I. Physikalisches Institut
Justus-Liebig-Universität Gießen

Design and Development of Miniaturized Epoxy-Based Colloid Emitters and Solid-State Ion-Emitters

DISSERTATION

zur Erlangung des akademischen Grades eines
Doktors der Naturwissenschaften
(Doctor rerum naturalium)

vorlegt dem
Fachbereich 07
Mathematik und Informatik, Physik, Geographie

von
Dipl.-Phys. Markus Piechotka
aus Ueckermünde

betreut von
Prof. Dr. Peter J. Klar

im
April 2015

Schrödinger's Cubicle

...grad students exist in a state of both productivity and unproductivity. Only direct intervention reveals whether or not an enormous amount of time has been wasted, a phenomenon known as "expectation collapse".

Jorge Cham[1]

[1] "Piled Higher and Deeper" by Jorge Cham www.phdcomics.com

Zusammenfassung

Diese Arbeit behandelt die Entwicklung und Untersuchung von zwei verschiedenen Konzepten miniaturisierter elektrostatischer Antriebsmethoden.

Um die, aufgrund der wachsenden Zahl von Nano- und Mikrosatelliten sowie Hochpräzisionsforschungsmissionen in Erscheinung tretenden, antriebsrelevanten Herausforderungen zu bewältigen, müssen die Antriebssysteme miniaturisiert werden, um kleinere Systemmassen, Schübe und Impulsbits zu realisieren. Übliche Triebwerktypen wurden in Bezug auf ihr Miniaturisierungspotenzial und ihre Treibstoffmasseneffizienz verglichen. Miniaturisierte Antriebssysteme (inklusive Treibstoff-, und Triebwerksmasse, Masse der Aufbau- und Verbindungstechnik und Kosten der elektrischen Versorgung) auf dem neuesten Stand der Technik wurden hinsichtlich ihrer Einsetzbarkeit auf Satelliten verschiedenster Masse untersucht. Da gewöhnliche Antriebskonzepte nicht beliebig verkleinert werden können, müssen moderne Technologien und skalierbare Konzepte außerhalb existierender Erfahrungen implementiert werden.

- Im ersten Teil dieser Arbeit werden die Entwicklung und das Design miniaturisierter Kolloidemitter behandelt, da Triebwerke dieses Konzepts bei Miniaturisierung effizienter arbeiten.

  Kolloidantriebe nutzen den Feldemissionseffekt aus, der beim Loslösen geladener Partikel von einer Flüssigkeitsoberfläche aufgrund hoher elektrischer Felder zum Tragen kommt. Nimmt man sehr enge Kapillaren, um eine leitende Flüssigkeit nahe an eine Elektrode zu bringen, und legt ein Potenzial zwischen Flüssigkeit und Elektrode an, so bildet sich ein Taylor-Kegel, wobei das elektrische Feld an seiner Spitze verstärkt wird und somit die Feldemission von geladenen Teilchen ermöglicht wird, welche danach mittels eines Beschleunigungsgittersystems beschleunigt werden können. Die benötigte Potenzialdifferenz nimmt ab, wenn der Abstand

zwischen Elektrode und Flüssigkeit oder die Kapillarenöffnung verkleinert werden.

Die in dieser Arbeit verwendeten Kolloidemitter wurden hauptsächlich aus dem Photolack SU-8 hergestellt. Dieser Lack ist im Rahmen der Mikrostrukturierung zur Herstellung stabiler Strukturen mit hohen Aspektverhältnissen weit verbreitet. Als Treibstoff wurde die ionische Flüssigkeit EMI-BF_4 eingesetzt, wodurch ein Kolloidemitter im bipolaren Betrieb arbeiten kann und auf eine zusätzliche Partikelneutralisation verzichtet werden kann. Das Benetzungsverhalten von EMI-BF_4 auf SU-8 und der Einfluss verschiedener Oberflächenbehandlungen auf ebenjenes wurden untersucht. Es wurden Extraktionstests an den im Rahmen dieser Arbeit hergestellten Prototypemittern durchgeführt.

- Der zweite Teil dieser Arbeit behandelt ein neuartiges elektrostatisches Emitterkonzept, wobei mit Hilfe eines alternativen Ansatzes geladene Teilchen generiert werden — der Festkörperionenemitter (solid-state ion-emitter — SSIE). Dieses Konzept basiert auf Festkörperelektrolyten (wie mit Yttriumoxid stabilisiertem Zirconiumdioxid (YSZ)) welche vorwiegend in Festoxidbrennstoffzellen Verwendung finden. Molekularer Sauerstoff wird ionisiert und als O^{2-}-Ion an einer Dreiphasengrenze auf der Rückseite einer dünnen Festkörperelektrolytmembran in ebenjene eingebaut. Nachdem die Sauerstoffionen die ionenleitende Membran durchquert haben, können sie mit Hilfe üblicher Ionengittersysteme extrahiert werden. Die Effizienz dieser, auf dem SSIE-Konzept basierenden, Emitter wird, noch stärker als im Fall der Kolloidemitter, verbessert, wenn die Emitter verkleinert werden.

  In dieser Arbeit wurden dünne Festkörperelektrolytmembranen hergestellt. Der Einfluss der lateralen Membranabmessungen auf die Stabilität dieser Membranen wurde untersucht. Die Eigenspannungen in YSZ-Dünnschichtmembranen und die daraus resultierenden Verspannungsmuster wurden mit Hilfe der Ramanspektroskopie analysiert.

  Die Anwendung des SSIE-Konzepts ist nicht auf Anionen beschränkt, da auch Kationen als Ladungsträger existieren. Kombiniert man beide Typen der Ionenleiter in einem SSIE-Triebwerkssystem, umgeht man das Problem der Ionenstrahlneutralisation.

Abstract

In this work the development and investigation of two different concepts of miniaturized electrostatic propulsion methods are discussed.

In order to fulfill the propulsion-related challenges emerging with a growing number of nano- and microsatellites and high-precision research missions, propulsion systems have to be miniaturized to enable lower system masses, thrust and impulse-bit ranges. Common thruster types with respect to miniaturization prospects and propellant-mass-efficiency were evaluated and state-of-the-art miniaturized propulsion systems (including propellant and thruster mass, packaging and power processing costs) were reviewed to study their working range in terms of satellite mass. As common propulsion systems cannot be down-scaled forever, modern techniques and novel scalable concepts going beyond established schemes have to be employed.

- The first part of this work treats the development and design of miniaturized colloid emitters as such emitters become more efficient when miniaturized.

  Colloid thrusters make use of the field emission effect which occurs when charged particles are ripped off of a liquid surface due to very high electric fields. Using narrow capillaries to supply the conductive liquid near an electrode and applying a potential difference between both the liquid and the electrode, a Taylor cone is formed. Increasing the electric field at its tip further leads to field emission of charged particles which are subsequently accelerated by an acceleration grid system. The required potential difference is lower, if the distance between electrode and liquid or the capillary orifice of a colloid emitter or both are reduced.

  The colloid emitters studied in this work were mainly made out of the photo resist SU-8, which is well-established in the microfabrication field as a photoresist allowing one to prepare robust microstructures with a high aspect ratio. The ionic liquid EMI-BF_4 was chosen as propellant, which enables the operation of a

colloid emitter in bipolar mode — no additional neutralizer is required. The wetting behavior of EMI-BF_4 on SU-8 was investigated and varied by applying different surface treatments. Sample emitters were fabricated and extraction tests were conducted.

- In the second part of this work a novel electrostatic emitter concept with an alternative approach for generating charged particles is proposed and investigated — the solid-state ion-emitter (SSIE). This concept is based on solid electrolytes (like yttria-stabilized zirconia (YSZ)), which are normally used in solid oxide fuel cells (SOFC). Molecular oxygen is ionized and incorporated as O^{2-}-ion into a thin solid-electrolyte membrane at a triple-phase boundary on the backside of the membrane. After passing the ion-conducting membrane, oxygen ions can be extracted by common ion grid systems. The efficiency of a thruster based on the SSIE concept should increase with miniaturization even more than for colloid thrusters.

  The fabrication and investigation of thin solid-electrolyte membranes were conducted in this work. In particular, the influence of lateral membrane dimensions on the stability of such ion conductor membranes was investigated. The residual stress in YSZ thin-film membranes and the resulting strain patterns were analyzed using Raman spectroscopy.

  The SSIE concept is not restricted to anions as ion conduction with cations as mobile carriers also exists. Combining the two types of ion conductors in a SSIE thruster system allows one to overcome the problem of ion-beam neutralization.

Table of contents

List of figures

Chapter 1

Introduction

Spacecraft propulsion systems take up a significant amount of mass and volume of a spacecraft and consume a considerable fraction of the available electric power. With the emerging number of very small satellites the corresponding propulsion systems also have to be miniaturized to maintain a reasonable mass, power and volume consumption. According to the *SpaceWorks 2014 Nano/Microsatellite Market Assessment*[1], 92 satellites in the mass range of 1 kg to 50 kg were launched in 2013, more than the total number in the previous 3 years. For 2014, 135 launches are projected in this satellite class. According to this assessment the annual number of launches of 1 kg to 50 kg satellites will increase to over 400 in the year 2020. In addition, 48 picosatellite or smaller satellite launches are planned in the near future. Table 1.1 lists the class definitions for small satellites.

Common propulsion systems cannot be down-scaled forever as the thruster efficiency may decrease and the propulsion concept may fail

Table 1.1: Different satellite categories[1,2] below a satellite wet mass $m_0 = 500\,\text{kg}$ and the average thrust F required to perform orbital station-keeping in a geostationary earth orbit (GEO) or in a low earth orbit (LEO), (refer to appendix A.1 and Eq. (A.1)).

satellite category	m_0 / kg	F(GEO) / µN	F(LEO) / µN
small satellite	100-500	200-1000	80-800
microsatellite	10-100	20-200	8-80
nanosatellite	1-10	2-20	0.8-8
picosatellite	0.1-1	0.2-2	0.08-0.8
femtosatellite	0.01-0.1	0.02-0.2	0.008-0.08

on miniaturization due to fundamental physical reasons. Furthermore the effect of miniaturization on the auxiliary components like the propellant storage and feed system as well as the power processing unit (PPU) have to be taken into account. These issues are well-known in the space propulsion community, Osiander wrote in his book *MEMS and Microstructures in Aerospace Applications* [3]: *"Current propulsion technology cannot meet the minimum thrust requirements (*$10\,\mu N$ *to* $1000\,\mu N$*) or impulse-bit requirements (*$1\,\mu N\,s$ *to* $1000\,\mu N\,s$*), or satisfy the severely limited system mass (*$< 0.1\,kg$*), volume (*$< 0.1\,cm^3$*), and power constraints (*$< 0.1\,W$*)."* Thus, there is a demand for integrated miniaturized systems since the ratio of auxiliary components mass to the overall thruster mass increases with decreasing satellite mass.

Another advantage of miniaturized propulsion systems are the very small minimum impulse bit values which are necessary for high-precision position control, especially for small spacecrafts with very low moments of inertia. An example for an extremely high-precision mission is the ST-7/LISA Pathfinder [4,5] and its successor, the New Gravitational wave Observatory (NGO) [6,7].

In order to fulfill the needs of small satellites and high-precision missions, modern techniques and novel scalable concepts going beyond established schemes have to be employed. The use of MEMS (micro electromechanical systems) technology enables the miniaturization of each component of a propulsion system. For example, individual emitters in the size of $400\,\mu m \times 250\,\mu m \times 250\,\mu m$ were fabricated already [8]. Arrays of such emitters may be bonded onto a miniaturized PPU. The knowledge in the field of MEMS-based micro-fluidics can be used to integrate the propellant storage and feed system together with the above stated components into a single assembly — yielding very small and compact devices only a few cubic centimeters in volume.

This evolution is depicted exemplarily in Fig. 1.1. A conventionally built and conventionally integrated electrostatic thruster (RIT-35) was already miniaturized by miniaturizing each component of this system, but the integration of each component within the propulsion system was performed conventionally (RIT-2), limiting the miniaturization capabilities. If miniaturized components are integrated using MEMS technology, the packing density can be enhanced further to fully benefit from the miniaturization of propulsion systems (shown for a colloid emitter system in Fig. 1.1).

To compare integrated propulsion systems consisting of miniaturized devices, we estimated (refer to Eqs. (A.2) to (A.10)) the mass ratio m_{prop}/m_0 of the propulsion system mass m_{prop} to the spacecraft mass

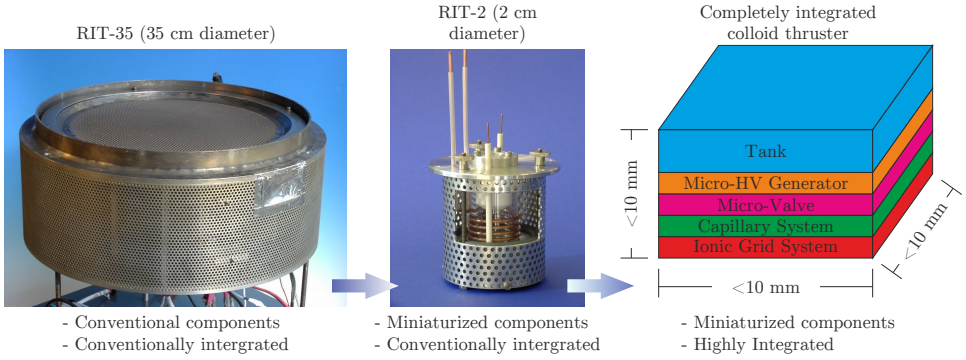

Figure 1.1: The way to highly integrated miniaturized MEMS-based micropropulsion systems. After Fig. 5 in Mueller et al. [9].

m_0 (at the beginning of a mission) of currently available miniaturized thruster systems over a wide range of wet masses of satellites down to $m_0 = 10\,\mathrm{g}$. In order to perform these estimates, the drag compensation of a spacecraft in the low earth orbit (LEO) at an altitude of 400 km is considered as sample mission due to its simplicity. Figure 1.2 shows the working range of state-of-the-art miniaturized thruster types for the above stated mission based on estimates of the ratio m_{prop}/m_0 performed in appendix A.2 and plotted in Fig. A.1. The investigated miniaturized thruster types and their corresponding parameters are listed in appendix A.2 and in tables A.1 and A.2, respectively.

Figure 1.2 yields the different m_0-thresholds for each thruster type at which the propulsion system would totally consume the whole satellite mass, $m_{\mathrm{prop}}/m_0 = 1$, the lower limit of the working range. For example, the electric VAT thruster type and the chemical MiPS cold gas thruster type do not appear in this figure as the propulsion systems investigated contain integrated propellant reservoirs with a propellant mass too low to perform this sample mission. I.e., it's not even possible to add the mission's Delta-v budget to the propulsion system mass yielding the physically impossible value $m_{\mathrm{prop}}/m_0 > 1$ for these thruster types. In relation to a survey of GEO satellites (refer to appendix A.2, Fig. A.1 and table A.4), thruster types with a ratio $m_{\mathrm{prop}}/m_0 \leq 0.5$ are suitable for the corresponding satellite wet mass. The minimal ratios m_{prop}/m_0 and the satellite wet masses m_0^i for $i \in \{1, 10, 50, 80, 100\}$ (according to a ratio $m_{\mathrm{prop}}/m_0 = i/100$) of each thruster type are listed in table A.3.

Figure 1.2 reveals, that both the RIT-2.5b and the µFEEP thruster types are extremely efficient above $m_0 = 200\,\mathrm{kg}$ ($m_{\mathrm{prop}}/m_0 \leq 0.01$). It also shows the limits of not fully integrated emitters (µPPT, µHET,

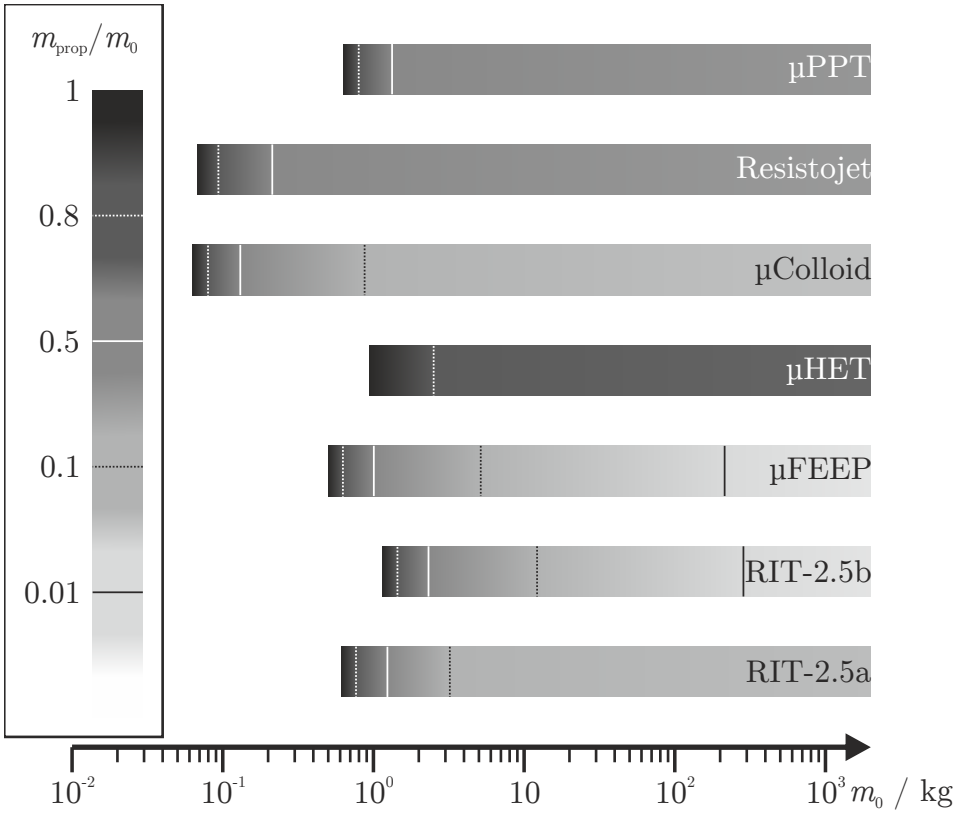

Figure 1.2: Working range of several miniaturized thruster designs in terms of satellite wet mass m_0 based on estimates performed in appendix A.2. A mission for providing ten years of drag compensation in a LEO (400 km) with an annual Delta-v budget $\Delta V = 25\,\mathrm{m\,s^{-1}}$ was chosen as basis. The working ranges are graduated in terms of color according to the ratio m_{prop}/m_0 of the propulsion system mass m_{prop} to m_0.

µFEEP, RIT-2.5a and RIT-2.5b) as only the Resistojet and µColloid thruster types as fully integrated emitters are suitable for satellites with wet masses below $m_0 = 500\,\mathrm{g}$. This reflects the evolution depicted in Fig. 1.1, i.e. the highest possible benefit of miniaturization is only achieved with a high level of integration of the peripheral components (PPU, packaging). Furthermore, a higher integration yields also a better adaption to different satellite and mission types.

The lowest suitable satellite wet mass was estimated for the µColloid thruster type with $m_0^{50} \approx 0.13\,\mathrm{kg}$, i.e. the propulsion system on a satellite with a wet mass of $m_0 \approx 130\,\mathrm{g}$ would consume $m_{\mathrm{prop}} \approx 65\,\mathrm{g}$ — providing a payload mass of 65 g. Additionally, this thruster type

enables the highest efficiency (of all investigated thruster types) up to a satellite wet mass of $m_0 \approx 10\,\mathrm{kg}$.

Therefore, this work treats the design and development of highly efficient miniaturized thrusters as well as the challenges arising in the corresponding miniaturization process. The study of different propulsion concepts in terms of mass efficiency and down-scalability led to the choice of miniaturized colloid emitters as the concept which may be miniaturized best. As an electrostatic thruster concept (ESP) it is possible for colloid emitters to generate very high propellant exhaust velocities which yield a reduction of propellant mass for a set of mission parameters in comparison to other propulsion concepts — the mass efficiency is very high (as will be discussed in more detail in section 2.1). This electrostatic thruster concept becomes more efficient at smaller thruster dimensions. Additionally, the ion generation is not as complicated as in other ESP concepts and the energy per particle required for ionization is very low. Therefore the colloid thruster is the concept of choice for highly efficient miniaturized thrusters.

A possible schematic design of a highly integrated, miniaturized colloid emitter is schematically depicted in Fig. 1.1 (right). The colloid thrusters studied in this work were mainly made out of the photo resist SU-8, which is well-established in the micro-fabrication field as a photoresist allowing one to prepare robust microstructures with a high aspect ratio. Details will be discussed in section 3.2. As propellant the ionic liquid EMI-BF_4 was chosen. Its properties and the advantages of ionic liquids over liquid metals are emphasized in section 3.1.2. Sample emitters were fabricated and extraction tests were conducted with the ionic liquid EMI-BF_4 and are described in chapter 3.

The second part of this work treats a novel, unconventional concept based on solid electrolytes normally used in miniaturized solid oxide fuel cells (μSOFC). This solid-state ion-emitter (SSIE) concept utilizes the ionization of molecular oxygen at a triple-phase boundary at the backside of a very thin ion conductor. After passing the ion-conducting membrane, oxygen ions can be extracted by common ESP extraction grid systems. The efficiency of a thruster based on the SSIE concept should increase with miniaturization even more than for colloid thrusters, this is discussed in section 2.3. The fabrication and investigation of the ionizing part of such a device was conducted in this work. In particular, the influence of lateral membrane dimensions on the stability of such ion conductor membranes was investigated and is described in chapter 4. It should be noted that the SSIE concept is not restricted to anions as ion conduction with cations as mobile

carriers also exists. Combining the two types of ion conductors in a SSIE thruster system allows one to overcome the problem of ion beam neutralization, which obviously is not possible by electrons in case of anion-based SSIE thrusters.

The next chapter comprises a short discussion of different propulsion principles yielding the concepts of choice for high-efficient miniaturized low-thrust engines, which are demanded by both economy and research. This work is concluded with a short comparison of both investigated concepts and an outlook.

Chapter 2

Preliminary considerations: From the rocket principle to miniaturized electrostatic propulsion

This chapter gives a short review of the theory of space propulsion with special emphasis on miniaturized electrostatic propulsion for spaceflight. Firstly, the general concept of space propulsion focussing on electric propulsion is shown as a short overview. Afterwards the need for miniaturized low-thrust high-efficient thrusters for both economic and research missions is briefly discussed. A discussion of the advantages for miniaturization of the thruster concepts treated in this work concludes this chapter.

2.1 The concept of (electric) space propulsion

A rocket in space consisting of the actual spacecraft and the fuel required for the mission may be accelerated by expelling some of the fuel. The total momentum in its center-of-mass system is zero, $\boldsymbol{p}_{\mathrm{tot}} = 0$. Its total mass is $\tilde{m} + \mathrm{d}\tilde{m}$. When the infinitesimal amount of mass $\mathrm{d}\tilde{m}$ is expelled with exhaust velocity $\boldsymbol{v}_{\mathrm{e}}$ (relative to the spacecraft), the remaining rocket mass $\tilde{m}$ experiences an infinitesimal change of velocity $\mathrm{d}\boldsymbol{v}$ in the opposite direction. This model is depicted in Fig. 2.1. Thus, the momenta $\boldsymbol{p}_{\mathrm{S}}$ and $\boldsymbol{p}_{\mathrm{E}}$ belonging to the spacecraft and the expelled

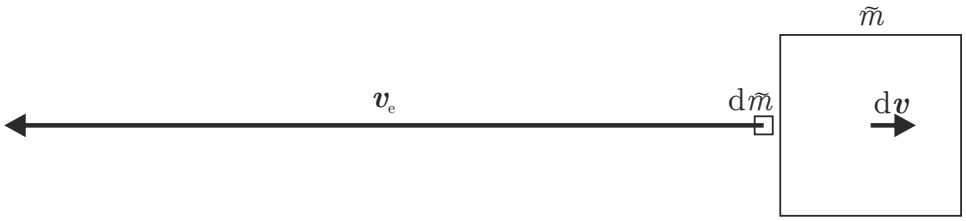

Figure 2.1: Schematic drawing of the rocket principle: In an infinitesimal time interval $\mathrm{d}t$ the rocket with a mass $\tilde{m}$ expels an infinitesimal amount of mass $\mathrm{d}\tilde{m}$ with an exhaust velocity $\boldsymbol{v}_\mathrm{e}$. Due to the conservation of momentum the rocket will experience a velocity gain $\mathrm{d}\boldsymbol{v}$. This is described in the rocket equation (2.2).

mass, respectively, can be written as

$$\begin{aligned} \boldsymbol{p}_\mathrm{S} &= \tilde{m}\mathrm{d}\boldsymbol{v} \\ \boldsymbol{p}_\mathrm{E} &= \mathrm{d}\tilde{m}\boldsymbol{v}_\mathrm{e}. \end{aligned} \tag{2.1}$$

Because of momentum conservation in this inertial system, it holds

$$\begin{aligned} \boldsymbol{p}_\mathrm{tot} &= \boldsymbol{p}_\mathrm{S} + \boldsymbol{p}_\mathrm{E} \\ 0 &= \tilde{m}\mathrm{d}\boldsymbol{v} + \mathrm{d}\tilde{m}\boldsymbol{v}_\mathrm{e}, \end{aligned}$$

or

$$\mathrm{d}\boldsymbol{v} = -\boldsymbol{v}_\mathrm{e}\frac{\mathrm{d}\tilde{m}}{\tilde{m}}, \tag{2.2}$$

which is the rocket equation in an inertial system, i.e. without external forces.

Accounting for the effect of external forces basically yields

$$\begin{aligned} \boldsymbol{p}_\mathrm{tot} &= \sum \boldsymbol{F}_i \\ \tilde{m}\frac{\mathrm{d}\boldsymbol{v}}{\mathrm{d}t} + \boldsymbol{v}_\mathrm{e}\frac{\mathrm{d}\tilde{m}}{\mathrm{d}t} &= \sum \boldsymbol{F}_i \\ \frac{\mathrm{d}\boldsymbol{v}}{\mathrm{d}t} &= \frac{1}{\tilde{m}}\left(\sum \boldsymbol{F}_i - \boldsymbol{v}_\mathrm{e}\frac{\mathrm{d}\tilde{m}}{\mathrm{d}t}\right). \end{aligned} \tag{2.3}$$

Neglecting external forces, it is now possible to determine the velocity gain $\Delta\boldsymbol{v}$ of a spacecraft during an acceleration mission by simply integrating the rocket equation (2.2).

The velocity gain Δv of a spacecraft with an initial mass m_0 and an end mass m_1 in a force-free environment (e.g., space) during a maneuver

Table 2.1: Exhaust velocities v_e and mass ratios (propellant mass to spacecraft final mass) m_2/m_1 of spacecraft thruster types with a TRL of 7 or above. The mass ratios are for the orbital station-keeping of a satellite in the GEO (geostationary earth orbit), which requires an annual Delta-v budget of $\Delta V_{\mathrm{OST}}\,(1\,\mathrm{a}) \approx 60$ m/s yielding a total Delta-v budget of $\Delta V_{\mathrm{OST}}\,(15\,\mathrm{a}) \approx 900$ m/s over a satellite lifetime of 15 years:

group	type	v_e $\mathrm{km\,s^{-1}}$	m_2/m_1 %
chemical	monopropellant (Monop)	2	57
	bipropellant (Bip)	4.7	21
electric propulsion	resistojet (Resisto)	6	16
	pulsed Plasma (PPT)	20	4.6
	Hall Effect (Hall)	50	1.8
	electrostatic (EST)	210	0.43

with a constant exhaust velocity v_e where propellant of mass $m_2 = m_0 - m_1$ is expelled opposite the flight direction will then be

$$\Delta v = v_e \ln\left(\frac{m_0}{m_1}\right) = v_e \ln\left(\frac{1}{1 - m_2/m_0}\right) = v_e \ln\left(1 + \frac{m_2}{m_1}\right). \quad (2.4)$$

This is the Tsiolkovsky rocket equation (2.4), named after Konstantin Tsiolkovsky. These considerations about space flight were first published in 1903 in his work "A Rocket into Cosmic Space"[10]. The total energy required by a mission consisting of single maneuvers of the type described above can be expressed by the mission's Delta-v budget ΔV which is just the sum of all maneuvers' single velocity gains

$$\Delta V = \sum \Delta v. \quad (2.5)$$

Based on these fundamental considerations, one may compare the different spacecraft propulsion principles with respect to their ΔV-budgets taking into account the differences in thruster exhaust velocities. According to Eq. (2.4), the satellite velocity gained is proportional to the exhaust velocity, which means, that the required propellant mass to achieve a certain velocity gain is significantly reduced by using a higher exhaust velocity. Table 2.1 shows the exhaust velocities of different types of thrusters which have at least a technology readiness level (TRL) of 7 (System prototyping demonstration in an operational

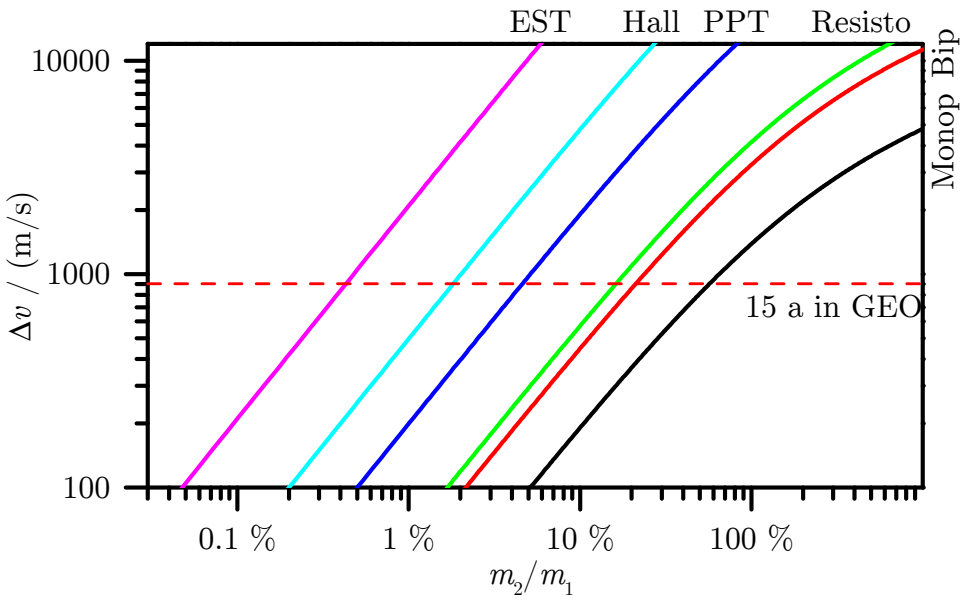

Figure 2.2: Velocity gain Δv as a function of the mass ratio m_2/m_1 of propellant mass m_2 to final mass m_1 during an acceleration maneuver for different thruster types with different exhaust velocities v_e, following Eq. (2.4). The black dashed horizontal line represents the total Delta-v budget ΔV required for the orbital station-keeping of a GEO (geostationary earth orbit) satellite with a lifetime of 15 years. The abbreviations used in the legend are those defined in table 2.1.

environment (ground or space))[11]. Based on Eq. (2.4) one can also plot Δv against m_2/m_1 for different v_e to compare the mass efficiencies of the various thruster types. Figure 2.2 shows the corresponding results.

An example may clarify the huge possibilities of mass-saving due to high v_e: If the designated Delta-v budget is $\Delta V = 900\,\mathrm{m\,s^{-1}}$, as needed for 15 years station-keeping in GEO, the monopropellant system would require a mass ratio of $m_2/m_1 = 57\,\%$. An electrostatic system would only need a very small fraction of propellant mass to the final mass: $m_2/m_1 = 0.43\,\%$. The mass ratios for this mission required by the different types of thrusters are listed in Table 2.1. It turns out that electrostatic thrusters offer the most mass-efficient way to accelerate a spacecraft in a force-free environment. Alternatively, in case of a given amount of propellant mass the lifetime of a satellite can be enhanced significantly by a higher exhaust velocity. As will be discussed below, the structural mass of the thruster itself and the corresponding

accessories like storage tanks, feeding, valves, pumps and PPU (power processing units) will also play a role in such considerations as they allow to reduce m_1 itself which is obviously advantageous in terms of propellant consumption, refer also to appendix A.2 and Fig. 1.2.

It can be seen from Table 2.1 that thrusters based on electric propulsion possess larger maximum exhaust velocities than chemical thrusters. This makes electric propulsion the principle of choice for achieving a better ratio of propellant mass to rocket mass based on higher exhaust velocity only. The electric propulsion principle will be briefly introduced in the next section.

Electric propulsion

Electric propulsion (EP) describes the general concept of altering the momentum of a spacecraft by using electric energy, generally provided by solar cell panels, radioisotope thermoelectricity or nuclear fission. Within EP, the following categories may be distinguished. Electrostatic thrusters (ESP) provide charged particles like electrons, ions or colloids, where the acceleration of these charged particles is caused by an electrostatic field. Electrothermal propulsion works by increasing the thermal energy of the propellant via converting electric energy, the former is then converted into kinetic energy by using a nozzle, like in a "conventional" rocket. If charged particles are accelerated by an electromagnetic field which is not in the direction of acceleration, like the usage of the Lorentz force, one speaks of electromagnetic propulsion. Additionally, there are the vacuum arc thruster, the laser ablation thruster or the electrodynamic tether which are not further grouped.

Electric propulsion as a concept in space technology was first mentioned by Robert Goddard in his personal notebook in 1906[12], where he considered the possibility of using fast electrons to propel spacecrafts:

> *Concerning reaction with electrons moving with the velocity of light.*
>
> 1. *At enormous potentials can electrons be liberated at velocity = Λ, and if the potential is still further increased will the reaction increase (to what extent) or will radioactivity be produced?*
> 2. *Will ultra-violet light hinder or accelerate the former action, or will it produce radio activity?*

3. *Can the necessary potential be controlled and the necessary power be developed?"*

He describes the possible acceleration of electrons by huge electric potentials to the speed of light or even beyond. Considering that Einstein's theory of special relativity was published only a few months earlier and given the only partial understanding of the origin of cathode rays at that time, Goddard was not able to capture the whole concept of electric propulsion. The suggestion of using electrons as propellant has some obvious drawbacks, mainly their very low mass to charge ratio, whose consequences will be shown in the following discussion of the contribution of Konstantin Tsiolkovsky to space technology.

Tsiolkovsky on his own proposed the idea of EP in 1911 [10] using the following expression: *"It is possible that in time we may use electricity to produce a huge velocity for the particles ejected from the rocket device. It is known at the present that the cathode rays in Crookes' tube, just like the rays of radium, are accompanied by a flux of electrons whose individual mass is* 4,000 *times less than the mass of the helium atom, while the velocities obtained are* 30,000 − 100,000 km/sec, *i.e.,* 6,000 *to* 20,000 *times greater than the velocity of the ordinary products of combustion flying from our reactive tube."* He mentioned that cathode ray electrons have a much higher velocity than the particles of a cold-gas thruster and that they may be used as a propulsion alternative, although the electron mass is very low.

Both the concepts of Goddard as well as of Tsiolkovsky describe electrostatic thrusters. Relating to the considerations of Tsiolkovsky, a 30 kV ESP thruster based on electrons would have an exhaust velocity of $v_\mathrm{e} \approx 10^8\,\mathrm{m\,s^{-1}}$. The acceleration power P_acc of an ESP thruster required for a given thrust F and acceleration voltage U is:

$$F = \frac{\mathrm{d}\tilde{m}}{\mathrm{dt}} v_\mathrm{e}, \tag{2.6}$$

$$P_\mathrm{acc} = \frac{\mathrm{d}\tilde{m}}{\mathrm{dt}} \frac{v_\mathrm{e}^2}{2},$$

$$v_\mathrm{e} = \sqrt{2\frac{q}{M}U},$$

$$P_\mathrm{acc} = F\sqrt{\frac{q}{2M}U}, \tag{2.7}$$

where M and q are the mass and the charge of each emitted particle, respectively. Even neglecting the effects of the special theory of relativity, a thrust of 1 N would require a power of 50 MW, i.e., to overcome

an external force like gravitation incredible amounts of energy would be necessary. This is due to the very low mass-to-charge ratio of electrons, although such a thruster would be very mass-efficient, it is impossible to use it for real missions.

Instead of electrons, common ESP thruster generally work with the heavy noble gas ions Xe^+ which yield power-to-thrust ratios in the range of $20\,\mathrm{kW\,N^{-1}}$ to $100\,\mathrm{kW\,N^{-1}}$ at extraction voltages in the range of 1 kV to 30 kV, considering only the power required for acceleration of ions, refer to Eq. (2.7). Common solar panels[13] deliver $300\,\mathrm{W\,kg^{-1}}$ revealing that electrostatic thrusters are only suitable for low-thrust maneuvers, e.g. for orbital station-keeping of satellites, propulsion of micro-satellites, interplanetary travel or high-precision missions, as will be discussed in section 2.2.

The orbital station-keeping of a GEO satellite with a satellite wet mass of 3000 kg would require an average thrust of 6.2 mN, refer to Eq. (A.1). If xenon is used as a propellant and the parameters given above are used, then the corresponding mass of solar power panels (840 W) would be 2.8 kg and the propellant mass for a satellite lifetime of 15 years would be 13 kg only. Additionally, the mass of the PPU with 25 kg has to be taken into account, yielding an overall propellant related mass of 31 kg. The overall propellant related mass consisting of the real propellant mass as well as the corresponding mass for power generation, despite the fairly high power consumption, is still far smaller than the propellant mass required for a chemical thruster to fulfill the same task. A monopropellant thruster would consume 1700 kg of propellant. Therefore electrostatic thrusters are the concept of choice for long range space travel or low-thrust maneuvers.

Considering low-thrust operations, the ratio of propellant mass to the mass of the thruster itself and its supply systems has to be as high as possible to benefit most of the thruster's mass efficiency. To achieve this, the engine has to be miniaturized. However, miniaturization in turn may affect the thruster performance. Therefore the advantages and disadvantages of the miniaturization of different electrostatic propulsion concepts are discussed in the following.

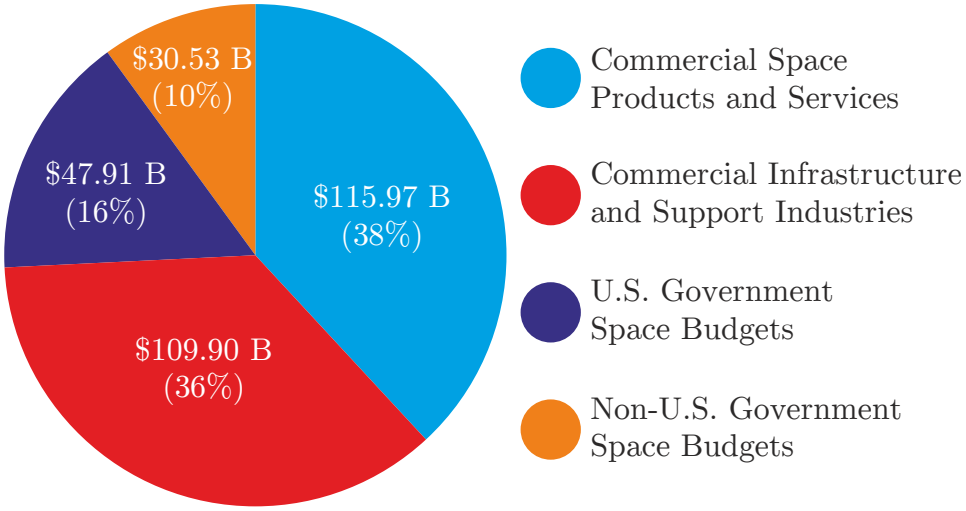

Total: $304.31 Billion

Figure 2.3: Pie chart of the global space activity in 2012. The data were published in *The Space Report 2013 Overview* [14].

2.2 The demand for miniaturized electrostatic propulsion in commercial space economy and research missions

This work deals with the development of high-efficient miniaturized thrusters, which are to be applied in low-thrust missions. In the following section the multitude of potential applications for these microthrusters is briefly discussed.

Astronautics has a huge impact on the global economy — the current (2012) annual value of the global space economy exceeds 300 billion US-dollars, as described in *The Space Report 2013 Overview* [14]. This number includes both government budgets and commercial revenues, as itemized in Fig. 2.3. The dominating part, commercial space products and services, is mainly driven by GNSS (global navigation satellite system) devices and chip-sets, GMSS (global mobile satellite system) devices, or DTH (direct-to-home) television.

The satellites required for these services are placed in different orbits [15] around the earth, namely the low earth orbits (LEO) up to altitudes of 2000 km, the geosynchronous earth orbits at an altitude of 35 786 km, and the medium earth orbits (MEO) in between at altitudes from 2000 km to 35 786 km. Governmental earth orbiting missions like weather fore-casting satellites, earth observing and other research mis-

Table 2.2: Annual Delta-v budgets required for station-keeping in different orbits.

orbit	height km	annual Delta-v budget $\Delta V_{\mathrm{OST}}\,(1\,\mathrm{a})$ for orbital station keeping / $\mathrm{m\,s^{-1}}$
LEO (ISS)	400	20 to 100
LEO	700 to 2000	2 to 7
GEO	35 786	50 to 100

sions also are placed in these earth orbit bands. For each of these orbits a spacecraft has to perform orbital maneuvers to maintain its altitude and inclination — orbital station-keeping.

The required overall Delta-v budget ΔV_{OST} for orbital station-keeping (OST) maneuvers differs for each intended orbit and for the mission duration. In the low earth orbits the annual $\Delta V_{\mathrm{OST}}\,(1\,\mathrm{a})$ required to compensate the atmospheric drag dominates the perturbation forces and strongly depends on the altitude — from $\Delta V_{\mathrm{OST}}\,(1\,\mathrm{a}) \ll 1\,\mathrm{m\,s^{-1}}$ above 700 km to $\Delta V_{\mathrm{OST}}\,(1\,\mathrm{a}) \approx 25\,\mathrm{m\,s^{-1}}$ at 400 km and even more below the latter altitude. In the most common type of geosynchronous orbit, the geostationary earth orbit (GEO), a satellite experiences the non-spherical earth's gravitation as well as perturbations from the gravitational forces of the moon and the sun and the pressure of solar radiation. For this orbital station-keeping an annual $\Delta V_{\mathrm{OST}}\,(1\,\mathrm{a})$ of about $50\,\mathrm{m\,s^{-1}}$ to $100\,\mathrm{m\,s^{-1}}$ is required[16]. Without such compensation a GEO-satellite would experience a shift of its orbital plane of about 0.85° per year. The Delta-v budgets for different orbits are summarized in Table 2.2.

As the required annual $\Delta V_{\mathrm{OST}}\,(1\,\mathrm{a})$ is relatively small compared to the ΔV required for orbit raising, the thrust may be very low and the most important property of orbital station-keeping thrusters is their mass efficiency to reduce the fuel consumption. Considering smaller satellites as stated in table 1.1, the required thrust is even lower, increasing the importance of mass efficiency.

Miniaturized thrusters may also be used on special research missions with very high requisites on position and attitude control as thrusters with very small and accurate minimal thrusts are required. For example, the ESA supervises the Evolved Large Interferometer Space Antenna (eLISA) also known as New Gravitational-wave Observatory (NGO)[6,7,17,18] and its preliminary test mission LISA Pathfinder[4,5]. The eLISA/NGO project will be based on a giant space interferometer

consisting of three single satellites containing test masses forming two antenna arms in a heliocentric orbit. The gravitational waves in the frequency range of 3×10^{-5} Hz to 1 Hz shall be measured by observing the length variations of the arms using laser interferometry. Each arm will have a length of one million kilometers while each satellite will be in an independent orbit. Although there is no need for station-keeping, it will be necessary to keep each satellite centered around its test mass. This shall be done with micro-thrusters working in the thrust range of 5 µN to 30 µN with a precision below 0.1 µN. The eLISA/NGO has passed the selection process of the ESA L3 mission (L-class missions, 'Large') with a launch scheduled for 2034[19–21].The NGO's predecessor, LISA Pathfinder, which is a down-scaled analog of the NGO, will be launched in 2015 to explore the feasibility of the drag-free attitude control with two test masses and of the laser interferometry and to perform hardware endurance tests in the space environment[4]. It will be placed in an orbit around the Lagrangian point L1 between sun and earth.

As shown above, astronautics has a huge impact on the global economy and research as well as on the everyday life. Many commercial satellites as well as several government funded space missions require highly mass-efficient and very precise thrusters in the µN-range. Recently, this demand is even higher as the amount of very small satellites with wet masses below 100 kg has increased rapidly. The projected number of these very small satellite launches in the next few years reveals a further growth as discussed in section 1. To fulfill these requirements one may consider electrostatic propulsion (ESP), where charged particles are accelerated by an electrostatic field to very high exit velocities which yields a better mass efficiency, cf. Fig. 2.2 and table 2.1. ESP thrusters exhibit the highest mass efficiency of all space thrusters, although the power consumption scales with the exit velocity (Eq. (2.7)). Another constriction for the above stated space missions is the very low thrust range of the engines which may only be achieved effectively by using miniaturized thrusters. Thus the main goal of this work was to develop miniaturized micro-propulsion ESP-thrusters and get a better understanding of the related fabrication steps.

In the next section the suitability of different electrostatic thrusters for miniaturization is discussed.

2.3 The miniaturization of common electrostatic propulsion concepts

In the previous sections the superiority of electrostatic propulsion over other space propulsion concepts in terms of mass efficiency has been shown. To benefit from the fuel mass saving to the maximum extent possible, a miniaturization of the thruster itself is necessary since the overall engine mass can be reduced further. This is especially important for low-thrust missions, either for high-precision maneuvers or on board of miniaturized space vessels. Therefore this section gives a brief overview of the most common electrostatic propulsion concepts with respect to miniaturization prospects. These include the Hall effect thrusters, the (radio-frequency) ion thrusters and the field-emission based thrusters.

2.3.1 HET

HET (Hall effect thrusters) consist of a hollow cylinder with a concentrically placed cylindrical magnetic coil within[22], cf. Fig. 2.4. Around this coil a hollow ring chamber made of a diamagnetic material is placed — the plasma chamber. Further outwards several magnets are placed to create a radial magnetic field within the plasma chamber. Through the base of the plasma chamber propellant feedthroughs are mounted to provide the thruster with neutral gas atoms. These feedthroughs also act as anode and are put at positive high voltage. The neutralizer works as cathode and is placed outside the plasma chamber. The electrons from the cathode are accelerated to the anode and experience the radial magnetic field. They will drift azimuthally due to the Hall effect and define a negative plasma potential acting as an effective cathode for the ions. The electrons gain very high velocities due to the cyclotronic acceleration and mainly collide with the gas atoms and ionize them. The ions are then accelerated in the electric field between anode and cathode and leave the thruster while collecting their neutralizing electrons.

Ions as well as electrons collide with each other and the plasma chamber wall. Furthermore, electrons freed from the magnetic entrapment are attracted by the anode. These processes lead to a net loss of efficiency.

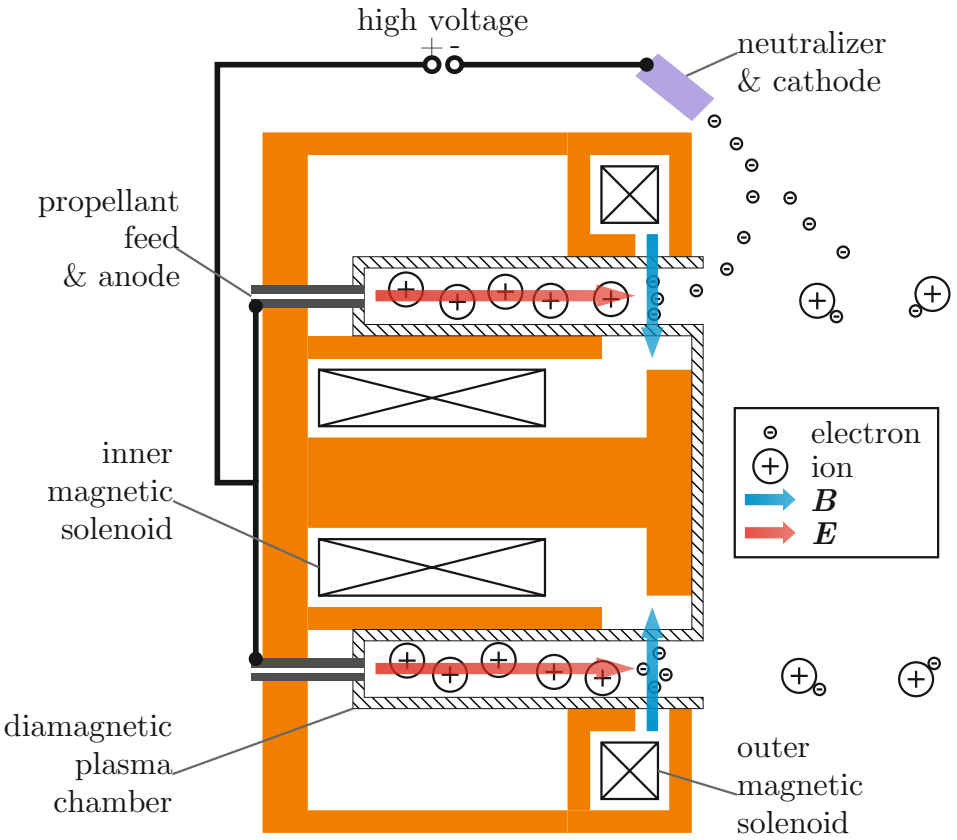

Figure 2.4: Schematic cross section of a Hall effect thruster (HET). A radial magnetic field is applied across a ring-shaped plasma chamber causing electrons to drift azimuthally due to the Hall effect and ionize the propellant. The acceleration of the ions happens without any additional grids. Upon leaving, the ions collect their neutralizing electrons. Image after[22].

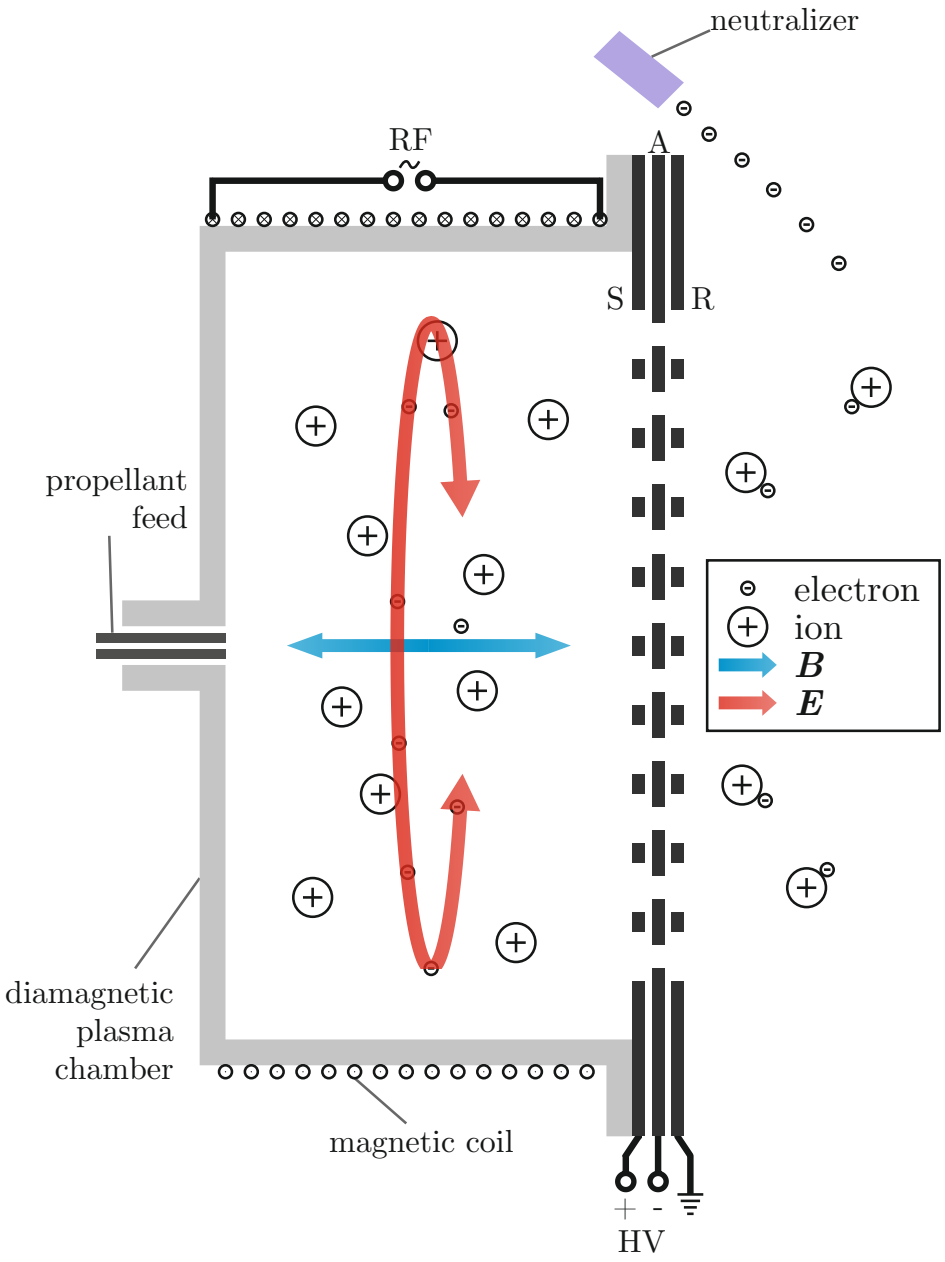

Figure 2.5: Schematic cross section of a radio-frequency ion thruster (RIT). A radio-frequency (RF) current through the solenoid around the plasma chamber leads to an ionization of the propellant gas. The plasma is put on a high positive potential using the screening grid (S). Ions are extracted by applying on the acceleration grid (A) a negative potential (HV) relative to the screening grid (S). A retarding grid (R) on vessel potential is used for further ion focusing. Image after [23].

2.3.2 RIT

RIT (radio-frequency ion thrusters) use an inductively coupled plasma to supply positively charged ions which are extracted from the plasma and accelerated by an ion grid system[23], a cross sectional schematic is shown in Fig. 2.5. An alternating axial magnetic field $\boldsymbol{B}$ is applied on the plasma chamber. This leads to an induced azimuthal electric field $\boldsymbol{E}$. Electrons gain high velocities in each half-cycle of the radio frequency ν. The relaxation time τ between collisions of the electrons is of the order of $(2\nu)^{-1}$ — they collide with neutral propellant atoms and ionize them. The ions cannot follow the electric field due to their greater inertia and a self-sustaining equilibrium can be obtained. The plasma is put on a positive high potential by a screening grid placed on the chamber orifice. The acceleration grid on negative potential is aligned to the first grid further outwards. The ions are accelerated between the first two grids and focused with a third retarding grid which is placed outermost and is on vessel potential. The extracted ions have to be neutralized with electrons from a hollow cathode neutralizer.

Ions as well as electrons collide with the plasma chamber wall and therefore cause a net loss of efficiency. These loss considerations hold for Kaufman-based or ECR (electron cyclotron resonance) ion thruster as well, which generate the plasma using electrons from a cathode discharge or microwave heated electrons, respectively.

2.3.3 FEEP/Colloid

Both FEEP as well as colloid thrusters make use of the field emission effect which occurs when ions or charged particles are ripped off of a liquid surface due to very high electric fields. Figure 2.6 shows a cross-sectional view of such a thruster in emitting mode. A conducting liquid is provided in a capillary or a slit opposite of an electrode. If a high voltage is applied between liquid and electrode, the occurring electric field will deform the liquid surface. This enhances the electric field near the liquid surface even more until a Taylor cone is formed. At the tip of that cone the electric field will be large enough to perform field emission of single ions or larger charged particles. These are then accelerated further in the electric field. For colloid thrusters using ionic liquids (IL) it is possible to alternate the charge of the colloids to prevent vessel charging. Liquid metal (LM) FEEP have to be neutralized by an additional electron source. The electric field is enhanced by a smaller distance d between liquid and electrode as well as by a smaller capillary

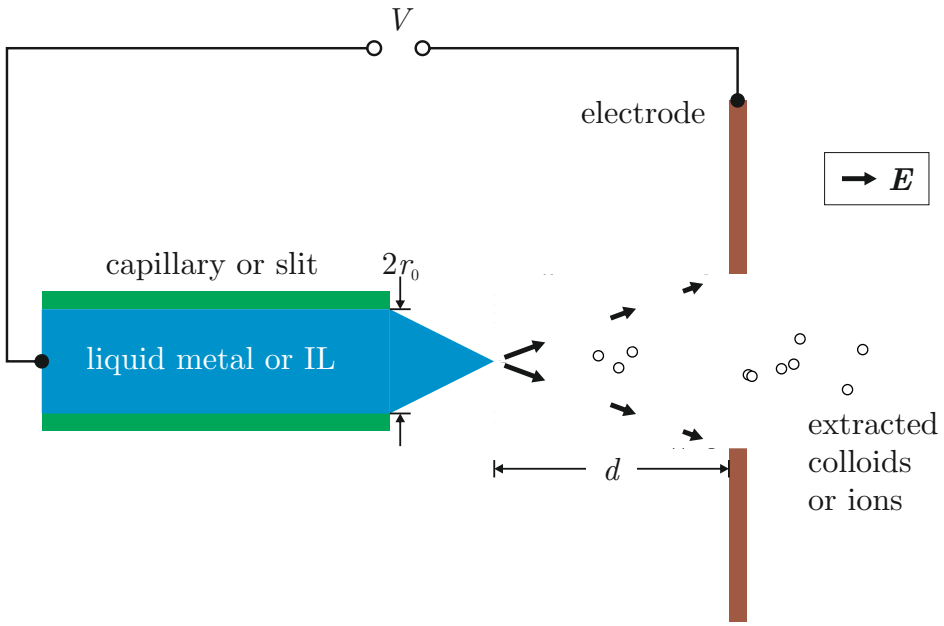

Figure 2.6: Schematic cross section of a FEEP (field emission electric propulsion) or colloid thruster. The potential V applied between extraction grid and propellant leads to the formation of the Taylor cone. Due to the enhancement of the electric field $\boldsymbol{E}$ near the cone tip, charged droplets or ions are ripped from the tip and accelerated to the electrode.

orifice r_o.

Therefore the required potential U_{ext} may be lower for a miniaturized thruster:

$$U_{ext} \propto \sqrt{r_o} \ln\left(\frac{d}{r_o}\right), \tag{2.8}$$

according to Eq. (3.4) in section 3.1.1.

2.3.4 Unconventional ESP concepts

Basically, all concepts which provide charged particles and show improved general efficiency by miniaturization are suitable concepts for miniaturized electrostatic thrusters. Therefore the concept of solid-state ion-emitters (SSIE) is proposed in this work. It is based on the well-established concept of ionic conduction through solid electrolytes. Thin membranes together with a porous back-side electrode facing a reservoir of gaseous molecular oxygen are heated and provide oxygen

Table 2.3: Overview of electrostatic propulsion concepts with respect to miniaturize their volume ($\propto a^3$) in every dimension a. The last column depicts the miniaturization capability of each concept.

concept	ionization	propellant	efficiency(a)	min?
HET	Hall effect plasma	Xe^+	$\propto a$	✗
RIT	RF-coupled plasma	Xe^+	$\propto a$	✗
FEEP	field emission	$LM^+/IL^{+/-}$	$\propto a^{-1/2}$	✓
SSIE	ionic conduction	O^-	$\propto a^{-1}$	✓

ions on the vacuum side of each membrane. These ions can be accelerated in the classic electrostatic way. The required thermal energy of such a device depends reciprocally on the thickness d of these membranes.

2.3.5 Conclusions

The above stated brief overview shows that the plasma-based electrostatic thrusters are not likely to be miniaturized. Their efficiency strongly depends on the particle-wall-interaction. It is proportional to the plasma volume with respect to the amount of wall surface — the volume-to-surface-ratio. Miniaturization of a plasma chamber will automatically lead to a reduction of this ratio as it is inversely proportional to the chamber's lateral dimension a. Furthermore, their efficiency may decrease with smaller dimensions since the mean free path of the particles must not exceed the dimension. Crudely, one may assume that the efficiency scales $\propto a$.

In contrast, FEEP or colloid thrusters even enhance their efficiency when miniaturized. The extraction voltage depends strongly on the dimension of such a thruster. A thinner capillary (radius r_0) as well as a smaller liquid-electrode distance d reduce the required extraction voltage U_{ext} according to Eq. (2.8). When the thruster dimension a is reduced ($r_0, d \propto a$), the efficiency of such a thruster increases $\left(\propto a^{-1/2}\right)$, as the energy required to ionize a particle with charge q is $E_{\text{ion}} = qU_{\text{ext}}$. This makes such a thruster the concept of choice for miniaturizing electrostatic propulsion. In the next chapter our work on miniaturized colloid thrusters is presented.

The efficiency of the SSIE concept scales with the ionization cost which is determined by the amount of thermal energy required to en-

able oxygen transport through a solid-electrolyte membrane of such a thruster. As the thermal energy decreases with the thickness d of these membranes ($d \propto a$), the efficiency scales $\propto a^{-1}$. Therefore this concept is well suitable for miniaturized electric propulsion. This behavior will be discussed further in chapter 4.

An overview of the presented electrostatic thruster concepts and their miniaturization prospects is given in Table 2.3. It shows the superiority in terms of miniaturization of the two concepts treated in this work to the other common electrostatic propulsion techniques. Based on this motivation, the miniaturization of both the concepts of colloid thrusters as well as of solid-state ion-emitters are investigated.

Chapter 3

Miniaturized colloid emitters using the epoxy-based resist SU-8

Following the conclusions made in the previous chapter, the most promising concept for the miniaturization of thrusters is the field-emission electric propulsion (FEEP) or colloid emitter concept. In this chapter the design and development of a miniaturized colloid emitter is described. After an illustration of the general colloid emitter concept, the advantages of ionic liquids as propellant choice are discussed (section 3.1). A survey of different capillary materials used in recent miniaturized colloid emitter designs was performed and the usage of SU-8 as capillary material is explained in section 3.2. In section 3.3 the microfabrication methods used for these emitters are described. The fully integrated miniaturized emitters were investigated microscopically, the permeability of these emitter arrays was tested and extraction tests were performed on single emitters as described in section 3.4. Simplified emitters were designed to perform further extraction tests on single capillaries and to improve the wetting behavior of the emitter surface (section 3.5). The results are concluded in section 3.6.

3.1 The concept of colloid emitters using IL

In this section the similarities and differences between the colloid emitter concept and other electrostatic propulsion (ESP) concepts are discussed (3.1.1) and ionic liquids (IL) as propellant are introduced (3.1.2).

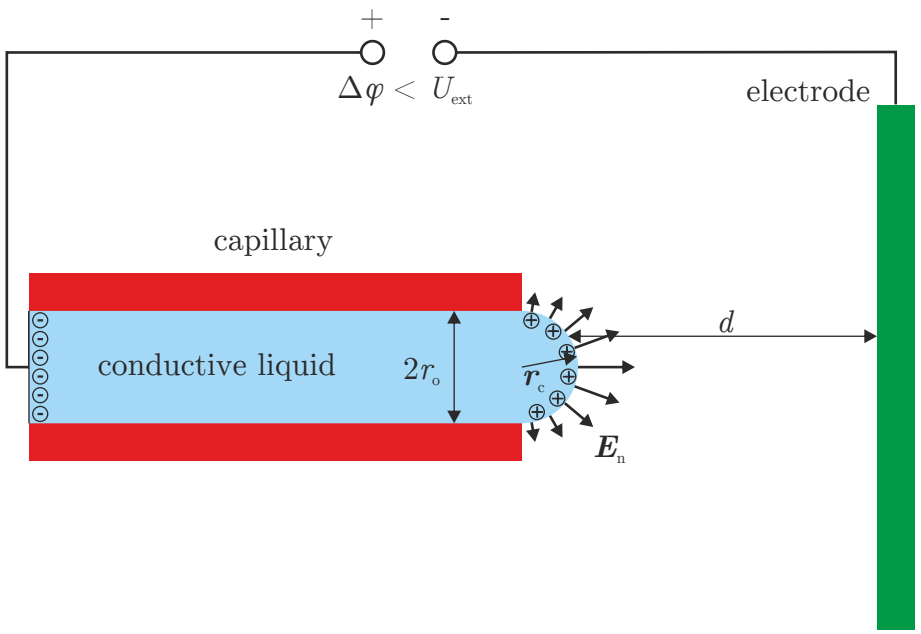

Figure 3.1: Scheme of a capillary with a diameter of $2r_0$ filled with a conductive liquid opposing an electrode at a distance d. A potential difference $\Delta\varphi$ between the liquid and the opposing electrode leads to charge separation within the liquid, i.e. a polarization of the liquid. The electric field normal to the liquid's surface $\boldsymbol{E}_\mathrm{n}$ causes an attractive pressure which is counteracted by the surface tension. The relating pressure depends on the curvature $\boldsymbol{r}_\mathrm{c}^{-1}$ which is maximal (r_0^{-1}) when $r_\mathrm{c} = r_0$.

3.1.1 General concept of colloid emitters

The concept of colloid emitters has much in common with other ESP concepts. It consists of a propellant reservoir, a part to ionize the propellant and an electrostatic acceleration part. In contrast to most other ESP concepts, the ionization process and the electrostatic acceleration process of colloid emitters occur more or less simultaneously and not sequentially. A colloid emitter uses high electric fields to extract charged droplets from a liquid surface. These droplets are then accelerated in the same or an additional electric field to increase the exhaust velocity and thus the mass efficiency of the thruster (refer to Eq. (2.4)). The additional acceleration process of the charged particles is basically the same for all electrostatic thrusters, see section 2.1. On the next few pages the effects behind the droplet extraction are explained.

The extraction is best understood when considering the effects of

an increasing external electric field on the surface of a liquid propellant. When applying a potential difference less than the extraction threshold between the metal electrode and the conductive liquid, the charge carriers attracted by the electrode potential will gather at the liquid surface while the oppositely charged carriers will move to the back electrode within the liquid — a charge separation occurs. This is shown in Fig. 3.1.

For an external electric field E_n, which is normal to the liquid's surface, the free surface charge density σ_f will approach an equilibrium value according to the discussion by Martínez-Sánchez[24] (refer to appendix A.3):

$$\sigma_\mathrm{f} = \frac{\kappa}{\varepsilon} \int_0^t e^{-\frac{t-t'}{\tau}} E_\mathrm{n}(t')\mathrm{d}t'. \tag{3.1}$$

The relaxation time $\tau = \varepsilon\varepsilon_0/\kappa$ depends on the dielectric permittivity $\varepsilon\varepsilon_0$ and the electric conductivity κ of the liquid. For a constant external electric field, Eq. (3.1) reduces to $\sigma_\mathrm{f} = \varepsilon_0 E_\mathrm{n}(1 - e^{-t/\tau})$.

Also, E_n induces an attraction of the accumulated surface charge σ_f, which is counteracted by the pressure related to the surface tension γ on an axisymmetric surface with the curvature $1/r_\mathrm{c}$:

$$\frac{\varepsilon_0}{2} E_\mathrm{n}^2 = \frac{2\gamma}{r_\mathrm{c}}. \tag{3.2}$$

When the traction tension exceeds the surface tension, the liquid surface will become unstable, i.e. for $E_\mathrm{n} > 2\sqrt{\frac{\gamma}{\varepsilon_0 r_\mathrm{c}}}$. As derived in appendix A.3, we assume the special case that the radius r_c of curvature of the surface of the ionic liquid in the capillary equals the radius r_0 of the capillary.

Figure 3.1 depicts a capillary filled with a conductive liquid and a plane electrode opposing the capillary orifice at a distance d. If a potential difference $\Delta\varphi$ is applied between the conductive liquid inside the reservoir and the outer electrode, the electric field normal to the liquid surface is determined by the following expression according to Martínez-Sánchez[24]:

$$E_\mathrm{n} = -\frac{2\Delta\varphi}{r_0 \ln\left(\frac{4d}{r_0}\right)}. \tag{3.3}$$

Using Eq. (3.2) this leads to a criterion for the unstable regime:

$$|\Delta\varphi| > \sqrt{\frac{\gamma r_\mathrm{c}}{\varepsilon_0}} \ln\left(\frac{4d}{r_\mathrm{c}}\right) := U_\mathrm{ext}. \tag{3.4}$$

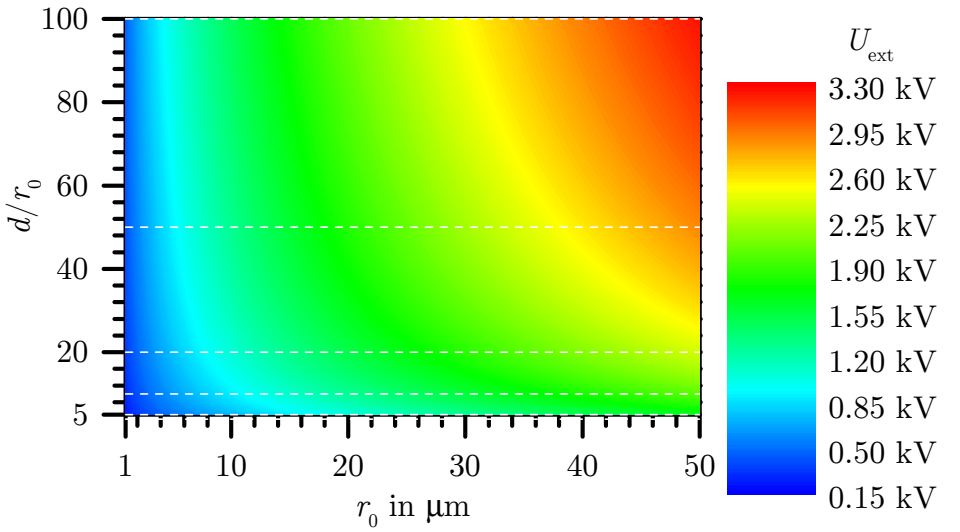

Figure 3.2: Extraction voltage U_{ext} for the ionic liquid EMI-BF_4 with respect to the ratio d/r_0 between the liquid-electrode-distance d and the radius r_0 of the capillary as well as to r_0 according to Eq. 3.4 and the setup depicted in Fig. 3.1. U_{ext} along the white dashed horizontal lines is shown in Fig. 3.3.

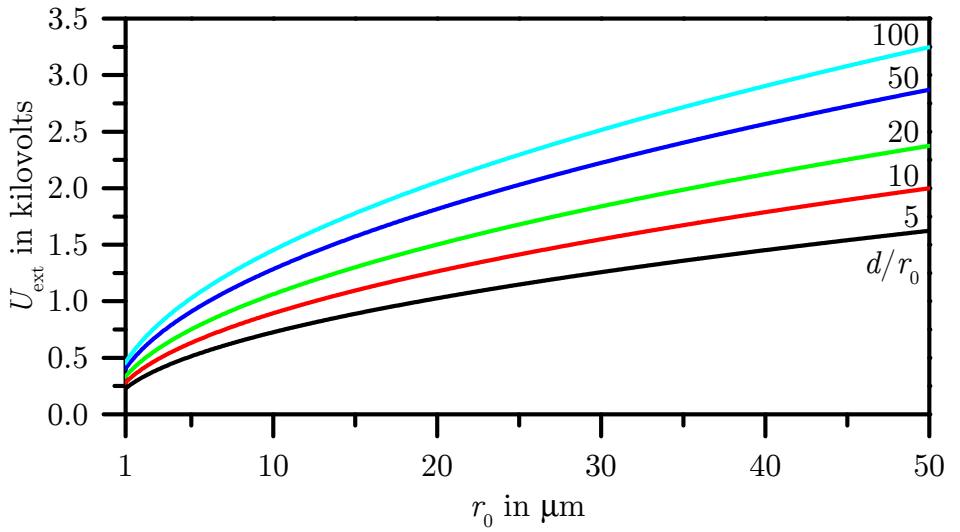

Figure 3.3: Extraction voltage U_{ext} for the ionic liquid EMI-BF_4 with respect to the radius r_0 of the capillary for different values of the ratio d/r_0 between the liquid-electrode-distance d and r_0 according to Eq. 3.4 and the setup depicted in Fig. 3.1. The graphs represent the white dashed horizontal lines in Fig. 3.2.

This means, that miniaturization of a colloid emitter strongly reduces the required potential for generating charged particles. A thinner capillary reduces the extraction voltage: $U_{\text{ext}} \propto \sqrt{r_0}\ln({r_0}^{-1})$ as well as a smaller electrode distance d: $U_{\text{ext}} \propto \ln(d)$. A contour plot of $U_{\text{ext}}(r_0, d/r_0)$ is shown in Fig. 3.2. In Fig. 3.3 line charts of $U_{\text{ext}}(r_0, d/r_0)$ with respect to r_0 for different values of d/r_0 are plotted.

This behavior is in contrast to all other established electrostatic devices, making colloid emitters the desired kind of ESP for miniaturization purposes.

Formation of the Taylor cone

When the electrostatic forces dominate the process, the shape of the liquid surface transforms further. This was investigated and analytically explained by Taylor in 1965 [25]. Taylor and the other early workers on electrospraying observed that the liquid surface at a tube end will transform into a conical shape in strong electric fields. From the apex of this cone a jet of particles can be extracted. Taylor defined two conditions: The surface of the cone must be an equipotential surface and the cone has to be in equilibrium. This yields $\frac{\varepsilon_0}{2}E_{\text{n}}^2 = \frac{\gamma}{r_{\text{c}}}$ at the cone surface (the curvature along the generator of the cone is zero). The radius of curvature r_{c} can be expressed by the distance to the apex r and the semi-vertical angle α of the cone: $r_{\text{c}} = r\tan\alpha$. Such a cone is depicted in Fig. 3.4.

The task now is to find an external electric field, that possesses a normal component of

$$E_{\text{n}} = \sqrt{\frac{2\gamma\cot\alpha}{\varepsilon_0 r}}. \tag{3.5}$$

To fulfill $E_{\text{n}} \propto r^{-1/2}$, the surface potential must have the following form in spherical coordinates:

$$\Phi = \Phi_0 + A\sqrt{r}P_{1/2}\left(\cos\theta\right), \tag{3.6}$$

which yields $\boldsymbol{E}_{\text{n}} = -\nabla\Phi$, where $P_{1/2}\left(\cos\theta\right)$ is the Legendre function of the order $1/2$. To have an equipotential surface,

$$\Phi = \Phi_0 \tag{3.7}$$

must hold for all r, i.e. $P_{1/2}\left(\cos\theta\right) = 0$. This results in $\theta_0 = 130.7°$ (for $0 \leq \theta \leq \pi$, refer to Fig. 3.5) yielding an equipotential conical surface, corresponding to a semi-vertical cone angle of

$$\alpha = 49.3°, \tag{3.8}$$

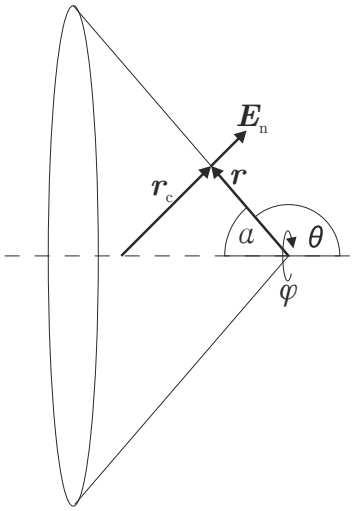

Figure 3.4: Spherical cone with a semi-vertical angle α. The normal electric field $\boldsymbol{E}_n$ at a surface point depends on the radius of curvature $\boldsymbol{r}_c$. r is the distance to the apex. The rotation axis is represented by $\theta = 0$ in spherical coordinates (r, θ, ϕ).

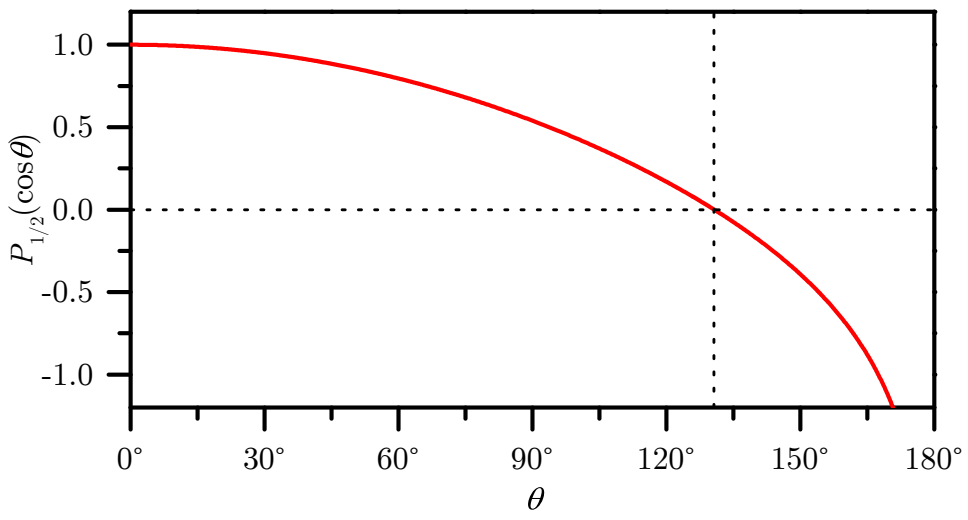

Figure 3.5: Legendre function $P_{1/2}(\cos\theta)$ of the order $1/2$. $P_{1/2}(\cos\theta) = 0$ leads to an equipotential conical surface in the model depicted in Fig. 3.4 ($\theta_0 = 130.7°$) following Eqs. (3.6) and (3.7).

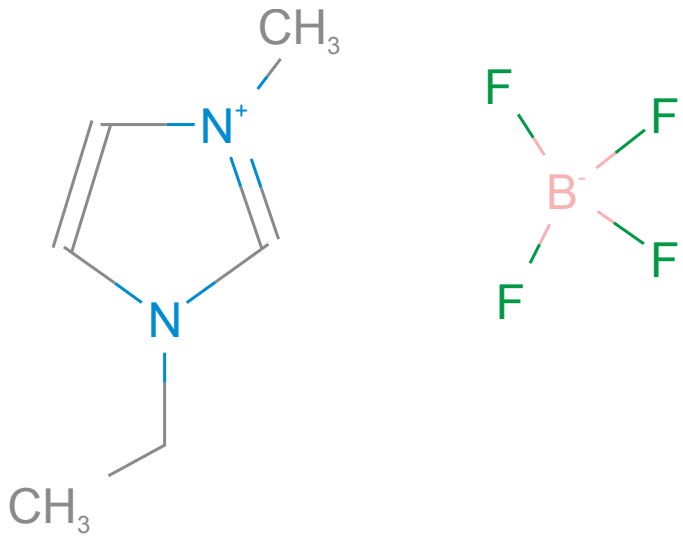

Figure 3.6: Structural formulae of the constituents of the ionic liquid EMI-BF_4 consisting of the cation 1-ethyl-3-methyl imidazolium (EMI, left) and the anion tetrafluoroborate (BF_4, right).

defining the so-called Taylor cone. This cone angle is independent of all other properties of the emitter, after establishing an equilibrium situation.

As the cone apex has an infinite curvature in this mathematical model, the electric field will exhibit a singularity. This means, that at the singularity the electrostatic traction overcomes the surface tension which will cause a droplet emission at the apex. This emission will occur jet-like as long as enough liquid is transported to the cone apex to supply the jet emission. It also means, that the emission will mainly occur at this spot and that the voltage required to maintain extraction may be lower than the starting extraction voltage U_{ext}. These droplets can be accelerated further by an electrostatic grid system to yield the desired thrust.

3.1.2 Ionic liquids as propellant for colloid emitters

In the early second half of the last century first experiments on colloid emitters were considered and performed using mainly liquid metals[26–29] or inorganic compounds dissolved in organic solvents like glycerol[30–32] as well as pure organic liquids[31,33] as propellant.

The so called liquid-metal ion-sources (LMIS) are also based on the concept described in section 3.1.1. Mercury as well as indium,

gallium and cesium were used in LMIS. Except for indium these metals are liquid at or near room temperature and have low vapor pressures[34]. Although they exhibit high conductivities $\sigma > 1\,\mathrm{S\,m^{-1}}$ their surface tensions γ are usually quite high ($\gamma > 0.5\,\mathrm{N\,m^{-1}}$) which requires high extraction voltages according to Eq. (3.4). Cesium with $\gamma_{\mathrm{Cs}} = 71\,\mathrm{mN\,m^{-1}}$ is an exception. Furthermore, the restriction to a single ion type (cations) and their toxicity disqualify liquid metals as ideal media for the use in colloid emitters. In general, the use of other metals is even more disadvantageous as they exhibit the same handicaps and require additional heating.

The use of non-metallic propellants exhibits also several drawbacks. The various solutions of glycerol and inorganic compounds like NaI[32], KOH[31] or $SbCl_3$[30] as well as Carbon[31] are clearly inefficient as the commonly used dilutions are in the range of a few percent (1 % to 10 %). Thus, a huge fraction of the substance is the solvent which cannot be used for propulsion. Therefore such dilute propellants are unsuitable for miniaturized electrostatic propulsion systems as their use contradicts the mass saving approach. Other organic compounds like bis(2-ethylhexyl) phthalate[33], bis(2-ethylhexyl) decanedioate[31] or propylene glycol[33] were also used as propellant. To be employed under vacuum conditions these propellants require an additional source of energetic electrons to initially break intermolecular bonds and provide the necessary amount of ions within the liquid to cause charge accumulation at the liquid tip and to allow for ionization[35] as described in section 3.1.1. Already in these early works, in 1959 Schultz and Branson[33] gave the possible benefits of ionic liquids a vague consideration: *"As an alternative to the electron-source techniques described above for creating positively charged liquid colloids in vacuum, it may be possible to find or synthesize liquid compositions with a sufficiently high number of charge carriers (i.e., positive and negative ions) in solution to permit automatic charging of the liquid surface. This approach will, however, require a great deal of research."*

This leaves the question whether there are better media than liquid metals that may serve as an ion supply. The main prerequisites for these materials are: to be in the liquid state close to or below room temperature, to possess low vapor pressure, high electric conductivity and low ionization energy. These prerequisites are fulfilled only partially by some metals, ionized water or organic liquids. However, during the last decades the focus in electrospray applications was directed onto molten salts[36]. These salts are not dissolved in water, they consist only of cations and anions like NaCl above 800 °C where it is in the

Table 3.1: Physical properties of the ionic liquid EMI-BF_4 at room temperature (25 °C)[40].

physical property	value
density ρ	$1.3\,\mathrm{g\,cm^{-3}}$
melting point T_m	12 °C
decomposition temperature T_d	450 °C
electrochemical window U_w	4.5 V
cation mass m_+	111 u
anion mass m_-	87 u
kinematic viscosity ν_vis	$27.5\,\mathrm{cm^3\,s^{-1}}$
surface tension γ	$52\,\mathrm{mN\,m^{-1}}$
electric conductivity σ	$1.3\,\mathrm{S\,m^{-1}}$
vapor pressure p_0	very low, i.e. not measurable

liquid state. If a salt is liquid near room temperature, it is called ionic liquid (IL). There exists a broad variety of ionic liquids with thousands of cation-anion-combinations. Many are already investigated — each with its own physical and chemical properties. This makes them perfect candidates for ion supply media, since it is possible to design an ionic liquid with the above stated necessary properties. An additional advantage of ionic liquids over liquid metals is their composition out of both cations and anions rather than cations and electrons as in the case of metals. Therefore it should be possible to either emit positive or negative particles[37,38]. To avoid degradation of the ionic liquid due to discharging effects at the back-side electrode, it is even preferable to use the emitter in bipolar mode[39]. To provide a stable thrust in this mode the usage of cations and anions with comparable masses is desirable.

In this work the well-investigated ionic liquid EMI-BF_4[34,38–41] is used. It consists of the cation 1-ethyl-3-methyl imidazolium (EMI) and the anion tetrafluoroborate (BF_4) which are both depicted in Fig. 3.6. The relevant physical properties of EMI-BF_4 are listed in table 3.1. It can be used in a wide temperature range, has a high electric conductivity and a very low surface tension. Its mass ratio between cation and anion is near unity ($m_+/m_- = 1.28$) which makes it suitable for usage

in bipolar emission mode. This makes EMI-BF_4 an ideal candidate as propellant for colloid emitters.

3.2 SU-8 as material for miniaturized colloid emitters

As shown by Eq. (3.4), the main benefit of miniaturized colloid emitters is the reduction of the required extraction voltage U_{ext} due to miniaturization. There are several approaches for fabricating small ionic-liquid feed-through systems and extraction structures, mainly based on micro-electro-mechanical systems (MEMS). In section 3.2.1 a brief review of the recent works in this area is given. The properties of SU-8 as an emitter material are presented in section 3.2.2. In section 3.2.3 the photoactivated chemistry of SU-8 is illustrated.

3.2.1 Review of recent works in miniaturized colloid emitters

The most recent works were performed in the groups of Martinez-Sanchez and Lozano at the MIT using mainly mechanically formed emitter tips[34,42], microfabricated externally wetted emitters[43,44], and porous emitters[45] as well as the groups of Shea at the EPFL[46,47] and Stark at the QMUL[48,49] within the MicroThrust project[50] using silicon-based capillary MEMS devices. Furthermore, the works of Gamero-Castaño[51,52] describing colloid thrusters conventionally build of individual capillaries and a perforated electrode without the usage of MEMS fabrication techniques and of Tajmar[53] using capillary-based MEMS-fabricated LMIS with the propellant indium have to be considered.

Electrospray thruster research at the Space Propulsion Laboratory at the Massachusetts Institute of Technology (MIT)

Preliminary investigations of ionic liquids, especially EMI-BF_4, during the extraction from externally wetted tip-shaped emitters and of their wetting behavior were carried out[34,42]. Based on these results the microfabrication of such externally wetted emitters was proposed[43]. Gassend[44] was able to microfabricate an integrated electrospray device comprising an emitter die with an array of silicon emitters and an electrode die with the extractor electrode and an insulation layer. He

used silicon batch MEMS technology including deep reactive ion etching (DRIE) to create an array of 502 emitters in an area of 113 mm^2. Using both the ionic liquids EMI-BF_4 as well as EMI-Im as propellant with a total extractor dry mass of 5 g (without PPU), an overall thrust of 13 µN at 1500 V extraction voltage could be achieved. A specific impulse of 3000 s at 1000 V extraction voltage was observed. Nevertheless, the amazing results could only be maintained for several minutes as there literally exists no feed system for the propellant. A common feedthrough in the emitter die would not ensure the wetting of the whole emitter array. Therefore more recent approaches were directed towards the fabrication of porous emitters[45]. They microfabricated arrays of up to 480 porous Ni emitters within a $1 \times 1\,cm^2$ area. With conventionally build stainless-steel extraction grids they achieved overall currents of 400 µA at 1600 V extraction voltage and 200 µA at 1100 V extraction voltage using EMI-Im and EMI-BF_4, respectively. Although the feeding issues could be solved by this approach, a strong current decay was observed.

Furthermore, Lozano[37] considered electrospray emission of ionic liquids from flat dielectric surfaces. We will come back to this point later in this section.

Microfabrication of electrospray thrusters based on capillary arrays within the MicroThrust project[50] at the École polytechnique fédérale de Lausanne (EPFL) and the Queen Mary University of London (QMUL)

The group of Shea at EPFL designed and fabricated several versions of integrated out-of-plane electrospray thruster arrays using microfabricated silicon capillaries[8,46,54]. In Krpoun and Shea[46], capillary arrays were formed in silicon using several etching and oxidation steps including DRIE. With these methods the capillary tops were additionally shaped to a flat ring surface with a wall thickness of at least 4.5 µm. The inner diameter of the capillaries was 24 µm, they possessed a height of 70 µm and a pitch of 250 µm while the distance to the 150 µm to 200 µm electrode openings was 90 µm. The extractor electrode was clamped onto the capillary chip and aligned using ruby balls. With the ionic liquid EMI-Im extraction voltages around 1000 V could be achieved, a stable operation in ionic mode was possible at 1200 V. The sign of the extraction voltage was alternated with 0.25 Hz to circumvent electrochemical reactions. A total thrust of 100 µN on a $5 \times 5\,cm^2$ surface could be extrapolated from the single emitter thrust of 2 nN. They

also employed a technique of placing 5 µm silica spheres within the capillaries by silanization to increase the hydraulic impedance which may facilitate the ionic mode of particle emission.

In the works of Ryan et al.[48] and Dandavino et al.[55] an attempt was made to further improve this kind of emitters by fabricating capillaries with an inner diameter as low as 5 µm using the same micromachining methods. Also, the electrode layer was bonded onto the emitter layer using a SU-8 based resist of 50 µm thickness. With this fabrication technique a packing density of 1600 emitters per cm^2 was realized. Capillaries with an inner diameter of about 10 µm could be achieved. TOF (time of flight) measurements on a single emitter in bipolar mode using EMI-BF_4 revealed emission only in droplet mode. A specific impulse of 1100 s at 700 V extraction voltage could be observed.

The most recent results of the MicroThrust project[47,49,56] show the incorporation of additional accelerator electrodes on arrays of these capillary emitters while the inner diameter of the capillaries could be reduced to (7.9 ± 0.5) µm. Emitter arrays of 91 and 127 emitters with packing densities of 125 and 213 emitters per cm^2 respectively, were built. TOF measurements in bipolar mode using EMI-BF_4 in a gravity-fed system yield up to 7 µN overall thrust at 2000 V acceleration voltage at a maximum I_{sp} of 1000 s.

Additional related research

Gamero-Castaño and Hruby[51,57] developed a complete colloid thruster system based on conventional stainless steel needles as capillaries. They fabricated an array of 57 emitters on a circular area of about 20 cm^2. The needles used had an inner diameter of 30 µm and a length of 1 cm, the outer diameter was 180 µm. Operating in unipolar mode, they achieved a thrust of 190 µN at a specific impulse of 120 s by maximizing the thrust and a thrust of 200 µN at a specific impulse of 390 s by maximizing the propellant speed. No MEMS fabrication technique was applied on this thruster, it was fully fabricated conventionally.

Finally, the work of Tajmar[53] has to be mentioned, as he developed a miniaturized FEEP emitter array based on capillaries. Although working with the liquid metal indium (if properly heated) as propellant, the concept for colloid emitters stays the same. The thruster comprised 21×21 emitters on 25 mm^2. Several fabrication approaches were tested taking into account the need for a metal as capillary material to ensure the wetting by indium. For this approach to work,

extremely sharp capillary edges are required according to Eq. (3.9). A device prepared by excimer laser processing proved to be operational. An extraction voltage as low as 300 V could be achieved. This device can only work in unipolar mode and requires additional neutralization. Furthermore, the operation temperature of these thrusters is well above room temperature, as the melting point of indium is at 150 °C, i.e. such a thruster has to be heated further than the other discussed colloid emitters (e.g. melting point of EMI-BF_4: 12 °C) to maintain a liquid state of the propellant.

Relevance of the above stated approaches on micro-fabricated SU-8-based capillary emitters shown in this work

All of the described approaches show at least a minor challenge on the way to a fully functional miniaturized field effect emitter. We propose a new concept which resembles mostly the emitter concept suggested by the group of Shea. The use of a capillary approach facilitates the propellant feed in contrast to an external-wetting approach. Conventionally built and clustered emitters like in the works of Gamero-Castaño are ruled out by the general approach of utilizing micro-fabrication techniques to fully benefit from the miniaturization as shown in section 3.1.1. In the previous section we discussed the benefits of ionic liquids over liquid metals - a design decision which negates an approach like that of Tajmar for our purposes.

Our approach is to micro-fabricate capillary structures in the epoxy-based resist SU-8. Additionally, our design includes integrated electrodes for each emitter, which cannot be realized using solely silicon as material. Using another material than silicon may also yield lower extraction voltages. The properties and chemical processes during fabrication of SU-8 are shown in the following.

3.2.2 Properties of SU-8 as an emitter material

In this work the epoxy-based resist SU-8 is employed as capillary and spacer material. SU-8 exhibits several properties which make it a promising alternative to silicon for fabricating such miniaturized devices. It was patented by IBM in 1989 as a photoresist which allows one to obtain very high aspect ratios in the lithographic process[58,59]. Such high aspect ratios give SU-8 the suitability to serve as a functional layer. The use of a photoresist makes the processing and fabrication of individual layers less complex and time-consuming than DRIE used for

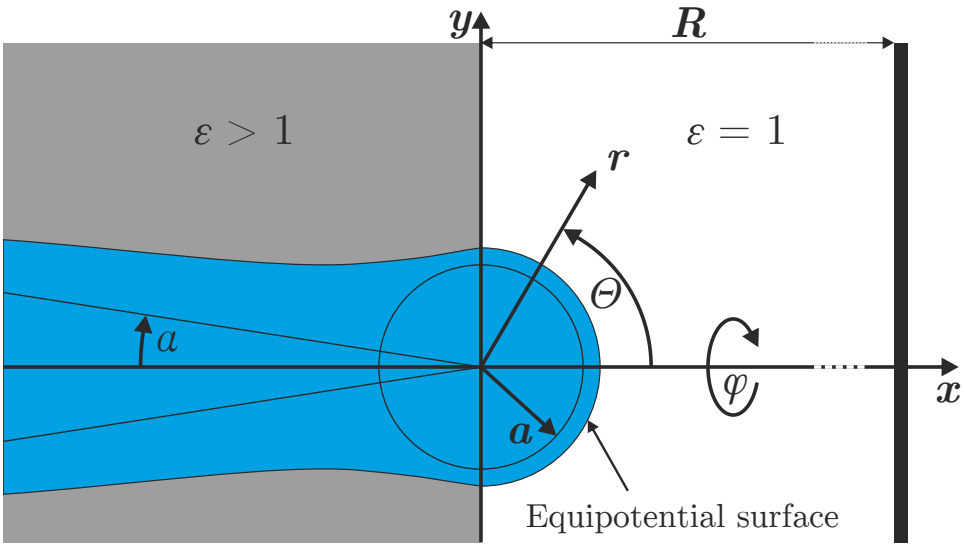

Figure 3.7: The SOC model after Lozano et al.[37] with $\varepsilon > 1$ for $x < 0$ (grey) for a sphere with radius a and an infinite cone with half-angle α. To represent the conductive liquid (blue) an equipotential surface was chosen. The electrode (black) is placed at a distance R.

fabricating high aspect silicon structures. Furthermore it is possible to use direct laser writing to create 3D-patterns in SU-8[59,60]. SU-8 may also be combined with established silicon technology to yield the most advantageous fabrication processes. In addition to these fabrication advantages, SU-8 possesses many desirable chemical and physical properties. It is chemically and mechanically stable and poses no biological hazard. The outgassing of SU-8 can also be reduced by established processing steps. The breakdown electric field[61,62] was measured to be $1.1 \times 10^5\,\mathrm{V\,\mu m^{-1}}$ to $4.4 \times 10^8\,\mathrm{V\,\mu m^{-1}}$. The electric volume resistivity[63] ρ_{SU8} is in the order of $10^{14}\,\Omega\,\mathrm{m}$. The relative permittivity[61] $\varepsilon_{\mathrm{SU8}}$ of the material is in the range of 3 to 4.5 which may enhance the emission behavior of ionic liquids in contrast to materials of higher dielectric constant such as silicon ($\varepsilon_{\mathrm{Si}} = 12$) as described in Lozano et al.[37].

Lozano et al.[37] propose a sphere-on-cone (SOC) model to represent the conductive liquid inside a dielectric capillary with a relative permittivity ε and an inner diameter of $2r_{\mathrm{m}}$, as shown in Fig. 3.7. A sphere with radius a is superimposed to the origin of an infinite cone with half-angle α. Two different electric potentials occur inside the dielectric and the vacuum space between capillary and an electrode at a distance R and a potential $-V$ according to their different permit-

tivities. The boundary condition is, that the SOC structure is at zero potential. A good approximation for a cylindrical liquid shaped with a meniscus at its tip is given by a combination of $\alpha = 4°$ and the factor $f = 1.15$ that determines the selected equipotential around the SOC structure. The separation constant ν describes the difference between the solutions of the Laplace's equation for the dielectric as well as the vacuum, respectively. ν can be determined for a set of ε, α according to Eq. (A.53). Above considerations cumulate in the following approximation for the threshold voltage V_m for extraction between conductive liquid and electrode at which the meniscus instability occurs (Eq. (15) of Lozano et al.[37]):

$$V_\mathrm{m} > \sqrt{\frac{\gamma r_\mathrm{m}}{\varepsilon_0}} F\left(r_\mathrm{m}, R, \nu, f\right), F = 2\frac{(R/r_\mathrm{m})^\nu + f^{-2\nu-1} - 1}{\nu + (\nu+1)f^{-2v-1}}. \tag{3.9}$$

The corresponding separation constants will be $\nu_\mathrm{SU8} = 0.249$ as well as $\nu_\mathrm{Si} = 0.295$ for SU-8 ($\varepsilon_\mathrm{SU8} = 3.7$) and silicon ($\varepsilon_\mathrm{SU8} = 12$), respectively. With the ionic liquid EMI-BF4, the corresponding starting voltages for a capillary diameter of 10 µm and a capillary-electrode distance of 100 µm will be $V_\mathrm{SU8} = 526\,\mathrm{V}$ and $V_\mathrm{Si} = 577\,\mathrm{V}$, i.e. a relative voltage reduction of 10 %. The gain is even higher, when the electrode is placed further away, e.g., $V_\mathrm{SU8} = 810\,\mathrm{V}$ to $V_\mathrm{Si} = 958\,\mathrm{V}$ at $R = 500\,\mu\mathrm{m}$, although the overall increase in voltage has to be taken into account in this case.

As SU-8 exhibits a very high resistivity $\rho_\mathrm{SU8} \approx 10^{14}\,\Omega\,\mathrm{m}$, especially in contrast to silicon $\rho_\mathrm{Si} < 10\,\Omega\,\mathrm{m}$, it is better suited for a use as a colloid emitter in bipolar mode (alternating applied voltage)[37]. The reason is the finite nature of the field enhancement effect of low-ε dielectrics in comparison to conducting capillary materials, i.e., the voltage alternation period T has to be lower than the charge relaxation time $\tau_\mathrm{r} = \varepsilon\varepsilon_0\rho$. Considering only this effect yields a lower boundary for the alternation frequency of $T_\mathrm{SU8}^{-1} = 1\,\mathrm{mHz}$ for SU-8 or $T_\mathrm{Si}^{-1} = 1\,\mathrm{GHz}$ for Si, respectively. The latter demands very fast high-voltage PPUs as well as an almost instantaneous buildup of the Taylor cone and the required charge separation within the ionic liquid.

This makes SU-8 the material of choice for the colloid emitter concept investigated in this work.

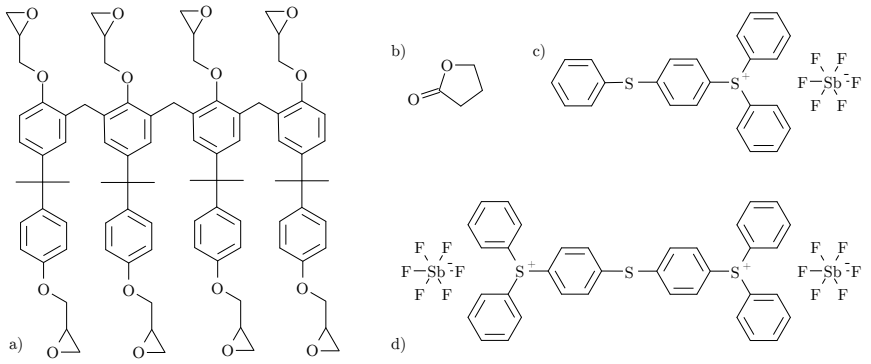

Figure 3.8: The constituents of the negative tone photoresist SU-8: epoxide oligomer based on bisphenol A diglycidyl ether (a), solvent γ-butyrolacton (b), and photoacid generators (PAG) (thiophenoxyphenyl)diphenylsulfonium hexafluoroantimonate (c) and bis(diphenylsulfonium(diphenylthioether hexafluoroantimonate)) (d).

3.2.3 Chemical reactions transforming SU-8 in the microfabrication process by photolithography

SU-8 consists of an epoxide-based oligomer (Fig. 3.8 (a)) and up to 10 wt. % of a photoacid generator (PAG) which are solved in γ-Butyrolactone (Fig. 3.8 (b)). The dilution grade defines the viscosity of the resist and the height of the resist film after coating. Recently, there are also SU-8 resists with cyclopentanone as solvent commercially available[64]. The oligomer consists of four bisphenol A diglycidyl ether. The name of the resist originates from the eight epoxide groups in the oligomer. This leads to eight possible polymerization sites, yielding a very strong cross-linking. As PAG a blend of (thiophenoxyphenyl)diphenylsulfonium hexafluoroantimonate (Fig. 3.8 (c)) and bis(diphenylsulfonium(diphenylthioether hexafluoroantimonate)) (Fig. 3.8 (d)) is used.

The PAG have a strong absorption band at 300 nm, which is redshifted with respect to the absorption of other triarylsulfonium salts due to the resonant phenylthio group[65]. When SU-8 is exposed to ultraviolet radiation, an incident photon excites the PAG molecule into the lowest singlet excited state as depicted in Fig. 3.9 (a). Besides the main relaxation paths like photon or phonon emission, the PAG molecule may undergo heterolytic (cleavage into anion and cation) or, with a lower probability, homolytic (cleavage into radicals) fission. Another path is the intersystem crossing (ISC) into a triplet state (cf. Fig. 3.9 (b)) from where the cleavage occurs. Dektar and

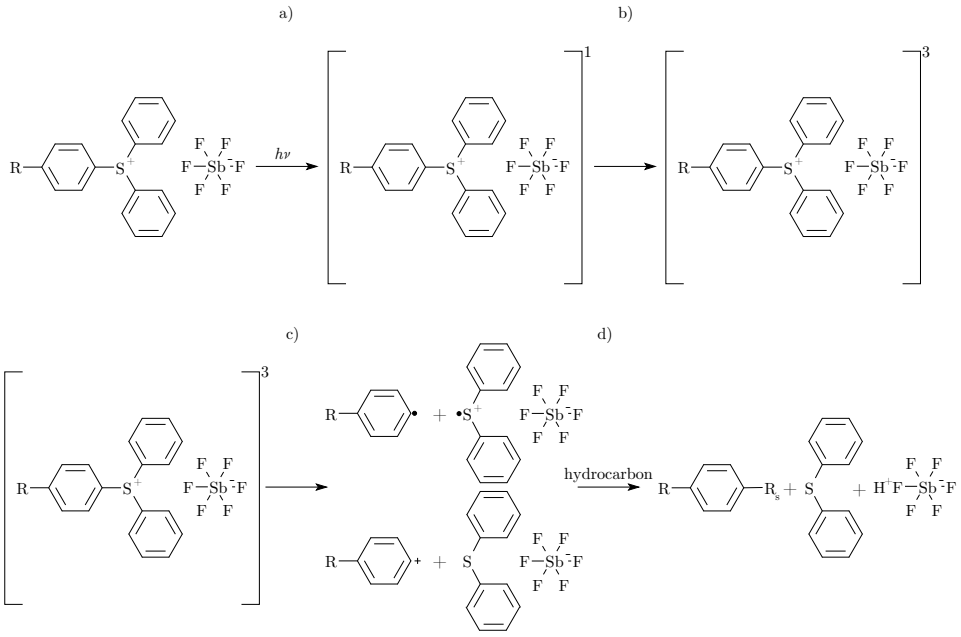

Figure 3.9: Chemical behavior of the photoacid generator (PAG) under ultraviolet radiation. Photoactivation of the PAG into a singlet state (a). Intersystem crossing into a more stable triplet state (b). Homolytic (top) and heterolytic (bottom) fission of the PAG (c). Creation of the acid $H^+(SbF_6)^-$ by reaction of the radicals and ions from (c) with each other as well as with the solvent and with the epoxide oligomer (d).

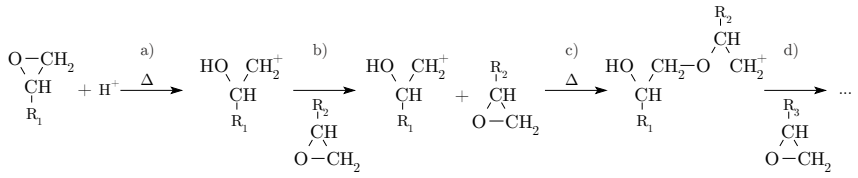

Figure 3.10: Cationic ring-opening polymerization of the epoxide oligomer. The acid generated by the photoactivation of the PAG activates an epoxide chain of the oligomer (a). The oligomer functions now as cationic intermediate. Another epoxide chain (b) can now be activated thermally (c) by this intermediate and thus leading to a chain growth. This process propagates further (d) and leads to a highly cross-linked polymer.

Hacker[65] mention, that the singlet state may be stabilized by the phenylthio group and that the ISC cross section may be enhanced. Both effects lead to a larger probability for the ISC path than the direct cleavage path from the singlet state. Therefore the heterolysis and homolysis occur mainly from the triplet state which is shown in Fig. 3.9 (c). Acid is now formed by the reactions between the radicals and the cations with solvent and epoxide oligomers as well as with the other fragments of the PAG cleavage (cf. Fig. 3.9 (d))[66].

The acid may now activate the epoxide sites of the oligomer if enough thermal energy is provided. This initiates a cationic ring-opening polymerization process[67–69]. When the epoxide chain is broken, a hydroxyl group is formed while the former epoxide oligomer functions as cationic intermediate to activate other epoxide sites which will then function as intermediate. This chain growth propagates through the UV exposed areas of the resist film. As each oligomer possesses eight epoxy sites a high degree of cross-linking can be achieved. The whole process is illustrated in Fig. 3.10.

This polymerization leads to fully cross-linked SU-8 which has a glass transition temperature of 200 °C and degrades at 380 °C. The thickness of the SU-8 layer can be varied in the range from 2 µm to 300 µm by diluting the SU-8. In this work SU-8 50 was used which leads to a resist thickness of 35 µm to 120 µm.

3.3 Micro-fabrication of colloid emitters

In the previous sections we showed the superiority of colloid emitters to other electrostatic propulsion concepts with respect to the miniaturization of spacecraft thrusters, the possibility of using ionic liquids as propellant, and the current research in the field of micro-fabricated FEEP/colloid emitters. These surveys led to the epoxy-based photoresist SU-8 as material of choice for the microfabrication of capillary-based colloid emitters. In this section the methods and sequences used for the microfabrication of such an emitter are described.

3.3.1 Process flow of the fabrication of the capillary emitters

Our final design approach comprises an array of capillary emitters each with its own orifice in the extraction electrode, refer to section 3.5.1, Fig. 3.13. To fabricate such a device, several microfabrication steps

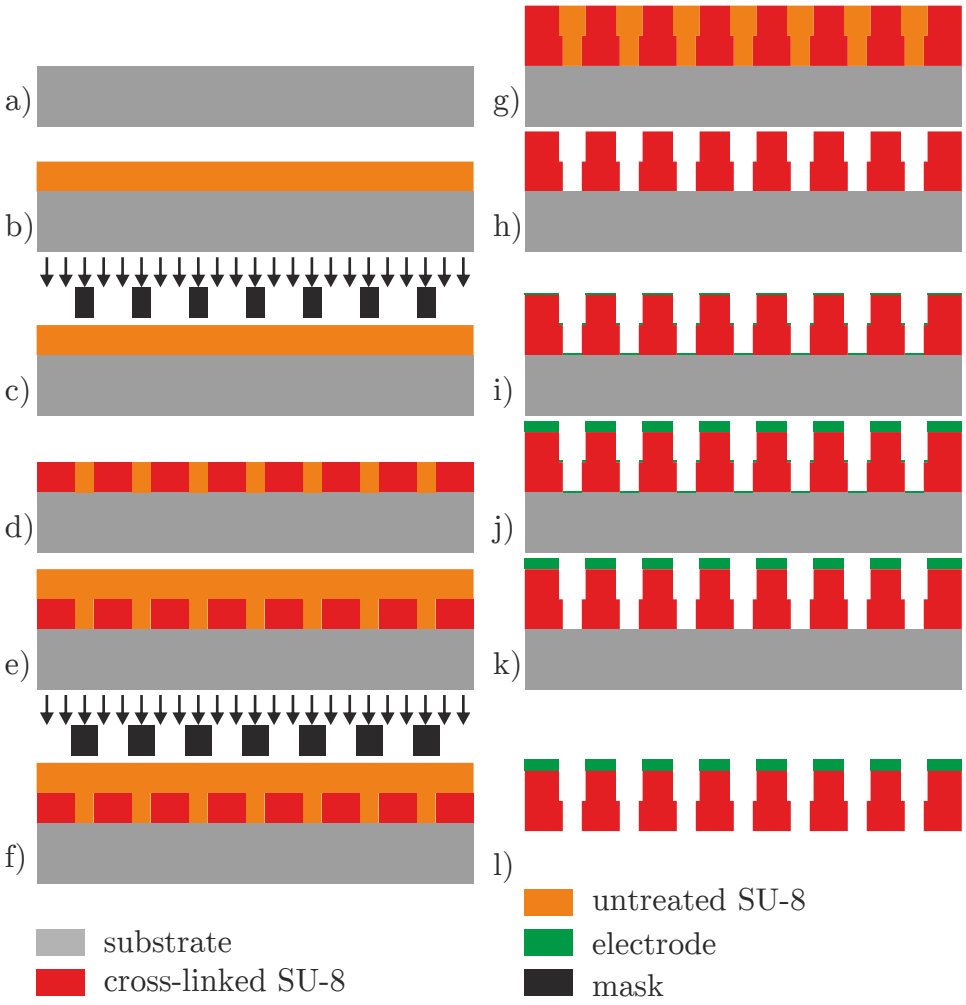

Figure 3.11: General process flow of device fabrication. Cleaning and dehydration of the substrate (a). Spin coating of the capillary SU-8 layer and soft bake (b). UV exposure using the capillary mask (c). Cross-linking of the exposed parts in the capillary SU-8 layer due to PEB (d). Spin coating of the spacer SU-8 layer and soft bake (e). UV exposure using the spacer mask (f). Cross-linking of the exposed parts in the spacer SU-8 layer due to PEB (g). Developing of both the capillary and spacer SU-8 layers (h). Thermal evaporation of the seed layer (i). Electroplating of the electrode (j). Removal of the seed layer on the substrate and capillary layer surface (k). Removal of the substrate (l). Depending on the device design, process steps may be iterated or omitted.

have to be conducted. These steps are shown in the order of the process flow in Fig. 3.11. Variations of the final design can be fabricated also by iterations or omissions of one or more steps. All parameters used during SU-8 treatment were generally chosen according to the SU-8 process guidelines[70] or slightly altered according to our experience.

(a) First, the substrate was cleaned and rinsed with acetone and isopropyl alcohol and then singe-baked on a hot plate at 200 °C for at least five minutes (Fig. 3.11 (a)). The singe-bake was carried out to volatilize remaining liquids and adsorbed water primarily to gain a better adhesion of the resist on the substrate. If not otherwise specified, 2 inch wafers of (100) silicon were used as substrates. This substrate orientation yields the possibility to etch liquid supply lines into the substrate after the top processing.

(b) The second step ensures the homogeneous deposition of the SU-8 resist on the substrate and the evaporation of the solvent. Therefore it was spin coated generally at 3000 revolutions per minute (rpm) for 30 s after a short spread cycle at 500 rpm. In addition to the above mentioned possibility to vary the layer thickness by different SU-8 dilutions, it could also be varied by altering the angular speed during spin coating. As we used only SU-8 50 of *MicroChem Corp.*[70] the layer thickness could be altered from 35 µm to 120 µm. Then the wafer was slowly heated on a hot plate in at least two steps: a pre-bake at 65 °C for 300 s and a final step at 95 °C for 1000 s. The hardened and (almost) solvent free resist is homogeneously deposited on the substrate (Fig. 3.11 (b)).

(c) Following spin coating the main part of photolithography took place using a *SUSS MA-56* mask aligner. The wafer was aligned roughly ($\approx 50\,\mu m$) to a photomask defining the capillary pattern, refer to Fig. 3.12 (a). The ultraviolet light emitted from a mercury-vapor lamp ($5\,mW\,cm^{-2}$ at 365 nm, $9\,mW\,cm^{-2}$ at 405 nm) exposed both the mask and the underlying resist film (Fig. 3.11 (c)) for 60 s. This yields the formation of photoactivated acid in the exposed parts of the resist due to the PAG according to Fig. 3.9.

(d) After the UV exposure the post exposure bake (PEB) was conducted. For this purpose, the exposed wafer was heated in two steps on a hot plate, at 65 °C for 60 s and at 95 °C for 250 s. The added thermal energy catalyzes the cross-linking process (Fig. 3.10) of the epoxide oligomers (Fig. 3.8 (a)) in those areas where the PAG was decomposed into an acid by UV exposure. The mask pattern has been transferred into the SU-8 capillary layer (Fig. 3.11 (d)).

(e) A second layer (spacer layer) of SU-8 was spin coated in a similar

fashion as in step (b) on top of the previously exposed and cross-linked capillary layer (Fig. 3.11 (e)). A soft bake was also conducted despite the additional heating of the underlying SU-8 layer. This was possible as it did not alter the already post exposure baked capillary layer.

(f) The wafer was aligned very accurately ($< 5\,\mu m$) to a photomask containing the spacer pattern (Fig. 3.12 (b)) using alignment marks both in the capillary layer pattern and spacer mask pattern. The wafer was then again exposed to UV radiation to transfer the layer pattern into the second SU-8 layer and activate the PAG (Fig. 3.11 (f)). The exposure time was increased in comparison to step (c) due to the lower reflectivity of the underlying SU-8 layer compared to the reflectivity of the substrate. As the spacer layer definition exposes only areas of the capillary SU-8 layer which were already exposed and post exposure baked, the additional UV exposure of the capillary layer did not influence its properties.

(g) The second PEB was carried out using the same parameters as in step (d) to deliver the thermal energy required to cross-link the epoxide oligomers within the SU-8 resist. This results in two SU-8 layers containing fully cross-linked SU-8 comprising both the capillary (first layer) and spacer (second, i.e. top, layer) pattern (Fig. 3.11 (g)).

(h) To remove the remaining unexposed and therefore not cross-linked SU-8 within both the capillary and spacer layer the development was conducted using the solvent-based developer *mr-Dev 600* of *micro resist technology GmbH* [71]. The wafer was developed for at least 600 s depending on the resist height and lateral structure dimensions. This was done in an ultrasonic bath to ensure a fully developed device structure comprising only fully cross-linked SU-8 forming an array of capillaries and an array of orifices with larger diameter as depicted in Fig. 3.11 (h).

(i) To deposit the electrode on top of the spacer layer, a seed layer consisting of 5 nm chromium followed by 30 nm copper was thermally evaporated on top of the spacer layer. The chromium yields a better adhesion of the actual seed layer of copper. This seed layer serves as electrode during the electroplating process described in step (j). The films of chromium and copper were also deposited on the unconcealed top surfaces of both the capillary layer and the substrate during the same process (Fig. 3.11 (i)).

(j) A 13 µm thick nickel electrode was electro-plated on top of the seed layer (Fig. 3.11 (j)). This was done by placing the wafer in a nickel sulphamate electrolyte bath [72] and applying a current between the seed layer and an additional electrode also placed in the electrolyte

for 2000 s at a current density of $10^4\,\mathrm{A\,m^{-2}}$.

(k) The remaining Cr/Cu-layer on the unconcealed top surfaces of both the capillary layer and the substrate was removed using Ar^+ ion beam etching (Fig. 3.11 (k)).

(l) To form an array of single emitter structures each comprising a capillary and an electrode orifice separated by a spacer layer the substrate was removed using wet chemical etching. Therefore the whole wafer was placed in a potassium hydroxide solution (20 wt. %) and stirred at an elevated temperature (50 °C) until only the SU-8 membrane of emitter arrays remained.

Depending on each individual device design slight variations of the process flow protocol have been conducted to fabricate that emitter. In the following the altered process sequences will be mentioned when ever such samples are discussed.

3.3.2 Pattern design for capillary and spacer layer

To fabricate arrays of colloid emitters using photolithography, several photomask patterns were used to define the capillary as well as the spacer layers. A major constraint was that the upper layers must not contain areas to expose which overlap with non-exposed areas in underlying layers. If the constraint is not followed, previously unexposed areas of the lower layer would be unintentionally exposed during the exposure of an upper layer and the intended pattern would be destroyed. This implies that in our design the orifices in the spacer layer have to be larger than the orifices of the underlying capillary layer. As the task of the spacer layer is to provide physical contact between capillary layer and electrode without allowing electrical contact, i.e. to prevent the liquid from flowing to the electrode, the spacer layer needs to have larger orifices than the capillary diameter in concordance with the design rule to fulfill the constraint.

A typical mask pattern of a capillary layer consists of a square grid pattern of filled circles of radius r in a square arrangement with pitch p. The side length of the whole pattern is a. As the exposed parts remain after the development process, orifices of the radius r were formed into the capillary layers. A scheme of the capillary mask pattern is depicted in Fig. 3.12 (a). The pattern size was $5 \times 5\,\mathrm{mm^2}$ for all samples. The capillary radii varied from 5 µm to 50 µm, while the pitch was either 200 µm or infinite (in 1 or 2 dimensions), i.e. a square grid of capillaries, a row of capillaries or a single capillary. Figure 3.12 (b) shows a scheme of the top view of a developed single capillary layer on the substrate,

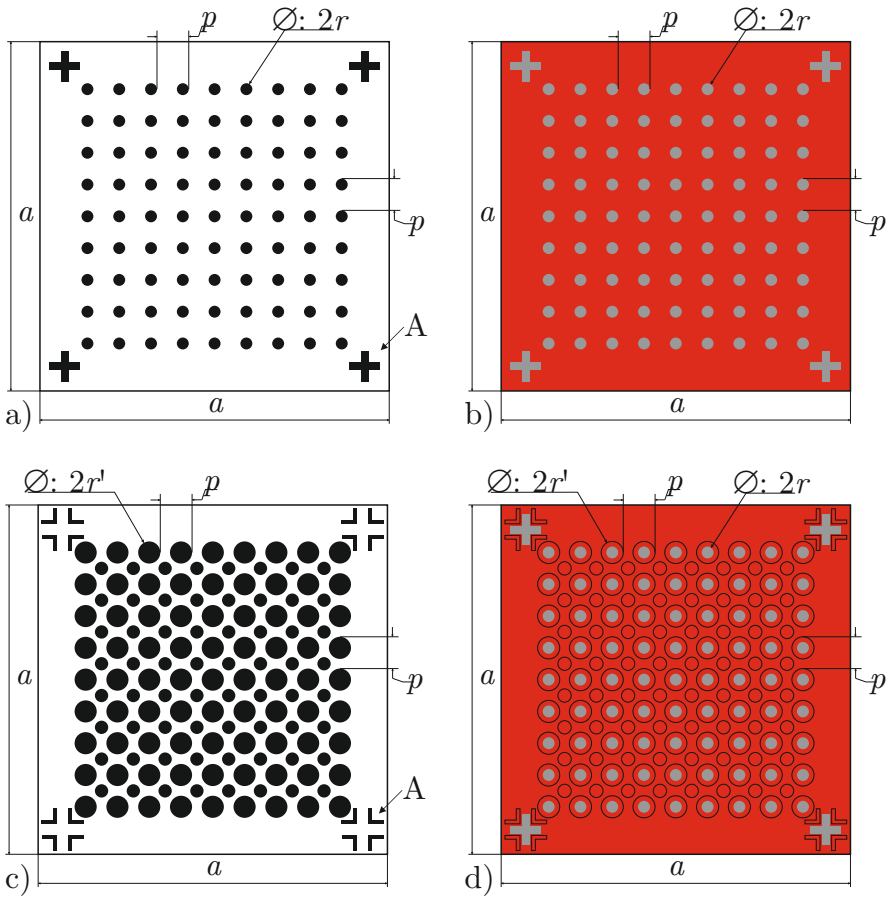

Figure 3.12: Schemes of photomask pattern for the capillary (a) and the spacer (c) layers and of top views of a developed capillary layer (b) and a spacer layer on top of a capillary layer (d). The according legend is the same as in Fig. 3.11. The capillary pattern consists of an array of capillaries with radii r and a pitch p. The spacer pattern comprises orifices with radii r' aligned concentrically to the capillaries and additional openings for stress reduction. The pattern of the SU-8 of the spacer layer on top of the SU-8 of the capillary layer is contoured in scheme (d). Alignment marks A are patterned in the corners of each sample, whose overall lateral dimension is a.

i.e. a structure after the process steps (a)-(d) and (h) according to Fig. 3.11.

The pattern for the spacer layer has the same pitch as that for the capillary layer but larger orifice radii r' in the range of 20 µm to 150 µm. Additionally, there are openings in the areas between the extraction grid orifices to reduce stress within the spacer layer, their size differs from the extraction grid orifice radii. Obviously, these openings cannot be implemented in the capillary layer, as the ionic liquid would fill these additional capillaries. The corresponding mask for the spacer layer is shown schematically in Fig. 3.12 (c). A scheme of a developed spacer layer pattern on top of a capillary pattern and the substrate is depicted in Fig. 3.12 (d), it shows the status after fabrication steps (a)-(h), i.e., before electrode deposition and substrate removal.

To precisely align both the capillary and spacer patterns as performed in process step (f) (Fig. 3.11 (f)), alignment marks were implemented in the pattern design. These marks are also shown in the schemes in Fig. 3.12 at the corners of each sample pattern.

In the next section samples microfabricated with the methods and processes described in this section are investigated microscopically to characterize their structural properties and test their functionality.

3.4 Fully integrated SU-8 capillary emitters

Several stages of the SU-8 capillary emitter array fabrication after different fabrication steps were investigated microscopically (3.4.1) and the permeability of these devices was tested (3.4.2). Extraction tests using an applied voltage between the integrated electrode and the propellant were also performed (3.4.3).

3.4.1 Microscopic investigations of the emitters

In section 3.3 the fabrication steps and photolithographic patterns for an array of capillary colloid emitters with an integrated extraction electrode were introduced.

Figure 3.13 depicts this integrated emitter design, consisting of a sample holder, 30 µm to 120 µm long SU-8 capillaries, a 30 µm to 120 µm thick spacer and a 13 µm thick extraction electrode. This design was fabricated via photolithographic SU-8 processing and with thermally evaporated as well as electroplated electrodes according to the process flow in Fig. 3.11. The whole set of process steps from step (a) to (l)

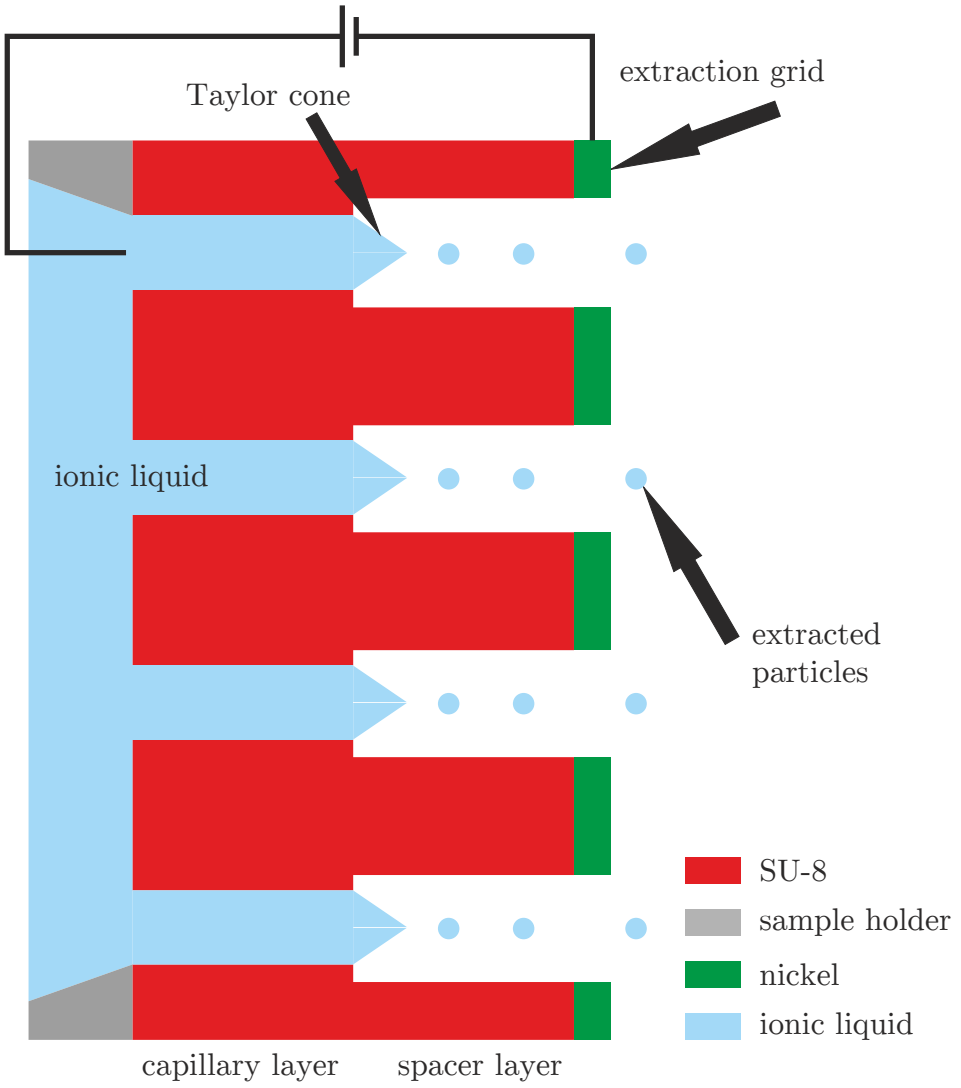

Figure 3.13: Scheme of a highly integrated emitter design according to the fabrication process flow shown in Fig. 3.11. An array of single capillary emitters made of SU-8 is bonded onto a sample holder. Each emitter consists of a capillary, a spacer and an extraction electrode. When applying a voltage between ionic liquid and grid, charged particles may be extracted from the tips of the field induced Taylor cones.

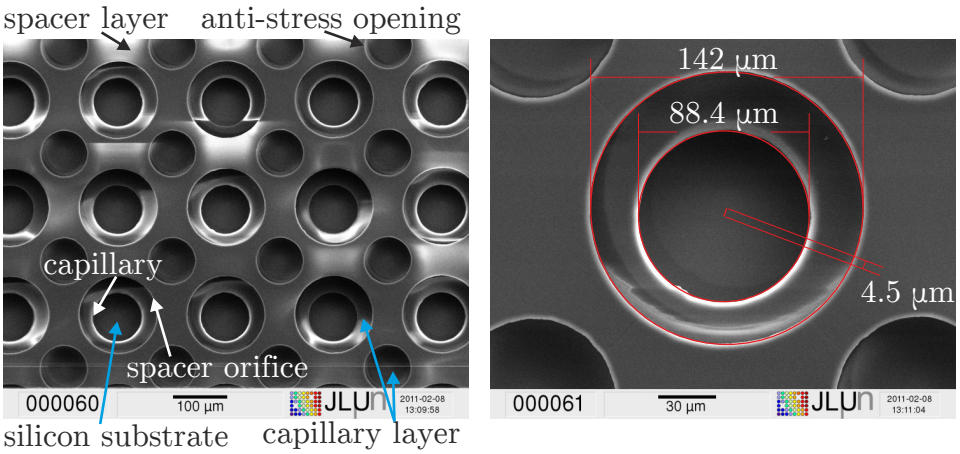

Figure 3.14: Left: SEM image of an array of SU-8 capillaries with corresponding spacer orifices on top of a silicon substrate. The additional openings in the space between the capillaries were implemented to prevent cracking of the SU-8 layers. Right: Zoom-in of the left image with an example measurement of the alignment. The concentric alignment of the spacer orifice and the capillary could be realized with an accuracy better than $< 5\,\mu m$.

(Fig. 3.11) was applied to fabricate samples of this design. Afterwards the sample arrays were each bonded onto a sample holder for testing. Samples produced using this design were characterized by scanning electron microscopy (SEM).

Alignment between the capillary and spacer SU-8 layers

To investigate the alignment between the spacer and capillary layer, samples at the stage of the process step (h) (Fig. 3.11) were investigated by SEM. A capillary pattern according to Fig. 3.12 (a) was written into a single layer of SU-8 deposited onto the silicon substrate. Then another layer was deposited on top of this capillary layer. This layer was exposed with a spacer pattern according to Fig. 3.12 (c). Before the second exposure the mask had to be aligned with the predefined pattern in the first SU-8 layer on the sample. After developing both layers the resulting structure should ideally resemble the pattern shown in Fig. (3.12) (d).

Figure 3.14 shows a SEM image of such a structure. An array of different sized orifices can be seen, it comprises stand-alone openings and two concentric openings. The first ones were written only in the

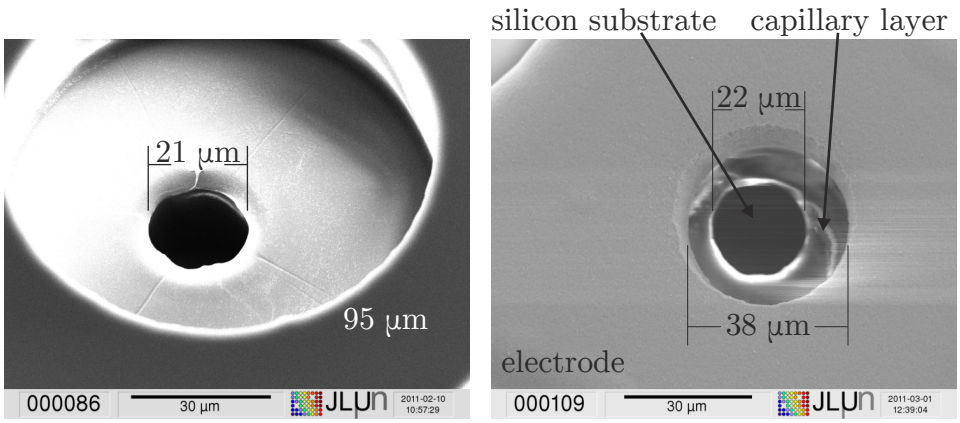

Figure 3.15: Left: SEM image of an array structure with narrow capillaries with an inner diameter of 21 µm and a spacer orifice of 95 µm. The sample is at process stage (h), refer to Fig. 3.11. Right: SEM image of a capillary array structure including an additional integrated nickel electrode. For handling reasons during the SEM imaging, the sample is at process stage (k), i.e. one stage before substrate removal. As the spacer orifice for this pattern is 42 µm and the opening in the electrode only is 38 µm, this shows the isotropic growth of the electrode during electro-plating. Figure 3.16 is a true to scale schematic cross section of this structure.

spacer layer and should prevent cracks inside the spacer layer. The latter ones are the capillaries in the capillary layer (inner openings) and the corresponding spacer openings in the spacer layer (outer openings). The alignment between spacer layer and capillary layer is very good (almost concentric). With these images the feasibility of fabricating large arrays of aligned structures using this approach is demonstrated. This is required for thruster applications, as the device has to consist of large arrays of single emitters to provide µN thrusts.

As a capillary inner diameter of < 10 µm is desirable[48,55], narrower capillaries were fabricated, too. Figure 3.15 (left) shows a SEM image of a structure comprising a rather narrow capillary with an inner diameter of 21 µm. Capillaries with inner diameters down to 15 µm at a height of 35 µm were fabricated. Even narrower capillaries may be produced if the fabrication process is further optimized.

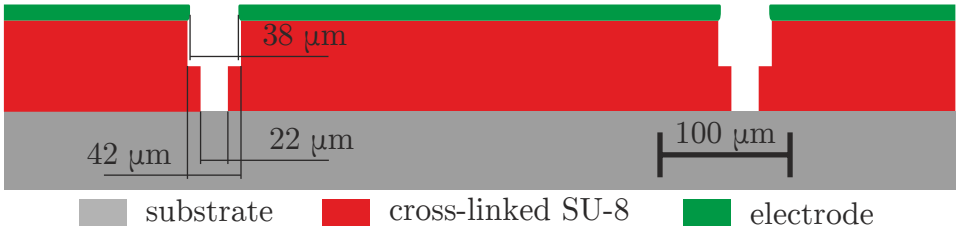

Figure 3.16: Schematic cross section of the structure shown on the right of Fig. 3.15. The spacer orifice is smaller than the electrode orifice due to the isotropic growth of the electrode. This yields a better extraction geometry as less particles may hit the spacer side walls, for example. All dimensions are true to scale, the lateral extent of the sketch and the bottom part of the substrate is cut off.

SU-8 capillary emitter arrays with an integrated electrode

According to the final layout shown in Fig. 3.13 an electrode has to be deposited on top of the spacer layer. This was done by electroplating nickel on an evaporated metal film on top of the spacer layer, according to step (j) in Fig. 3.11. A sample with a SU-8 capillary layer, a SU-8 spacer layer and an electroplated nickel electrode is shown in Fig. 3.15 (right). It is possible to distinguish between the two SU-8 layers and the nickel electrode as the surface structures are different as can be seen when comparing Fig. 3.15 (right) with Fig. 3.15 (left), for example. Furthermore, the electrode extends slightly over the edges of the spacer layer since electroplating is an isotropic growth process as schematically shown in Fig. 3.16. This overlapping fits perfectly with the demands of an extraction device as it serves as a single extraction grid orifice facing each capillary opening.

3.4.2 Permeability tests on SU-8 capillary emitter arrays with integrated electrode

We showed the feasibility of the microfabrication of SU-8 capillary emitter arrays with integrated electrode and proved the good alignment between capillaries and electrode. To perform extraction tests and ensure device functionality as micro-thruster we preliminarily tested the permeability of these arrays. In order to conduct such tests the substrate was removed following process step (l) from samples comprising a capillary and a spacer SU-8 layer, i.e. steps (a)-(h) and (l) of Fig. 3.11 were performed.

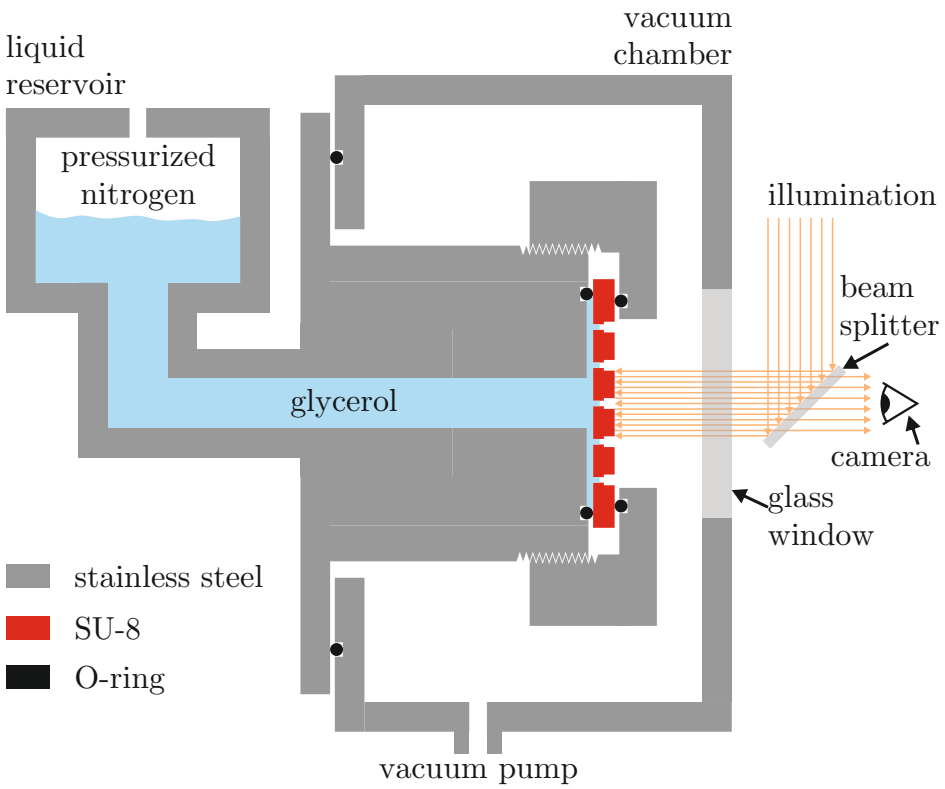

Figure 3.17: Schematic set-up for permeability tests on SU-8 capillary emitter arrays with a spacer layer (for an integrated electrode). The sample is clamped with O-rings between a sample holder and the liquid feed-through which is connected with the liquid reservoir. On the reservoir a hydrostatic pressure is applied using pressurized nitrogen. Optical observation of the sample is carried out in a reflective geometry with direct illumination using a beam-splitter.

The resulting samples, square membranes with a lateral dimension of 5 mm, were mounted into an experimental set-up depicted in Fig. 3.17. A sample holder is screwed onto a liquid feed-through with the sample clamped in between O-rings. The backside of the sample is in direct contact with the liquid in the reservoir which is pressurized using nitrogen gas. The experiments were carried out in a vacuum chamber with a glass window for optical access. Illumination of the sample was provided through this glass window. A beam splitter was used to provide the possibility of observing the experiment through the same window. The magnified image of the sample was projected onto a CCD camera.

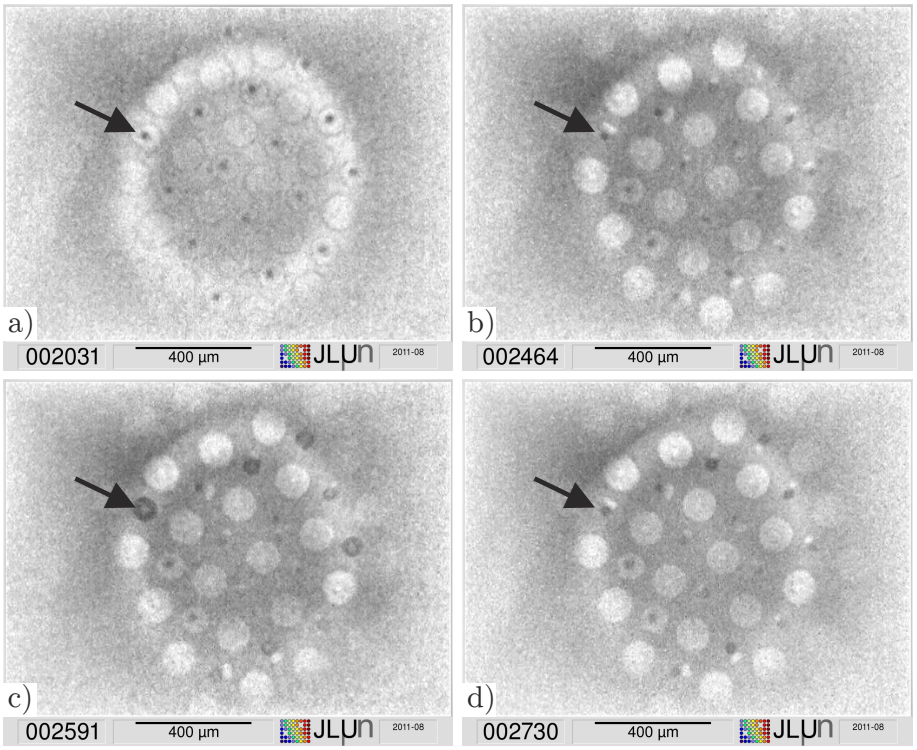

Figure 3.18: Optical images during permeability tests of a SU-8 membrane comprising a capillary and a spacer layer. When a variable pressure is applied on glycerol beneath the membrane, the evolution of the drop formation can be observed. The arrow indicates a single capillary, from which a drop is formed and changed in size under pressure variation. Image without liquid beneath the membrane (a). Glycerol in contact with the backside of the membrane (b). Hydrostatic pressure applied on the glycerol (c). Release of the hydrostatic pressure (d).

Figure 3.18 shows a series of images taken with the experimental set-up described above. In this experiment glycerol was used as liquid instead of an IL as it exhibits a similar viscosity. The image series follows a variation of the applied hydrostatic pressure. Image (a) was taken without liquid beneath the membrane as an optical reference. When the glycerol is in contact with the backside of the sample, the whole image is darkened (b). If enough pressure is applied, glycerol exits some capillaries and also wets their surface (c). Reduction of the applied pressure results in the liquid being drawn back inside the capillaries and the disappearance of the wetting of the surface (d). This behavior was observed repeatedly when the pressure was varied

periodically.

The experiment showed the reversibility of drop formation and verified the permeability of the fabricated SU-8 capillary arrays for viscous liquids. As these preliminary results indicate that an uniform behavior of all capillaries in an array is challenging, the experiments performed in the following sections were carried out using single emitters to investigate the extraction behavior under more controlled conditions.

3.4.3 Extraction tests on single emitters with integrated electrodes

To perform optical extraction measurements we used test samples consisting of only one emitter to investigate the extraction mechanism in a more controlled environment. Therefore we manufactured an extraction measurement chamber which enabled us to carry out an optical investigation of SU-8 membranes under vacuum conditions with an applied voltage between the extraction electrode and the ionic liquid reservoir. The extraction tests were carried out in vacuum to prevent arc discharges at high voltages and to simulate space conditions. The illumination was provided by a ring-shaped LED array within the chamber. Through a glass window the extraction could be observed using an inverted microscope equipped with a camera for recording images. To maintain a constant supply of liquid at the backside of the sample the device was mounted upside down to use gravity as a kind of "liquid pump". Additionally, the liquid could be pressurized to ensure a filling of the capillary. A cross section of the whole setup is depicted in Fig. 3.19.

To perform these measurements the substrate of each sample was entirely removed by wet-chemical etching and the remaining SU-8 foil was bonded onto a sample holder with a pre-drilled hole. Two different types of sample holder were used to vary the observation angle of the sample. The sample plane could be mounted either perpendicular to the optical axis (Fig. 3.20 (a,c)) or at an angle of 60° (Fig. 3.20 (b,d)). Both configurations are depicted in Fig. 3.20. A photograph of the actual setup is shown in Fig. 3.21.

Single emitter with integrated electrode — drop formation

First extraction measurements were carried out in perpendicular geometry (Fig. 3.20 (a,c)) on a sample consisting of a SU-8 capillary and a spacer layer, both 40 µm thick. 80 nm of chromium were thermally

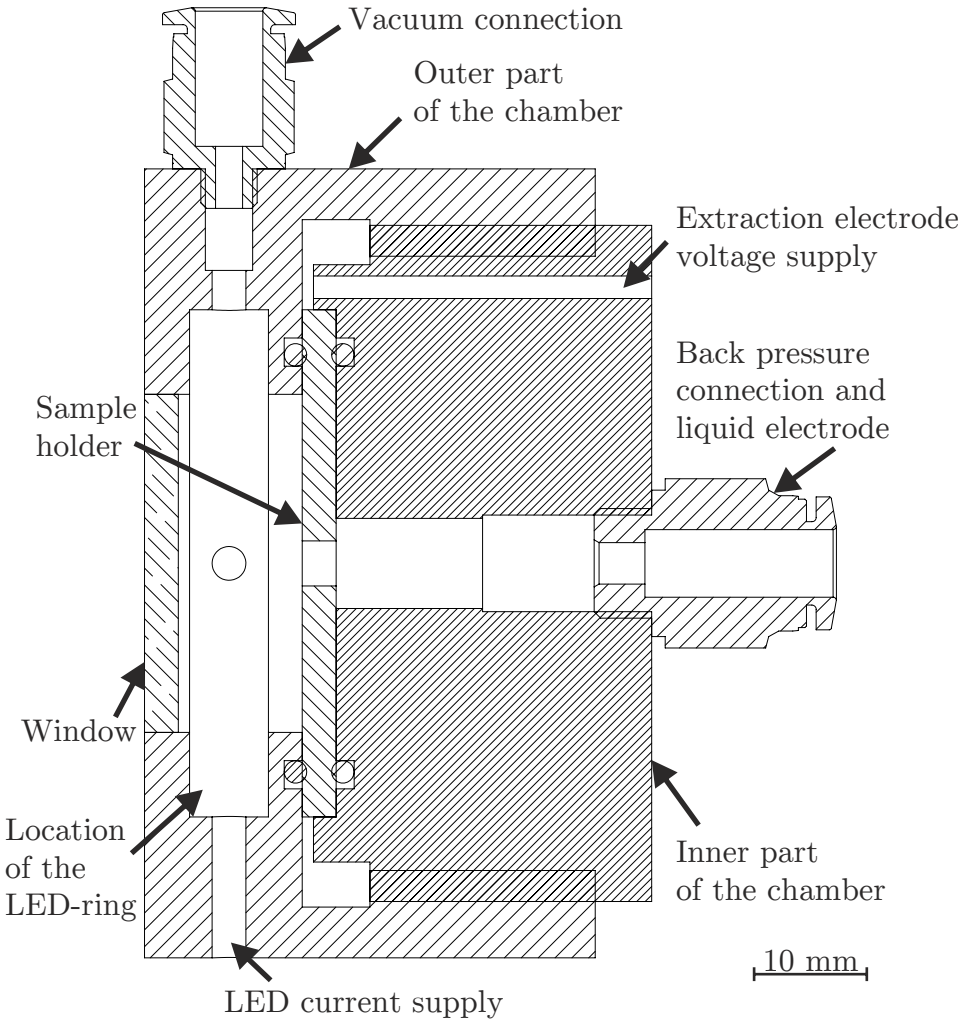

Figure 3.19: Cross section of the extraction measurement chamber for the optical observation of highly integrated colloid emitters in reflected-light geometry. The illumination of the sample, which was bonded onto a sample holder, was provided by a ring-shaped LED array within the vacuum recipient. This recipient was sealed by a glass window to enable an optical investigation of the sample mounted onto the holder (by an optical microscope). On the backside of the sample holder a liquid feedthrough was connected to the liquid reservoir. In the measurement setup, this chamber employed with the window facing downwards to make use of the gravitational force on the liquid supply in order to facilitate extraction.

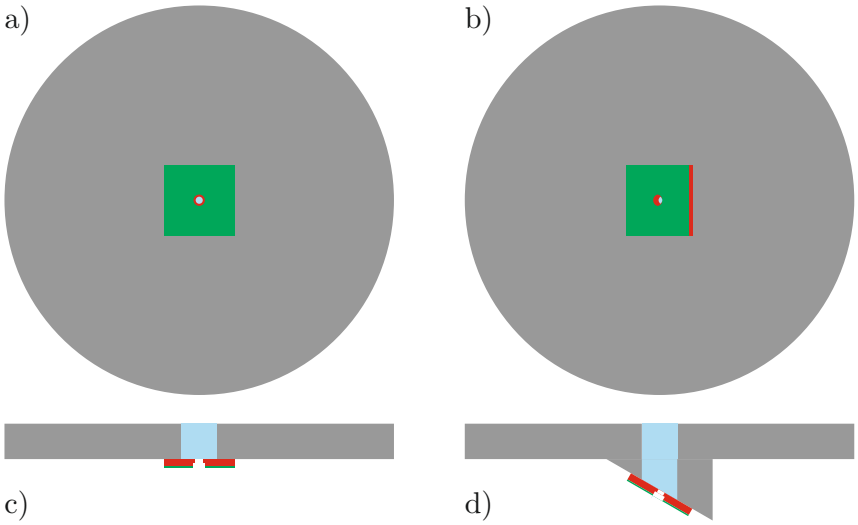

Figure 3.20: Schemes of both types of sample holders with a sample bonded on each of them. (a) and (b) showing the views through the microscope. Cross sectional views are depicted in (c) and (d). A flat sample holder (c) ensures an optical observation perpendicular to the sample surface (a). If the sample holder is tilted at 30° (d) the observation axis is at an angle of 60° to the sample's surface (b).

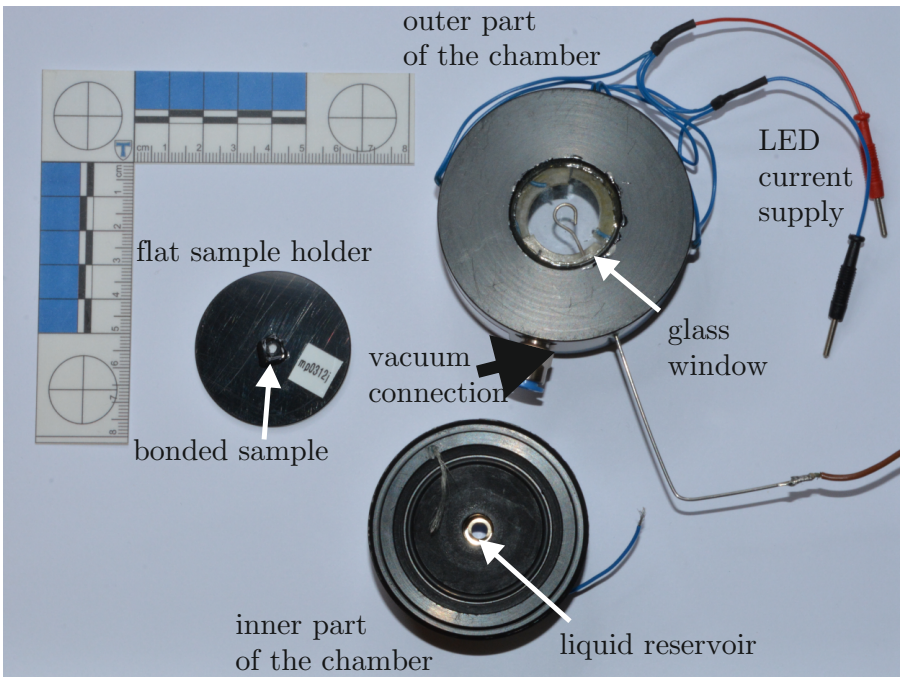

Figure 3.21: Measurement chamber according to Fig. 3.19 and flat sample holder according to Fig. 3.20 (a,c).

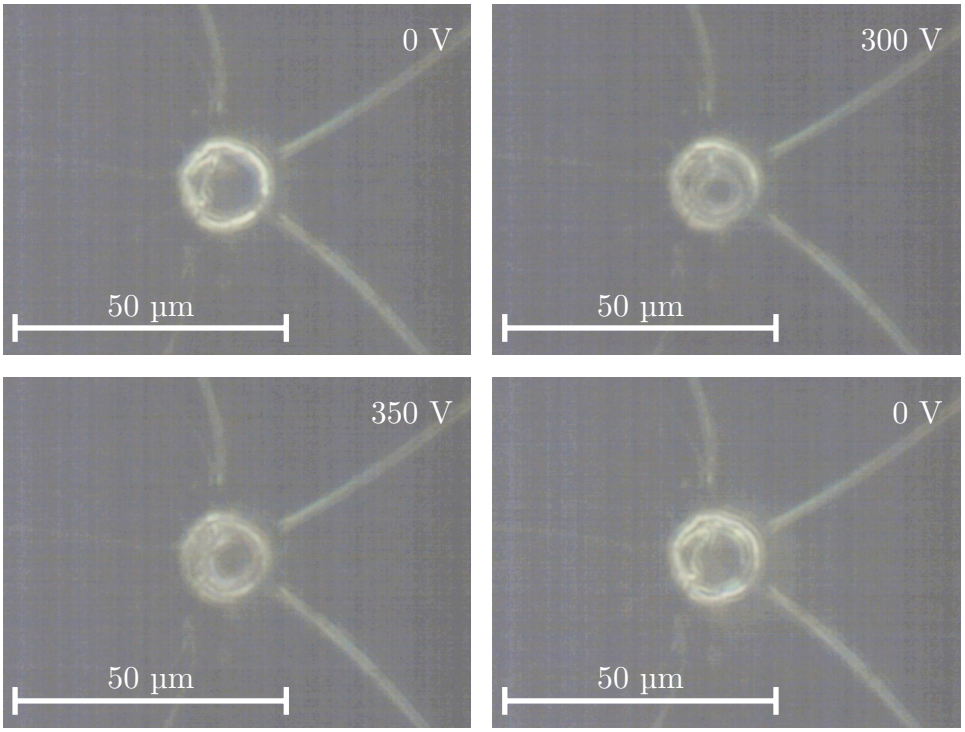

Figure 3.22: Series of optical images of extraction tests with a single emitter (capillary diameter: 10 µm) according to Fig. 3.13, an integrated electrode (30 nm of Au on 80 nm of Cr) was deposited onto a spacer layer (opening diameter: 20 µm). The sample was bonded flat onto the sample holder in Fig. 3.19. The ionic liquid stayed in the capillary as no voltage was applied. At 300 V the formation of a liquid drop on top of the capillary could be observed. At 350 V the drop size reached its maximum and almost touched the electrode. As the voltage was decreased again the liquid crept back into the capillary.

evaporated on top of the sample followed by 30 nm of gold. This metallic double layer served as the extraction electrode. This corresponds to process steps (a-i,l) of the process flow in Fig. 3.11. The capillary diameter was 10 µm and the opening in the spacer layer and therefore in the extraction electrode was 20 µm. A series of voltage variation is shown in Fig. 3.22. The first image shows the emitter filled with ionic liquid without applied voltage. As the voltage increased a liquid drop began to form on top of the capillary at approximately 300 V. In the next image it is visible that the drop filled almost the whole spacer layer opening at a voltage of 350 V. The last image shows the emitter after the drop formation at zero voltage and reveals that the liquid has

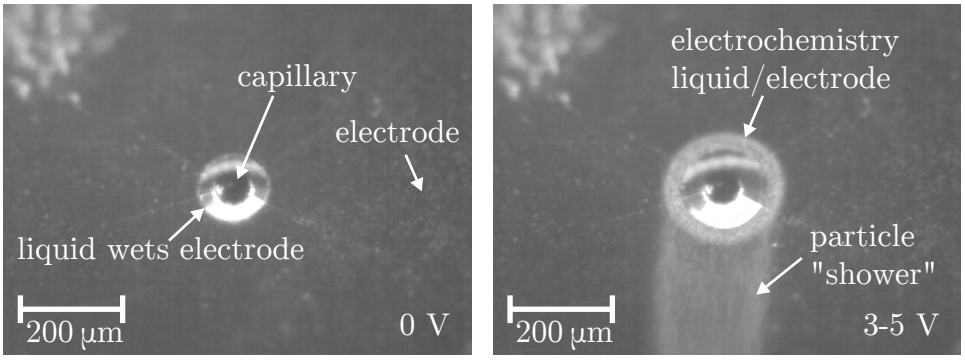

Figure 3.23: Optical images of extraction tests with a single emitter (capillary diameter: 20 µm) according to Fig. 3.13, an integrated electrode (120 nm of Cr) was thermally evaporated onto the spacer layer with an opening of 50 µm. The sample was mounted at an angle of 30° (Fig. 3.20 (b,d)) to the sample holder in Fig. 3.19. Although no voltage was applied the ionic liquid wetted the capillary layer and crept along the walls of the spacer layer leading also to a wetting of the electrode (left). Therefore even small voltages of the order of several volts caused electrochemical reactions between liquid and the chromium electrode — a particle shower occured (right).

crept inside the capillary again.

Although no Taylor cone or droplet emission was observable optically with this image series, the formation of a liquid meniscus due to an applied electric field could be demonstrated. To improve the visibility of the meniscus formation in the optical investigation, the next sample discussed was mounted with a tilt towards the observation axis.

Single emitter with integrated electrode — electrochemical reactions

Figure 3.23 shows a sample with a capillary diameter of 50 µm and an orifice of the spacer layer of 100 µm. Capillary and spacer layer were both 40 µm thick while the electrode was a film of 120 nm thermally evaporated chromium. This corresponds to process steps (a-i,l) of the process flow in Fig. 3.11. The sample was mounted on the tilted sample holder as depicted in Fig. 3.20 (b,d). The left image shows the emitter filled with ionic liquid as no voltage was applied. Already, the ionic liquid wetted the whole capillary layer surface up to the walls of the spacer layer. This unintended behavior occurred due to the tilted mounting of the sample and the resulting component of the gravitational force

parallel to the sample surface. A short-circuit occurred between liquid and electrode. This resulted in the particle shower shown on the right image after the application of a voltage of 3 V to 5 V. With increasing voltage the liquid wetted more of the spacer layer surface and almost instantly reacted electrochemically with the electrode. The reaction was not reversible, i.e. after lowering the voltage the liquid did not flow back.

As the observation of droplet extraction could not be shown on samples with an integrated electrode in this setup and the second sample was even destroyed due to a short-circuit of liquid and electrode, further investigations of the extraction behavior were carried out using a simplified approach. For this purpose samples consisting only of one single capillary layer with a single capillary were fabricated and an external electrode was used instead of the integrated electrode. Different illumination geometries and electrode designs for these fundamental measurements are discussed and simulated in the next section.

3.5 Experiments on single SU-8 capillary emitters using external electrodes

To improve the optical observation of extraction tests of SU-8 capillary emitters simplified measurement setups using an external electrode were designed and the influence of the external electrode geometry was investigated (3.5.1). Extraction tests were performed on simplified emitters with a tip-shaped externally mounted electrode and observed optically (3.5.2). The influence of different surface treatments of the emitters surface on the wetting behavior of EMI-BF_4 on this surface was investigated (3.5.3). Further extraction tests were performed on PTFE-coated simplified emitters (3.5.4).

3.5.1 Different emitter designs – Comparison with FEM simulations

In the previous section we showed the extraction behavior of single emitters with an integrated electrode. The optical observation proved to be difficult due to illumination issues and electrochemical reactions between liquid and electrode. To investigate the extraction behavior of single SU-8 capillary emitters in more detail than in the previous section two simplified measurement setups were designed.

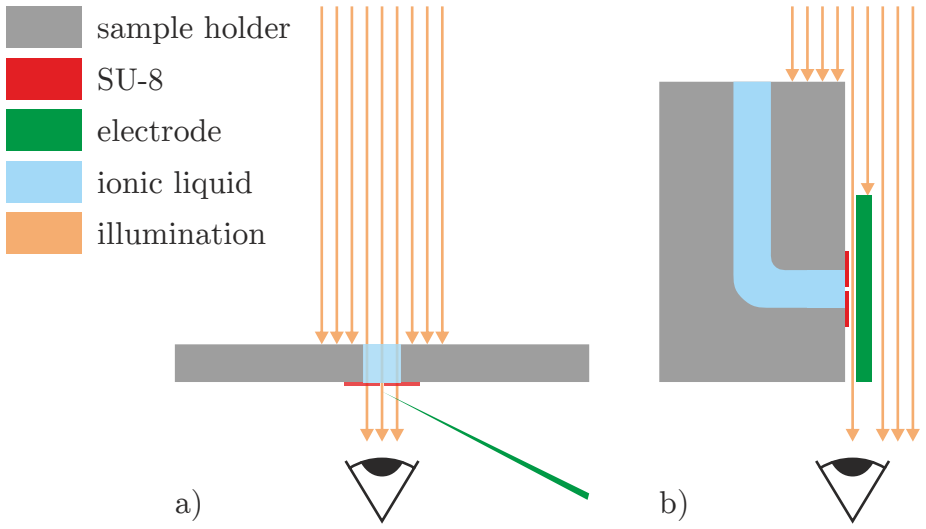

Figure 3.24: Schemes of simplified setups for extraction experiments on emitters comprising only a capillary layer. Both configurations are in back-light geometry to ensure a good illumination. A needle shaped electrode allows illumination through the ionic liquid and the sample (left). In this setup both types of sample holders depicted in Fig. 3.20 can be used. The other configuration allows an observation parallel to the sample's surface and utilizes a flat electrode for a homogenous electric field (right).

Both setups rely on a single capillary emitter comprising only a capillary layer which is bonded onto a sample holder while the electrode was mounted externally. No spacer layer was deposited and no integrated electrode was fabricated. The substrate was removed by wet chemical etching after the fabrication of the single SU-8 layer. This corresponds to process steps (a-d,h,l) of the process flow in Fig. 3.11.

Two different illumination techniques were considered. In the first scheme the illumination provided is passing through the SU-8 foil as shown in Fig. 3.24 (a). A tip-shaped electrode is used intending to not conceal the observed image. In the second scheme the illumination is perpendicular to the sample surface. This second configuration is designed to ensure a silhouette observation of the extraction (Fig. 3.24 (a)). A flat electrode opposite to the sample surface is proposed in this case. In both cases the observation is carried out using back-light illumination, i.e. the camera objective faces the light source.

As a flat electrode like in the second configuration promises a more homogenous electric field distribution, simulations were carried out to

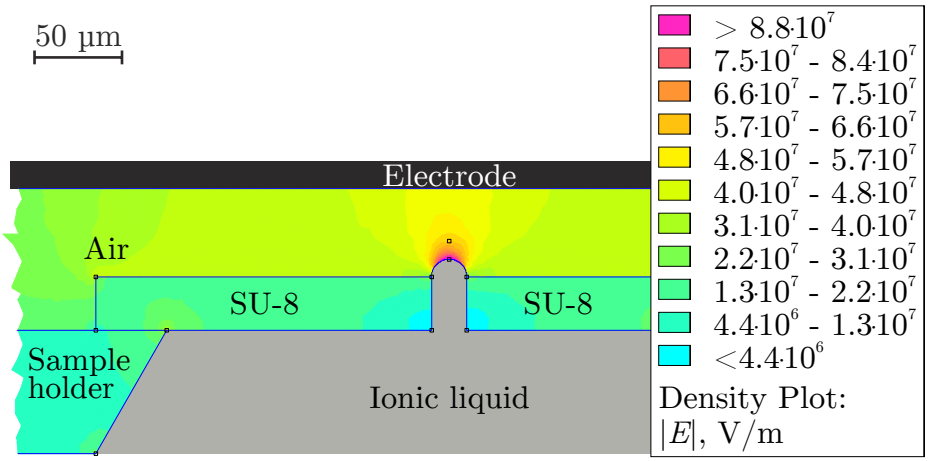

Figure 3.25: Electrostatic FEM simulation of the electric field between a hemisphere-shaped liquid surface at negative high potential of 2000 V and a flat electrode at ground potential which is mounted 50 µm away from the capillary orifice (40 µm distance to liquid). One can clearly see the field enhancement near the liquid surface. The dot above the liquid meniscus is located at a 10 µm distance. It defines the upper limit of the distance range of the graph in Fig. 3.27.

compare both the needle-shaped and the flat electrode configurations to investigate the electric field distribution between a liquid meniscus on top of the capillary and the electrode.

FEM simulations

The influence of different emitter geometries on the electromagnetic field distribution was investigated. For this purpose FEM simulations were carried out for emitter geometries according to Fig. 3.24. Simulations with the electrode facing a confined liquid surface were performed.

It was assumed that the liquid surface can be considered as a spherically shaped meniscus. The field distribution for a static environment was simulated using the software *Finite Element Method Magnetics* which is distributed under the terms of the Aladdin Free Public License[73]. The liquid was set on negative high potential while the electrode was set to ground potential. The FEM simulations were performed for a constant capillary orifice of 20 µm and a constant distance from the sample surface to the electrode of 50 µm. Therefore the distance between electrode and top of the spherically shaped (radius = half the capillary diameter) liquid was 40 µm. The potential difference

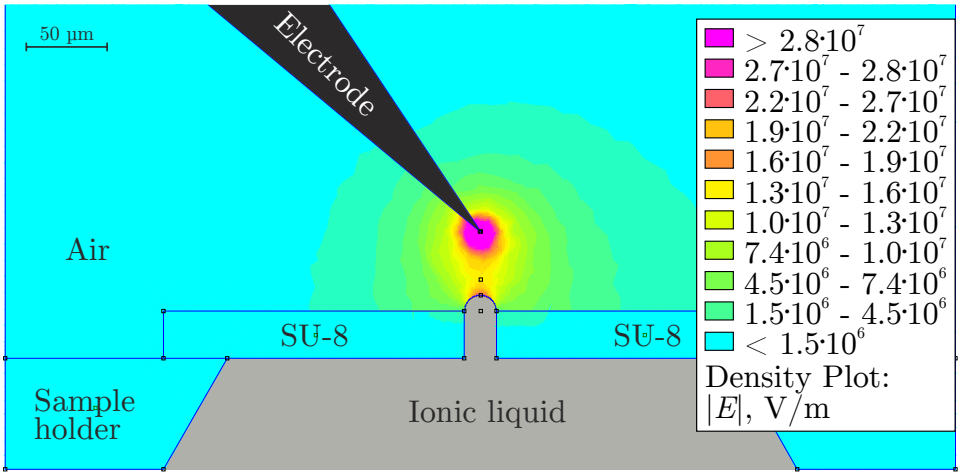

Figure 3.26: Electrostatic FEM simulation of the electric field between a hemisphere-shaped liquid surface at negative high potential of 2000 V and a tip-shaped electrode at ground potential which is mounted 50 µm away from the capillary orifice (40 µm distance to liquid). The global field maximum occurs at the electrode tip. Another local maximum is observable near the liquid surface. The dot above the liquid meniscus is at a 10 µm distance and corresponds to the upper range limit of the plot in Fig. 3.27.

was set to 2000 V. The results are shown in Fig. 3.25 and Fig. 3.26 for a flat electrode and a tip-shaped electrode, respectively.

With a flat electrode the electric field has a maximum of more than 80 MV m^{-1} near the liquid meniscus. It decreases continuously with increasing distance from the liquid surface up to the electrode surface. In case of the tip-shaped electrode the maximum of the electric field occurs near the electrode tip with $|\boldsymbol{E}| >> 30\,\mathrm{MV\,m^{-1}}$. It decreases as a function of distance from the electrode tip, but increases again close to the liquid surface. The local maximum of the electric field near the liquid surface possesses a value of about 25 MV m^{-1}.

This means that the maximum electric field in case of a flat electrode for this particular set of values of potential difference, electrode-surface distance, and capillary radius is more than three times higher than that in the case of a tip electrode. This is illustrated further in Fig. 3.27. The electric field along the direction from the top of the liquid meniscus to the electrode is shown along the first 10 µm. As the electric field at the liquid surface is decisive for the extraction of particles according to the considerations made in the section dealing

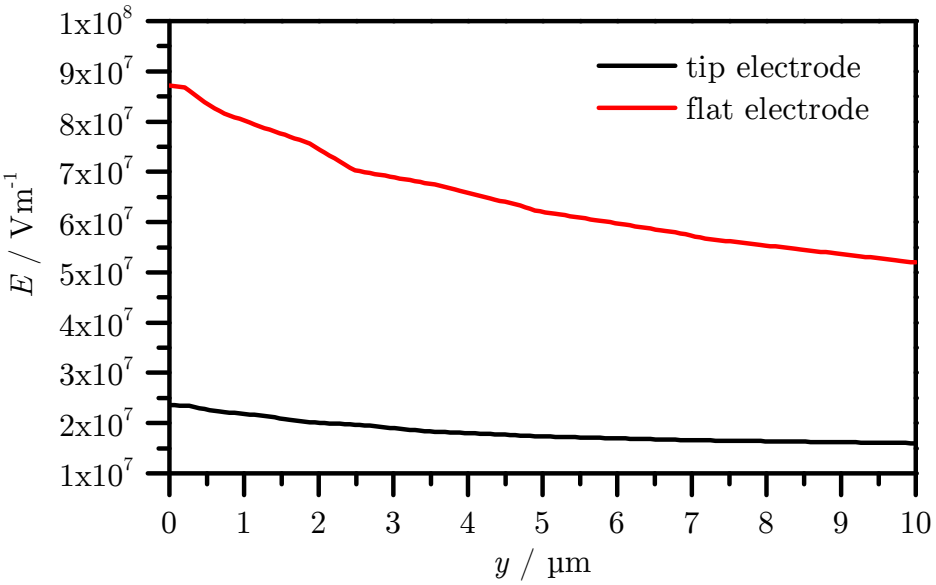

Figure 3.27: Magnitude of the electric field E as a function of the distance to the liquid surface. Origin in y-direction is the highest point of the spherical-shaped liquid according to Fig. 3.25 and Fig. 3.26. The electric field is shown for the first 10 µm along the direction from that point to the electrode.

with the extraction mechanism of colloid thrusters (section 3.1.1), the quantitative difference between the two geometries is clearly visible.

Despite yielding lower electric fields a tip-shaped electrode is still suitable for extraction experiments. Especially for optical extraction experiments the use of a tip-shaped electrode is necessary as it minimizes concealing of the capillary when the illumination through the ionic liquid and emitter as depicted in Fig. 3.24 (a) is used. Therefore further extraction tests were performed using only the configuration with a tip-shaped electrode.

3.5.2 Optical measurements on single SU-8 capillary emitters with an externally mounted tip-shaped electrode

In section 3.4.3 we have shown that the formation of a liquid meniscus due to an applied electric field can be observed in a single emitter with an integrated electrode (cf. Fig. 3.22). But further extraction measurements on emitters with integrated electrodes proved to be diffi-

cult as electrochemical reactions between liquid and electrode occurred (cf. Fig. 3.23). To avoid these chemical reactions and to improve the illumination during measurement, simplified setups were designed and simulated in section 3.5.1. The use of a tip-shaped electrode together with illumination through both the ionic liquid and the sample turned out to be a suitable and promising approach.

Thus, the following extraction measurements were carried out using an experimental setup as depicted in Fig. 3.24 (a). A tip-shaped electrode made of a sharpened silicon carbide needle was used. The samples consisted only of a single capillary layer and were bonded onto either a flat or a tilted sample holder (refer to Fig. 3.20) which contains the ionic liquid reservoir. The extraction was observed via the optical microscope during the application of high voltages up to 3500 V between the needle electrode and the ionic liquid. Extraction experiments with this setup were performed under atmospheric conditions as the optical observation of the extraction is more detailed than in a vacuum chamber.

Extraction test on simplified single emitters

Figure 3.28 shows a chronological series of video still during a voltage variation during an extraction test on a single capillary layer sample which is 80 µm thick and was bonded onto a flat sample holder like in Fig. 3.20 (a). It contains a single SU-8 emitter which a diameter of 50 µm. This corresponds to process steps (a-d,h,l) of the process flow in Fig. 3.11. A needle electrode made of SiC was placed 1 mm away from the capillary (refer to Fig. 3.24 (a)). As the voltage was raised from 0 V to approximately 1450 V no effect was observed. Further voltage increase to 1705 V led to a formation of a liquid drop inside the capillary. The drop grew with increasing voltage. As 1705 V were reached, the liquid wetted the sample surface very rapidly (186 s to 186.1 s). The wetted surface increased despite a constant voltage of 1705 V for approximately 2 s. No further enhancement of the wetting occurred in the following 50 s even as the voltage was increased after 20 s (absolute time: 210 s). As the voltage reached 2400 V after 4 minutes of observation, the wetted surface increased very fast until the electric field overcame the stability of the sample and the sample was destroyed shortly afterwards. The voltage trend on time during this extraction test is shown in Fig. 3.29.

The behavior shown above highlights a serious issue since the wetting of the surface prevents the formation of the Taylor cone. The

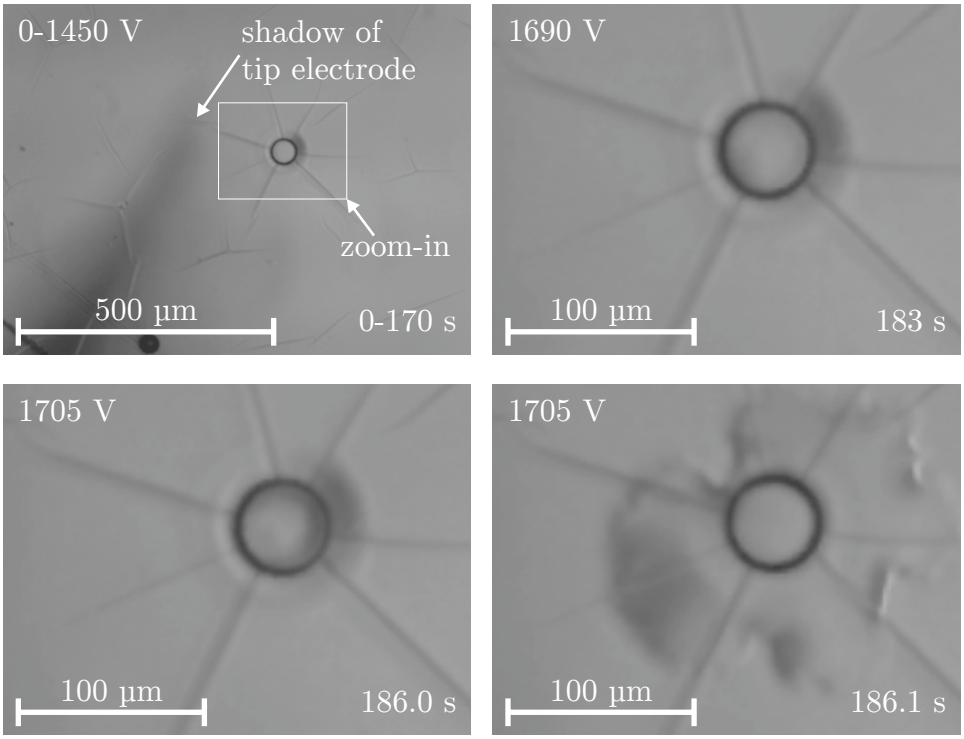

Figure 3.28: Chronological series of optical images of an extraction test with a single SU-8 emitter comprising a 80 µm thick capillary layer. The capillary diameter was approximately 50 µm and the sample was bonded onto a flat sample holder (cf. Fig. 3.20 (a)). As shown in Fig. 3.24 (a) a tip-shaped SiC electrode was used to apply a high voltage between it and the ionic liquid. The tip of the electrode was placed at a distance of 1 mm away from the capillary. The voltage was raised over time as is shown in Fig. 3.29. Up to 1450 V no variation of the sample was observed. Increasing the voltage further a drop was formed inside the capillary (1690 V). At a voltage of 1705 V the liquid reached the top of the capillary layer (186.0 s) and shortly after wetted the sample's surface (186.1 s).

benefit of the lateral confinement of the liquid by the capillary is annihilated. Furthermore, this behavior correlates with the results of the extraction measurements on single SU-8 emitters with an integrated electrode (refer to section 3.4.3). The electrochemical reaction between ionic liquid and integrated electrode was only possible when the liquid wetted the surface of the capillary layer as well as the inner walls of the spacer layer and therefore reached the electrode.

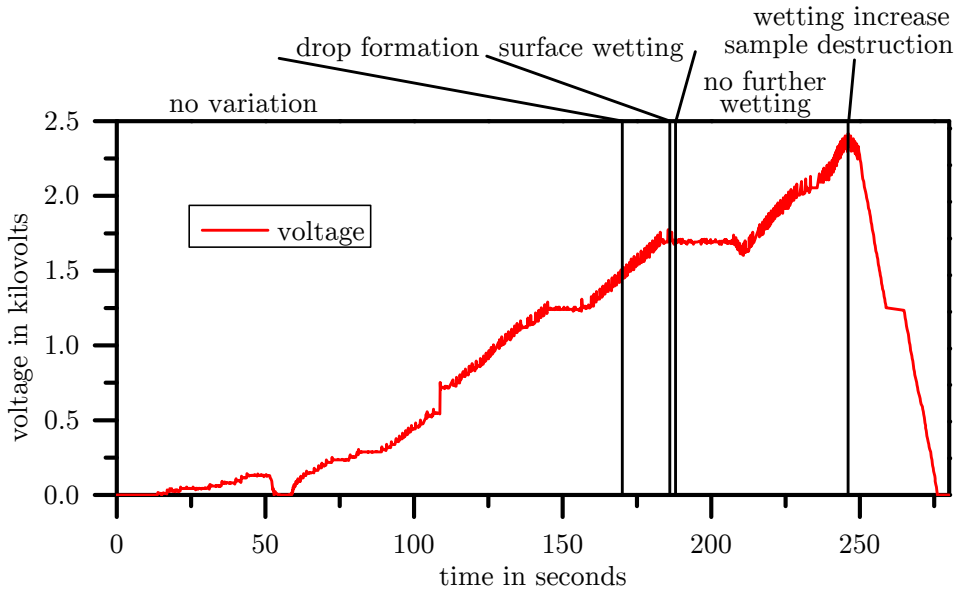

Figure 3.29: Time dependence of the applied voltage between ionic liquid and tip-shaped SiC electrode of the sample shown in Fig. 3.28. The different stadiums of the liquid extraction are separated by solid black vertical lines. Until 1450 V no action was visible. From 1450 V to 1705 V the formation of a liquid drop could be observed. The drop wetted the surface at the voltage reached 1705 V. At a constant voltage of 1705 V the wetted surface increased which is followed by a phase of a halt in the voltage raise until the voltage reached 2400 V. At this point the wetted surface increased again until the electric field overcame the mechanical stability of the sample, which was destroyed subsequently.

Extraction test on simplified single emitters comprising very narrow capillaries

Another approach to overcome the wetting related issues during the formation of a Taylor cone is the fabrication of very narrow capillary emitters to increase the hydraulic impedance and the electric field near the capillary surface. Figure 3.30 shows a time-resolved optical imaging series during voltage variation of a sample with a capillary diameter lower than 5 µm. The 80 µm thick sample comprising a single SU-8 layer with an individual capillary was fabricated according to the process steps (a-d,h,l) of the process flow in Fig. 3.11. It was mounted onto a flat sample holder as shown in Fig. 3.20 (a) and filled with ionic liquid. A tip-shaped SiC needle electrode was placed at a distance of 500 µm to the capillary perpendicular to the sample surface following

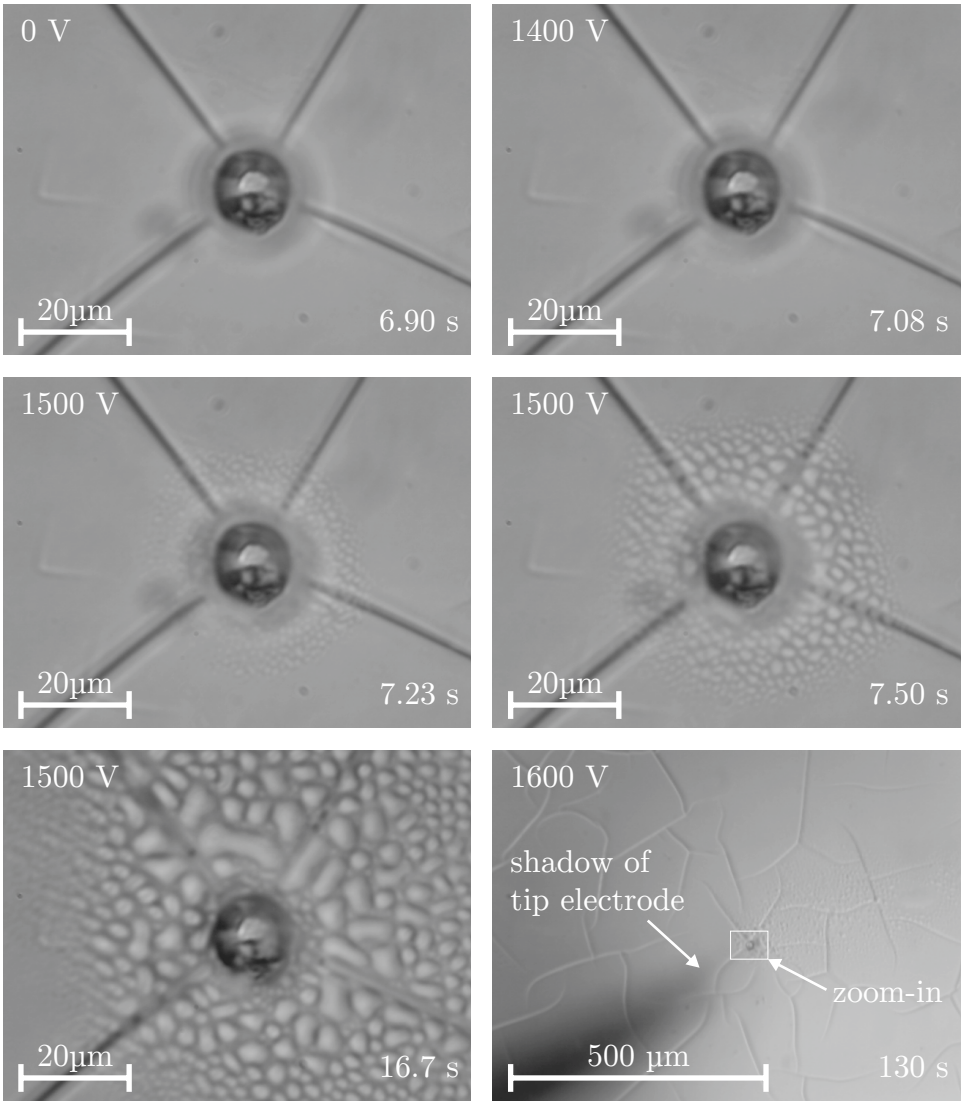

Figure 3.30: Chronological series of micrographical images during a voltage variation series according to Fig. 3.31. The sample comprised a 80 µm thick capillary layer with a single SU-8 emitter and was bonded onto a flat sample holder (cf. Fig. 3.20 (a)). The capillary with a nominal diameter of 15 µm was not fully developed, only a small opening of < 5 µm was permeable. The voltage was applied between the needle-shaped SiC electrode at a distance of 500 µm from the capillary and the ionic liquid inside the capillary (cf. Fig. 3.24 (a)). A droplet deposition around the capillary could be observed as the voltage was increased. The droplet distribution became asymmetric.

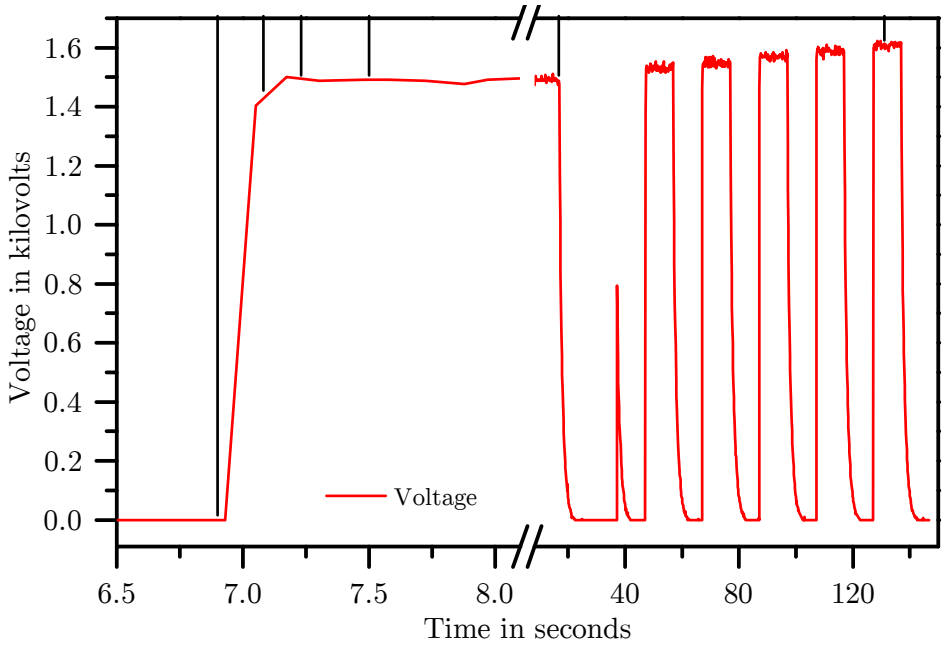

Figure 3.31: Applied voltage between ionic liquid and tip-shaped SiC electrode of the sample shown in Fig. 3.30 over time. The different times of the images in Fig. 3.30 are indicated by solid black vertical lines. The beginning of the droplet deposition is resolved higher to distinguish the first four images. The second part of this graph shows the periodic evolution of the voltage variation and the timings of the other two images.

the design introduced in Fig. 3.24 (a). The small diameter of the capillary occurred due to an incomplete development of the sample which arose as the aspect ratio was very large and swelling of SU-8 during curing additionally narrowed the pathway for the developing agent. This generally unintended behavior could be controlled to produce samples with nominal diameters of 15 µm and physical diameters below 5 µm. The chronological image series in Fig. 3.30 follows the voltage alternation shown in Fig. 3.31. Each time-step marked with a vertical solid black line in the latter graph has a corresponding micrograph in the image series. Shortly after the application of the first voltage cycle of 1500 V at 7.08 s the deposition of droplets around the capillary could be observed at 7.23 s. At a constant voltage level the coverage of the sample surface with these droplets increased further (compare image at 7.50 s) until it filled more than the image section at the end of the first cycle at 16.7 s. Noteworthy is the asymmetric distribution of the

droplet deposition which is fully visible in the general view which was made five voltage cycles later at the 1600 V cycle at 130 s. The droplets were deposited mainly in a jet-like pattern away from the electrode. This behavior occurred due to the scattering of extracted ionic liquid droplets by the electrode.

The droplet deposition in the present distribution pattern is an indirect proof of the operability of the micro-fabricated out-of-plane SU-8 capillary emitter as a colloid emitter.

3.5.3 Investigation and optimization of the wetting behavior of ionic liquids on SU-8

As we have shown in sections 3.4.3 and 3.5.2 the wetting of the capillary layer surface can inhibit the functioning of a colloid emitter. Therefore an analysis of the wetting behavior of EMI-BF_4 on SU-8 was carried out and the effect of different surface treatments on the wetting behavior was investigated. Similar problems were reported by Nabity[74] and Dandavino et al.[75] on SiO_2, the authors also tried to alter the wetting behavior with surface treatments.

Considering a thin tube or capillary with two fluids inside like pictured for air and a liquid in Fig. 3.32 (a), the interaction of the surface tensions of the three phases air, liquid and wall yield a pressure difference which is balanced by the gravitational force. This capillary action leads to a change of the liquid height level h (in relation to the equilibrium level outside the capillary) within a capillary with a diameter of $2r$. It depends on the surface tension γ of the liquid, the contact angle Θ between liquid and the inner wall of the capillary, the density ρ of the liquid, and the actual gravitational acceleration g:

$$h = \frac{\gamma \cos \Theta}{\rho r g}. \tag{3.10}$$

For a wetting liquid, i.e. $\Theta \leq \pi/2$, the liquid will rise against an external force like mg in a capillary. When the contact angle exceeds $\pi/2$ the liquid shows a non-wetting behavior, i.e. the liquid height inside the capillary will be lower than outside.

In space the capillary pressure will be balanced by the pressure in the reservoir. This means for a liquid which wets the inner wall of a capillary the following will happen: If the counter-pressure is too small, the liquid will be pulled to the end of the capillary — a self-driven pump mechanism.

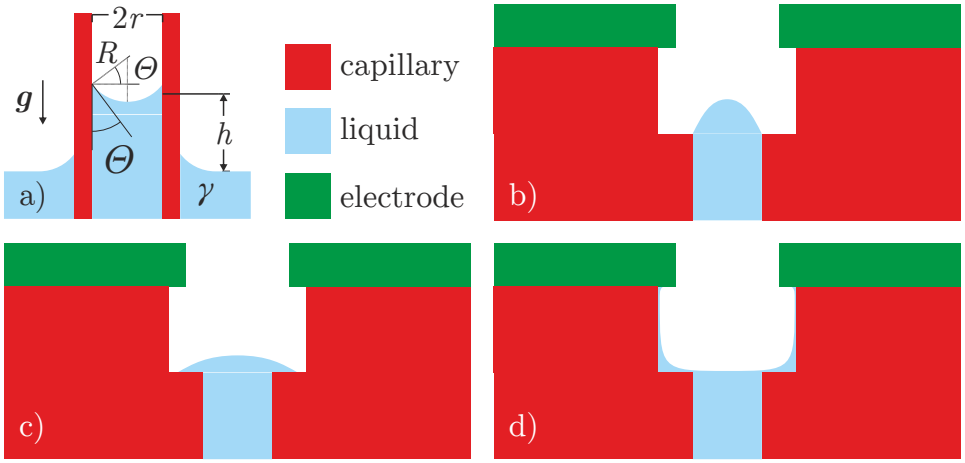

Figure 3.32: Capillary action and the effect of wetting on the emitter function. (a): Illustration of the principle of capillary action — a wetting liquid (surface tension γ) will flow to a height h inside a capillary (radius r) until the capillary pressure $2\gamma/R$ (R: radius of meniscus) balances the pressure correlated to the gravitational acceleration g, cf. Eq. (3.10). If the contact angle Θ between liquid and capillary is lower than $\pi/2$, the feeding of the liquid can be self-sufficient. (b): Desired formation of liquid meniscus due to the electric field between electrode and liquid. (c): Problem with a wetting capillary layer surface — no formation of a liquid meniscus or a Taylor cone due to the enhanced radius of the liquid surface. (d): Problem with a wetting capillary layer surface and a wetting spacer layer wall — short-circuit between electrode and liquid due to creepage of the liquid to the electrode.

Though the above stated behavior is desired, an emersion of the liquid onto the capillary layer surface has to be prevented under all circumstances. The liquid must not wet the capillary layer surface, i.e. the contact angle between the liquid and the capillary layer surface has to be larger than 90°. In that ideal case, when applying an electric potential between liquid and electrode this will lead to the behavior depicted in Fig. 3.32 (b). If the liquid is wetting the capillary layer surface it will come to an enlargement of the liquid radius which will increase the required extraction voltage and therefore inhibit controlled extraction (cf. Fig. 3.32 (c)). This behavior occurred with SU-8 emitters comprising a single capillary layer and a capillary diameter larger than 10 µm as discussed in section 3.5.2, especially in Fig. 3.28 and Fig. 3.29. An even worse case will occur, if the liquid wets the

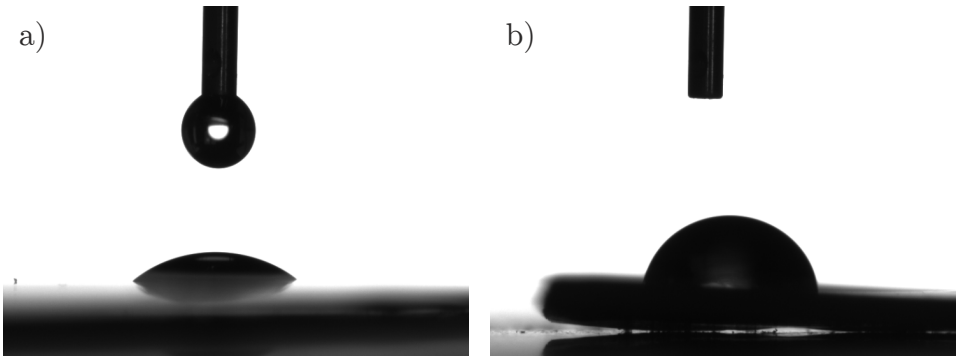

Figure 3.33: Optical images of contact angle measurements of EMI-BF4 on an untreated SU-8 surface (a) as well as on a 500 nm thick PTFE film on SU-8 (b). The contact angles were measured to 38° on the untreated sample and to 86° on the PTFE film, respectively.

spacer layer inner wall and may creep to the electrode and therefore will short-circuit both liquid and electrode. This behavior is depicted in Fig. 3.32 (d) and will lead to the decomposition of the liquid and the electrode due to electrolysis — the emitter will be destroyed. Emitters comprising an integrated electrode and untreated SU-8 surfaces like in section 3.4.3 showed this behavior, e.g. the emitter in Fig. 3.23 experienced electrochemical reactions due to short-circuits between electrode and ionic liquid.

Contact angle measurements of EMI-BF_4 on untreated and coated SU-8 surfaces

To investigate the wetting behavior of EMI-BF_4 on the used surfaces we performed contact angle measurements on SU-8. For this purpose, optical images were taken in a back-light geometry using the sessile drop method. The contact angle was calculated using the Young-Laplace method, which accounts for the influence of the gravity on the drop formation. Ideally, the resulting contact angle Θ is only determined by the surface tensions between liquid and surrounding gas phase (γ_{lg}), the free surface energy between solid surface and gas phase (γ_{sg}) and the interfacial energy between solid phase and liquid (γ_{ls}). This is described in Young's equation[76]:

$$\cos\Theta = \frac{\gamma_{\mathrm{sg}} - \gamma_{\mathrm{ls}}}{\gamma_{\mathrm{lg}}}. \tag{3.11}$$

Figure 3.33 (a) depicts an image of such a contact angle measure-

ment of EMI-BF_4 on SU-8. The contact angle of 38° reflects the wetting behavior. Using the rather simple Zisman theory[77] it is possible to determine the free surface energy γ_{sub} of a substrate, if at least two contact angles α_i (to the substrate) for a series of probe liquids and the corresponding surface tensions between liquid and air γ_i are known (for two probe liquids):

$$\gamma_{\text{sub}} = \frac{\cos\alpha_1\gamma_2 - \cos\alpha_2\gamma_1 + \gamma_1 - \gamma_2}{\cos\alpha_1 - \cos\alpha_2}. \tag{3.12}$$

Together with the investigations of Gao et al.[78] with DI-water on SU-8 (contact angle of DI water on SU-8: 79°) and the known values for the surface tensions of DI water ($72.8\,\text{mJ}\,\text{m}^{-2}$) and EMI-$BF_4$ ($52\,\text{mJ}\,\text{m}^{-2}$) this relates to a SU-8 free surface energy of $45\,\text{mJ}\,\text{m}^{-2}$.

This wetting behavior is intended for the inner wall of the capillary but has to be avoided on the surface of the capillary layer. Therefore either the liquid has to be changed or the surface has to be treated to yield different surface tensions between the three phases according to Eq. (3.11). As the liquid fulfills all prerequisites as stated in section 3.1.2 and the wetting behavior inside the capillary fits perfectly to the application, we chose the latter approach. There are two ways of achieving a non-wetting behavior. Firstly, a lower surface tension of the treated surface yields a higher contact angle (cf. Eq. (3.11)). Secondly, a rougher surface may result in a non-wetting behavior.

To reduce the surface tension, thin films of polytetrafluoroethylene (PTFE) were sputtered onto the SU-8 capillary layers, sputter deposition is described in section 4.2.1. PTFE is well-known for its hydrophobic behavior and its low friction coefficient. Its surface energy[79] is around $20\,\text{mJ}\,\text{m}^{-2}$ which is significantly lower than that of SU-8, determined above. The contact angles of EMI-BF_4 were measured on PTFE films of various thicknesses. Above a thickness of 500 nm the contact angle kept constant and had its maximum. It could be determined to 86° as depicted in Fig. 3.33 (b).

In order to enhance the contact angle of a liquid on a surface it is also possible to roughen the surface. Young's equation (3.11) does not hold for a non-flat surface anymore. There exist two models to describe the wetting behavior of a liquid on a roughened surface. Wenzel's model on the one hand considers a homogeneous wetting of the surface and sets the contact angle Θ on a flat surface in relation to the one Θ_{r} on the roughened surface:

$$\cos\Theta_{\text{r}} = r\cos\Theta, \tag{3.13}$$

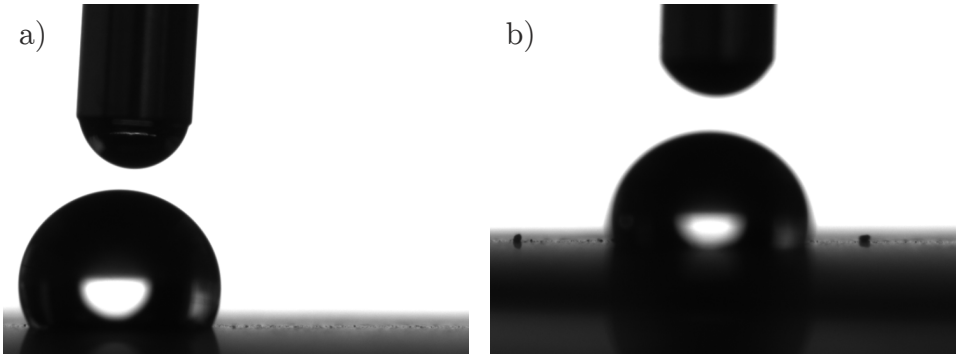

Figure 3.34: Optical images of drops of DI-water (a) and EMI-BF_4 (b) on a PDMS/SiO_2 treated SU-8 surface. Contact angle measurements were carried out resulting in 117° (DI) and 121° (EMI-BF_4), respectively.

with $r = A_{\mathrm{wet}}/A_0$ as the ratio between the wetted surface A_{wet} and the projected surface A_0. The Cassie-Baxter model on the other hand describes the effective contact angle Θ_{r} on a heterogeneous surface where the liquid is in contact with a composite surface. If the composite consists of a roughened solid surface and of air as second component, it depends only on the original liquid-solid contact angle Θ and the areal fraction f of solid-liquid interface to entire surface as the liquid-air contact angle is 180°:

$$\cos \Theta_{\mathrm{r}} = f(\cos \Theta + 1) - 1, \tag{3.14}$$

the so-called Cassie's law. I.e., the smaller the contact surface of a liquid on a roughened surface in relation to an air buffer underneath the liquid, the larger the contact angle.

He et al.[80] proposed a superamphiphobic coating based on a mixture of the silicone polydiethylsiloxane (PDMS) and SiO_2-nanoparticles. Superamphiphobic means that the contact angle of this coating is more than 150° for both water and oils. The coating uses the enhancement of the surface roughness by covering it with a film of SiO_2-nanoparticles as well as the low free surface energy of PDMS ($\gamma = 20\,\mathrm{mJ\,m^{-2}}$). Using this coating, He et al.[80] realized contact angles up to 153° for DI water and 141° for diiodomethane (MI) after a series of treatments of glass surfaces. In this work an attempt to transfer those results to a SU-8 treatment with PDMS and SiO_2-nanoparticles was carried out in order to investigate the wetting behavior of EMI-BF_4 on such a treated surface. For this purpose, 1.5 wt. % SiO_2-nanoparticles together with 0.5 wt. % and 0.05 wt. % curing agent

Table 3.2: Contact angles of EMI-BF_4 on different surface treatments of SU-8.

treatment	none	PTFE (500 nm)	PDMS/SiO_2
contact angle	38°	85°	121°

in toluene were dispersed in a supersonic bath. The SiO_2-nanoparticles were 10 nm to 30 nm in diameter. The dispersion was spin-coated on the capillary layer of a sample. The sample was baked for 2 h on a heating plate at 80 °C to achieve the polymerization of the PDMS and to evaporate the toluene. This corresponds to the preparation step (a) in the work of He et al.[80], at which they measured contact angles of 152° and 117° for DI-water and MI, respectively.

Contact angle measurements with DI-water as reference (a) and EMI-BF_4 (b) were taken as depicted in Fig. 3.34. They result in 117° for DI-water and 121° for EMI-BF_4. Although the reference value was lower than in the literature, the contact angle for the used ionic liquid EMI-BF_4 reveals a strong non-wetting behavior. This makes the PDMS/SiO_2-treatment of SU-8 perfect for the capillary layer surface in order to ensure no wetting. It is the highest measured contact angle of EMI-BF_4 on a surface known in the literature. The highest value reported previously by Dandavino et al.[75] was 94° for silicon which had undergone a silane-based surface treatment.

An overview of the contact angles of EMI-BF_4 on differently treated SU-8 surfaces is shown in table 3.2. We showed the enhancement of the contact angle of EMI-BF_4 between PTFE- and PDMS/SiO_2-coated SU-8 films compared to untreated samples. These treatments allow us to obtain non-wetting coatings of the SU-8 capillary layer surface of our emitter structures.

Although the PDMS/SiO_2-coating exhibits the highest contact angle, the fabrication process is very sensitive to the process parameters, i.e., the distribution of SiO_2-nanoparticles tends to agglomerations. Therefore we chose to perform final extraction measurements with the PTFE-coated emitter structures only, as shown in the next section.

3.5.4 Extraction from PTFE-coated single emitters

Extraction measurements of untreated simplified emitters revealed the wetting of the sample surface when an high voltage was applied between

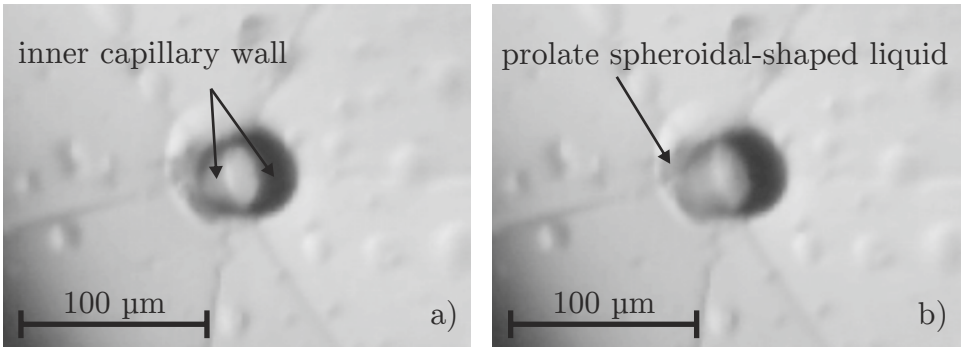

Figure 3.35: Optical images of an extraction test with a single PTFE-coated (520 nm) SU-8 emitter comprising a 40 µm thick capillary layer before and after switching-on of a high voltage. The capillary diameter was approximately 40 µm and the sample was bonded onto a tilted sample holder (cf. Fig. 3.20 (b)). As depicted in Fig. 3.24 (a) a tip-shaped SiC electrode (1 mm distance) was used to apply a high voltage between it and the ionic liquid. The voltage was switched on following the time dependence shown in Fig. 3.36. Without an applied voltage the liquid stayed inside the capillary, whose inner walls are the darker areas in the images due to the tilted observation (a). Right after the high level of 1960 V was reached, the liquid forms a prolate spheroidal shape heading towards the lower left direction of the image (b).

the ionic liquid inside the capillary and an externally mounted electrode (section 3.5.2). Surface wetting contradicts the concept of the liquid confinement using a capillary, refer to section 3.1.1. In the case of integrated emitters (section 3.4.3), wetting may lead to the destruction of emitters due to short-circuits between the integrated electrode and the ionic liquid and subsequently occurring electrochemical reactions.

Thus, different SU-8 surface treatments and their influence on the wetting behavior of EMI-BF_4 were investigated in section 3.5.3. For further extraction tests on simplified emitters the PTFE-coating was chosen as its deposition quality is very reproducible and it increased the contact angle to 85° compared to 38° for an untreated SU-8 surface. Extraction measurements with PTFE-coated emitters were performed in the same setup configuration (cf. Fig. 3.24 (a)) used for the investigations in section 3.5.2. This means, a silicon carbide needle was used as electrode while the observation was carried out under atmospheric conditions in back-light geometry. The samples used for the tests in this section comprised a single SU-8 layer with one capillary hole. This corresponds to process steps (a-d,h,l) of the process flow in Fig. 3.11.

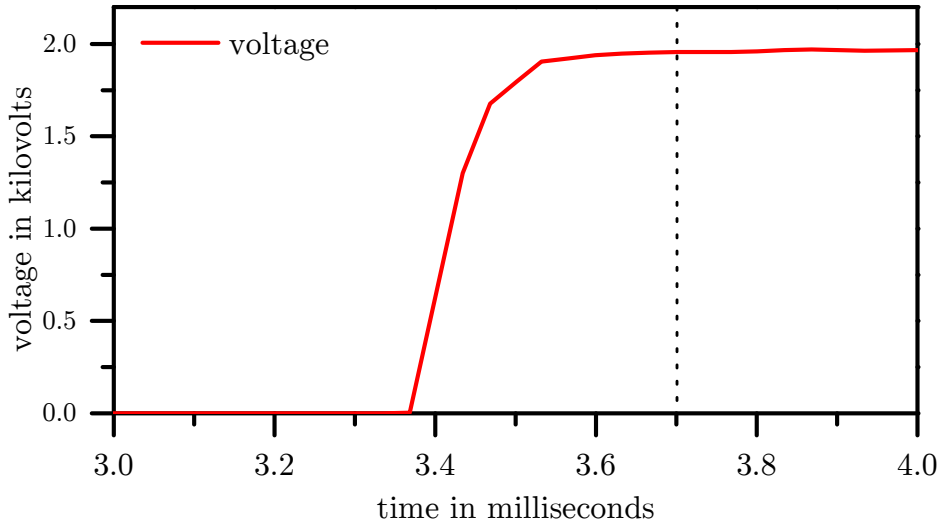

Figure 3.36: Time dependence of the voltage applied between ionic liquid and tip-shaped SiC electrode of the sample shown in Fig. 3.35. At 3.3 s the voltage was switched on. At 3.7 s the formation of a prolate spheroidal drop outside the capillary could be observed (dotted black line).

Figure 3.35 shows the formation of a liquid prolate spheroid instead of surface wetting as in the case of untreated SU-8 emitters. The sample was coated with a 520 nm thick PTFE film prepared by sputter deposition. Prior to the PTFE coating a 40 µm diameter capillary was microfabricated into a SU-8 layer of 40 µm thickness. After removal of the substrate, the sample was mounted onto a tilted sample holder (cf. Fig. 3.20). The SiC electrode was placed 1 mm away from the capillary orifice. Without an applied voltage the liquid remains within the capillary (a). Several hundred milliseconds after the voltage was set to a high level of 1960 V a prolate spheroidal shape occurs at the capillary opening (b). The time difference between switching on and prolate spheroidal formation is depicted in the voltage-time-chart in Fig. 3.36. This behavior indicates the formation of a prolate shape and is a clear improvement overcoming the wetting issues during the extraction of EMI-BF_4 out of untreated SU-8 emitters.

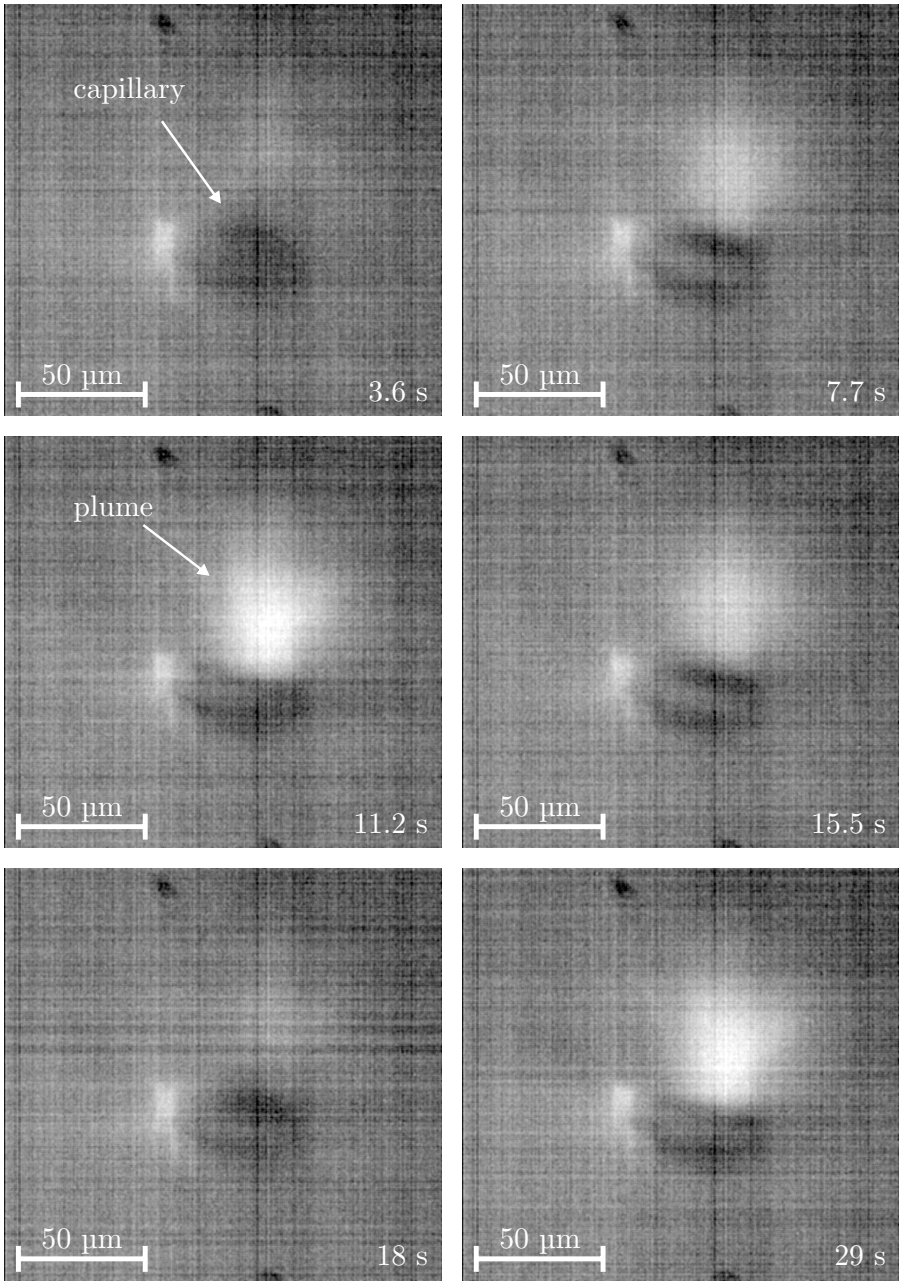

Figure 3.37: Chronological series of optical images of an extraction test with a single SU-8 emitter comprising an 80 µm thick capillary layer coated with 520 nm PTFE. The capillary diameter was 50 µm. A tip-shaped SiC electrode (500 µm distance) was used to apply a high voltage between it and the ionic liquid. Following the time dependence of the voltage shown in Fig. 3.38 a plume occurred when the high level of voltage was applied.

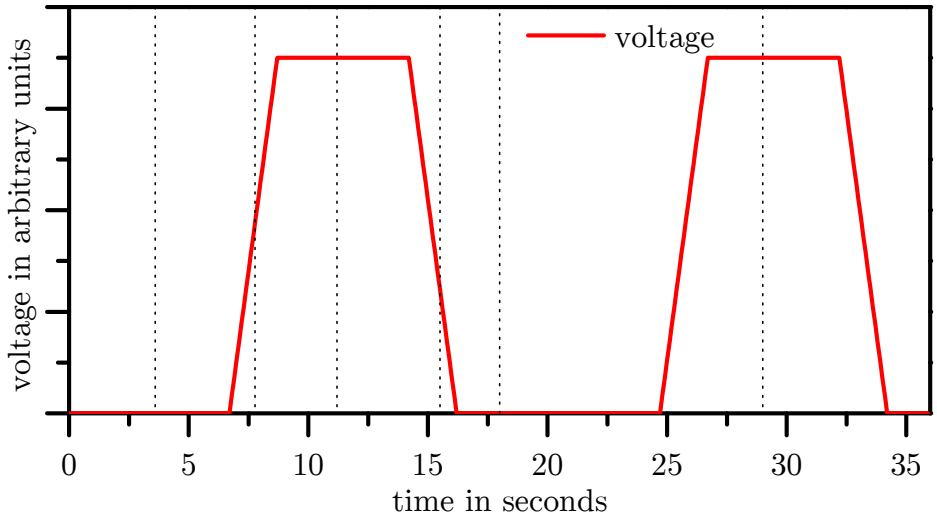

Figure 3.38: Time dependence of the voltage applied between ionic liquid and tip-shaped SiC electrode of the sample shown in Fig. 3.37. The points in time of the images in Fig. 3.37 correspond to the dotted vertical black lines.

Extraction tests of PTFE-coated single SU-8 capillary emitters in an evacuated environment

After the proof that a PTFE-coating decreases wetting of EMI-BF_4 on SU-8, an extraction experiment under vacuum conditions was performed. For this purpose, a sample comprising a single capillary layer of 80 µm thickness and a capillary diameter of 50 µm was microfabricated using process steps (a-d,h,l) of the process flow in Fig. 3.11. The sample was mounted onto the tilted (30°) sample holder and illuminated by a light source placed in extraction direction. The observation was performed parallel to the plane of the sample holder, i.e. the angle between observation axis and sample surface was 30°. A SiC needle served as electrode and was placed at a distance of 500 µm from the sample.

Figure 3.37 shows a time-dependent series of images during the voltage alternation run depicted in Fig. 3.38. The first image shows the sample when no voltage was applied (3.6 s). As the voltage increased, a plume is slightly recognizable along the direction from the capillary to the top right corner of the second image (7.7 s). At 11.2 s the voltage was at its high level and the plume exhibited a constant shape and brightness. In the decreasing slope of the voltage the plume

regressed again (15.5 s) until it vanished as the voltage reached its low level at 0 V (18 s). As the voltage was raised again, the plume occurred again exhibiting the same shape and appearance as before (29 s). All points in time are highlighted as dotted vertical black lines in the time dependence of the voltage (Fig. 3.38).

This last series of images proves that the extraction of particles or droplets of ionic liquids out of single microfabricated SU-8 emitters is feasible, if the SU-8 surface is treated to overcome the wetting issues. This can be done by employing sputtered PTFE-coatings on the surface of the capillary layer.

In future investigations on fully integrated single SU-8 emitters and emitter arrays should be possible. This will allow one to gain the full benefits of microfabrication.

3.6 Conclusions about colloid emitters

We introduced a concept for a miniaturized colloid emitter array based on the epoxy-type resist SU-8 as the main material and using the ionic liquid EMI-BF_4 as propellant. These out-of-plane emitters enable one to obtain a high packing density and therefore a high thrust per area and device mass. We microfabricated arrays of 2500 emitters per cm^2 comprising a capillary and spacer layer as well as an integrated electrode. The capillary diameter was varied in the range of 5 µm to 50 µm while the overall thickness was in the order of 100 µm.

The permeability for liquid propellants (i.e. ionic liquids like EMI-BF_4) of such emitter arrays was demonstrated. Optical investigations of single emitters during extraction tests using both integrated and externally mounted electrodes revealed that the surface of the capillary layer is wetted by the ionic liquid and therefore inhibits proper extraction.

Different surface treatments were applied to SU-8 films to alter the wetting behavior. The contact angle of EMI-BF_4 on the capillary layer surface was enhanced from 38° to 86° and even 121° using a PTFE-coating and a surface treatment with silicon dioxide nanoparticles in PDMS, respectively.

Further extraction tests on very narrow capillaries with an untreated sample's surface and single emitters coated with PTFE showed the extraction of a positive species.

Chapter 4

Miniaturized solid-state ion-emitters based on the oxygen-ion conductor YSZ

In this chapter a second approach of providing charged particles for electric propulsion purposes is presented. In contrast to the colloid emitter concept discussed in chapter 3 where droplets out of a liquid propellant function as charged particles, single ions are provided by extraction from a solid electrolyte here. The concept of this solid-state extraction principle, the ionization mechanism, and the benefits of the miniaturization of such emitters are shown in the next section. The fabrication and miniaturization of the emitter components are depicted in the second section of this chapter. In the third section, the manufactured films and membranes are investigated crystallographically and microscopically. The stress in YSZ thin films and the resulting strain patterns are analyzed using Raman spectroscopy in the fourth section. The chapter is concluded by a short discussion of the feasibility of this approach for miniaturized thrusters.

4.1 The concept of solid-state ion-emitters

Figure 4.1 depicts the layout of a solid-state ion-emitter (SSIE). It consists of a propellant reservoir, a device to ionize the propellant and an electrostatic acceleration grid system like most ESP thruster concepts. The reservoir is manufactured out of a silicon substrate by anisotropic silicon etching. Gaseous oxygen is filled into the reservoir chamber and will be ionized using the additional parts of the device. A thin film of

the solid electrolyte yttria-stabilized zirconia (YSZ) is deposited on top of the substrate. It will form a free-standing membrane at the feed-through areas to the reservoir. On the backside of this membrane and the walls of the reservoir feed-through a very thin and porous metal film of platinum is deposited to provide electrons for the reduction of molecular oxygen to incorporate O^{2-}-ions into the electrolyte. This is possible due to oxygen vacancies in the YSZ lattice. Via these vacancies ionic transport can take place in the electrolyte. The oxygen ions shall be extracted from the YSZ/vacuum interface by applying an electrostatic field. Once extracted, the acceleration process follows common ESP techniques using ion optics and a multiple grid design.

A similar approach was proposed by Wilbur et al.[81], the authors also suggested the use of solid-state ionic membranes to extract ions in order to produce thrust. The investigated CeO_2-based membranes were comparably thick with a thickness of 1 mm. Similar to our approach, O_2-molecules were converted to two O^{2-}-ions. A current density of $0.3\,\mathrm{mA\,cm^{-2}}$ was measured at a working temperature of 600 °C when a voltage of 2.5 kV was applied between the reservoir side of the membrane and an acceleration electrode at a distance of 1 mm to the membrane. In this work, significantly thinner membranes are investigated instead, which allow an operation at lower working temperatures.

As the unconventional part of this approach concerns the ionization process, brief descriptions of the solid electrolyte YSZ, the occurrence of oxygen vacancies in the oxide lattice, the incorporation of ionized oxygen into the electrolyte, the related transport process within the electrolyte, and the emission mechanics of oxygen are given.

4.1.1 The solid electrolyte yttria-stabilized zirconia

YSZ is a commonly used solid electrolyte, i.e. a solid with a high ion mobility.

History of solid electrolytes and YSZ

The first solid electrolytes Ag_2S and PbF_2 were discovered by Michael Faraday in 1833[82] and 1838[83], respectively. Michael Faraday wrote: *"1340. I formerly described a substance, sulphuret of silver, whose conducting power was increased by heat (433. 437. 438.); and I have since then met with another as strongly affected in the same way: this is fluoride of lead. When a piece of that substance, which had been fused and cooled, was introduced into the circuit of a voltaic battery,*

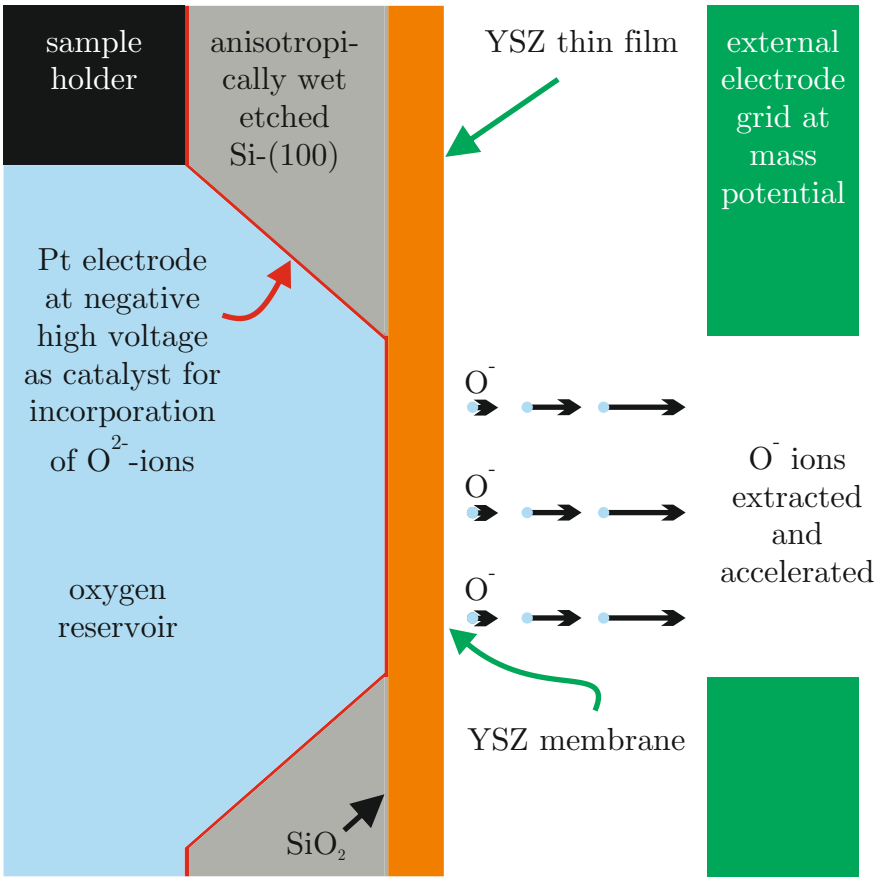

Figure 4.1: Conceptual design of a solid-electrolyte membrane based ion-emitter. A YSZ thin film is deposited onto a Si-(100) wafer where the latter is subsequently partially removed so that a free-standing YSZ membrane occurs. Oxygen molecules from the reservoir are incorporated as O^{2-}-ions into the YSZ membrane through a thin porous Pt electrode. The ions are transported through the membrane to the vacuum side from where they are extracted by the field between external electrode and the Pt electrode layer on the reservoir side of the membrane.

it stopped the current. Being heated, it acquired conducting powers before it was visibly red-hot in daylight; and even sparks could be taken against it whilst still solid. The current alone then raised its temperature (as in the case of sulphuret of silver) until it fused, after which it seemed to conduct as well as the metallic vessel containing it... "

In 1884 Warburg[84] proposed the occurence of Na^+-transport in

heated glass, whose conductivity was also investigated by Buff[85] in 1854. Warburg stated: *"Eine solche Hülle würde sich nur in dem Falle nicht bilden, wenn bei der Wanderung der Ionen das Anion (SiO_3) fest stehen bliebe und allein das Kation, nämlich das Natrium, durch das Glas hindurchwanderte; wenn also beim Glase das Anion im Verhältniss zum Kation ausserordentlich schwer beweglich wäre."*

YSZ as solid electrolyte was patented by Nernst[86,87] as he presented the *Nernst glower*, a ceramic rod which was heated to enable ionic conduction so that a current could flow through the rod heating it further leading to an even better ionic conduction until the rod thermally radiated light in a broad spectrum. Nernst wrote: *"Thus an excellent mixture which I have used in practical glowers with great success is one composed of eighty-five parts of the oxid of zirconium and fifteen parts of the oxid of yttrium."* YSZ was also the first material used in a solid oxide fuel cell (SOFC) by Baur and Preis[88] 1937. Today YSZ is established as a material used in high temperature SOFC and in lambda probes.

Zirconia

Zirconia, i.e. zirconium dioxide, naturally occurs in a monoclinic crystal structure which is stable up to 1170 °C. Above that temperature and up to 2370 °C zirconia adopts a tetragonal phase. The phase of the highest crystal symmetry occurs at even higher temperatures where the crystal structure of ZrO_2 becomes cubic. The cubic phase is of fluorite-type, i.e. the Zr^{4+}-ions form a face-centered cubic lattice while the O^{2-}-ions form a cubic sub-lattice — each O^{2-} occupies interstitial sites of the fcc sub-lattice of the Zr^{4+}-ions. This is shown on the left picture in Fig. 4.2.

Yttria-stabilized zirconia

The ionic conductivity of the cubic phase excels the conductivities of the other zirconia phases due to the very high symmetry of this phase and its high concentration of oxygen vacancies[89]. Sintered cubic zirconia will undergo the above mentioned phase transitions during cooldown resulting in monoclinic zirconia. Therefore a stabilization of the cubic phase is necessary to preserve high ionic conductivity at lower temperatures. The most common method is to replace some of the small Zr^{4+}-ions with larger Y^{3+}-ions to enable stable fluorite-type cubic crystals at normal conditions. In general, zirconia is blended with yttria (Y_2O_3) — resulting in YSZ (yttria-stabilized zirconia). At a blend

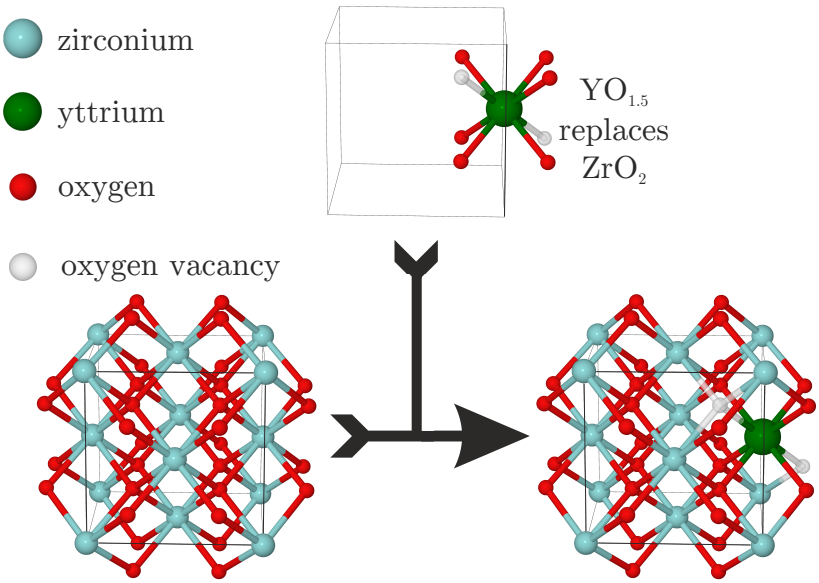

Figure 4.2: Left: Structure of cubic fluorite zirconia which is not stable at atmospheric pressure and at temperatures below 2370 °C. Right: Fully stabilized zirconia due to the blend of zirconia with yttria. When yttrium replaces a zirconium on its site, it generates half an oxygen vacancy, i.e. 2 out of the 8 surrounding oxygen sites are unoccupied.

ratio of 4 mol % yttria or higher, zirconia is stabilized in the tetragonal phase, so called partially stabilized zirconia (PSZ). A blend with more than 8 mol % Y_2O_3 exhibits the fluorite cubic phase and is also called fully stabilized zirconia (FSZ). Since Y_2O_3 substitutes $2ZrO_2$, some oxygen sites in the lattice are not occupied in YSZ — oxygen vacancies are generated. In this work 9.5 mol % YSZ was used to grow the membrane structures. According to the considerations by Chen et al.[89] and Scott[90], this electrolyte is in a stable fluorite cubic phase from room temperature up to its melting point of 2700 °C. The fully yttria-stabilized zirconia exhibits its maximum oxygen ion conductivity in the range of 7.5 mol % to 10 mol % yttria. YSZ with higher yttria concentrations have a lower ion conductivity which can be explained by short range ordering of the anion sublattice[89]. The stabilized zirconia as well as the vacancy formation are shown in Fig. 4.2.

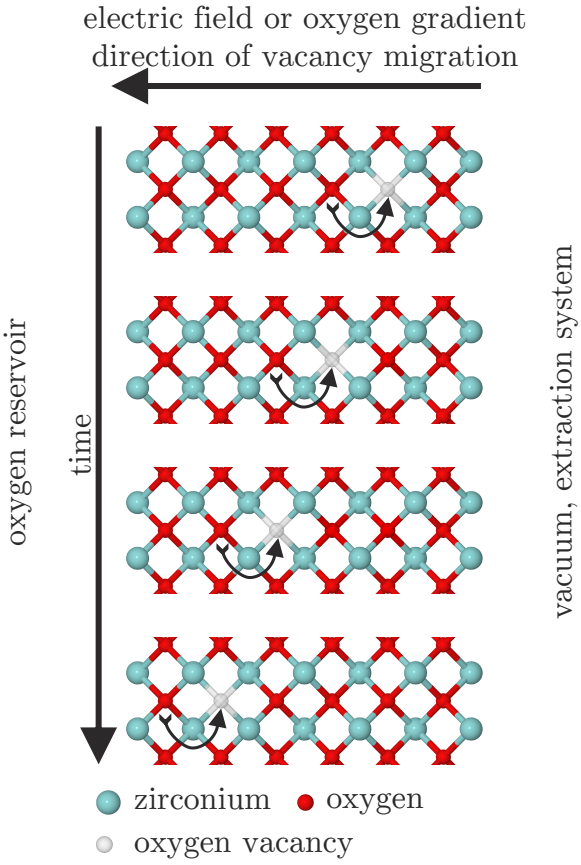

Figure 4.3: Vacancy migration in yttria-stabilized zirconia. The electric field or an oxygen gradient is applied from the right to the left. An oxygen ion will then likely hop to an adjacent vacancy on the right (top situation). Now the vacancy is a site further to the left and an adjacent oxygen to the left may hop into it (second step). This continues (third and fourth step) as long as the electric field is applied or an oxygen gradient is present. The vacancy moves along the gradient and or electric field.

4.1.2 Incorporation and transport of oxygen ions in the solid electrolyte yttria-stabilized zirconia

To incorporate molecular oxygen into the YSZ membrane on the reservoir side, additional electrons have to be provided. Oxygen has to be implemented as O^{2-} into a vacancy, therefore 2 electrons are required. This leads to the defect reaction for the oxygen incorporation:

$$2e' + V_O^{\bullet\bullet} + \frac{1}{2}O_2(g) \rightarrow O_O^{\times}. \tag{4.1}$$

To provide these electrons, an electrode has to be placed at the interface between the reservoir of molecular oxygen and the backside of the YSZ electrolyte, cf. Fig. 4.1. This membrane has to be porous to generate a large three-phase boundary between electrode, electrolyte and gaseous oxygen. Platinum has proven to be a suitable electrode material and has been widely investigated as a porous thin film electrode material[91–95] for μ-SOFC and lambda probe applications.

Once the oxygen is incorporated according to Eq. (4.1), it has to be transported via the membrane to the vacuum/membrane interface: An oxygen ion may hop into an adjacent vacancy. Since the oxygen vacancies in the electrolyte are generally not nearest neighbors a movement of vacancies into the opposite direction can be observed. Figure 4.3 shows the vacancy migration if an oxygen gradient or an electric field are present.

This transport can be described analogously to hopping transport of holes in an electronic conductor. This vacancy migration is mainly influenced by an 'activation energy' E_a which determines the hopping probability of an oxygen ion to an adjacent vacancy. The ionic hopping conductivity σ in solid electrolytes is generally described by:

$$\sigma = \alpha T^{-1} \exp(-E_a/k_B T), \tag{4.2}$$

where α expresses the intrinsic properties of the electrolyte, such as carrier densities (ions, electrons) and vacancy densities[96]. k_B and T are the Boltzmann constant and the temperature, respectively. The activation energy in YSZ varies from 1.2 eV for bulk YSZ[97,98] to 1 eV in thin-film YSZ[99].

4.1.3 Extraction of O^--ions from the membrane's surface

If a concentration gradient or electric field is applied over the membrane, O^{2-}-ions will accumulate at the emission surface of the membrane. From there oxygen can be extracted by applying an external field. Investigations on the extraction behavior of oxygen species from a heated YSZ film were performed by Torimoto et al.[100,101] and Fujiwara et al.[102–104].

Torimoto et al.[100] conducted experiments on 2 mm thick YSZ films with gold electrodes on both the air and vacuum (10^{-3} Pa) side. With an external electrode at a distance of 15 mm from the emission surface and voltages of 100 V and 150 V between this electrode and the Au electrode on the air side of the YSZ film quadrupole mass spectrometry showed the emission of both O^--ions and electrons at temperatures in the range of 470 °C to 580 °C. The extraction voltage could be reduced to values below 30 V with a microstructured gold ion-grid on a 1 mm thick YSZ film at 550 °C.

Fujiwara et al.[102–104] investigated the emission of oxygen from a bare surface of YSZ by quadrupole mass spectrometry. The authors

used a 1.5 mm thick YSZ film with an Y_2O_3 concentration of 8 mol %. The backside of the film was coated with a porous platinum electrode and exposed to air atmosphere. An extraction electrode was placed at a distance of 3 mm to the untreated emission side of the YSZ film which faced vacuum of the order of 10^{-3} Pa. Mass spectrometry detected only O^--ions as emitted particles while the YSZ was heated to 725 °C to 950 °C at extraction voltages up to 450 V. The O^--ion count rate was found to be temperature dependent with an activation energy of 2 eV to 3 eV. It also exhibited a strong time dependence, i.e. the O^--ion count rate decreased exponentially with time constants in the order of a few seconds. This effect was reversible after a relaxation time of the order of the voltage pulse duration. The authors also proposed a model of the O^--ion emission mechanism, *"Oxygen will be provided to emission surface as oxygen atoms rather than oxygen negative species. ...the dominant emission process of O^- ions will be the emission from chemisorption sites on the emission surface rather than the direct emission from anion sites in solid oxides..."* I.e., the migrating oxygen ion O^{2-} within the oxide will be released at the emission surface in the reverse way as the incorporation (Eq. (4.1)):

$$O_O^{\times} \rightarrow 2e' + V_O^{\bullet\bullet} + O, \tag{4.3}$$

yielding two free electrons, an oxygen vacancy and an oxygen atom O. The electrons have to be conducted to the backwards electrode. The oxygen atoms capture electrons due to their positive electron affinity yielding an accumulation of O^--ions on the emission surface. The authors state that the production of O^--ions on the emission surface and hence the emission current is limited by electron capture of oxygen atoms rather than the oxygen permeation by electronic conduction[102,103]. Experiments with a platinum coated emission surface of the YSZ film were also performed yielding an effect of electrochemical polarization on the emission of O^--ions and the possible emission of electrons[104].

4.1.4 Benefits of the miniaturization of solid-state ion-emitters

We showed in the previous section, that the ionic transport through a solid electrolyte is dominated by the vacancy migration inside the electrolyte. According to Eq. (4.2) the conductivity depends exponentially on temperature — in common YSZ-based SOFC temperatures above

800 °C are required to yield suitable conductivities. To lower these temperatures one may optimize the chemical composition in order to enhance the α-value. A reduction of the activation energy E_a would also lower the temperature but E_a is also determined by the lattice parameters. YSZ with 8 mol % to 10 mol % yttria generally fulfill these conditions and exhibit one of the highest conductivities amongst YSZ compositions[89,90].

In a very simple approach the absolute conductance G is proportional to the conductivity σ:

$$G = \sigma \frac{A}{l}, \tag{4.4}$$

where A is the surface perpendicular to the current direction, l is the transport length in current direction. G can be enhanced by the simple geometrical approach of length reduction or, in the case of electrolyte films, by the reduction of the film thickness. Therefore the required temperature can be minimized by using solid-electrolyte membranes.

The same approach is applied in the development of miniaturized SOFC (μSOFC) where thin electrode membranes are used instead of thick layers in order to reduce the operating temperature of such fuel cells[93,105–108].

4.2 Micro-fabrication of miniaturized solid-state ion-emitters

In the last section the concept of a solid-state ion-emitter was discussed. This SSIE concept is based on the ionization of molecular oxygen by the solid electrolyte YSZ. To enable the required oxygen transport within the electrolyte, the device has to be operated at elevated temperatures. The use of a thin membrane of this electrolyte leads to a lower temperature and hence to a better energy efficiency.

In this section we describe the fabrication of such miniaturized membranes. Firstly, the deposition of a thin YSZ film is described. Secondly, the deposited films are characterized by X-ray diffraction (XRD) and by scanning electron microscopy (SEM). Thirdly, the fabrication of a membrane starting with a silicon wafer is shown.

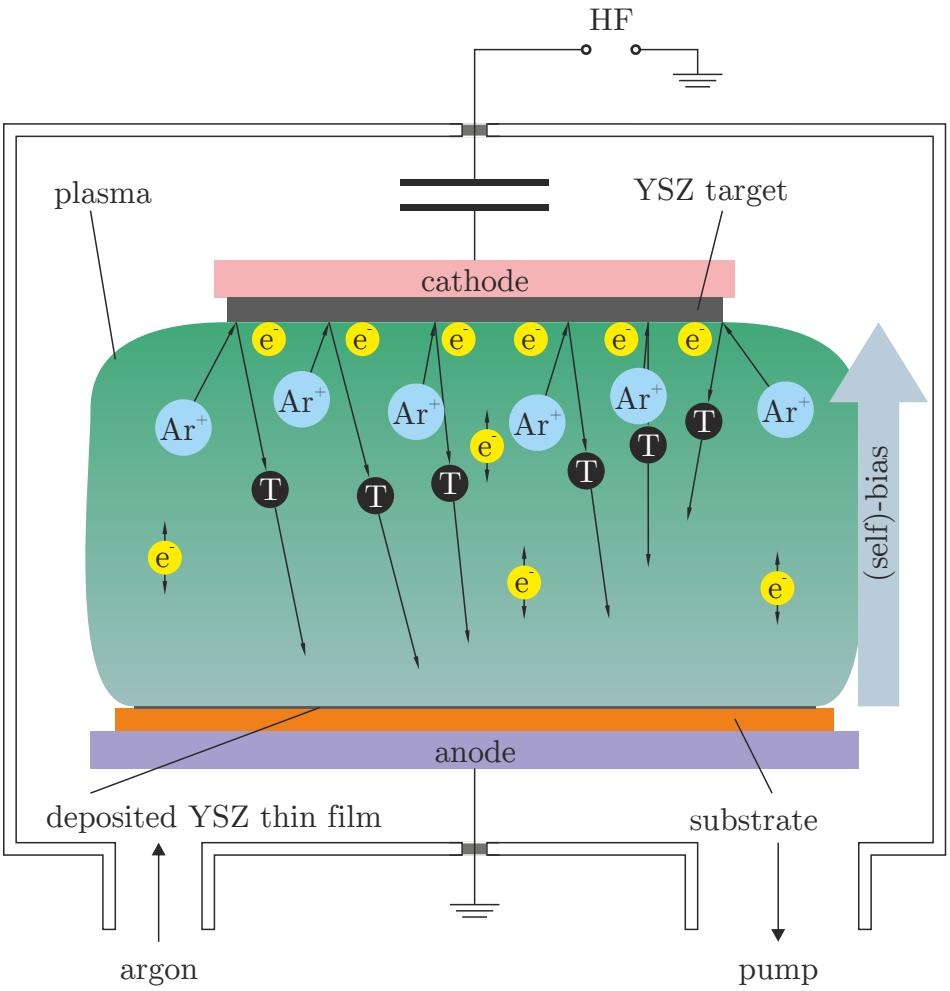

Figure 4.4: Cross section of a RF-sputter-deposition chamber. A RF voltage is coupled capacitively to the cathode on which the YSZ target is mounted. The electrons (yellow) follow the RF field and gather at the cathode. They build up a self-bias between anode and cathode. The argon Ar^+-ions (blue) cannot follow the RF field but move in the DC self-bias to the YSZ target and sputter YSZ particles (grey, T) off it. These particles are then deposited onto the substrate and form a YSZ thin film [109].

4.2.1 Growth of thin films of the solid electrolyte YSZ

As depicted in section 4.1, SSIE are based on thin solid-electrolyte membranes. These membranes were manufactured out of thin films of the solid electrolyte YSZ. There are several techniques to deposit YSZ as thin film such as the physical vapor deposition (PVD) techniques of spin-coating[110], electron beam evaporation[111], pulsed laser deposition (PLD)[112,113] or sputter-deposition[114–116]. They all have in common, that they use sintered YSZ or YSZ powder which is then deposited onto a substrate during the process. Other growth methods of YSZ thin films are electrodeposition[117] or the chemical vapor deposition (CVD) methods of plasma enhanced CVD (PECVD)[118] or atomic layer deposition (ALD)[106]. The thin films used in this work were grown by the PVD technique of sputter-deposition.

Sputter-deposition was observed accidentally during low pressure gas discharge experiments by Grove[119] in 1852. Sputtering describes the pulverization of a solid surface due to the impact of energetic ions. Generally, ions are provided by the ionization of a working gas like argon. These ions are accelerated onto a cathode which acts as the so called target consisting of the material to be deposited. The atoms sputtered off the target are then deposited on a substrate in the plasma sheath. There are several modifications of the sputter-deposition technique. To circumvent space charge effects and in order to enable one to use insulating targets it is possible to alternate the electrode polarization and to generate a RF-field (radio frequency field). With the use of an additional magnetron, the sputter yield can be further enhanced as higher plasma densities are achieved. Other ways of ionization are used in ion-beam sputter-deposition as well as in the ECR-sputter-deposition (electron cyclotron resonance). Additionally, reactive gases can be used to create chemical compounds with the target atoms[120].

In this work, argon was used as the working gas with a working pressure of 3×10^{-1} Pa in an RF-sputter-deposition chamber. A YSZ target with a blend ratio of 9.5 mol % Y_2O_3 and a purity of 99.9 % was used as target material. Figure 4.4 shows a schematic cross section of a RF-sputter-deposition chamber. In the AC field between anode and cathode, both ions and electrons of the plasma are accelerated alternating in both directions. A self-bias is built up between substrate and target. The ions cannot follow the RF field but are affected by the self-bias and are accelerated towards the target where they sputter off target atoms. The latter are deposited onto the substrate surface and

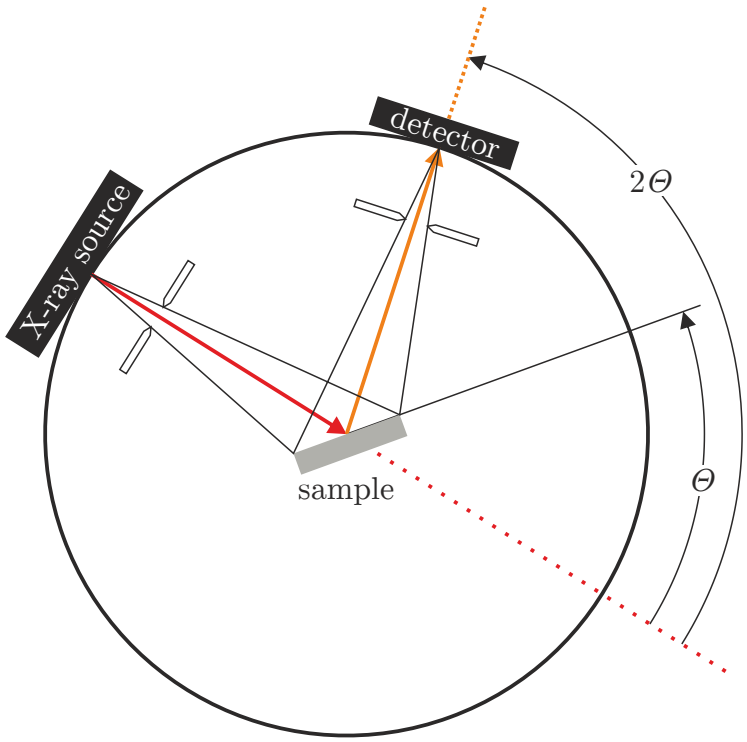

Figure 4.5: Schematic view of an X-ray diffractometer in the Bragg-Brentano-setup[121]. The X-ray source is kept at a constant position with a constant emitting direction. When the sample surface is turned to an angle Θ to the incident radiation, the detector will be turned to an angle 2Θ to the incident radiation, i.e. the angular velocity of the detector is twice as high as that of the sample. Thus, the incident and reflected X-rays are both at an angle of Θ to the sample surface.

form a thin film.

4.2.2 Properties of the YSZ thin film

The RF-sputtered YSZ thin films were investigated by X-ray diffraction (XRD) and by scanning electron microscopy (SEM) to analyze their structural properties.

Crystallographic investigations

The samples were analyzed with a *SIEMENS* X-ray diffractometer *D5000* in Bragg-Brentano-setup[121] which is depicted in Fig. 4.5. This setup is suitable for investigations of polycrystalline films. It consists

of a monochromatic X-ray source which is coupled with the detector to ensure that the reflection angle Θ' stays the same as the incident angle Θ — the angle between incident and reflected X-rays is then 2Θ. Measurements of the detected X-ray intensity are taken over a set of different incident angles Θ. If under certain angles the Bragg condition is fulfilled:

$$2d\sin(\Theta) = n\lambda, \tag{4.5}$$

an enhancement of the detected intensity will be observed. The n-th maximum occurs at a certain Θ. If the wavelength λ of the X-ray source is known, the spacing between planes in the crystal lattice d may be determined. An X-ray diffractogram depicts the detected intensity versus the angle 2Θ between incident and detected light. The X-ray ($\lambda = 1.542\,\text{Å}$) diffractogram of a YSZ thin film on an oxidized silicon-(100) substrate is shown in Fig. 4.6 (black). A reference sample was also investigated to yield the substrate background, the corresponding diffractogram is also depicted in Fig. 4.6 (red).

To yield the lattice parameters, d has to be calculated by using Eq. (4.5). Depending on the lattice structure and the sample orientation, d can be expressed by the lattice parameters, in case of a cubic structure this relation is quite simple:

$$\frac{1}{d^2} = \frac{h^2 + k^2 + l^2}{a^2}. \tag{4.6}$$

The cubic unit cell is a cube with edge length a which is the lattice constant. The Miller indices (hkl) describe the planes whose spacing is d.

Both the $\Theta - 2\Theta$ traces of YSZ on SiO_2 on Si (black) and that of SiO_2 on Si (red) patterns are dominated by a reflex at $2\Theta_{\text{Si}} = 69.19°$ and were normalized to its intensity to ensure good comparability. Using Eqs. (4.6) and (4.5), this reflex of the Si-(100) substrate lattice corresponds to the (400) planes of silicon, as silicon has a lattice constant of $a_{\text{Si}} = 5.431\,\text{Å}$. Comparing both patterns, the only difference is the reflex occurring at $2\Theta_{\text{c-YSZ}} = 29.8°$. It has to originate from the YSZ thin-film layer. Scott[90] expressed the lattice constant $a_{\text{c-YSZ}}$ of cubic YSZ with respect to the mole fraction x of $YO_{1.5}$ in ZrO_2:

$$a^{\text{Scott}}_{\text{c-YSZ}}(x) = 5.104\,\text{Å} + x \cdot 0.204\,\text{Å}, \text{ for } 0.18 < x < 0.9. \tag{4.7}$$

As we used YSZ with a blend ratio of 9.5 mol % Y_2O_3 this corresponds to $x = 0.19$, yielding a scattering angle closest to 29.8° of

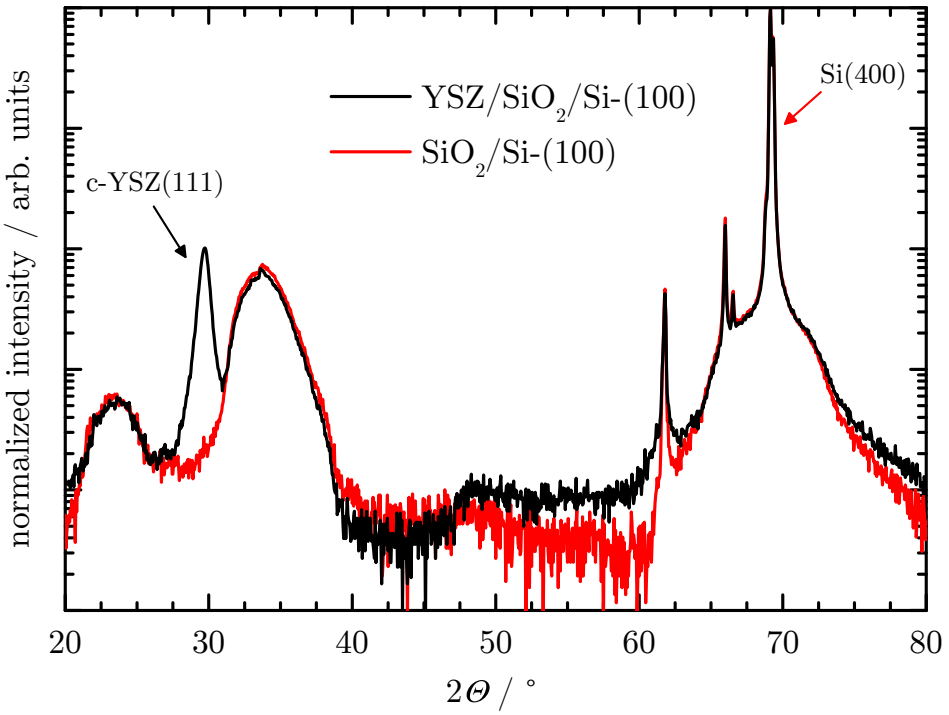

Figure 4.6: X-ray ($\lambda = 1.542\,\text{Å}$) diffractogram of YSZ on SiO_2 on Si-(100) (black curve). The reference sample was SiO_2 on Si-(100) (red curve). The data are normalized to the Si (400)-reflex at 69.15°. The only distinguishable feature of the YSZ film is the reflex at 29.8°. This is correlated to the cubic YSZ (111)-reflex which is expected [90] for 9.5 mol % Y_2O_3 at 30.1°. But it is shifted down either due to the growth induced stress or a larger lattice constant due to strain relaxation.

$2\Theta^{\text{Scott}}_{\text{c-YSZ}}(0.19)(111) = 30.1°$. The discrepancy with the measured scattering angle may be due to the heteroepitaxial growth, i.e. the mismatch between the two lattice constants $a^{\text{Scott}}_{\text{c-YSZ}}(0.19) = 5.143\,\text{Å}$ and $a_{\text{Si}} = 5.431\,\text{Å}$. Thus, either the growth induced stress or a larger lattice constant due to strain relaxation yields the discrepancy between calculated and measured scattering angle. A fully relaxed YSZ film would exhibit a lattice constant of $a_{\text{c-YSZ}} = 5.193\,\text{Å}$.

Surface morphology and granular structure

To investigate the surface morphology and to obtain knowledge about grain size, growth mode, growth direction, and film thickness, SEM images were taken with a *JSM 7001F* from *JEOL*. With the detection of

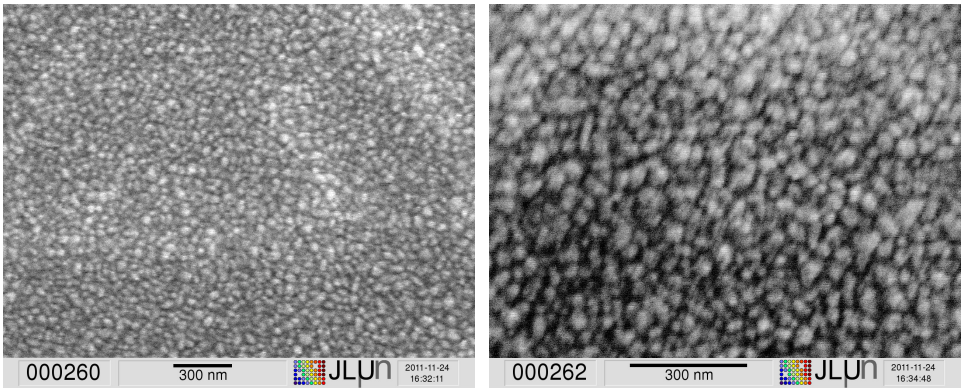

Figure 4.7: SEM images of surfaces of a roughly 1.1 µm thick YSZ film which was grown by RF-sputtering. The polycrystalline structure of the film is clearly observable with the SEM images above. A grain size of about 50 nm was measured.

secondary electrons after the bombardment of the sample surface with high energy electrons ($E \approx 10\,\mathrm{keV}$) it is possible to resolve features in the range of few nanometers. To circumvent space charge issues due to the insulating character of YSZ at room temperature, a thin metal film was evaporated onto the samples to enhance the electronic conductivity at the surface.

Figure 4.7 shows SEM images of YSZ on a silicon substrate revealing the granular structure of the surface, i.e. the polycrystalline growth is clearly observable. The grain distribution is very homogenous. To determine the grain size, the right image with a higher magnification was used. The grain size is $(50 \pm 10)\,\mathrm{nm}$.

In Fig. 4.8 broken edges of YSZ thin-film samples are shown. A columnar growth normal to the substrate surface is observed. The column diameter is consistent with the grain size. The film thickness is 1.1 µm.

The successful growth of the YSZ thin films is the basis for the fabrication of free-standing membranes of YSZ for SSIE purposes. In the next section membranes fabricated out of YSZ thin films and following the process flow discussed in section 4.2.3 are investigated optically.

4.2.3 Process flow for the miniaturization of SSIE using micro-fabrication

In the previous section the growth method of YSZ thin films was described. Figure 4.9 depicts the overall process flow for fabricating

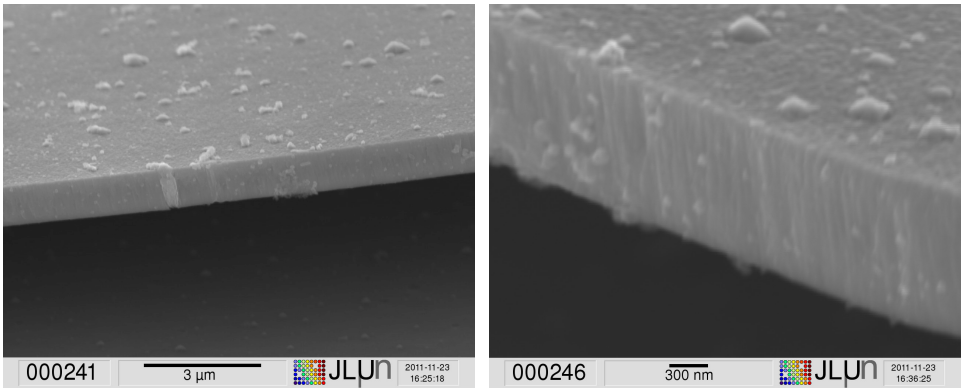

Figure 4.8: SEM images of broken edges of a YSZ film which was grown by RF-sputtering. Columnar growth along the growth direction of the film is clearly observable. A film thickness of 1.1 µm was measured.

membranes of YSZ. It starts with the silicon substrate and results in free-standing YSZ membranes. The individual steps of the membrane fabrication are briefly described in the following.

Prior to the actual micro-fabrication process, the silicon substrate has to be oxidized for two reasons: First, the oxide layer should insulate the solid electrolyte from the silicon substrate to ensure a reservoir side electrical contact only by the porous electrode depicted in the SSIE concept, cf. Fig. 4.1. Second, it is also required for the fabrication process as it works as an etch stop for the anisotropic silicon etching which is described later in this section. The substrates used in this work were double side polished (DSP) silicon wafers with a (100) surface and a diameter of 4 inches. To oxidize the surface they were put into an oven filled with ambient air at 1200 °C for 2 h. This led to an oxide layer with a thickness of roughly 200 nm (cf. Fig. 4.9 (a)).

Afterwards each 4-inch wafer was broken to reduce the sample size in order to perform the next step of electron beam lithography (EBL). The EBL was used to define specific patterns onto the oxide layer which was intended as the reservoir side of the substrate. After the oxidized samples were cleaned and singe baked, the EBL-resist poly(methyl methacrylate) (PMMA) was spin coated on top of both sides (cf. Fig. 4.9 (b)). In the EBL process itself, the electron beam was scanned over the desired area to expose the PMMA by cracking its polymer chains. The resist was then dissolved in diluted isopropyl alcohol which resulted in the removal of the exposed parts of the PMMA (cf. Fig. 4.9 (c)). The resulting pattern defines the etch mask for the following etching of SiO_2.

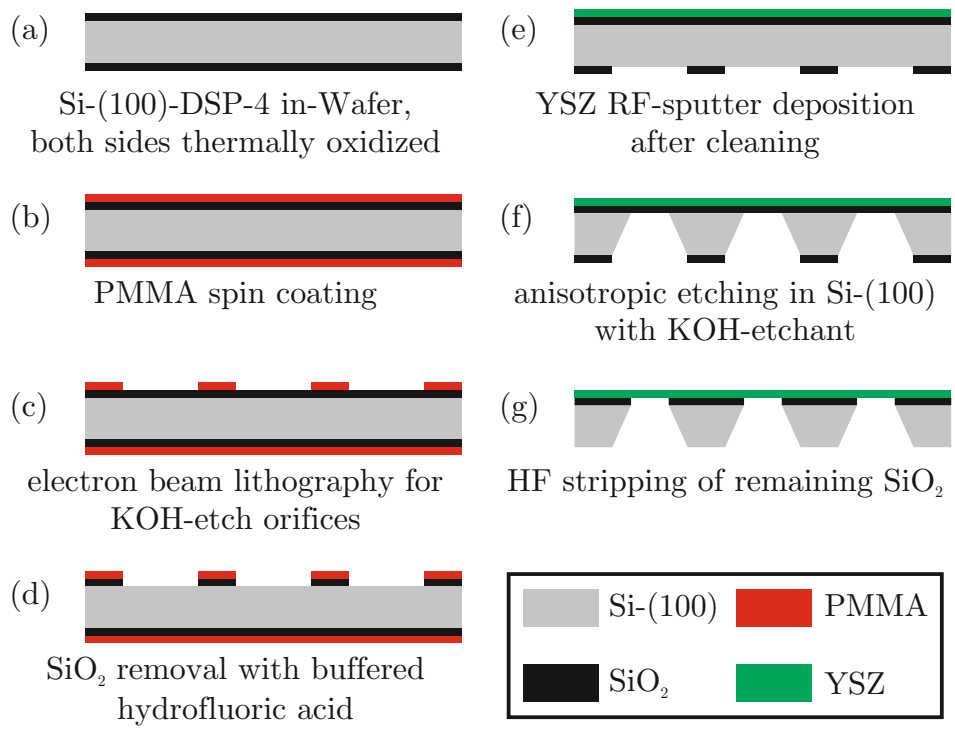

Figure 4.9: Process flow of YSZ membrane fabrication. The sample was turned upside down between step (d) and step (e).

The masking described above is only an intermediate step to produce a hard mask comprising SiO_2 for the subsequent step of silicon etching. The SiO_2 layer was etched in buffered hydrofluoric acid (BHF). This isotropic etch only affected the uncovered parts of the SiO_2. Underetching was negligible, since it was only a few hundred nanometers in lateral direction while the orifice of the mask pattern was of the order of ten or more micrometer. The resulting sample (cf. Fig. 4.9 (d)) was then cleaned and ready for the YSZ thin-film sputter-deposition as described in section 4.2.1. It is important to note, that the sample sides were changed before, i.e. before the deposition took place on the untreated SiO_2 side (cf. Fig. 4.9 (e)).

After the YSZ deposition, the anisotropic etch of the substrate had to be performed. Potassium hydroxide in solution (KOH) worked as etchant which reacts with silicon as described below and yielded frustums of pyramid in the silicon substrate and membranes consisting of both a SiO_2 and a YSZ layer (cf. Fig. 4.9 (f)).

Finally, the SiO_2 layer of each membrane was removed by HF etching (cf. Fig. 4.9 (g)).

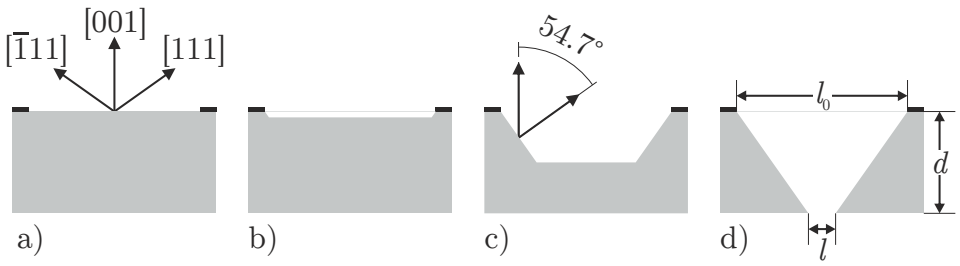

Figure 4.10: Scheme of anisotropic Si etching with KOH. The silicon is (100)-oriented (a). The (111)-surfaces are not etched at all. Right after the beginning of the etch (b), an etch pit with sidewalls at an angle of 54.7° to the edge direction are formed (c). Finally, either a pyramidal shape or a frustum will be etched (d). The final length l of the short side of the frustum depends on the mask pattern size l_0 and the wafer thickness d: $l = l_0 - \sqrt{2}d$.

Anisotropic silicon etching

KOH is dissolved in water, the OH^--ions will attach to the free bonds of the atoms on a silicon surface releasing an electron. If a silicon surface-atom possesses two free bonds, two OH^--ions are attached:

$$Si + 2OH^- \rightarrow Si(OH)_2 + 2e^-. \tag{4.8}$$

This silicon is still bound to the crystal by two more bonds. These bonds will be broken if another two electrons are released:

$$Si(OH) \rightarrow (Si(OH)_2)^{++} + 2e^-. \tag{4.9}$$

This dissolved complex reacts with two other free hydroxide ions:

$$(Si(OH)_2)^{++} + 2OH^- \rightarrow Si(OH)_4. \tag{4.10}$$

Now it dissociates under the release of hydrogen directly into:

$$Si(OH)_4 \rightarrow (SiO_2)OH_2^{2-} + 2H^+. \tag{4.11}$$

The hydrogen reacts with hydroxide to water:

$$2H^+ + 2OH^- \rightarrow 2H_2O. \tag{4.12}$$

Together with two more water molecules the 4 electrons react to hydroxide ions and molecular hydrogen:

$$4H_2O + 4e^- \rightarrow 4OH^- + 2H_2. \tag{4.13}$$

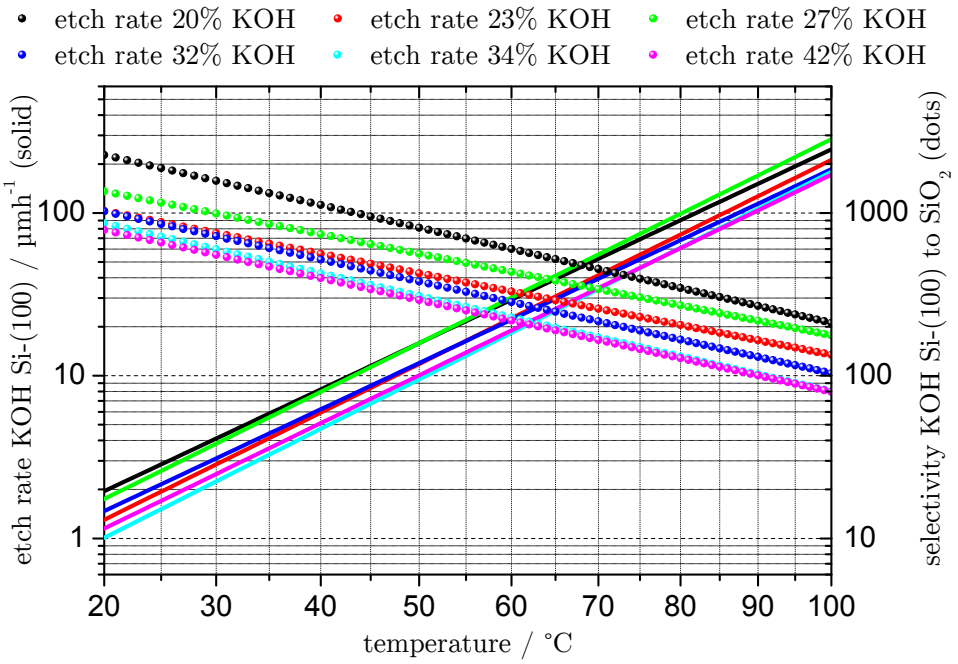

Figure 4.11: Temperature dependence of the etch rate (solid lines) of Si-(100) and the selectivity (dotted lines) of Si-(100) to SiO_2 in different KOH solutions.[123]

This leads to the total reaction equation[122]:

$$Si + 2H_2O + 2OH^- \rightarrow (SiO_2)OH_2^{2-} + 2H_2. \qquad (4.14)$$

Let us now consider a (100) terminated silicon sample with a masking orifice on the surface (Fig. 4.10 (a)). As the atoms of the silicon (100)-surface have two free bonds and another two which are pointing into the crystal volume the etching will start normal to the surface (Fig. 4.10 (b)). However, although the etching in the middle of the orifice still occurs normal to the surface, it will more or less stop gradually near the orifice boundaries (Fig. 4.10 (c)). It happens due to the crystal structure of silicon. Once the first layer of silicon is etched, almost the whole surface stays (100)-oriented. On the side planes of the etching pit an etch boundary occurs — the (111)-surface. In contrast to (100)-atoms, atoms of the silicon (111)-surface have only one free bond, while the other three bonds are with neighboring silicon atoms within the crystal volume. Therefore the reaction described above is not possible. The (111)-surface has an angle of about 54.7° or exactly $\arctan\sqrt{2}$ to the (100)-surface. E.g., etching from a quadratic mask

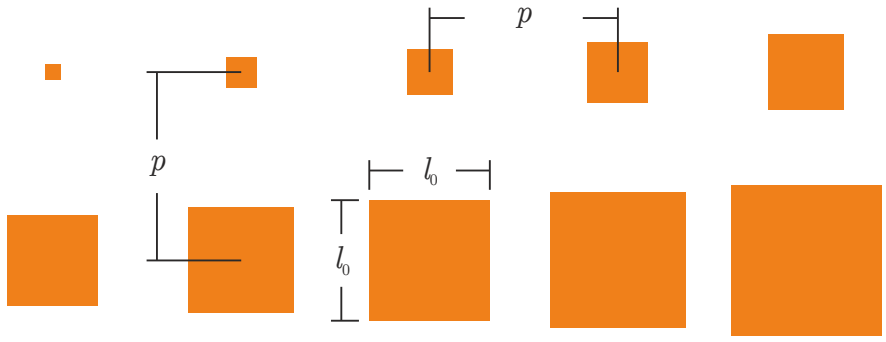

Figure 4.12: Scheme of the mask pattern in order to investigate the influence of different mask sizes on the membrane size and shape. Square patterns with side length l_0 of a mask orifice and pitch p were written into the SiO_2 mask by EBL and subsequent BHF etching as described in section 4.2.3.

will yield a pyramidal shape of the etching pit. If there is an etch stop like the SiO_2 layer on the opposite surface of the sample before reaching the tip of the pyramid, a frustum will occur instead (cf. Fig. 4.10 (d)). Thus, the membrane size l could be estimated for a quadratic orifice quite easily:

$$l = l_0 - \sqrt{2}d, \tag{4.15}$$

where l_0 is the size of the orifice in the mask and d is the substrate thickness.

The etch selectivity of Si-(100) versus Si-(111) is very high, i.e., no etching could be observed in [111] direction. But the etch selectivity of Si-(100) versus SiO_2 is considerably lower and depends on the dilution of the KOH solution as well as on the temperature of the etching bath. Additionally, the absolute etch rate of Si-(100) also depends on these parameters. An overview of the etch rates versus temperature for several KOH solutions is depicted in Fig. 4.11. For most of the etching, a 20 mol % KOH solution was used, since the selectivity against SiO_2 is highest and thus the oxide thickness could be kept comparatively low.

The influence of different mask sizes (cf. Fig. 4.12) on the membrane size and shape was investigated in great detail and is discussed in section 4.3.

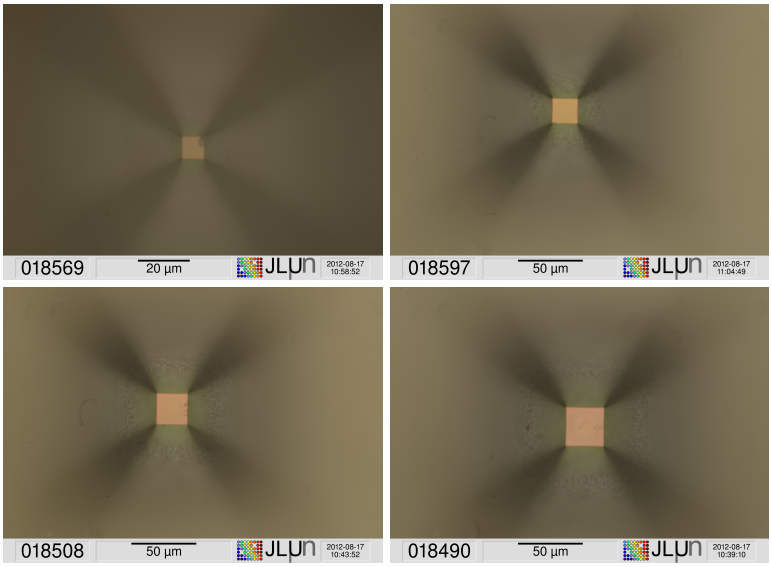

Figure 4.13: Optical images of free-standing membranes without an observable strain pattern. The membrane sizes varied from 10 µm (top left) over 20 µm (top right) and 30 µm (bottom left) to 40 µm (bottom right).

4.3 Optical investigations of ion-conductor membranes of different sizes

In the previous sections, we described the concept of a solid-state ion-emitter (SSIE) based on solid electrolyte membranes. We showed the growth process of YSZ thin films and the fabrication of free-standing YSZ membranes out of these thin films by anisotropic silicon etching. In this section, the YSZ membranes manufactured in the above mentioned way are investigated optically to analyze the influence of the membrane size on their stability and on the strain state of the membranes.

In section 4.2.3 we described the microfabrication process of the membranes. Making use of the anisotropic etching behavior of the silicon substrate it was possible to fabricate quadratic membranes with different lateral dimensions l. For a constant substrate thickness $d = 100\,\mu\text{m}$, l only depends on the size l_0 of the orifice in the mask pattern (cf. Eq. (4.15)). Patterns with varying orifice dimensions as depicted in Fig. 4.12 were written into the SiO_2 mask on the samples. This leads to a series of membranes with different lateral dimensions.

Figure 4.13 shows samples with the smallest membrane sizes up to

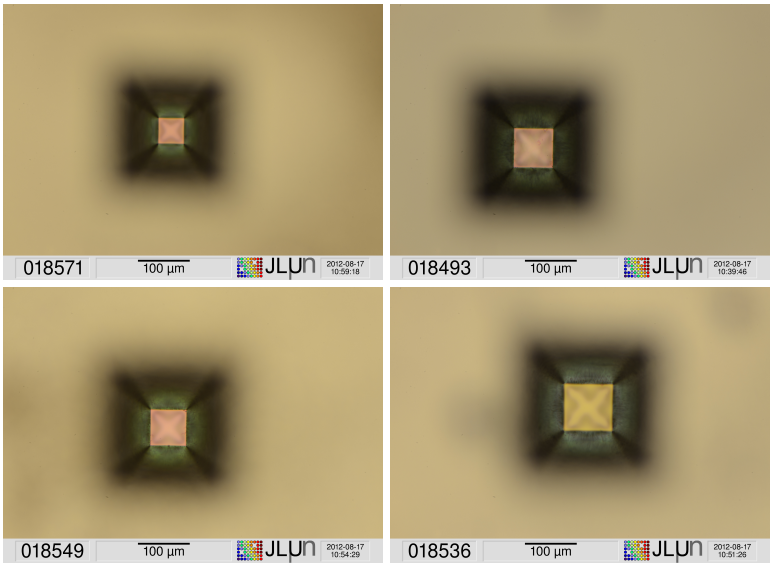

Figure 4.14: Optical images of free-standing membranes with a cross-like strain pattern. The membrane sizes varied from 50 µm (top left) over 75 µm (top right) and 80 µm (bottom left) to 90 µm (bottom right).

$l = 40\,\mu\text{m}$. They are very stable and have a smooth surface morphology. The shadows along the corners are artifacts from the etching pit in the silicon substrate. The images were taken from the substrate side of the samples.

The next larger membranes are also stable. But they exhibit a pattern on the surface. This occurs due to stress relaxation within the membrane. In addition to the different lattice parameters of YSZ and Si (refer to section 4.2.2), the two materials also have different thermal expansion coefficients which yield an internal stress during the cool-down after the thin-film deposition. The membranes in the size range of 50 µm to 90 µm exhibit a cross-like surface pattern, as shown in Fig. 4.14. The crosses possess an $\times$-like shape, i.e., along the diagonals of each square membrane the strain is mainly constant. This is analogous to a macroscopic thin tissue covering a quadratic opening. They exhibit 90°-rotational symmetry and possess mirror planes along the diagonals as well as the middle horizontal and vertical. Deviations occur for the membrane on the bottom right image. The reflection symmetry breaks down but the rotational symmetry persists.

Increasing the membrane size to edge lengths above 100 µm led to two effects. First, the surface pattern became more complicated and developed into a swastika-like shape as depicted in Fig. 4.15. Second,

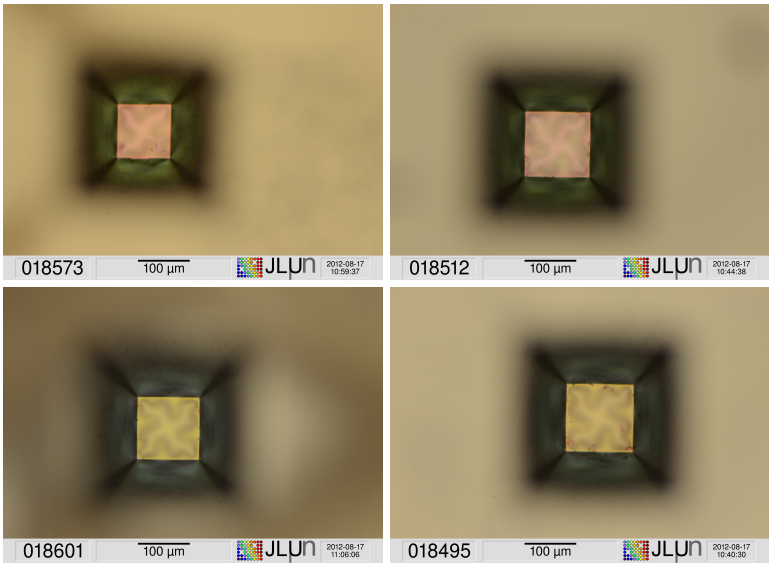

Figure 4.15: Optical images of free-standing membranes with a swastika-like strain pattern. The membrane sizes varied from 100 µm (top left) over 110 µm (top right) and 120 µm (bottom left) to 125 µm (bottom right).

defective membranes occurred with increasing membrane size. This supports the assumption of internal stress within the YSZ thin film.

Although it was possible to fabricate membranes with sizes in the range about 200 µm, the ratio of the number of defective membranes to the number of membranes prepared also increased non-linearly. The surface shape became also more complicated, the corners of the swastika developed a dendritic texture (cf. Fig. 4.16).

Membranes with sizes above 200 µm are mainly defective as shown in Fig. 4.17. Sometimes, very large stable membranes were produced, e.g. up to a 400 µm × 400 µm membrane like in Fig. 4.17 (bottom right).

With the series of membranes of different sizes it was possible to categorize the membranes according to their surface pattern. Four categories were defined: membranes without any visible surface pattern, membranes with a cross-like pattern and membranes with even more complicated patterns like swastika or highly dendritic cross patterns. The fourth category comprises defective membranes. The membranes assigned to the categories were sorted according to their size given by the edge length l, so that a correlation between surface pattern and membrane size is revealed. This is shown in Fig. 4.18. Smooth membranes without any surface pattern could be produced up to 70 µm in

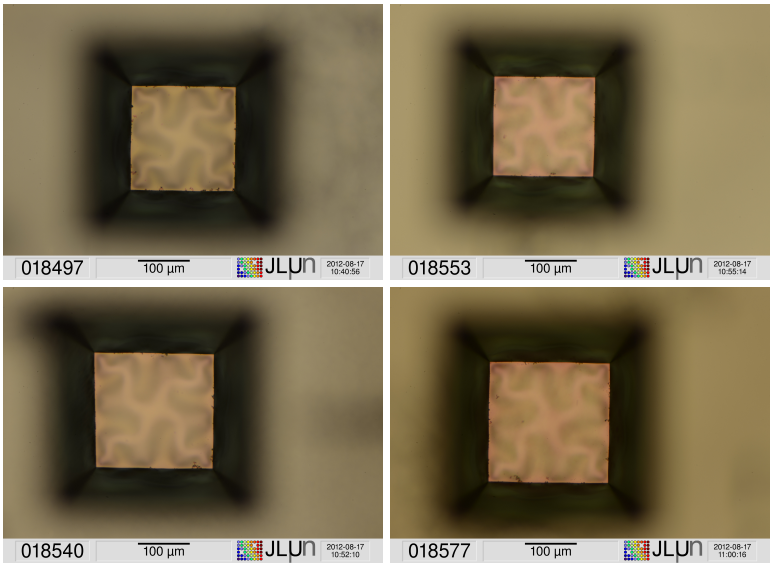

Figure 4.16: Optical images of free-standing membranes with a complicated swastika-like strain pattern with reticulate cross edges. The membrane sizes varied from 140 µm (top left) over 150 µm (top right) and 175 µm (bottom left) to 200 µm (bottom right).

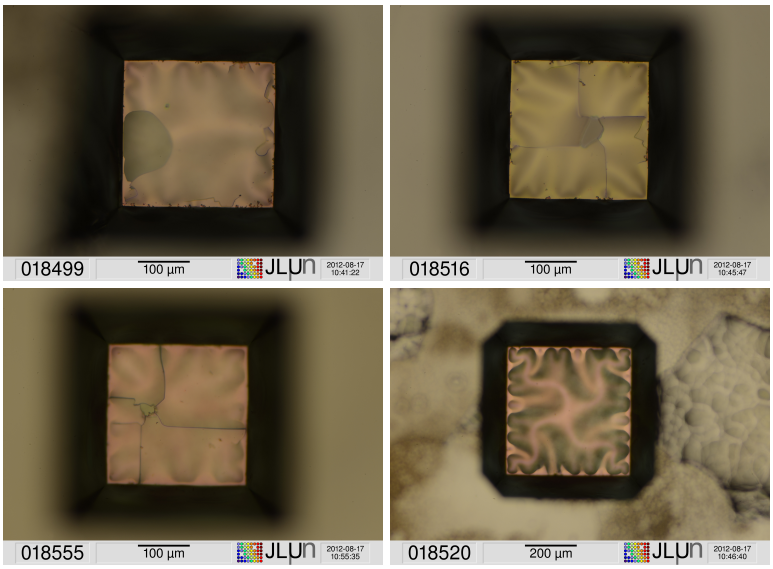

Figure 4.17: Optical images of defective free-standing membranes. The membrane sizes varied from 250 µm (top left) over 280 µm (top right) to 300 µm (bottom left). The image on the bottom right shows the largest membrane which was stable, it has a side length of 400 µm.

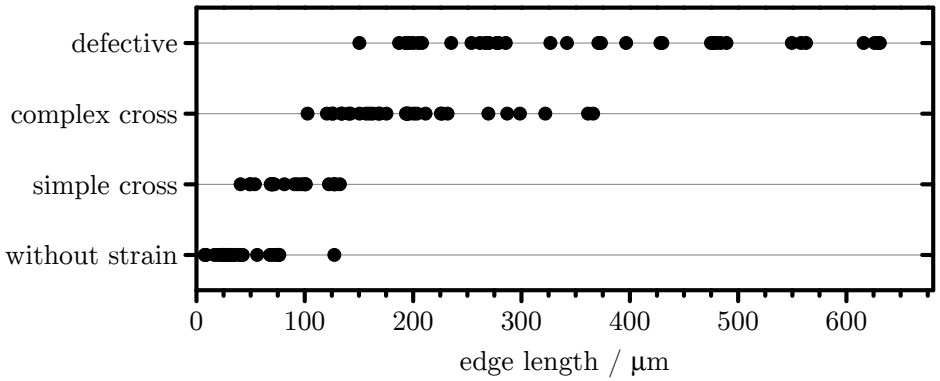

Figure 4.18: Influence of membrane size on the shape of the strain pattern within the membrane. Four categories could be distinguished. The smallest membranes up to 70 µm exhibit no observable strain. When the membrane size is enlarged (70 µm to 120 µm), the strain occurs in a simple cross shape. Further enlargement of the membrane size (120 µm to 300 µm) leads to a more complex structure of the strain pattern — it becomes swastika-like with reticulate cross edges. Above a certain membrane size of 300 µm almost every membrane becomes defective due to strain exceeding the threshold for breaking.

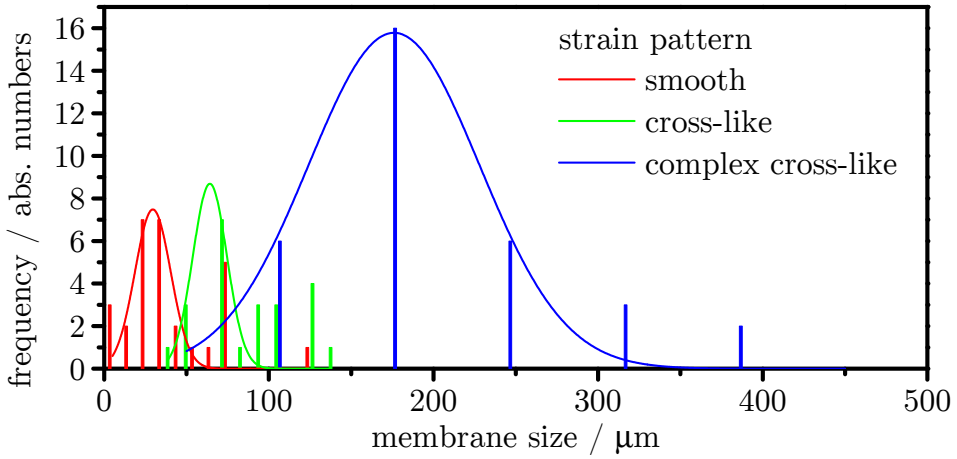

Figure 4.19: Frequency distribution of the stable membrane categories over the membrane size (solid columns). A normal distribution was fitted into the frequency distribution for each category (solid lines).

edge length. Membranes with a simple cross shape were mainly produced in the size range of 70 µm to 120 µm. The more complex patterns were observed in membranes with an edge length of 120 µm to 300 µm, while above 300 µm almost every membrane became defective (more than 90 %).

The pattern distribution versus membrane size was also statistically analyzed. The frequency distribution of the samples categorized in Fig. 4.18 were derived for each category except for the fourth category which includes the defective membranes. The results for the smooth pattern, the cross-like pattern, and the complex cross-like pattern are shown in Fig. 4.19. Thus, it is possible to predict the shape of the surface pattern for a given membrane size of 1.1 µm thick 9.5 mol % RF-sputtered YSZ on 2 µm thick SiO_2 on Si-(100): The membranes without any observable surface pattern occur in a range of 17 µm FWHM around the mean size of 30 µm. The cross-like pattern can be expected in a membrane size range of (64 ± 12) µm. The more complex pattern are to be found around 174 µm while the FWHM is 102 µm.

To investigate the origin of the strain in the membranes and to figure out the amount of residual stress within the membranes, Raman mappings were recorded. The results of this analysis are shown in the next section.

4.4 Analysis of the residual stress in free-standing membranes by Raman spectroscopy

In the previous section strain patterns were observed in the membranes by optical microscopy. The shape of these patterns becomes more complicated with increasing membrane size. Raman mappings of the membranes were recorded to analyze the residual stress within membranes.

4.4.1 The Raman effect

Raman spectroscopy utilizes a light scattering effect predicted by Smekal[124] and first experimentally observed by Raman[125,126]. The Raman effect describes the inelastic scattering of photons by vibrational modes of molecules or crystals. The following considerations the Raman effect on solid state crystals is treated. In a macroscopic consideration, light impinging on matter provides an oscillating electromagnetic field

$\boldsymbol{E}(\boldsymbol{r},t)$ ($\boldsymbol{r}$...position, t...time) which can be described as a plane wave ($\boldsymbol{k}$...wave vector, ω...frequency):

$$\boldsymbol{E}(\boldsymbol{r},t) = \boldsymbol{E}(\boldsymbol{k},\omega)\cos(\boldsymbol{k}\boldsymbol{r} - \omega t). \tag{4.16}$$

This field induces a polarization:

$$\boldsymbol{P}(\boldsymbol{r},t,\boldsymbol{Q}) = \varepsilon_0 \boldsymbol{\chi}(\boldsymbol{r},t,\boldsymbol{Q})\boldsymbol{E}(\boldsymbol{r},t). \tag{4.17}$$

Using Eq.(4.16), it follows that:

$$\begin{aligned} \boldsymbol{P}(\boldsymbol{k},\omega,\boldsymbol{Q})\cos(\boldsymbol{k}\boldsymbol{r} - \omega t) &= \varepsilon_0 \boldsymbol{\chi}(\boldsymbol{k},\omega,\boldsymbol{Q})\boldsymbol{E}(\boldsymbol{k},\omega)\cos(\boldsymbol{k}\boldsymbol{r} - \omega t) \\ \Leftrightarrow \boldsymbol{P}(\boldsymbol{k},\omega,\boldsymbol{Q}) &= \varepsilon_0 \boldsymbol{\chi}(\boldsymbol{k},\omega,\boldsymbol{Q})\boldsymbol{E}(\boldsymbol{k},\omega), \end{aligned} \tag{4.18}$$

where ε_0 is the electric permittivity of free space. The second-rank tensor $\boldsymbol{\chi}$ denotes the electric susceptibility, which describes how easily the material is polarized. The susceptibility can be expanded in a Taylor series of the powers of the lattice displacement along the normal coordinates $\boldsymbol{Q}_m$ of the vibrations:

$$\boldsymbol{\chi}(\boldsymbol{k},\omega,\boldsymbol{Q}) = \boldsymbol{\chi}_0(\boldsymbol{k},\omega) + \sum_m [\partial\boldsymbol{\chi}/\partial\boldsymbol{Q}_m]_0 \boldsymbol{Q}_m(\boldsymbol{r},t) + O(\boldsymbol{Q}^2). \tag{4.19}$$

Each $\boldsymbol{Q}_m$ can be written as a plane wave with the phonon wave vector $\boldsymbol{q}$ and the phonon frequency ω_{vib}:

$$\boldsymbol{Q}_m(\boldsymbol{r},t) = \boldsymbol{Q}_m(\boldsymbol{q},\omega^m_{\text{vib}})\cos(\boldsymbol{q}\boldsymbol{r} - \omega^m_{\text{vib}} t). \tag{4.20}$$

Inserting Eq. (4.20) into Eq. (4.19) and the corresponding result into Eq. (4.18), the polarization can be expressed as:

$$\begin{aligned} \boldsymbol{P}(\boldsymbol{r},t,\boldsymbol{Q}) &= \varepsilon_0 \boldsymbol{\chi}_0(\boldsymbol{k},\omega)\boldsymbol{E}(\boldsymbol{k},\omega)\cos(\boldsymbol{k}\boldsymbol{r} - \omega t) \\ &+ \sum_m \frac{1}{2}\left.\frac{\partial\boldsymbol{\chi}}{\partial\boldsymbol{Q}_m}\right|_0 \boldsymbol{Q}_m(\boldsymbol{q},\omega^m_{\text{vib}})\boldsymbol{E}(\boldsymbol{k},\omega)\cos[(\boldsymbol{k}+\boldsymbol{q})\boldsymbol{r} - (\omega + \omega^m_{\text{vib}})t] \\ &+ \sum_m \frac{1}{2}\left.\frac{\partial\boldsymbol{\chi}}{\partial\boldsymbol{Q}_m}\right|_0 \boldsymbol{Q}_m(\boldsymbol{q},\omega^m_{\text{vib}})\boldsymbol{E}(\boldsymbol{k},\omega)\cos[(\boldsymbol{k}-\boldsymbol{q})\boldsymbol{r} - (\omega - \omega^m_{\text{vib}})t]. \end{aligned} \tag{4.21}$$

The first line of Eq. (4.21) describes the elastic scattering of light with matter — the Rayleigh scattering. The two sums in Eq. (4.21) correspond to the Stokes-Raman scattering and the Anti-Stokes-Raman scattering.

In order for a vibrational mode $\boldsymbol{Q}_m$ to be Raman-active, the first-order terms of susceptibility in that vibrational mode have to be non-zero:

$$\left.\frac{\partial \boldsymbol{\chi}}{\partial \boldsymbol{Q}_m}\right|_0 \boldsymbol{Q}_m \neq 0, \text{ i.e.: } \left.\frac{\partial \boldsymbol{\chi}}{\partial \boldsymbol{Q}_m}\right|_0 \neq 0. \tag{4.22}$$

The tensor of derivatives of the susceptibility components along the normal coordinates of the vibration $\boldsymbol{Q}_m$ is called Raman tensor of this mode:

$$\boldsymbol{R}^m = \left.\frac{\partial \boldsymbol{\chi}}{\partial \boldsymbol{Q}_m}\right|_0 . \tag{4.23}$$

With the Raman tensors it is possible to determine the expected Raman modes contributing to the Raman signal in a certain measurement geometry:

$$I_{\mathrm{is}} \propto \sum_m \left|\boldsymbol{e}_{\mathrm{i}} \boldsymbol{R}^m \boldsymbol{e}_{\mathrm{s}}\right|^2, \tag{4.24}$$

with the overall intensity I_{is} of Raman-scattered light polarized along $\boldsymbol{e}_{\mathrm{s}}$ and the direction of polarization of the incident light $\boldsymbol{e}_{\mathrm{i}}$.

Considering the energy conservation during the scattering of photons with phonons, a phonon is generated in the Stokes-Raman scattering process while in the Anti-Stokes-Raman scattering process a phonon is annihilated. In the Stokes case, the scattered photon looses energy to the generated phonon. If the energy of the scattered photon is increased compared to the incident photon, the latter case will occur. As shown above, in the elastic case of Rayleigh scattering the incident and scattered photon possess the same energy.

The momentum conservation holds:

$$\begin{aligned} \hbar \boldsymbol{k}_{\mathrm{i}} &= \hbar \boldsymbol{k}_{\mathrm{s}} \pm \hbar \boldsymbol{q} \\ \hbar \boldsymbol{q} &= \hbar \boldsymbol{q}_{\mathrm{BZ}} + \hbar \boldsymbol{K} \\ \boldsymbol{k}_{\mathrm{i}} - \boldsymbol{k}_{\mathrm{s}} &= \pm \left(\boldsymbol{q}_{\mathrm{BZ}} + \boldsymbol{K}\right), \end{aligned} \tag{4.25}$$

with the wave vectors of the incident $\boldsymbol{k}_{\mathrm{i}}$ and scattered $\boldsymbol{k}_{\mathrm{s}}$ photons and of the phonon $\boldsymbol{q}$, the latter consisting of the wave vector $\boldsymbol{q}_{\mathrm{BZ}}$ in the first Brillouin zone and a reciprocal lattice vector $\boldsymbol{K}$. As the wave vectors of photons in the visible and near-UV spectrum are of the order $|\boldsymbol{k}_{\mathrm{i}}| \approx |\boldsymbol{k}_{\mathrm{s}}| \leq 2 \times 10^6\,\mathrm{cm}^{-1}$ and the wave vector of a phonon near the border of the first Brillouin zone generally is two orders of magnitude larger, only phonons near the center of the first Brillouin zone are generated or annihilated in first-order Raman processes, respectively, i.e.

$$\boldsymbol{q}_{\mathrm{BZ}} \approx 0. \tag{4.26}$$

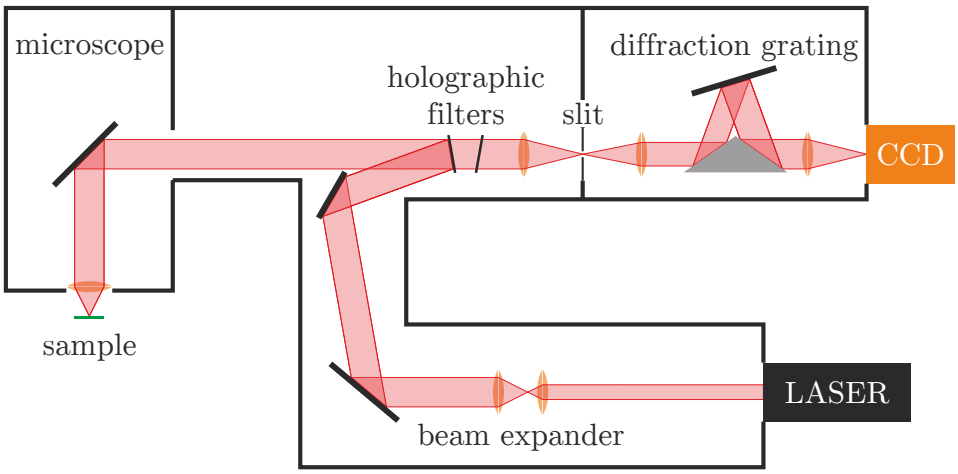

Figure 4.20: Schematic view of the setup used for the Raman spectroscopy.

A Raman spectrum shows the amount of detected scattered light versus the relative wave number $\Delta\bar{\nu}$, i.e. the difference $\Delta\bar{\nu} := \bar{\nu} - \bar{\nu}'$ between the incident wave number $\bar{\nu}$ and the detected wave number $\bar{\nu}'$. $\Delta\bar{\nu}$ correlates with the frequency ω_{vib} of the vibrational mode via the speed of light c:

$$\Delta\bar{\nu} = \frac{\omega_{\text{vib}}}{2\pi c}. \tag{4.27}$$

Therefore, the term "phonon frequency" is used synonymously to the "relative wave number" or "Raman shift" in this section.

All Raman spectra and mappings in this work were acquired using a *Renishaw* Raman microscope system, cf. Fig. 4.20. The samples were measured in back-scattering geometry and only the Stokes-Raman shift was investigated. In this work an excitation wavelength of 532 nm from a frequency-doubled Nd:YAG laser was used. With a $\lambda/2$-plate and a polarizer oriented parallelly to the excitation polarization direction it was possible to either detect light with perpendicular or parallel polarization with respect to the incident light, respectively. If the polarizer has been removed, all polarizations of the scattered light are detected.

4.4.2 Raman spectroscopy on YSZ membranes

As we have shown in section 4.2.2 by XRD measurements, the YSZ thin films grown by RF-sputtering exhibit a cubic structure, i.e. zirconia was stabilized by doping with yttria as discussed in section 4.1.1. Cubic zirconia occurs in the fluorite-type structure with space group

Table 4.1: Wykoff positions for zirconium and oxygen in cubic zirconia (space group ($Fm\bar{3}m$)).

atom	Wyckoff position	site symmetry	coordinates
Zr	4a	O_h	$0, 0, 0$
O	8c	T_d	$\pm\left(\frac{1}{4}, \frac{1}{4}, \frac{1}{4}\right)$

O_h^5 ($Fm\bar{3}m$) with the corresponding Wykoff positions of zirconium and oxygen listed in Table 4.1.

With one zirconium and two oxygen atoms per primitive cell, three acoustic phonon branches and six optical branches are expected. The three acoustic modes have F_{1u} symmetry. An infrared-active mode is also of F_{1u} symmetry and is split into one longitudinal (LO) and two transverse (TO) optical branches. The Raman-active F_{2g}-mode is triply degenerate[127–131].

The corresponding Raman tensors of the F_{2g}-mode (refer Eq. (4.23)) for the corresponding point group O_h ($m\bar{3}m$) are[127,128]:

$$\boldsymbol{R}_1^{F_{2g}} = \begin{pmatrix} \cdot & \cdot & \cdot \\ \cdot & \cdot & d \\ \cdot & d & \cdot \end{pmatrix}, \boldsymbol{R}_2^{F_{2g}} = \begin{pmatrix} \cdot & \cdot & d \\ \cdot & \cdot & \cdot \\ d & \cdot & \cdot \end{pmatrix}, \boldsymbol{R}_3^{F_{2g}} = \begin{pmatrix} \cdot & d & \cdot \\ d & \cdot & \cdot \\ \cdot & \cdot & \cdot \end{pmatrix}. \quad (4.28)$$

Considering the (111)-orientation of the YSZ thin film plane according to Fig. 4.6 and back-scattering geometry (refer Fig. 4.20), the z-coordinate in our setup is:

$$\boldsymbol{e}_z = \frac{1}{\sqrt{3}} \begin{pmatrix} 1 \\ 1 \\ 1 \end{pmatrix}. \quad (4.29)$$

Therefore, $-\boldsymbol{e}_z$ and $\boldsymbol{e}_z$ are the propagation directions of the incident and the scattered light, respectively. Both the polarization of incident and scattered light have to be in the x-y-plane spanned by:

$$\boldsymbol{e}_x = \frac{1}{\sqrt{2}} \begin{pmatrix} 1 \\ -1 \\ 0 \end{pmatrix}, \boldsymbol{e}_y = \frac{1}{\sqrt{6}} \begin{pmatrix} 1 \\ 1 \\ -2 \end{pmatrix}. \quad (4.30)$$

The incident light is then polarized at an angle θ to the x-coordinate:

$$\boldsymbol{e}_i = \frac{1}{\sqrt{6}} \begin{pmatrix} \sin\theta + \sqrt{3}\cos\theta \\ \sin\theta - \sqrt{3}\cos\theta \\ -2\sin\theta \end{pmatrix} = \boldsymbol{e}_s(||), \quad (4.31)$$

which equals the polarization direction $\boldsymbol{e}_\mathrm{s}(||)$ of the scattered light in parallel detection mode. Eq. (4.24) yields together with Eqs. (4.28) and (4.31) the expected intensity $I_\mathrm{is}(||)$ in parallelly polarized geometry:

$$I_\mathrm{is}(||) \propto \sum_m \left|\boldsymbol{e}_\mathrm{i}\boldsymbol{R}^m\boldsymbol{e}_\mathrm{i}\right|^2 = d^2, \tag{4.32}$$

with the Raman tensor elements d corresponding to the F_{2g}-vibration.

Similarly the intensity $I_\mathrm{is}(\perp)$ of a spectrum recorded in back-scattering geometry with perpendicular polarization of incident and scattered light can be derived using Eqs. (4.24) and (4.28):

$$I_\mathrm{is}(\perp) \propto \sum_m \left|\boldsymbol{e}_\mathrm{i}\boldsymbol{R}^m\boldsymbol{e}_\mathrm{s}(\perp)\right|^2 = \frac{2}{3}d^2, \tag{4.33}$$

where the polarization $\boldsymbol{e}_\mathrm{s}(\perp)$ of the scattered light perpendicular to $\boldsymbol{e}_\mathrm{i}$ is given by:

$$\boldsymbol{e}_\mathrm{s}(\perp) = \frac{1}{\sqrt{6}}\begin{pmatrix}\cos\theta - \sqrt{3}\sin\theta\\ \cos\theta + \sqrt{3}\sin\theta\\ -2\cos\theta\end{pmatrix}. \tag{4.34}$$

Therefore, a Raman spectrum of a (111)-YSZ film recorded in back-scattering geometry with perpendicular polarizations should exhibit a behavior similar to a Raman spectrum taken in back-scattering geometry with parallel polarizations. Only quantitative differences in the overall absolute intensity are expected, which will occur in any case as the overall sensitivity of the experimental setup is influenced by the measurement configuration.

Figure 4.21 shows normalized Raman spectra of a (111)-YSZ membrane taken in back-scattering geometry with parallel (black) and perpendicular (red) polarizations of incident and scattered light, respectively. The spectra exhibit three broad maxima at $\omega_1 \approx 313\,\mathrm{cm}^{-1}$, $\omega_\mathrm{R} \approx 585\,\mathrm{cm}^{-1}$, and $\omega_2 \approx 684\,\mathrm{cm}^{-1}$, respectively. As we have shown before, only one (triply degenerate and with F_{2g}-symmetry) mode is Raman-active for fluorite-type cubic zirconia. The occurrence of several, very broad peaks in Raman spectra of stabilized cubic zirconia was observed by different groups[129,132–134]. For example, Keramidas and White[132] investigated CaO-stabilized cubic zirconia which *"behaves more like an amorphous than a crystalline compound"* and found *"few broad, poorly defined maxima at* 590 , 420 , 275 *and* 148 cm^{-1}*"*. This behavior originates from the structural disorder in the stabilized cubic zirconia caused by the generation of oxygen vacancies as described in section 4.1.1. This disorder leads to the breakdown of Raman-scattering

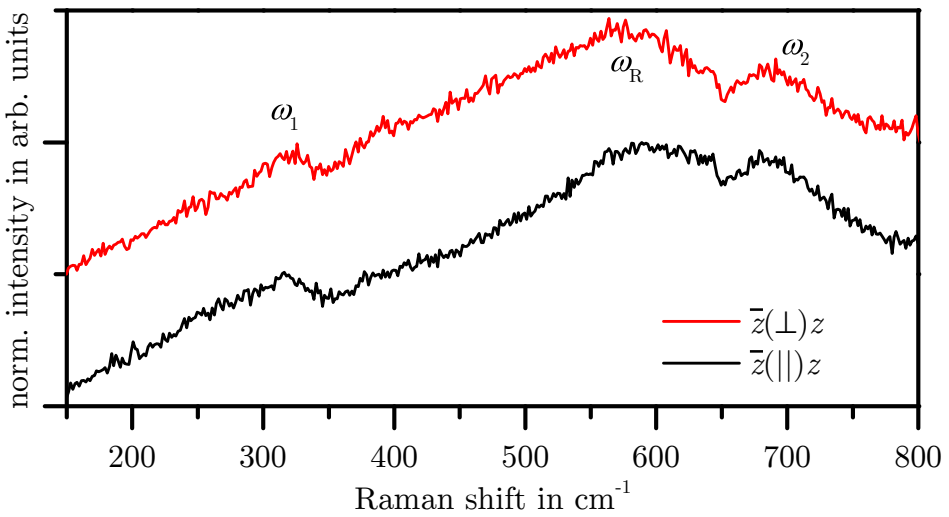

Figure 4.21: Raman spectra of a free-standing YSZ membrane. The black ($\bar{z}(||)z$) and red ($\bar{z}(\perp)z$) curve correspond to spectra which were recorded in back-scattering geometry. The spectra are vertically offset for clarity. The spectra exhibit three main features at $\omega_1 \approx 313\,\mathrm{cm}^{-1}$, $\omega_R \approx 585\,\mathrm{cm}^{-1}$, and $\omega_2 \approx 684\,\mathrm{cm}^{-1}$, respectively.

selection rules including the $\boldsymbol{q}_{BZ} \approx 0$ selection rule (Eq. (4.26)). Thus, all phonons of all parts in the Brillouin zone, longitudinal and transverse, optic and acoustic will contribute to a Raman spectrum. Keramidas and White[132], and López et al.[129] also recorded Raman spectra at decreased temperatures (liquid nitrogen at $T \approx 80\,\mathrm{K}$[132] and liquid helium at $T \approx 2\,\mathrm{K}$[129]). The authors observed similar spectra compared to spectra taken at room temperature and ruled out that the additional features are due to two-phonon processes. Therefore, similar to amorphous materials the Raman spectra reflect the one-phonon density of states.

Comparing the Raman spectra recorded by Feinberg and Perry[133] and Ishigame and Yoshida[134], peaks at $140\,\mathrm{cm}^{-1}$, $270\,\mathrm{cm}^{-1}$, $310\,\mathrm{cm}^{-1}$, $390\,\mathrm{cm}^{-1}$, $550\,\mathrm{cm}^{-1}$, $600\,\mathrm{cm}^{-1}$, and $690\,\mathrm{cm}^{-1}$ were observed. A similar behavior was observed by Yashima et al.[135] and Cai et al.[136]. Thus, the spectra in Fig. 4.21 were fitted using a 6-peak-model with the peak centers around $270\,\mathrm{cm}^{-1}$, $315\,\mathrm{cm}^{-1}$, $390\,\mathrm{cm}^{-1}$, $550\,\mathrm{cm}^{-1}$, $590\,\mathrm{cm}^{-1}$ and $690\,\mathrm{cm}^{-1}$ to determine the position of the $\omega_R = 590\,\mathrm{cm}^{-1}$-peak, which experiences a significant strain-induced shift as discussed next.

4.4.3 Pressure dependence of the F_{2g}-mode

The behavior of inelastic scattering like Raman scattering in the presence of stress was investigated widely in the last century on materials exhibiting the same structure as YSZ (point group O_h ($m\bar{3}m$)). For example, Anastassakis et al.[137], and Papadopoulos et al.[138] investigated the frequency shift of the F_{2g}-type phonons of silicon and strontium fluoride, respectively, in the case of uniaxial stress. Anastassakis[139] discussed the influence of uniaxial stresses on the behavior of the F_{2g}-type phonons of several materials such as Si, Ge, C, Mg_2Si, Mg_2Sn, CaF_2, and BaF_2. Anastassakis and Burstein[140] investigated the effect of strain on the selection rules for Raman scattering. They demonstrated, that for centrosymmetric (CS) crystals, the IR-active modes remain Raman-inactive in the presence of strain (Raman-active modes are IR-inactive and vice versa due to the rule of mutual exclusion for CS crystals). According to their considerations, the expansion of the Raman tensors to first order with strain $\boldsymbol{\eta}$ of the F_{2g}-type phonons in the case of a O_h structure can be written as the sum $\boldsymbol{R}_i^{F_{2g}}(\eta)$ of the intrinsic (Eq. (4.28)) and strain-induced $\boldsymbol{R}_{i_\eta}^{F_{2g}}(\eta)$ Raman tensors ($i \in \{1,2,3\}$ corresponding to the vibration along $(1,0,0)$, $(0,1,0)$, and $(0,0,1)$, respectively):

$$
\begin{aligned}
\boldsymbol{R}_{1_\eta}^{F_{2g}}(\eta) &= \begin{pmatrix} c\eta_{23} & f\eta_{31} & f\eta_{12} \\ f\eta_{31} & e\eta_{23} & b\eta_{11} + d\,(\eta_{22} + \eta_{33}) \\ f\eta_{12} & b\eta_{11} + d\,(\eta_{22} + \eta_{33}) & e\eta_{23} \end{pmatrix}, \\
\boldsymbol{R}_{2_\eta}^{F_{2g}}(\eta) &= \begin{pmatrix} e\eta_{31} & f\eta_{23} & b\eta_{22} + d\,(\eta_{33} + \eta_{11}) \\ f\eta_{23} & c\eta_{31} & f\eta_{12} \\ b\eta_{22} + d\,(\eta_{33} + \eta_{11}) & f\eta_{12} & e\eta_{31} \end{pmatrix}, \\
\boldsymbol{R}_{3_\eta}^{F_{2g}}(\eta) &= \begin{pmatrix} e\eta_{12} & b\eta_{33} + d\,(\eta_{11} + \eta_{22}) & f\eta_{23} \\ b\eta_{33} + d\,(\eta_{11} + \eta_{22}) & e\eta_{12} & f\eta_{31} \\ f\eta_{23} & f\eta_{31} & c\eta_{12} \end{pmatrix}.
\end{aligned} \tag{4.35}
$$

Hooke's law in a continuous medium describes the relation between the second-order tensors of strain $\boldsymbol{\eta}$ within and stress $\boldsymbol{\sigma}$ applied to the medium, respectively:

$$
\boldsymbol{\sigma} = \boldsymbol{C}\boldsymbol{\eta}, \text{ or } \boldsymbol{\eta} = \boldsymbol{S}\boldsymbol{\sigma}. \tag{4.36}
$$

The proportionality is given by the (generally, fourth-order) stiffness $\boldsymbol{C}$ or the compliance $\boldsymbol{S}$ tensors, respectively.

Taking advantage of the symmetry of both the stress and strain

tensor, i.e. $\sigma_{ij} = \sigma_{ji}$ and $\eta_{ij} = \eta_{ji}$, one may write in Voigt notation:

$$\boldsymbol{\sigma} = \begin{pmatrix} \sigma_{11} \\ \sigma_{22} \\ \sigma_{33} \\ \sigma_{23} \\ \sigma_{13} \\ \sigma_{12} \end{pmatrix} = \begin{pmatrix} \sigma_1 \\ \sigma_2 \\ \sigma_3 \\ \sigma_4 \\ \sigma_5 \\ \sigma_6 \end{pmatrix}, \text{ and } \begin{pmatrix} \eta_{11} \\ \eta_{22} \\ \eta_{33} \\ 2\eta_{23} \\ 2\eta_{13} \\ 2\eta_{12} \end{pmatrix} = \begin{pmatrix} \eta_1 \\ \eta_2 \\ \eta_3 \\ \eta_4 \\ \eta_5 \\ \eta_6 \end{pmatrix}. \tag{4.37}$$

The considerations made above reduce the stiffness and strain tensors to second-order, which also can be shown to be symmetric, leaving 21 independent components for each tensor, which can be further reduced for a crystal with cubic symmetry to three independent components each:

$$\boldsymbol{C} = \begin{pmatrix} C_{11} & C_{12} & C_{12} & 0 & 0 & 0 \\ C_{12} & C_{11} & C_{12} & 0 & 0 & 0 \\ C_{12} & C_{12} & C_{11} & 0 & 0 & 0 \\ 0 & 0 & 0 & C_{44} & 0 & 0 \\ 0 & 0 & 0 & 0 & C_{44} & 0 \\ 0 & 0 & 0 & 0 & 0 & C_{44} \end{pmatrix}, \tag{4.38}$$

$$\boldsymbol{S} = \begin{pmatrix} S_{11} & S_{12} & S_{12} & 0 & 0 & 0 \\ S_{12} & S_{11} & S_{12} & 0 & 0 & 0 \\ S_{12} & S_{12} & S_{11} & 0 & 0 & 0 \\ 0 & 0 & 0 & S_{44} & 0 & 0 \\ 0 & 0 & 0 & 0 & S_{44} & 0 \\ 0 & 0 & 0 & 0 & 0 & S_{44} \end{pmatrix}. \tag{4.39}$$

As $\boldsymbol{C}^{-1} = \boldsymbol{S}$, the tensor elements of the compliance tensor are:

$$S_{11} = \frac{C_{11} + C_{12}}{C_{11}^2 + C_{11}C_{12} - C_{12}^2},\ S_{12} = \frac{-C_{12}}{C_{11}^2 + C_{11}C_{12} - C_{12}^2}, \text{ and } S_{44} = \frac{1}{C_{44}}. \tag{4.40}$$

Assuming a growth-induced biaxial stress σ normal to the growth direction $\boldsymbol{e}_z$ (i.e., along $\boldsymbol{e}_x$ and $\boldsymbol{e}_y$, according to Eqs. (4.29) and (4.30)), as indicated in section 4.2.2:

$$\boldsymbol{\sigma}(x, y, z) = \begin{pmatrix} \sigma & 0 & 0 \\ 0 & \sigma & 0 \\ 0 & 0 & 0 \end{pmatrix}. \tag{4.41}$$

Transformed in the $\boldsymbol{e}_1 = (1, 0, 0)$, $\boldsymbol{e}_2 = (0, 1, 0)$, and $\boldsymbol{e}_3 = (0, 0, 1)$

coordinate system, the stress tensor will read:

$$\boldsymbol{\sigma}(1,2,3) = \frac{\sigma}{3}\begin{pmatrix} 2 & -1 & -1 \\ -1 & 2 & -1 \\ -1 & -1 & 2 \end{pmatrix} = \frac{\sigma}{3}\begin{pmatrix} 2 \\ 2 \\ 2 \\ -1 \\ -1 \\ -1 \end{pmatrix}, \tag{4.42}$$

yielding with Eq. (4.36) the strain tensor:

$$\begin{aligned} \boldsymbol{\eta} &= \frac{\sigma}{3}\boldsymbol{S}\begin{pmatrix} 2 \\ 2 \\ 2 \\ -1 \\ -1 \\ -1 \end{pmatrix} = \frac{\sigma}{3}\begin{pmatrix} 2S_{11}+4S_{12} \\ 2S_{11}+4S_{12} \\ 2S_{11}+4S_{12} \\ -S_{44} \\ -S_{44} \\ -S_{44} \end{pmatrix} \\ \boldsymbol{\eta} &= \frac{\sigma}{3}\begin{pmatrix} 2S_{11}+4S_{12} & -S_{44}/2 & -S_{44}/2 \\ -S_{44}/2 & 2S_{11}+4S_{12} & -S_{44}/2 \\ -S_{44}/2 & -S_{44}/2 & 2S_{11}+4S_{12} \end{pmatrix}. \end{aligned} \tag{4.43}$$

Inserting the matrix elements of the strain tensor $\boldsymbol{\eta}$ of Eq. (4.43) into Eq. (4.35), the resulting strain-induced Raman tensors $\boldsymbol{R}_i^{\mathrm{F_{2g}}}(\eta) = \boldsymbol{R}_i^{\mathrm{F_{2g}}} + \boldsymbol{R}_{i_\eta}^{\mathrm{F_{2g}}}(\eta)$ obviously alter the polarization selection rules, e.g. the $\boldsymbol{R}_i^{\mathrm{F_{2g}}}(\eta)$ comprise no longer the same non-zero elements like the original Raman tensors (Eq. (4.28)). This also leads to Raman spectra exhibiting additional peaks in comparison to an unstressed ordered zirconia thin film for instance.

Additionally, strain leads to a removal of the degeneracy of the $\mathrm{F_{2g}}$-mode and to strain-induced shifts of the phonon frequencies following the discussion in Anastassakis and Burstein[141]: The frequency ω_j of a phonon (j) can be associated with an effective spring constant $\boldsymbol{K}_j$ of the corresponding vibration with its normal coordinate Q_j, which, in the case of an applied external force F, comprises an intrinsic part $\boldsymbol{K}_{j0}$ and an additional part related to the force $\boldsymbol{K}_{j\mathrm{F}}$:

$$\begin{aligned} \boldsymbol{K}_j &= \boldsymbol{K}_{j0} + \boldsymbol{K}_{j\mathrm{F}}, \\ (K_{j0})_{\alpha\beta} &= \frac{1}{2}\left(\frac{\partial^2\varphi}{\partial Q_\alpha \partial Q_\beta}\right), \\ (K_{j\mathrm{F}})_{\alpha\beta\nu} &= \frac{1}{2}\left(\frac{\partial^3\varphi}{\partial Q_\alpha \partial Q_\beta \partial F_\nu}\right), \end{aligned} \tag{4.44}$$

where the crystal potential energy $\varphi\left(Q_j, F \ldots\right)$ is normalized to unit volume and mass. They showed, that the intrinsic spring constant has only one independent component K_{j0} and is diagonal if referred to the crystallographic axes, i.e. $K_{j0} = \omega_{j0}^2$ with the intrinsic mode frequency ω_{j0}. If a force is present, one obtains the following secular equation:

$$\left|\left(K_{j0} + K_{j\mathrm{F}}\right)_{\alpha\beta} - \omega_j^2 \delta_{\alpha\beta}\right| = 0, \tag{4.45}$$

with the force-induced mode frequency $\omega_j = \omega_{j0} + \Delta\omega_j$. The effect of the force can be separated by introducing $\lambda_j = \omega_j^2 - \omega_{j0}^2$:

$$\left|\left(K_{j\mathrm{F}}\right)_{\alpha\beta} - \lambda_j \delta_{\alpha\beta}\right| = 0. \tag{4.46}$$

Quoting Anastassakis and Burstein[141], *"Thus, once the type of mode and force is given, one has first to derive the non-zero components of* $\boldsymbol{K}_{jF}$ *and then deduce the eigenvalues* λ_j *of Eq.* (4.46)." The difference between the intrinsic and force-induced mode frequency $\Delta\omega_j$ can be approximated by:

$$\Delta\omega_j \cong \frac{\lambda_j}{2\omega_{j0}}. \tag{4.47}$$

In their work, Anastassakis and Burstein[141] also discussed the influence of a homogenous strain $\eta_{\mu\nu} = \eta_{\nu\mu}$ on the $\mathrm{F_{2g}}$-mode of the O_h structure and derived the following secular equation using Eq. (4.46):

$$\begin{vmatrix} K_{11} - \lambda_{\mathrm{F_{2g}}} & K_3\eta_{12} & K_3\eta_{13} \\ K_3\eta_{12} & K_{22} - \lambda_{\mathrm{F_{2g}}} & K_3\eta_{23} \\ K_3\eta_{13} & K_3\eta_{23} & K_{33} - \lambda_{\mathrm{F_{2g}}} \end{vmatrix} = 0, \tag{4.48}$$

with

$$\begin{aligned} K_{11} &= K_1\eta_{11} + K_2(\eta_{22} + \eta_{33}), \\ K_{22} &= K_1\eta_{22} + K_2(\eta_{33} + \eta_{11}), \\ K_{33} &= K_1\eta_{33} + K_2(\eta_{11} + \eta_{22}), \end{aligned}$$

with three independent components K_1, K_2, K_3 of $\boldsymbol{K}_{\mathrm{F_{2g}F}}$.

Using the derived form for a strain (Eq. (4.43)) related to a growth-induced biaxial stress σ (Eq. (4.41)), the eigenvalues $\lambda_i^{\mathrm{F_{2g}}}$ of the secular equation (4.4.3) are:

$$\begin{aligned} \lambda_{\mathrm{D}}^{\mathrm{F_{2g}}} = \lambda_{1,2}^{\mathrm{F_{2g}}} &= \frac{\sigma}{6}\left[K_1\left(4S_{11} + 8S_{12}\right) + K_2\left(8S_{11} + 16S_{12}\right) + K_3 S_{44}\right], \\ \lambda_{\mathrm{S}}^{\mathrm{F_{2g}}} = \lambda_3^{\mathrm{F_{2g}}} &= \frac{\sigma}{6}\left[K_1\left(4S_{11} + 8S_{12}\right) + K_2\left(8S_{11} + 16S_{12}\right) - 2K_3 S_{44}\right]. \end{aligned} \tag{4.49}$$

This means, the triply degenerate F_{2g}-mode is split into a doublet ($\lambda_D^{F_{2g}}$) and a singlet ($\lambda_S^{F_{2g}}$). Using the phonon deformation potentials $\tilde{K}_{11} \equiv K_1/\omega_{F_{2g}0}^2, \tilde{K}_{12} \equiv K_2/\omega_{F_{2g}0}^2, \tilde{K}_{44} \equiv K_3/\omega_{F_{2g}0}^2$ for the spring constant elements, the frequency shifts of the doublet and singlet to the frequency $\omega_{F_{2g}0}$ of the unstrained F_{2g}-mode are given using Eqs. (4.47) and (4.49):

$$\Delta\omega_D^{F_{2g}} = \frac{\sigma\omega_{F_{2g}0}}{3}\left[\tilde{K}_{11}(S_{11}+2S_{12}) + \tilde{K}_{12}(2S_{11}+4S_{12}) + \tilde{K}_{44}S_{44}/4\right], \tag{4.50}$$

$$\Delta\omega_S^{F_{2g}} = \frac{\sigma\omega_{F_{2g}0}}{3}\left[\tilde{K}_{11}(S_{11}+2S_{12}) + \tilde{K}_{12}(2S_{11}+4S_{12}) - \tilde{K}_{44}S_{44}/2\right], \tag{4.51}$$

respectively.

The experimental setup used in this work allows polarization in the x-y-plane in back-scattering geometry along the z-axis, refer to Fig. 4.20 and Eqs. (4.29) and (4.30). The eigenvector of the singlet is parallel to the z-axis, whereas the eigenvectors of the doublet are in the x-y-plane, which equals the stress plane of the thin film and the polarization plane of the experimental setup, respectively. Therefore, only the doublet is observable in our experimental geometry and discussed further. Introducing the stress-Raman-shift coefficient $b_{D\sigma}^{F_{2g}}$ which relates the applied biaxial stress σ to the change $\Delta\bar{\nu}_D^{F_{2g}}$ of the Raman shift $\bar{\nu}_D^{F_{2g}}$ of the doublet to the intrinsic Raman shift $\bar{\nu}_{F_{2g}0}$:

$$\sigma = b_{D\sigma}^{F_{2g}}\Delta\bar{\nu}_D^{F_{2g}},$$
$$b_{D\sigma}^{F_{2g}} \equiv \frac{3}{\bar{\nu}_{F_{2g}0}}\left[\tilde{K}_{11}(S_{11}+2S_{12}) + \tilde{K}_{12}(2S_{11}+4S_{12}) + \tilde{K}_{44}S_{44}/4\right]^{-1}, \tag{4.52}$$

it is possible to determine the growth-induced biaxial stress at different locations on a thin-film sample by comparing Raman spectra recorded at these locations.

We used the phonon deformation potentials calculated by Cai et al.[142] for YSZ with 8.8 mol % and 12 mol % Y_2O_3 and the compliance constants used by the authors[143] to interpolate these values for 9.5 mol % Y_2O_3. The corresponding values are listed in table 4.2. We used an intrinsic Raman shift of $\bar{\nu}_{F_{2g}0} = \omega_R \approx 587.2\,\mathrm{cm}^{-1}$ according to our measurements (cf. Fig. 4.21) and the calculated value of ω_R in Liu et al.[144]. This yields a stress-Raman-shift coefficient of $b_{D\sigma}^{F_{2g}} = -0.263\,\mathrm{GPa\,cm}$, i.e. tensile stress leads to a negative shift of the F_{2g}-mode while a positive shift corresponds to compressive stress.

Table 4.2: Parameters used to determine the stress-Raman-shift coefficient $b_{\mathrm{D}\sigma}^{\mathrm{F_{2g}}}$ for YSZ with 9.5 mol % Y_2O_3 in Eq. (4.52). The phonon deformation potentials $\tilde{K}_{11}, \tilde{K}_{12}, \tilde{K}_{44}$ and compliance constants S_{11}, S_{12}, S_{44} were interpolated to the data in Cai et al.[142]. The intrinsic Raman shift $\bar{\nu}_{\mathrm{F_{2g}}0} = \omega_{\mathrm{R}}$ is based on our own data (cf. Fig. 4.21) and Liu et al.[144].

parameter	value
$\tilde{K}_{11}$	-4.44
$\tilde{K}_{12}$	-3.91
$\tilde{K}_{44}$	0.204
S_{11}/TPa^{-1}	2.73
S_{12}/TPa^{-1}	-0.537
S_{44}/TPa^{-1}	17.2
$\bar{\nu}_{\mathrm{F_{2g}}0}/\mathrm{cm}^{-1}$	587.2
$b_{\mathrm{D}\sigma}^{\mathrm{F_{2g}}}/\mathrm{GPa\,cm}$	-0.263

4.4.4 Raman and stress mapping of free-standing YSZ membranes

For this purpose a grid of points was defined on the membrane surface and a Raman spectrum was acquired at each point of the grid.

Figure 4.22 shows an optical microscope image of a free-standing YSZ membrane on which a Raman mapping was performed. The mapping grid comprised 10×10 points with a gap of 15 µm between neighbouring points. The locations of each spectrum are depicted in Fig. 4.22 by the dot array. A 6-peak-model was fitted to each spectrum, the peak centers were around $270\,\mathrm{cm}^{-1}$, $315\,\mathrm{cm}^{-1}$, $390\,\mathrm{cm}^{-1}$, $550\,\mathrm{cm}^{-1}$, $590\,\mathrm{cm}^{-1}$ and $690\,\mathrm{cm}^{-1}$. Thus, it was possible to determine the position of the $\omega_{\mathrm{R}} = 590\,\mathrm{cm}^{-1}$-peak.

Figure 4.23 and Fig. 4.24 show the spectra recorded at the positions along the horizontal ($y = 85\,\mu\mathrm{m}$) and vertical ($x = 80\,\mu\mathrm{m}$) solid line drawn in Fig. 4.22, respectively.

In Fig. 4.25 the corresponding Raman mapping of the ω_{R}-mode position is shown. The Raman shift of the ω_{R}-mode is represented by a color code given in the legend, dark red color denotes a low Raman shift while brighter red color corresponds to a higher Raman shift. According to Eq. (4.52) the map of the ω_{R}-mode Raman shift can be transformed

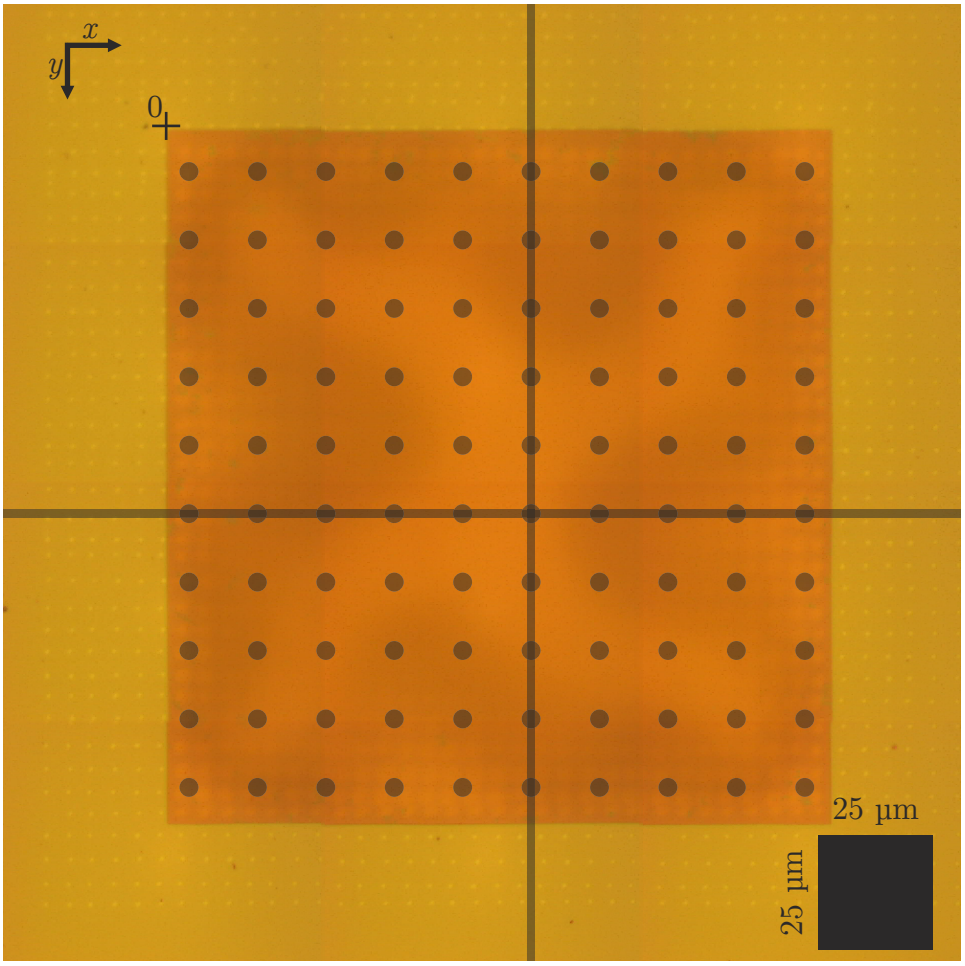

Figure 4.22: Optical microscope image of the scanned YSZ membrane. The dots denote the locations where Raman spectra were obtained. The crossing point of the two solid lines represents the position of the reference spectrum for the stress determination. The spectra in Fig. 4.23 and in Fig. 4.24 are recorded by measurements performed along the horizontal ($y = 85\,\mu m$) and vertical ($x = 80\,\mu m$) solid line, respectively.

into a map of the biaxial stress within the membrane. Figure 4.25 represents also a map of the stress in the membrane relative to the stress value corresponding to the spectrum recorded at the horizontal position $x = 80\,\mu m$ and vertical position $y = 85\,\mu m$ according to the cross point of the two solid lines drawn in Fig. 4.22. The color code also represents the relative biaxial stress σ. Comparing the stress map in Fig. 4.25 with the optical microscope image in Fig. 4.22 reveals that

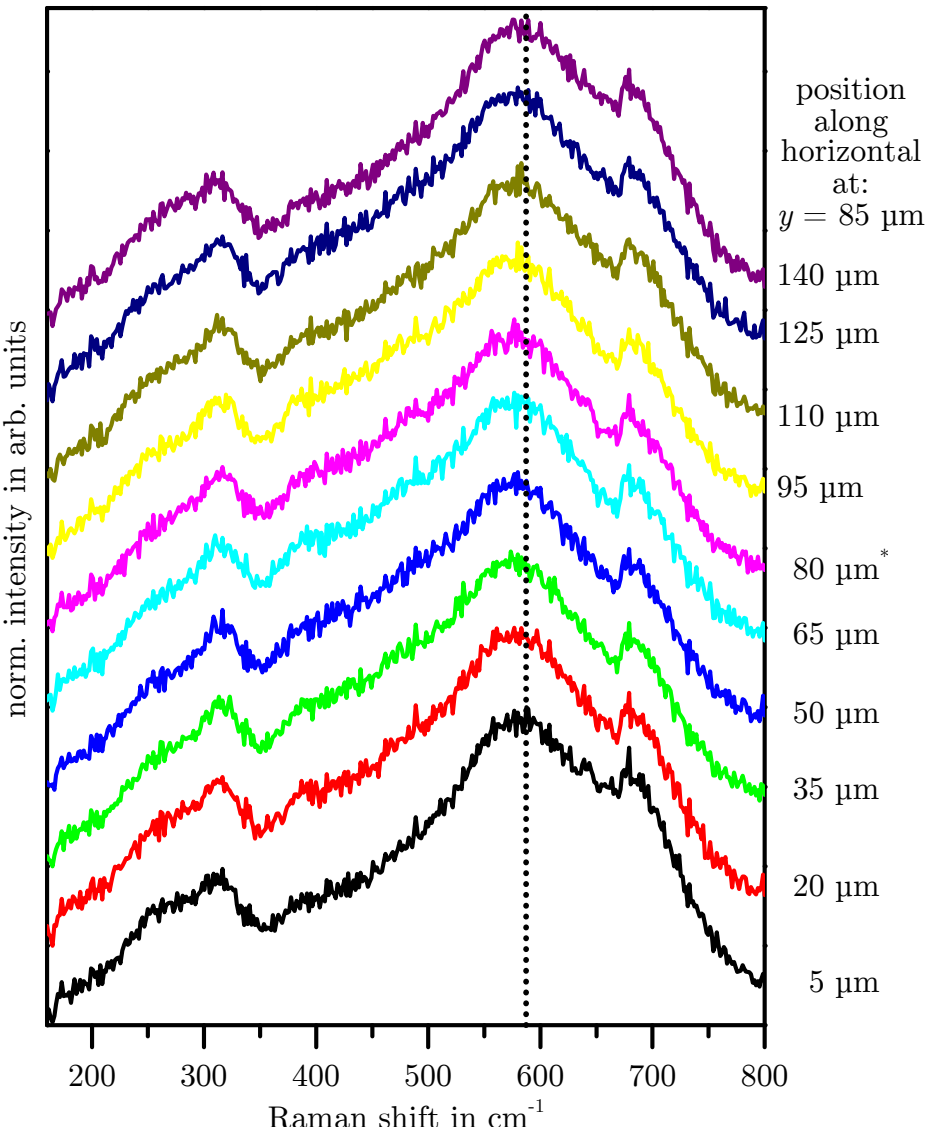

Figure 4.23: Raman spectra recorded at the positions along the horizontal solid line drawn in Fig. 4.22. The vertical position was kept constant at a value of $y = 85\,\mu\text{m}$ The dotted vertical line denotes the Raman shift reference at $\bar{\nu}_{\text{F}_{2\text{g}}0} = 587.2\,\text{cm}^{-1}$, the corresponding spectrum is marked with *.

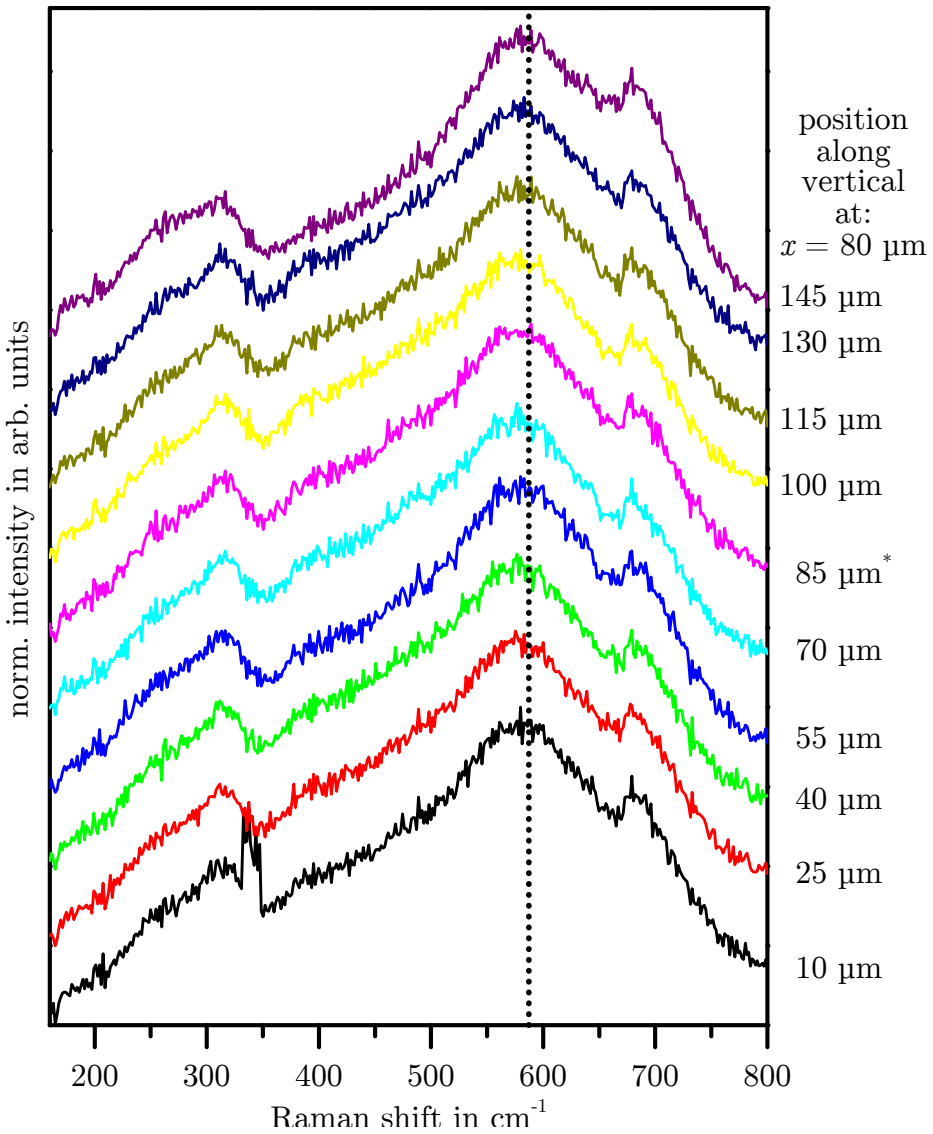

Figure 4.24: Raman spectra recorded at the positions along the vertical solid line drawn in Fig. 4.22. The horizontal position was kept constant at a value of $x = 80\,\mu\text{m}$. The dotted vertical line denotes the Raman shift reference at $\bar{\nu}_{\text{F}_{2g}0} = 587.2\,\text{cm}^{-1}$, the corresponding spectrum is marked with *.

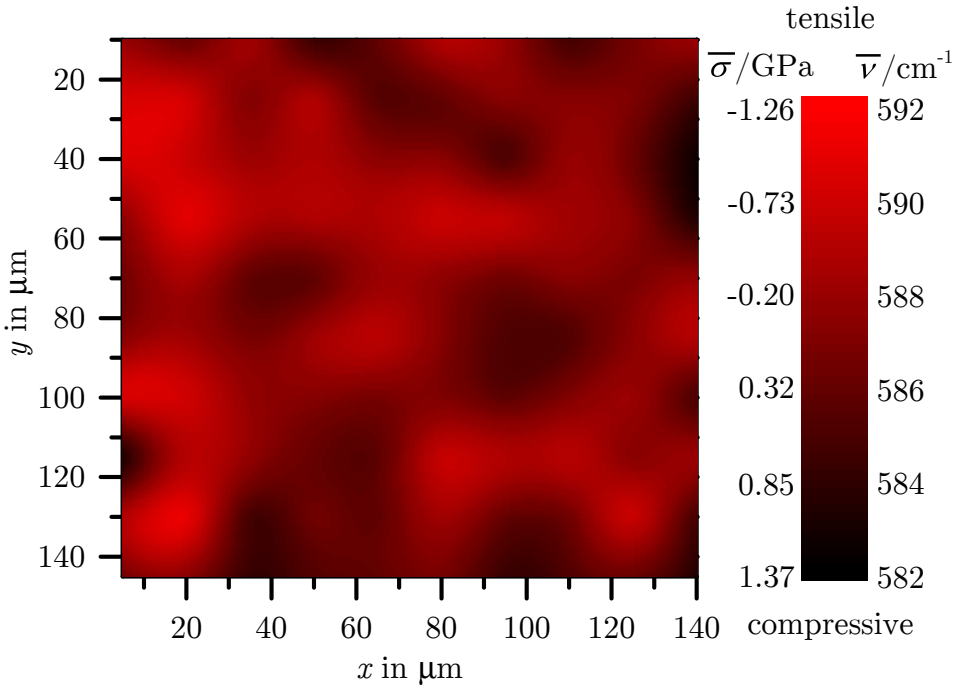

Figure 4.25: Raman mapping of the position of the $\omega_R = 590\,\mathrm{cm}^{-1}$-peak, which was fitted using a 6-peak-model on each spectrum recorded at the positions marked in Fig. 4.22. The color code represents both the Raman shift of the ω_R-mode and the relative stress σ to the stress value corresponding to the Raman shift of the ω_R-mode of the spectrum recorded at $\{x, y\} = \{80\,\mu\mathrm{m}, 85\,\mu\mathrm{m}\}$, respectively. Figure 4.27 and Fig. 4.26 show the ω_R-mode Raman shift and the relative stress σ along the vertical ($x = 80\,\mu\mathrm{m}$) and horizontal ($y = 85\,\mu\mathrm{m}$) solid line drawn in Fig. 4.22, respectively.

the brighter parts forming the cross-shaped pattern visible in the latter image correspond to the parts of compressive relative stress depicted in the stress map (brighter red color in Fig. 4.25).

Figure 4.26 and Fig. 4.27 show the Raman shift of the ω_R-mode along both the horizontal ($y = 85\,\mu\mathrm{m}$) and vertical ($x = 80\,\mu\mathrm{m}$) line in Fig. 4.22, respectively. The Raman shift values correspond to the left-hand axis of both graphs. On the right-hand axis of Fig. 4.26 and Fig. 4.27 the values of the relative stress σ to the stress value corresponding to the Raman shift of the ω_R-mode of the spectrum recorded at $\{x, y\} = \{80\,\mu\mathrm{m}, 85\,\mu\mathrm{m}\}$ can be found.

With the use of Raman spectroscopy and group theoretical con-

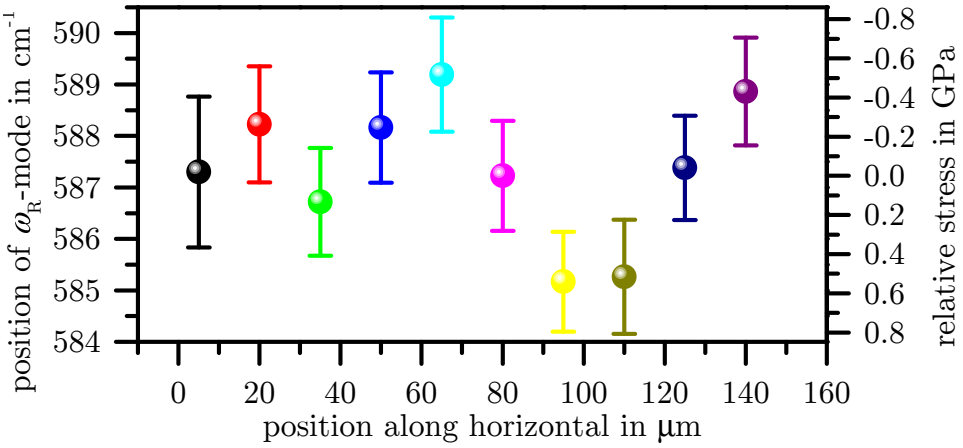

Figure 4.26: Raman shift of the ω_R-mode (left scale) and relative stress σ to the stress value corresponding to the Raman shift of the ω_R-mode of the spectrum recorded at $\{x, y\} = \{80\,\mu m, 85\,\mu m\}$ (right scale) along the horizontal line at $y = 85\,\mu m$ in Fig. 4.22, respectively.

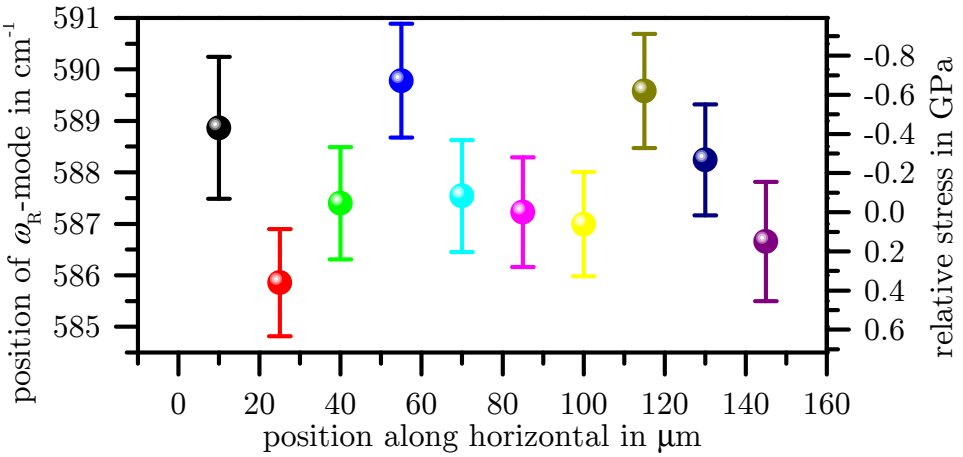

Figure 4.27: Raman shift of the ω_R-mode (left scale) and relative stress σ to the stress value corresponding to the Raman shift of the ω_R-mode of the spectrum recorded at $\{x, y\} = \{80\,\mu m, 85\,\mu m\}$ (right scale) along the vertical line at $x = 80\,\mu m$ in Fig. 4.22.

siderations it was possible to determine a proportionality constant $b_{\mathrm{D}\sigma}^{\mathrm{F_{2g}}} = -0.263\,\mathrm{GPa\,cm}$ between the growth-induced biaxial stress σ normal to the growth direction (111) and the relative position $\Delta\bar{\nu}_{\mathrm{D}}^{\mathrm{F_{2g}}}$ of the stress-induced Raman shift of the ω_{R}-doublet-mode to a reference value $\bar{\nu}_{\mathrm{F_{2g}0}} = 587.2\,\mathrm{cm}^{-1}$, cf. Eq. (4.52). Raman mappings on a YSZ thin film membrane were recorded and transformed into a relative stress map of the relative biaxial stress within this membrane. The relative biaxial stresses were in the range of $-1.5\,\mathrm{GPa}$ to $1.5\,\mathrm{GPa}$.

4.5 Conclusions about the solid-state ion-emitters based on the solid electrolyte YSZ

We have presented a new concept for miniaturized microthrusters — the solid-state ion-emitters (SSIE). The unconventional part of those emitters is the ionization utilizing the unique properties of a solid electrolyte. In this work the solid electrolyte yttria-stabilized zirconia (YSZ) with an yttria content of $9.5\,\mathrm{mol\,\%}$ Y_2O_3 was used. Using thin free-standing membranes of YSZ, molecular oxygen may be ionized to oxygen ions. Optical investigations and stress analyses of micro-fabricated YSZ membranes were conducted to provide the fundamentals for future research of solid-state ion-emitters based on thin free-standing ion-conducting membranes.

YSZ exhibits oxygen vacancies, whose enable an oxygen ion transport through the lattice via vacancy migration. Oxygen molecules are incorporated into the YSZ lattice with electrons provided by a porous metal electrode on the reservoir side of a membrane. Once oxygen ions are accumulated at the vacuum surface by electric potential or concentration gradients, they can be extracted by an external electric field. The SSIE concept benefits from miniaturization, as the working temperature can be decreased for electrolyte membranes with reduced thickness.

To fabricate such membranes, thin films ($1\,\mu\mathrm{m}$ thick) were RF-sputtered on silicon substrates. Scanning electron microscope investigations revealed a columnar structure of the thin films with lateral column dimensions of about $50\,\mathrm{nm}$. X-ray diffractometric measurements showed a (111) orientation of the thin YSZ films. Using anisotropic silicon etching, free-standing membranes were fabricated.

These membranes were investigated by optical microscopy and size-

dependent surface patterns were observed. Four different categories of membranes were defined with increasing size, according to their strain patterns:

- up to 70 µm: membranes without any observable strain patterns.
- 70 µm to 120 µm: cross-shaped strain patterns in the membranes.
- 120 µm to 300 µm: membranes with more complex cross strain patterns.
- above 300 µm: defective membranes.

It was found, that these strain patterns are related to thermal stress inside the thin YSZ films due to the heteroepitaxial growth on oxidized silicon substrates. Quantitative residual stress analysis of the free-standing membranes was performed using Raman spectroscopy. Relative residual biaxial stress values of -1.5 GPa to 1.5 GPa have been observed within the membranes.

This fundamental research enables the future development of thin free-standing ion-conducting membranes for the use in electrostatic thruster. Other ions than oxygen are possible as propellant, as there is a wide variety of solid electrolytes enabling ionic conduction for different ions, e.g. H^+, F^-, Ag^+, or Li^+.

Chapter 5

Conclusions

We showed the necessity of modern techniques and novel scalable concepts going beyond established schemes of propulsion systems with evaluations of common thruster types with respect to miniaturization prospects and propellant-mass-efficiency, and of state-of-the-art miniaturized propulsion systems (including propellant and thruster mass, packaging and power processing costs) with respect to their working range in terms of satellite mass. These surveys show that electrostatic propulsion (ESP) with its very high propellant mass efficiency is the most promising propulsion method — but the power efficiency of plasma-based ESP thrusters decreases rapidly when the thrusters are miniaturized.

5.1 Colloid emitters

The working range survey revealed, that a silicon-based miniaturized colloid thruster type using ionic liquids is applicable at the lowest satellite wet mass of this survey.

The miniaturized colloid emitters developed in this work are microfabricated using photolithography, thermal evaporation and electroplating methods — enabling dense packed arrays of emitter capillaries with integrated electrodes. The ionic liquid EMI-BF_4 was used as propellant due to its low surface tension and capability of emitting both cat- and anions enabling a lower extraction voltage and the possibility of voltage alternation (no neutralizer required) compared with liquid metals as propellant, respectively. The negative-tone photoresist SU-8 was chosen as capillary material to simplify the fabrication process, integrate the extraction electrode, and to benefit of its physical properties of a low permittivity and a high electric resistivity yielding a

lower extraction voltage and lower alternation frequency than silicon as capillary material, respectively.

Fully integrated arrays of highly integrated SU-8 capillary emitters were fabricated and the excellent alignment of their substructures and the permeability of emitter arrays was demonstrated. We microfabricated arrays of 2500 emitters per cm^2 comprising a capillary and spacer layer as well as an integrated electrode. The capillary diameter was varied in the range of 5 µm to 50 µm while the overall thickness was in the order of 100 µm.

Optical investigations by video microscopy of single emitters during extraction tests using both integrated and externally mounted electrodes revealed that the surface of the capillary layer is wetted by the ionic liquid and therefore inhibits proper extraction. Thus, the wetting behavior of EMI-BF_4 on SU-8 was investigated and the contact angle of EMI-BF_4 on SU-8 was enhanced from 38° to 86° and even 121° using a PTFE-coating and a surface treatment with silicon dioxide nanoparticles in PDMS, respectively.

Extraction tests on very narrow capillaries with an untreated sample's surface and single emitters coated with PTFE showed the extraction of positive species.

We created the foundation for future experiments with highly-integrated, surface-treated, SU-8-based capillary emitter arrays. Quantitative measurements of the particle currents for different ionic liquids and emitter geometries may be conducted. More complicated three-dimensional emitter structures may be designed and fabricated using direct laser writing in SU-8 or other equivalent photo resists or both. The next step of integration includes MEMS-fabricated propellant reservoirs, acceleration grid systems or miniaturized PPUs.

5.2 Solid-state ion-emitters

We introduced the novel ESP emitter concept of solid-state ion-emitters (SSIE) based on the solid electrolyte yttria-stabilized zirconia (YSZ) with an yttria content of 9.5 mol % Y_2O_3. Optical investigations and stress analyses of micro-fabricated YSZ membranes were conducted to provide the fundamentals for future research of solid-state ion-emitters based on thin free-standing ion-conducting membranes.

We fabricated free-standing YSZ membranes by RF-sputtering thin films (1 µm thick) on (100)-silicon substrates and subsequently anisotropic silicon etching. Scanning electron microscope investigations

revealed a columnar structure of the thin films with lateral column dimensions of about 50 nm. X-ray diffractometric measurements showed a (111) orientation of the thin YSZ films.

These membranes were investigated by optical microscopy and size-dependent surface patterns were observed. Four different categories of membranes were defined with increasing size, according to their strain patterns:

- up to 70 µm: membranes without any observable strain patterns.
- 70 µm to 120 µm: cross-shaped strain patterns in the membranes.
- 120 µm to 300 µm: membranes with more complex cross strain patterns.
- above 300 µm: defective membranes.

It was found, that these strain patterns are related to thermal stress inside the thin YSZ films due to the heteroepitaxial growth on oxidized silicon substrates. Quantitative residual stress analysis of the free-standing membranes was performed using Raman spectroscopy. Relative residual biaxial stress values of $-1.5\,\mathrm{GPa}$ to $1.5\,\mathrm{GPa}$ have been observed within the membranes. The stress pattern correlated with pattern visible in optical images of the membranes.

These fundamental results may be used to enhance the fabrication of thin solid-state ion-conducting membranes of other solid electrolytes. Other ions than oxygen are possible as propellant, as there is a wide variety of solid electrolytes enabling ionic conduction for different ions, e.g. H^+, F^-, Ag^+, or Li^+.

Future tasks are further investigations of the stress distribution within YSZ membranes in order to find a way to increase the stability of the membranes. Later on extraction tests of the SSIE and mass spectrometric analyses of the extracted particles need to be performed. Other propellant reservoirs than the gaseous molecular oxygen reservoir, e.g. solid-state oxides, may be employed.

Bibliography

[1] E. Buchen. SpaceWorks' 2014 Nano/Microsatellite Market Assessment. In *Proceedings of the 28th AIAA/USU Conference on Small Satellites, Logan, UT, USA*, number SSC14-I-3, 2014.

[2] Defense Industry Daily staff. Small Is Beautiful: US Military Explores Use of Microsatellites. Online, 2011. URL `http://www.defenseindustrydaily.com/Small-Is-Beautiful-US-Military-Explores-Use-of-Microsatellites-06720/`.

[3] R. Osiander, A. Garrison Darrin, and J. L. Champion. *MEMS and Microstructures in Aerospace Applications*. CRC Press, 2005. ISBN 9780824726379.

[4] ESA. LISA Pathfinder: Overview. Online, 2013. URL `http://sci.esa.int/lisa-pathfinder/31436-overview/`.

[5] G. D. Racca and P. W. McNamara. The LISA Pathfinder Mission. *Space Science Reviews*, 151(1-3):159–181, 2010.

[6] ESA. NGO: Mission Description. Online, 2012. URL `http://sci.esa.int/ngo/50144-mission-description/`.

[7] ESA. LISA: Mission Status. Online, 2012. URL `http://sci.esa.int/lisa/48728-mission-status/`.

[8] R. Krpoun, M. Räber, and H. R. Shea. Microfabrication and test of an integrated colloid thruster. In *Proceedings of the 21st IEEE International Conference on Micro Electro Mechanical Systems, Tucson, AZ, USA*, pages 964–967, 2008.

[9] J. Mueller, C. Marrese, J. Polk, et al. An overview of MEMS-based micropropulsion developments at JPL. *Acta Astronautica*, 52(9–12):881–895, 2003.

[10] K. E. Tsiolkovsky. *"The Investigation of Universal Space by Means of Reactive Devices" in Works on Rocket Technology*, chapter 2, pages 60–98. Publishing House of the Defense Industry, Moscow, 1947. NASA Technical Translation F-243, originally written in 1911.

[11] NASA. Definition Of Technology Readiness Levels. Online. URL `http://esto.nasa.gov/files/trl_definitions.pdf`.

[12] R. Goddard. The green notebooks. The Dr. Robert H. Goddard Collection at Clark University Archives, Clark University, Worcester, MA, USA, 1906.

[13] M. O'Neill, J. Howell, L. Lollar, et al. Stretched Lens Array SquareRigger (SLASR) Technology Maturation. In *19th Space Photovoltaic Research and Technology Conference, Brook Park, OH, USA*, 2005.

[14] The Space Foundation. The Space Report 2013 Overview. Online, 2013. URL `http://www.spacefoundation.org/sites/default/files/downloads/The_Space_Report_2013_overview.pdf`.

[15] NASA Global Change Master Directory. Ancillary Description Writer's Guide. Online, 2014. URL `http://gcmd.nasa.gov/add/ancillaryguide/platforms/orbit.html`.

[16] Faculty of Aerospace Engineering, TU Delft. Typical delta V (velocity increment) value(s) for various space manoevres. Online, 2015. URL `http://www.lr.tudelft.nl/?id=29271&L=1`.

[17] Albert Einstein Institute, Hannover. eLISA: The Mission. Online, 2013. URL `https://www.elisascience.org/articles/elisa-mission/elisa-mission-gravitational-universe`.

[18] ESA. NGO Assessment Study Report (Yellow Book). Online, 2012. URL `http://sci.esa.int/cosmic-vision/NGO_YB.pdf`.

[19] ESA. ESA's new vision to study the invisible Universe. Online, 2013. URL `http://www.esa.int/Our_Activities/Space_Science/ESA_s_new_vision_to_study_the_invisible_Universe`.

[20] ETHZ, Zürich. Suche nach Gravitationswellen eingeläutet. Online, 2013. URL `https://www.ethz.ch/de/news-und-veranstaltungen/eth-news/news/2013/12/suche-nach-gravitationswellen-eingelaeutet.html`.

[21] UZH, Zürich. Die Wellenjäger. Online, 2013. URL `http://www.uzh.ch/news/articles/2013/die-wellenjaeger.html`.

[22] R. R. Hofer, P. Y. Peterson, A. D. Gallimore, and R. S. Jankovsky. A high specific impulse two-stage Hall thruster with plasma lens focusing. In *27th International Electric Propulsion Conference, Pasadena, CA, USA*, number IEPC-2001-036, 2001.

[23] H. J. Leiter, R. Killinger, H. Bassner, et al. Development and performance of the advanced radio frequency ion thruster RIT-XT. In *28th International Electric Propulsion Conference, Toulouse, France*, number IEPC-2003-0115, 2003.

[24] M. Martínez-Sánchez. Space Propulsion. Lecture Notes, 2004. URL `http://ocw.mit.edu/courses/aeronautics-and-astronautics/16-522-space-propulsion-spring-2004/lecture-notes/lecture23_25.pdf`.

[25] G. Taylor. Disintegration of water drops in an electric field. *Proceedings of the Royal Society of London. Series A. Mathematical and Physical Sciences*, 280(1382):383–397, 1964.

[26] V. E. Krohn, Jr. Liquid metal droplets for heavy particle propulsion. *Progress in Astronautics and Aeronautics*, 5:73–80, 1961.

[27] D. S. Swatik. Electrohydrodynamic Spraying of Gallium-Indium Alloy. Technical report, DTIC Document, Charged Particle Research Lab, University of Illinois, Urbana, IL, USA, 1967.

[28] C. D. Hendricks and D. S. Swatik. Production of ions by electrohydrodynamic spraying techniques. *AIAA Journal*, 6(8):1596–1597, 1968.

[29] R. Gomer. On the mechanism of liquid metal electron and ion sources. *Applied Physics*, 19(4):365–375, 1979.

[30] V. E. Krohn, Jr. Glycerol droplets for electrostatic propulsion. *Progress in Astronautics and Aeronautics*, 9:435–440, 1963.

[31] C. D. Hendricks and J. Hogan. Investigation of the charge-to-mass ratio of electrically sprayed liquid particles. *AIAA Journal*, 3(2):296–301, 1965.

[32] P. Kidd and H. Shelton. Life test/4350 hours/of an advanced colloid thruster module. In *10th Electric Propulsion Conference, Lake Tahoe, NV, USA*, number 73-1078, 1973.

[33] R. D. Schultz and L. K. Branson. The Colloid rocket: Progress toward a charged-liquid-colloid propulsion system. In *Proceedings of Second Symposium on Advanced Propulsion Concepts, Boston, MA, USA*, volume 1, pages 53–72, 1959.

[34] P. Lozano and M. Martínez-Sánchez. Ionic liquid ion sources: characterization of externally wetted emitters. *Journal of Colloid and Interface Science*, 282(2):415–421, 2005.

[35] T. J. Lewis. Mechanism of electrical breakdown in saturated hydrocarbon liquids. *Journal of Applied Physics*, 27(6):645–650, 1956.

[36] T. Welton. Room-temperature ionic liquids. Solvents for synthesis and catalysis. *Chemical Reviews*, 99(8):2071–2084, 1999.

[37] P. Lozano, M. Martínez-Sánchez, and J. M. Lopez-Urdiales. Electrospray emission from nonwetting flat dielectric surfaces. *Journal of Colloid and Interface Science*, 276(2):392–399, 2004.

[38] P. Lozano and M. Martínez-Sánchez. Ionic liquid ion sources: suppression of electrochemical reactions using voltage alternation. *Journal of Colloid and Interface Science*, 280(1):149–154, 2004.

[39] P. Lozano and M. Martínez-Sánchez. On the dynamic response of externally wetted ionic liquid ion sources. *Journal of Physics D: Applied Physics*, 38(14):2371, 2005.

[40] J. Fuller, R. T. Carlin, and R. A. Osteryoung. The Room Temperature Ionic Liquid 1-Ethyl-3-methylimidazolium Tetrafluoroborate: Electrochemical Couples and Physical Properties. *Journal of the Electrochemical Society*, 144(11):3881–3886, 1997.

[41] I. Romero-Sanz, R. Bocanegra, J. F. de la Mora, and M. Gamero-Castaño. Source of heavy molecular ions based on Taylor cones

of ionic liquids operating in the pure ion evaporation regime. *Journal of Applied Physics*, 94(5):3599–3605, 2003.

[42] P. C. Lozano. Energy properties of an EMI-Im ionic liquid ion source. *Journal of Physics D: Applied Physics*, 39(1):126–134, 2006.

[43] L. F. Velasquez-Garcia. *The design, fabrication and testing of micro-fabricated linear and planar colloid thruster arrays*. PhD thesis, MIT, Cambridge, MA, USA, 2004.

[44] B. L. P. Gassend. *A fully microfabricated two-dimensional electrospray array with applications to space propulsion*. PhD thesis, MIT, Cambridge, MA, USA, 2007.

[45] D. G. Courtney, H. Q. Li, and P. Lozano. Emission measurements from planar arrays of porous ionic liquid ion sources. *Journal of Physics D: Applied Physics*, 45(48):485203, 2012.

[46] R. Krpoun and H. R. Shea. Integrated out-of-plane nanoelectrospray thruster arrays for spacecraft propulsion. *Journal of Micromechanics and Microengineering*, 19(4):045019, 2009.

[47] S. Dandavino, Ç. Ataman, C. N. Ryan, et al. Microfabricated electrospray emitter arrays with integrated extractor and accelerator electrodes for the propulsion of small spacecraft. *Journal of Micromechanics and Microengineering*, 24(7):075011, 2014.

[48] C. N. Ryan, J. P. W. Stark, Ç. Ataman, et al. MicroThrust MEMS electrospray emitters – integrated microfabrication and test results. In *Space Propulsion 2012, Bordeaux, France*, 2012.

[49] C. N. Ryan, A. Daykin-Iliopoulos, J. A. Stark, et al. Experimental progress towards the MicroThrust MEMS electrospray electric propulsion system. In *Proceedings of the 33rd International Electric Propulsion Conference, Washington, DC, USA*, number IEPC-2013-146, 2013.

[50] MicroThrust. Microthrust. Online, 2013. URL `http://microthrust.eu/home/93-23.html`.

[51] V. Hruby, M. Gamero-Castaño, P. Falkos, and S. Shenoy. Micro newton colloid thruster system development. In *27th International Electric Propulsion Conference, Pasadena, CA, USA*, number IEPC-2001-281, 2001.

[52] M. Gamero-Castaño and V. Hruby. Electrospray as a source of nanoparticles for efficient colloid thrusters. *Journal of Propulsion and Power*, 17(5):977–987, 2001.

[53] M. Tajmar. MEMS Indium FEEP Thruster: Manufacturing Study and First Prototype Results. In *40th AIAA/ASME/SAE/-ASEE Joint Propulsion Conference and Exhibit, Fort Lauderdale, FL, USA*, number AIAA 2004-3619, 2004.

[54] R. Krpoun, M. Räber, K. L. Smith, J. P. W. Stark, and H. R. Shea. Design and fabrication of an integrated MEMS-based colloid micropropulsion system. In *30th International Electric Propulsion Conference, Florence, Italy*, number IEPC-2007-099, 2007.

[55] S. Dandavino, Ç. Ataman, S. Chakraborty, et al. Progress Towards a Miniaturized Electrospray Thruster for Propulsion of Small Spacecraft. In *48th AIAA/ASME/SAE/ASEE Joint Propulsion Conference & Exhibit, Atlanta, GA, USA*, number AIAA 2012-4024, 2012.

[56] S. Dandavino, Ç. Ataman, S. Chakraborty, et al. Design and fabrication of the thruster heads for the MicroThrust MEMS electrospray propulsion system. In *33rd International Electric Propulsion Conference, Washington, DC, USA*, number IEPC-2013-127, 2013.

[57] M. Gamero-Castaño and V. Hruby. Characterization of a colloid thruster performing in the micro-Newton thrust range. In *27th International Electric Propulsion Conference, Pasadena, CA, USA*, number IEPC-2001-282, 2001.

[58] R. J. Cox, J. D. Gelorme, and S. A. R. Gutierrez. Photoresist composition and printed circuit boards and packages made therewith. US Patent 4,882,245, 1989.

[59] A. Del Campo and C. Greiner. SU-8: a photoresist for high-aspect-ratio and 3D submicron lithography. *Journal of Micromechanics and Microengineering*, 17(6):R81, 2007.

[60] M. Deubel, G. Von Freymann, M. Wegener, et al. Direct laser writing of three-dimensional photonic-crystal templates for telecommunications. *Nature Materials*, 3(7):444–447, 2004.

[61] L. S. Clair, H. Lorenz, A. Bertsch, et al. SU-8: Thick Photo-Resist for MEMS. Online, 2013. URL `http://memscyclopedia.org/su8.html`.

[62] J. Melai, C. Salm, S. Smits, J. Visschers, and J. Schmitz. The electrical conduction and dielectric strength of SU-8. *Journal of Micromechanics and Microengineering*, 19(6):065012, 2009.

[63] MicroChem. SU-8 Table of Properties. Online. URL `http://www.microchem.com/pdf/SU-8-table-of-properties.pdf`.

[64] MicroChem. SU-8 2000 Permanent Epoxy Resists. Online. URL `http://microchem.com/Prod-SU82000.htm`.

[65] J. L. Dektar and N. P. Hacker. Photochemistry of triarylsulfonium salts. *Journal of the American Chemical Society*, 112(16): 6004–6015, 1990.

[66] J. V. Crivello. The discovery and development of onium salt cationic photoinitiators. *Journal of Polymer Science Part A: Polymer Chemistry*, 37(23):4241–4254, 1999.

[67] A. Yahiaoui, M. Belbachir, and A. Hachemaoui. Cationic Polymerization of 1,2-Epoxypropane by an Acid Exchanged Montmorillonite Clay in the Presence of Ethylene Glycol. *International Journal of Molecular Sciences*, 4(11):572–585, 2003.

[68] L. Matějka, K. Dušek, P. Chabanne, and J. P. Pascault. Cationic polymerization of diglycidyl ether of bisphenol A. III. Comparison of the theory with experiment. *Journal of Polymer Science Part A: Polymer Chemistry*, 35(4):665–672, 1997.

[69] G. Genolet. *New photoplastic fabrication techniques and devices based on high aspect ratio photoresist*. PhD thesis, EPFL, Lausanne, Switzerland, 2001.

[70] MicroChem. NANO® SU-8 Negative Tone Photoresist Formulations 50-100. Online. URL `http://www.microchem.com/pdf/SU8_50-100.pdf`.

[71] micro resist technology GmbH. Online. URL `http://www.microresist.de/`.

[72] M. Piechotka, K. Huhn, T. Henning, D. Feili, and P. J. Klar. Microfabrication of Colloid Emitters based on the Photo Resist SU-8 and Electro Plating. In *32nd International Electric Propulsion Conference, Wiesbaden, Germany*, number IEPC-2011-276, 2011.

[73] FEMM. Finite element method magnetics: License. Online. URL `http://www.femm.info/wiki/License`.

[74] J. A. Nabity. *The Miniaturization of the Colloid Thruster to the Micro Scale*. PhD thesis, CU, Boulder, CO, USA, 2007.

[75] S. Dandavino, Ç. Ataman, H. R. Shea, C. N. Ryan, and J. P. W. Stark. Microfabrication of Capillary Electrospray Emitters and ToF Characterization of the Emitted Beam. In *32nd International Electric Propulsion Conference, Wiesbaden, Germany*, number IEPC-2011-131, 2011.

[76] T. Young. An essay on the cohesion of fluids. *Philosophical Transactions of the Royal Society of London*, 95:65–87, 1805.

[77] W. A. Zisman. *Contact Angle, Wettability, and Adhesion*, volume 43 of *Advances in Chemistry*, chapter 1, pages 1–51. American Chemical Society, 1964. ISBN 9780841200449.

[78] Z. Gao, D. B. Henthorn, and C.-S. Kim. Enhanced wettability of an SU-8 photoresist through a photografting procedure for bioanalytical device applications. *Journal of Micromechanics and Microengineering*, 18(4):045013, 2008.

[79] A. H. Ellison and W. A. Zisman. Wettability of halogenated organic solid surfaces. *The Journal of Physical Chemistry*, 58(3): 260–265, 1954.

[80] Z. He, M. Ma, X. Lan, et al. Fabrication of a transparent superamphiphobic coating with improved stability. *Soft Matter*, 7(14): 6435–6443, 2011.

[81] P. J. Wilbur, M. Wilson, K. Hutchings, and J. D. Williams. Emissive Membrane Ion Thruster Concept. *Journal of Propulsion and Power*, 23(5):1049–1054, 2007.

[82] M. Faraday. Experimental Researches in Electricity. Fourth Series. *Philosophical Transactions of the Royal Society of London*, 123:507–522, 1833.

[83] M. Faraday. Experimental Researches in Electricity. Twelfth Series. *Philosophical Transactions of the Royal Society of London*, 128:83–123, 1838.

[84] E. Warburg. Ueber die Electrolyse des festen Glases. *Annalen der Physik*, 257(4):622–646, 1884.

[85] H. Buff. Ueber die electrische Leitfähigkeit des erhitzten Glases. *Justus Liebigs Annalen der Chemie*, 90(3):257–283, 1854.

[86] W. Nernst. Material for electric-lamp glowers. US Patent 685,730, 1901.

[87] W. C. Heraeus. Über die elektrolytische Leitung fester Körper bei sehr hohen Temperaturen. *Zeitschrift für Elektrochemie*, 6 (2):41–43, 1899.

[88] E. Baur and H. Preis. Über Brennstoff-Ketten mit Festleitern. *Zeitschrift für Elektrochemie und Angewandte Physikalische Chemie*, 43(9):727–732, 1937.

[89] M. Chen, B. Hallstedt, and L. J. Gauckler. Thermodynamic modeling of the ZrO_2–$YO_{1.5}$ system. *Solid State Ionics*, 170(3): 255–274, 2004.

[90] H. Scott. Phase relationships in the zirconia-yttria system. *Journal of Materials Science*, 10(9):1527–1535, 1975.

[91] E. Mutoro, B. Luerssen, S. Günther, and J. Janek. Structural, morphological and kinetic properties of model type thin film platinum electrodes on YSZ. *Solid State Ionics*, 179(21):1214–1218, 2008.

[92] G. Beck, H. Fischer, E. Mutoro, et al. Epitaxial Pt (111) thin film electrodes on YSZ (111) and YSZ (100)—Preparation and characterisation. *Solid State Ionics*, 178(5):327 – 337, 2007.

[93] K. Kerman, B.-K. Lai, and S. Ramanathan. $Pt/Y_{0.16}Zr_{0.84}O_{1.92}/Pt$ thin film solid oxide fuel cells: Electrode microstructure and stability considerations. *Journal of Power Sources*, 196(5):2608–2614, 2011.

[94] J. Poppe, S. Völkening, A. Schaak, et al. Electrochemical promotion of catalytic CO oxidation on Pt/YSZ catalysts under low

pressure conditions. *Physical Chemistry Chemical Physics*, 1(22): 5241–5249, 1999.

[95] B. Luerßen, J. Janek, and R. Imbihl. Electrocatalysis on Pt/YSZ electrodes. *Solid State Ionics*, 141:701–707, 2001.

[96] P. P. Kumar and S. Yashonath. Ionic conduction in the solid state. *Journal of Chemical Sciences*, 118(1):135–154, 2006.

[97] J. Luo, D. P. Almond, and R. Stevens. Ionic mobilities and association energies from an analysis of electrical impedance of ZrO_2–Y_2O_3 alloys. *Journal of the American Ceramic Society*, 83 (7):1703–1708, 2000.

[98] O. H. Kwon and G. M. Choi. Electrical conductivity of thick film YSZ. *Solid State Ionics*, 177(35):3057 – 3062, 2006.

[99] C. Korte, A. Peters, J. Janek, D. Hesse, and N. Zakharov. Ionic conductivity and activation energy for oxygen ion transport in superlattices—the semicoherent multilayer system YSZ (ZrO_2 + 9.5 mol% Y_2O_3)/Y_2O_3. *Physical Chemistry Chemical Physics*, 10 (31):4623–4635, 2008.

[100] Y. Torimoto, A. Harano, T. Suda, and M. Sadakata. Emission of O-radical anions from a solid electrolyte surface into the gas phase. *Japanese Journal of Applied Physics*, 36(2B):L238, 1997.

[101] Y. Torimoto, K. Shimada, T. Nishioka, and M. Sadakata. High Energy Efficiency of O-Emission from Microstructure Device on YSZ. *Journal of Chemical Engineering of Japan*, 33(6):914–917, 2000.

[102] Y. Fujiwara, A. Kaimai, J.-O. Hong, et al. Emission characteristics of O-ions from a bare surface of yttria-stabilized zirconia (YSZ) at elevated temperatures. *Japanese Journal of Applied Physics*, 41(6A):L657, 2002.

[103] Y. Fujiwara, A. Kaimai, J.-O. Hong, et al. An oxygen negative ion source of a new concept using solid oxide electrolytes. *Journal of the Electrochemical Society*, 150(2):E117–E124, 2003.

[104] Y. Fujiwara, T. Sakai, A. Kaimai, et al. Effect of Electrochemical Polarization on the Emission of O-ions from the Surface of YSZ. *Journal of the Electrochemical Society*, 150(11):E543–E547, 2003.

[105] A. Evans, A. Bieberle-Hütter, J. L. M. Rupp, and L. J. Gauckler. Review on microfabricated micro-solid oxide fuel cell membranes. *Journal of Power Sources*, 194(1):119–129, 2009.

[106] P.-C. Su, C.-C. Chao, J. H. Shim, R. Fasching, and F. B. Prinz. Solid oxide fuel cell with corrugated thin film electrolyte. *Nano Letters*, 8(8):2289–2292, 2008.

[107] A. Bieberle-Hütter, D. Beckel, A. Infortuna, et al. A micro-solid oxide fuel cell system as battery replacement. *Journal of Power Sources*, 177(1):123–130, 2008.

[108] J. L. M. Rupp. Ionic diffusion as a matter of lattice-strain for electroceramic thin films. *Solid State Ionics*, 207:1–13, 2012.

[109] A. Kronenberger. *Herstellung und Charakterisierung von $ZnO_{1-x}S_x$ -Dünnschichten : Dotierung mit Wasserstoff und Einsatz in $ZnO_{1-x}S_x$ /GaN-Heterostruktur-Leuchtdioden.* PhD thesis, JLU, Giessen, Germany, 2013.

[110] X. Xu, C. Xia, S. Huang, and D. Peng. YSZ thin films deposited by spin-coating for IT-SOFCs. *Ceramics International*, 31(8): 1061–1064, 2005.

[111] H. Fukumoto, T. Imura, and Y. Osaka. Heteroepitaxial growth of yttria-stabilized zirconia (YSZ) on silicon. *Japanese Journal of Applied Physics*, 27(8A):L1404, 1988.

[112] S. Heiroth, T. Lippert, A. Wokaun, et al. Yttria-stabilized zirconia thin films by pulsed laser deposition: Microstructural and compositional control. *Journal of the European Ceramic Society*, 30(2):489–495, 2010.

[113] C.-H. Chen, N. Wakiya, K. Shinozaki, and N. Mizutani. Effects of thermal coefficient and lattice constant mismatches on mosaic dispersion of heteroepitaxial YSZ/Si (001) thin films. *Journal of Physics D: Applied Physics*, 35(2):151, 2002.

[114] H. Tomaszewski, J. Haemers, J. Denul, N. De Roo, and R. De Gryse. Yttria-stabilized zirconia thin films grown by reactive r.f. magnetron sputtering. *Thin Solid Films*, 287(1):104–109, 1996.

[115] B. Pachner, A. Polity, S. O. Steinmueller, and J. Janek. Properties of YSZ thin films prepared by RF sputter deposition using a ceramic target. In *Verhandlungen der Deutschen Physikalischen Gesellschaft, Regensburg, Germany*, volume 45, 2010. Abstract only.

[116] F. Kuhl, M. Piechotka, D. Reppin, et al. Influence of size variation on the strain distribution in ysz membranes on si substrates. In *Symposium I – Functional Materials for Solid Oxide Fuel Cells*, volume 1495 of *MRS Proceedings*, 2013.

[117] Z. Ogumi, Y. Uchimoto, Y. Tsuji, and Z.-i. Takehara. Electrodeposition of thin yttria-stabilized zirconia layers using glow-discharge plasma. *Journal of Applied Physics*, 72(4):1577–1582, 1992.

[118] H. Holzschuh and H. Suhr. Textured (100) yttria-stabilized zirconia thin films deposited by plasma-enhanced chemical vapor deposition. *Applied Physics Letters*, 59(4):470–472, 1991.

[119] W. R. Grove. On the electro-chemical polarity of gases. *Philosophical transactions of the Royal Society of London*, 142:87–101, 1852.

[120] K. Wasa and S. Hayakawa. *Handbook of sputter deposition technology*. Noyes Publications, Park Ridge, NJ, USA, 1992. ISBN 9781437734836.

[121] J. Brentano. Focussing method of crystal powder analysis by X-rays. *Proceedings of the Physical Society of London*, 37(1):184, 1924.

[122] E. D. Palik, V. M. Bermudez, and O. J. Glembocki. Ellipsometric Study of Orientation-Dependent Etching of Silicon in Aqueous KOH. *Journal of the Electrochemical Society*, 132(4):871–884, 1985.

[123] H. Seidel, L. Csepregi, A. Heuberger, and H. Baumgärtel. Anisotropic etching of crystalline silicon in alkaline solutions I. Orientation dependence and behavior of passivation layers. *Journal of the Electrochemical Society*, 137(11):3612–3626, 1990.

[124] A. Smekal. Zur Quantentheorie der Dispersion. *Naturwissenschaften*, 11(43):873–875, 1923.

[125] C. V. Raman. A new radiation. *Indian Journal of Physics*, 2: 387–398, 1928.

[126] C. V. Raman and K. S. Krishnan. A new type of secondary radiation. *Nature*, 121(3048):501–502, 1928.

[127] M. I. Aroyo, J. M. Perez-Mato, D. Orobengoa, et al. Crystallography online: Bilbao Crystallographic Server. *Bulgarian Chemical Communications*, 43(2):183–97, 2011.

[128] E. Kroumova, M. I. Aroyo, J. M. Perez-Mato, et al. Bilbao Crystallographic Server : Useful Databases and Tools for Phase-Transition Studies. *Phase Transitions*, 76(1-2):155–170, 2003.

[129] E. F. López, V. S. Escribano, M. Panizza, M. M. Carnasciali, and G. Busca. Vibrational and electronic spectroscopic properties of zirconia powders. *Journal of Materials Chemistry*, 11:1891–1897, 2001.

[130] W. Lacina and P. Pershan. Phonon Optical Properties of $Ca_{1-x}Sr_xF_2$. *Physical Review B*, 1(4):1765, 1970.

[131] R. Loudon. The Raman effect in crystals. *Advances in Physics*, 13(52):423–482, 1964.

[132] V. Keramidas and W. White. Raman scattering from $Ca_xZr_{1-x}O_{2-x}\square_x$, a system with massive point defects. *Journal of Physics and Chemistry of Solids*, 34(11):1873 – 1878, 1973.

[133] A. Feinberg and C. H. Perry. Structural disorder and phase transitions in ZrO_2-Y_2O_3 system. *Journal of Physics and Chemistry of Solids*, 42(6):513–518, 1981.

[134] M. Ishigame and E. Yoshida. Study of the defect-induced Raman spectra in cubic zirconia. *Solid State Ionics*, 23(3):211–218, 1987.

[135] M. Yashima, K. Ohtake, M. Kakihana, H. Arashi, and M. Yoshimura. Determination of tetragonal-cubic phase boundary of $Zr_{1-X}R_XO_{2-X/2}$ (R= Nd, Sm, Y, Er and Yb) by Raman scattering. *Journal of Physics and Chemistry of Solids*, 57(1): 17–24, 1996.

[136] J. Cai, C. Raptis, Y. S. Raptis, and E. Anastassakis. Temperature dependence of Raman scattering in stabilized cubic zirconia. *Physical Review B*, 51(1):201, 1995.

[137] E. Anastassakis, A. Pinczuk, E. Burstein, F. H. Pollak, and M. Cardona. Effect of static uniaxial stress on the Raman spectrum of silicon. *Solid State Communications*, 8(2):133–138, 1970.

[138] A. D. Papadopoulos, Y. S. Raptis, and E. Anastassakis. Raman study of SrF_2 under uniaxial stress. *Solid State Communications*, 58(9):645–648, 1986.

[139] E. Anastassakis. Inelastic light scattering in the presence of uniaxial stresses. *Journal of Raman Spectroscopy*, 10(1):64–76, 1981.

[140] E. Anastassakis and E. Burstein. Morphic effects I-effects of external forces on photon-optical phonon interactions. *Journal of Physics and Chemistry of Solids*, 32(2):313–326, 1971.

[141] E. Anastassakis and E. Burstein. Morphic effects II-effects of external forces on the frequencies of the $q \approx 0$ optical phonons. *Journal of Physics and Chemistry of Solids*, 32(3):563–570, 1971.

[142] J. Cai, Y. S. Raptis, and E. Anastassakis. Stabilized cubic zirconia: A Raman study under uniaxial stress. *Applied Physics Letters*, 62(22):2781–2783, 1993.

[143] H. M. Kandil, J. D. Greiner, and J. F. Smith. Single-Crystal Elastic Constants of Yttria-Stabilized Zirconia in the Range 20° C to 700° C. *Journal of the American Ceramic Society*, 67(5):341–346, 1984.

[144] D. W. Liu, C. H. Perry, A. A. Feinberg, and R. Currat. Neutron-scattering studies of phonons in disordered cubic zirconia at elevated temperatures. *Physical Review B*, 36(17):9212, 1987.

[145] K. Udeshi and Y. Gianchandani. A DC-Powered High-Voltage Generator using a Bulk Pt-Rh Oscillating Micro-Relay. In *Solid-State Sensors, Actuators and Microsystems Conference (TRANSDUCERS) 2007, Lyon, France*, pages 1151–1154, 2007.

[146] R. E. Pelrine and I. Polyakov. Miniature high-voltage power supplies. US Patent Application 20120019223, 2012.

[147] C. H. Yun, C. S. Lo, C. Zuo, and J. Kim. Piezoelectric MEMS transformer. US Patent Application 20130134838, 2013.

[148] Cubesat. Online. URL `http://cubesat.calpoly.edu/`.

[149] P. Gessini and G. Paccani. Ablative Pulsed Plasma Thruster System Optimization for Microsatellites. In *Proceedings of the 27th IEPC, Pasadena, California, USA*, number IEPC-2001-182, 2001.

[150] F. Rysanek and R. Burton. Performance and Heat Loss of a Coaxial Teflon Pulsed Plasma Thruster. In *Proceedings of the 27th IEPC, Pasadena, California, USA*, number IEPC-2001-151, 2001.

[151] D. Feili, B. Lotz, S. Bonnet, et al. μNRIT-2.5 – A New Optimized Microthruster Of Giessen University. In *Proceedings of the 31st IEPC, Ann Arbor, MI, USA*, number IEPC-2009-174, 2009.

[152] T. Ito, N. Gascon, W. S. Crawford, and M. A. Cappelli. Experimental characterization of a micro-Hall thruster. *Journal of Propulsion and Power*, 23(5):1068–1074, 2007.

[153] S. Marcuccio, A. Genovese, and M. Andrenucci. Experimental Performance of Field Emission Microthrusters. *Journal of Propulsion and Power*, 14(5):774–781, 1998.

[154] M. Tajmar, A. Genovese, N. Buldrini, and W. Steiger. Miniaturized Indium-FEEP Multiemitter Design and Performance. In *NanoTech 2002 - "At the Edge of Revolution", Houston, TX, USA*, number 2002-5718, 2002.

[155] J. Cardin, K. Coste, D. Williamson, and P. Gloyer. A Cold Gas Micro-Propulsion System for CubeSats. In *Small Satellite Conference 2003 - Access to Space: Getting There is More Than Half the Battle, North Logan, UT, USA*, number SSC03-XI-8, 2003.

[156] Intelsat Licence LLC. Engineering Statement at the FCC - The Federal Communications Commission. Online. URL `http://licensing.fcc.gov/myibfs/download.do?attachment_key=791132`.

[157] Spacecom. About the AMOS-2 Satellite. Online, 2009. URL `http://www.amos-spacecom.com/content.cfm/amos-2`.

[158] Satbeams. Online. URL `https://www.satbeams.com/`.

Appendix A

More comprehensive calculations

A.1 Thrust approximation

The average thrust F can be approximated for a mission with an overall Delta-v budget ΔV and a mission duration T, if the exhaust velocity v_e of the propellant of mass m_2 is much greater than ΔV:

$$
\begin{aligned}
F &= \left|\frac{\mathrm{d}\tilde{m}}{\mathrm{d}t}\right| v_\mathrm{e} \\
\text{average thrust: } \left|\frac{\mathrm{d}\tilde{m}}{\mathrm{d}t}\right| &= \frac{m_2}{T} \\
F &= \frac{m_2}{T} v_\mathrm{e} = \frac{m_0\left(1 - e^{-\frac{\Delta V}{v_\mathrm{e}}}\right)}{T} v_\mathrm{e} \\
v_\mathrm{e} \gg \Delta V\text{: } F &\approx \frac{m_0 \Delta V}{T}, \qquad \text{(A.1)}
\end{aligned}
$$

where the actual mass of the spacecraft is $\tilde{m}$, its starting mass is m_0 at the beginning of the mission and the time is t. The values in Table 1.1 were calculated for the orbital station keeping in a geostationary earth orbit (GEO) ($\Delta V/T = 65\,\mathrm{m\,s^{-1}\,a^{-1}}$) and for the drag compensation in a low earth orbit (LEO) at 400 km ($\Delta V/T = 25\,\mathrm{m\,s^{-1}\,a^{-1}}$).

A.2 Mass ratio of miniaturized thrusters

The mass ratio m_prop/m_0 of the propulsion system mass m_prop to the spacecraft starting mass m_0 was estimated for different types of minia-

turized thrusters. As sample mission, the drag compensation of a spacecraft in the lower earth orbit (LEO) at an altitude of 400 km is proposed due to its simplicity. The mission requires mainly the regularly firing of a thruster arrangement in one direction. The annual Delta-v budget is 25 m/s. The following estimates are based on a mission duration $T = 10\,\mathrm{a}$, yielding an overall Delta-v budget of $\Delta V = 250\,\mathrm{m/s}$.

A spacecraft with a total starting wet mass m_0 carries a propellant mass m_2 for a mission with an overall Delta-v budget ΔV:

$$\begin{aligned} m_0 &= m_1 + m_2 \\ m_0 &= m_{\mathrm{sat}} + m_{\mathrm{PPU}} + m_{\mathrm{thrust}} + m_{\mathrm{pack}} + m_2 \\ m_0 &= m_{\mathrm{sat}} + m_{\mathrm{prop}} \\ m_{\mathrm{prop}} &= m_{\mathrm{thrust}} + m_{\mathrm{pack}} + m_2, \end{aligned} \tag{A.2}$$

where the parameters are the dry spacecraft mass m_1, the mass m_{sat} of the spacecraft without components related to propulsion, and the overall propulsion system mass m_{prop} comprising the power processing unit (PPU) mass m_{PPU}, the dry mass m_{thrust} of all thrusters, the packaging mass m_{pack} (including storage tanks, feedings, valves etc.) and m_2.

The PPU mass can be expressed as:

$$m_{\mathrm{PPU}} = n\gamma P = n\gamma \left(P_{\mathrm{gen}} + P_{\mathrm{acc}} + P_{\mathrm{fun}}\right), \tag{A.3}$$

with the electric power P (per thruster) required for the generation (P_{gen}) and acceleration (P_{acc}) of particles and to maintain the function of valves etc. (P_{fun}). The specific PPU mass γ covers the linear relation between the mass of a PPU to the average power it can handle[3] and commonly scales as $30\,\mathrm{g\,W^{-1}}$. This relation also holds for miniaturized components[145–147]. If the PPU is already integrated into a single thruster unit, m_{PPU} is part of m_{thrust} which is covered by $\gamma = 0$ in the estimates for such thruster types. The mass related to the power supplied of the solar panels for propulsion scales with a tenth of γ[13] and is neglected for the estimates performed here, as the overall solar panel mass of a satellite is given by the spacecraft standard, especially for nanosatellites, e.g. the CubeSat standard[148].

The number n of thrusters required for that mission depends on either the minimal thrust F_{min} required or the propellant mass of the mission. If the propellant is stored in a storage tank which is not

already included in the thruster mass, n is given by:

$$\begin{aligned} n &= \left\lceil \frac{\beta F_{\min}}{F_{\text{thrust}}} \right\rceil \\ F_{\min} &= \frac{m_2 v_{\text{e}}}{T} \\ n &= \left\lceil \frac{\beta m_2 v_{\text{e}}}{T F_{\text{thrust}}} \right\rceil , \end{aligned} \tag{A.4}$$

where F_{thrust} is the thrust of a single thruster. $F_{\min}$ of the mission type considered here is defined by m_2 expelled with the exhaust velocity v_{e} over the mission duration T, i.e. permanently firing thrusters to compensate the drag in LEO, refer to Eq. (2.6). The coefficient β covers the emergency reserve overhead and is set to 1.5 in our estimates. The brackets $\lceil\rceil$ denote the ceiling function. If the propellant $m_{2_{\text{single}}}$ is stored within each single thruster unit, Eq. (A.4) changes to:

$$n = \max\left(\left\lceil \frac{\beta F_{\min}}{F_{\text{thrust}}} \right\rceil , \left\lceil \frac{\beta m_2}{m_{2_{\text{single}}}} \right\rceil \right). \tag{A.5}$$

The overall thruster mass obviously depends on the mass m_{single} of a single thruster:

$$m_{\text{thrust}} = n m_{\text{single}}. \tag{A.6}$$

The packaging mass scales with the propellant mass, as mainly the storage tank size increases with more propellant:

$$m_{\text{pack}} = \kappa m_2. \tag{A.7}$$

The overhead coefficient κ is assumed to be 20 % of the propellant mass, if the propellant is separated from the single thruster unit. If the propellant is stored and integrated in the single thruster unit, κ is obviously 0.

The propellant mass results from the Tsiolkovsky Equation (2.4):

$$m_2 = m_0 \left(1 - e^{-\frac{\Delta V}{v_{\text{e}}}} \right). \tag{A.8}$$

With Eqs. (A.2) to (A.8), it is possible to determine the propulsion system mass $m_{\text{prop}}(m_0)$ for a thruster type and the LEO drag compen-

sation mission described above.

$$m_{\text{prop}}^{\text{out}} = (1+\kappa)\left(1-e^{-\frac{\Delta V}{v_{\text{e}}}}\right)m_0 + (m_{\text{single}}+\gamma P) \times \left\lceil \frac{\beta\left(1-e^{-\frac{\Delta V}{v_{\text{e}}}}\right)m_0 v_{\text{e}}}{TF_{\text{thrust}}} \right\rceil \tag{A.9}$$

$$m_{\text{prop}}^{\text{in}} = (1+\kappa)\left(1-e^{-\frac{\Delta V}{v_{\text{e}}}}\right)m_0 + (m_{\text{single}}+\gamma P) \times \max\left(\left\lceil \frac{\beta\left(1-e^{-\frac{\Delta V}{v_{\text{e}}}}\right)m_0 v_{\text{e}}}{TF_{\text{thrust}}} \right\rceil , \left\lceil \frac{\beta\left(1-e^{-\frac{\Delta V}{v_{\text{e}}}}\right)m_0}{m_{2_{\text{single}}}} \right\rceil \right). \tag{A.10}$$

$m_{\text{prop}}^{\text{out}}$ and $m_{\text{prop}}^{\text{in}}$ are m_{prop} for thruster types with additional storage tanks or integrated propellant reservoirs, respectively.

It is now possible to determine the ratio m_{prop}/m_0 of the total mass m_{prop} of the propellant system to the satellite wet mass m_0 for different m_0. The following miniaturized thruster types were used for these calculations (data was also taken from the review of Osiander et al.[3]):

- Electric propulsion:
  - Miniaturized pulsed plasma thruster (μPPT) studied by Gessini and Paccani[149], Rysanek and Burton[150].
  - Miniaturized vacuum arc thruster (VAT)[3].
  - Micro-resistojet (Resistojet)[3].
  - Electrostatic propulsion:
    - Miniaturized radio-frequency ion thruster (RIT-2.5) studied by Feili et al.[151]. Two working regimes calculated:
      - RIT-2.5a: low-thrust regime.
      - RIT-2.5b: high-thrust regime.
    - Miniaturized Hall effect thruster (μHET) investigated by Ito et al.[152].
    - Miniaturized indium field-emission electric propulsion thruster (μFEEP) studied by Marcuccio et al.[153], Tajmar et al.[154].

Table A.1: Parameters used in Eqs. (A.9) and (A.10) for the miniaturized thruster types compared in this survey.

parameter unit	P W	F_{thrust} µN	v_{e} km/s	m_{single} g	$m_{2_{\text{single}}}$ g	κ	γ g/W
µFEEP[3]	5	100	100	500	0	0.2	0
µPPT[3,149,150]	10	100	5	600	240	0	0
VAT[3]	10	50	20	500	5	0	0
Resistojet[3]	3	500	1	50	0	0.2	0
RIT-2.5a[151]	13.1	50	23	210	0	0.2	0.3
RIT-2.5b[151]	31.2	500	50	210	0	0.2	0.3
MiPS[3,155]	0	55 000	0.65	456	53	0	0
µColloid[47,49,56]	0.05	7	10	60	0	0.2	0.3
µHET[152]	10	600	0.3	5	0	0.2	0.3

  - ∗ Miniaturized EMI-BF_4 colloid thruster (µColloid) investigated by Dandavino et al.[47], Ryan et al.[49], Dandavino et al.[56].

- Chemical propulsion:

  - Cold gas micro-propulsion system (MiPS) investigated by Cardin et al.[155].

For the RIT-2.5, two different working regimes were treated as different thruster types to account for the different power and propellant efficiency in both regimes.

In Table A.1 the parameters used in Eqs. (A.9) and (A.10) are listed. If the propellant $m_{2_{\text{single}}}$ is stored within each single thruster unit, the packaging factor κ is set to zero and Eq. (A.10) is used to determine $m_{\text{prop}}(m_0)$. Analogously, (A.9) is used, if the thruster mass does not include the propellant.

The power per µColloid thruster unit was not stated explicitly, but could be easily obtained from the thrust and exhaust velocity following Eq. (2.7) for the acceleration power[47,49,56]. The power for the generation of the colloid particles is simply the product of extraction current and voltage. A droplet regime with a mean charge-to-mass ratio of

Table A.2: Parameters used in Eqs. (A.9) and (A.10) which are constant for the estimates of thruster types. These parameters are for a sample mission of LEO (400 km) drag compensation.

parameter	T / a	ΔV / $\mathrm{m\,s^{-1}}$	β
value	10	250	1.5

$3900^{-1}\,e/u$ could be determined by both the extraction and acceleration parameters, e and u are the elementary charge and the unified atomic mass unit, respectively.

The remaining parameters T, ΔV and β are constant for all thruster types and are listed in Table A.2.

Based on the parameters in tables A.1 and A.2 we estimated the ratio m_{prop}/m_0 using Eqs. (A.9) and (A.10) over a wide range of wet masses of satellites, $10\,\mathrm{g} < m_0 < 10\,000\,\mathrm{kg}$. The estimated curves are shown in Fig. A.1.

At low masses, i.e. below the mass of a single thruster unit m_{single} ($n = 1$), $m_{\mathrm{prop}}/m_0\,(m_0 < m_{\mathrm{single}}) \propto m_0^{-1}$ with a proportionality factor $m_{\mathrm{single}} + \gamma P$. At higher satellite masses, where $n \gg 1$, the ratio approximates a constant value $m_{\mathrm{prop}}/m_0\,(m_0 \gg m_{\mathrm{single}}) \approx \xi \propto m_2/m_0$. The values of ξ for the different thruster types are listed in Table A.3.

Obviously, the maximal value for the ratio m_{prop}/m_0 is 1, describing the case of a satellite comprising only propulsion system components. In Fig. A.1 the ratio $(m_0 - m_1)/m_0$ for a number of satellites in the geostationary earth orbit (GEO) is also shown, the data are listed in Table A.4. The Delta-v budget of the GEO satellites is driven by an annual $\Delta V_{\mathrm{OST}} \approx 65\,\mathrm{m\,s^{-1}}$ for orbital station keeping and a nonrecurring $\Delta V_{\mathrm{GTO}} \approx 1600\,\mathrm{m\,s^{-1}}$ for the orbit transfer into the GEO from the geostationary transfer orbit (GTO), where the satellite is ejected from the launch vehicle. Comparing the estimated values of m_{prop}/m_0 for the miniaturized thruster types with the ratio $(m_0 - m_1)/m_0$ of the GEO satellites, where the ratio $(m_0 - m_1)/m_0$ is $50\,\% \pm 7\,\%$ (not accounting for peripheral equipment of the propulsion system), ratios of $m_{\mathrm{prop}}/m_0 \leq 0.5$ are suitable.

Thus, it is possible to define a satellite wet mass threshold $m_0^{50} = m_0\,(m_{\mathrm{prop}}/m_0 = 0.5)$ for each thruster type which is the minimal satellite wet mass for which each thruster type suitable as listed in Table A.3. Additionally, the values of the satellite wet mass threshold for $m_{\mathrm{prop}}/m_0 = \{1, 0.8, 0.5, 0.1, 0.01\}$ are listed in Table A.3. These values define the color range in Fig. 1.2.

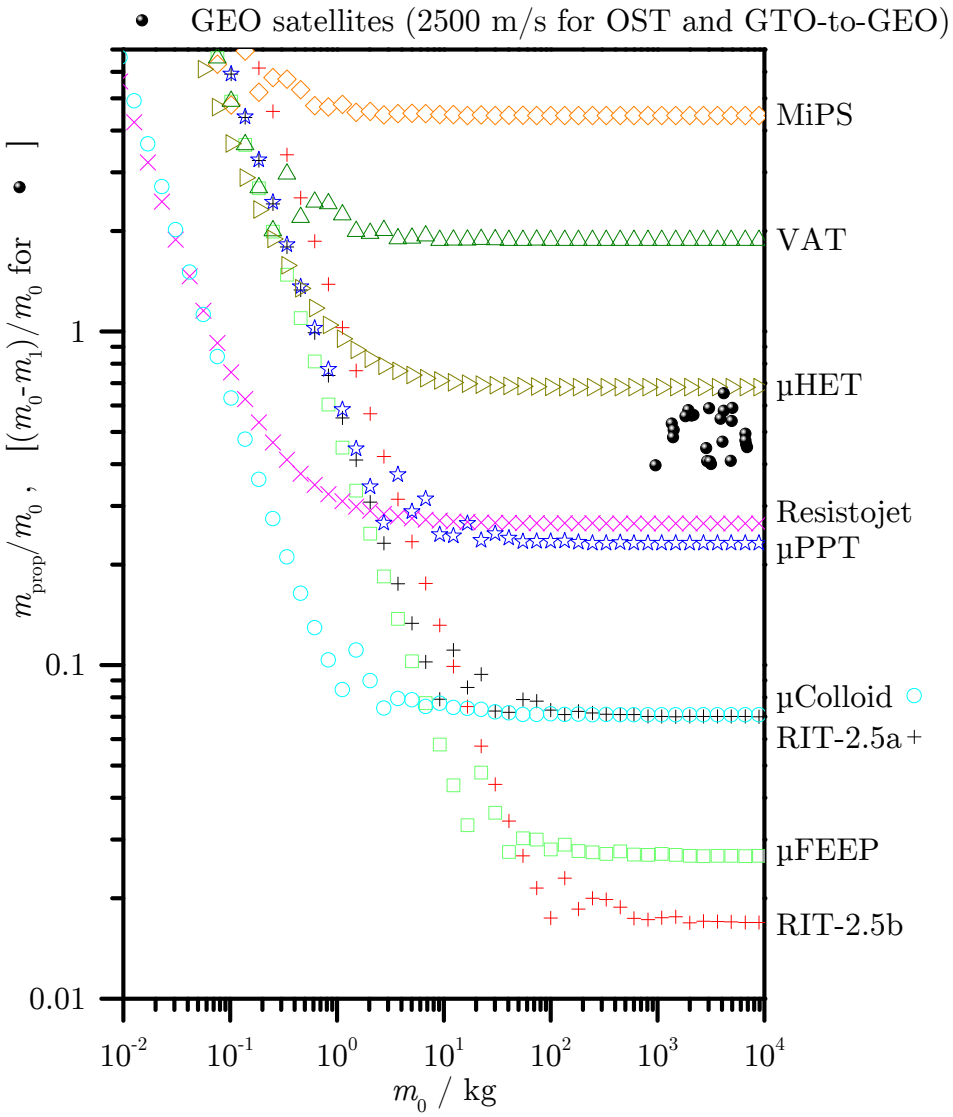

Figure A.1: Ratio m_{prop}/m_0 of the total mass m_{prop} of the propellant system to the satellite wet mass m_0 for different m_0. The estimates were calculated using Eqs. (A.9) or (A.10) for thruster system without and with integrated propellant, respectively. The related data are listed in tables A.1 and A.2 for a sample mission of LEO (400 km) drag compensation. The ratio $(m_0 - m_1)/m_0$ for a number of satellites in the geostationary earth orbit (GEO) is also shown and denoted as black spheres, the data are listed in Table A.4.

Table A.3: ξ is the threshold value of m_{prop}/m_0 which is approximated for $m_0 \gg m_{\text{single}}$. m_0^{50} is the minimal satellite wet mass for which each thruster type suitable, i.e. $m_{\text{prop}}/m_0 \leq 0.5$. According to m_0^{50}, m_0^{100} to m_0^1 are defined. A sample mission of LEO (400 km) drag compensation was used as basis for these results.

quantity unit	ξ	m_0^{50} kg	m_0^{100} kg	m_0^{80} kg	m_0^{10} kg	m_0^1 kg
µFEEP	0.01	1.0	0.50	0.63	5.2	214
µPPT	0.23	1.3	0.63	0.80		
VAT	1.9					
Resistojet	0.27	0.21	0.07	0.09		
RIT-2.5a RIT-2.5b	0.03 0.01	1.2 2.3	0.61 1.2	0.77 1.4	6.9 12	 285
MiPS	4.4					
µColloid	0.04	0.13	0.06	0.08	0.9	
µHET	0.68		0.95	2.51		

Both the VAT and the MiPS thruster type are not suitable at all ($\xi > 1$) for this mission, as the overall Delta-v budget $\Delta V = 250\,\text{m}\,\text{s}^{-1}$ is too high for their $m_{2_{\text{single}}}/m_{\text{single}}$-ratios and their exhaust velocities v_{e}, respectively. Although the µHET thruster type has a threshold ratio below 1 ($\xi \approx 0.7$), its not suitable due to the maximal suitability ratio $m_{\text{prop}}/m_0 = 0.5$ set in this scenario. The other thruster types are suitable on satellite wet masses below $m_0 = 10\,\text{kg}$ (µFEEP, µPPT and RIT-2.5) or even below $m_0 = 1\,\text{kg}$ (Resistojet and µColloid).

It has to be noted, that the estimated values are only valid for this special type of mission, i.e. LEO drag compensation (as stated at the beginning of this section). Other thrust requirements, Delta-v budgets or more complicated station-keeping demands change the number of minimal thrusters, the working ranges etc. For example, the orbital station keeping of a GEO satellite requires at least three thrusters to ensure the North-South and East-West control and the apogee boost from the GTO into the GEO requires a much higher thrust than the thrust required for station keeping.

Although the Resistojet and µColloid thruster types are suitable at very low satellite wet masses, the µFEEP and RIT-2.5 thruster

Table A.4: Data for GEO satellites in Fig. A.1.

satellite	satellite bus	launch	m_0 kg	m_1 kg	$\frac{m_0-m_1}{m_0}$
Intelsat 25[156]	FS-1300	2008	4180	1764	0.58
AMOS-2[157]	AMOS-Bus	2003	1360	640	0.53
Intelsat 2[158]	HS-601	1994	2920	1727	0.41
InmarSat XL[158]	Alphabus	2013	6650	3370	0.49
Echostar T1[158]	LS-1300S	2009	6910	3801	0.45
ViaSat 1[158]	LS-1300	2011	6740	3650	0.46
Echostar 16[158]	LS-1300	2012	6650	3520	0.47
Eutelsat 21B[158]	Spacebus-4000C3	2012	5012	2060	0.59
NSS 10[158]	Spacebus-4000C3	2009	4953	2286	0.54
Galaxy 3C[158]	BSS-702	2002	4860	2873	0.41
Intelsat 706[158]	LS-1300	1995	4180	1450	0.65
Superbird B2[158]	BSS-601HP	2000	4051	2160	0.47
AMC 6[158]	A2100 AX	2000	3901	1769	0.55
Eutelsat 33B[158]	Spacebus-3000B2	2002	3170	1900	0.40
Intelsat 26[158]	HS-601	1997	3105	1841	0.41
Thor 6[158]	Spacebus-4000B2	2009	3049	1255	0.59
Optus B3[158]	HS-601	1994	2858	1582	0.45
Insat 4CR[158]	I-2000 Bus	2007	2168	950	0.56
AMC 18[158]	A2100 A	2006	2081	918	0.56
EduSat[158]	I-2000 Bus	2004	1951	819	0.58
NileSat 102[158]	Eurostar-2000	2000	1827	810	0.56
Intelsat 24[158]	AMOS-Bus	1996	961	580	0.40
Astra 2D[158]	BSS-376HP	2000	1420	700	0.51
Chinasat 5D[158]	HS-376	1996	1400	726	0.48

types are more efficient on satellites with wet masses above 5 kg and 50 kg as the Resistojet and μColloid thruster type, respectively. The same behavior holds for the two regimes of the RIT-2.5 thruster type, the low-thrust regime RIT-2.5a has a lower suitable satellite wet mass m_0^{50} and is more efficient at satellite wet masses below 30 kg whereas the high-thrust regime is more efficient at higher satellite wet masses ($m_0 > 50\,\mathrm{kg}$).

The lowest suitable satellite wet mass was estimated for the μColloid thruster type with $m_0^{50} \approx 0.13\,\mathrm{kg}$, i.e. the propulsion system on a satellite with a wet mass of $m_0 \approx 130\,\mathrm{g}$ would consume $m_{\mathrm{prop}} \approx 65\,\mathrm{g}$ — providing $m_{\mathrm{sat}} \approx 65\,\mathrm{g}$ as payload mass. Additionally, this thruster type enables the highest efficiency up to a satellite wet mass of $m_0 \approx 10\,\mathrm{kg}$. Therefore, this work treats the development of high-efficient miniaturized colloid thrusters.

A.3 Relations for the colloid emitter concept

In section 3.1.1 we discussed the influence of an external electric field on a conductive liquid and the origin of the colloid extraction according to Martínez-Sánchez[24]. In the following we conduct a more detailed derivation of these equations.

Charge separation due to an external field

Assuming an electric field $\boldsymbol{E}_{\mathrm{n}}$ normal to a flat surface of a conductive liquid as depicted in Fig. A.2, a charge separation will occur in the liquid until a free surface charge density σ_{f} is built up. This behavior is easily understood using Gauss' law on the Gaussian pillbox also shown in Fig. A.2:

$$\Phi = \oiint_A \boldsymbol{E}\mathrm{d}\boldsymbol{A} = \frac{Q}{\varepsilon_0}, \tag{A.11}$$

i.e. the electric flux Φ through the Gaussian surface A (normal differential surface element $\mathrm{d}\boldsymbol{A}$) is determined by the charge Q enclosed by this surface, ε_0 is the vacuum permittivity. As the total charge inside the pillbox is the free surface charge $\sigma_{\mathrm{f}}A$ and the electric field is normal to the cylindrical disks of the pillbox, Eq. (A.11) simplifies to:

$$\left(E_{\mathrm{n}} - \varepsilon E_{\mathrm{n}}^{\mathrm{l}}\right) \int_A \mathrm{d}A = \frac{\sigma_{\mathrm{f}} A}{\varepsilon_0}, \tag{A.12}$$

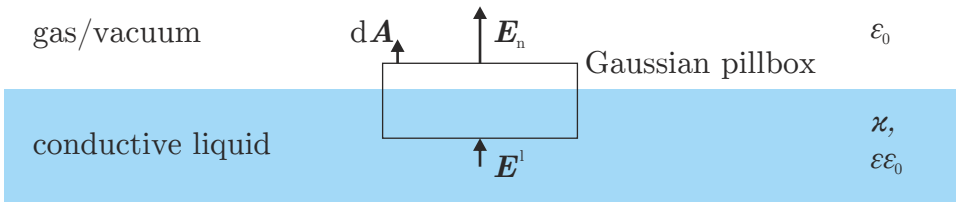

Figure A.2: Scheme of a flat interface between a conductive liquid (conductivity κ) with a permittivity $\varepsilon\varepsilon_0$ and a gas or vacuum. Outside the liquid is an electric field $\boldsymbol{E}_\mathrm{n}$ normal to the interface with the normal differential surface element d$\boldsymbol{A}$. The electric flux through a Gaussian pillbox is related to the free surface charge density σ_f by Gauss' law: $\Phi = \oiint_A \boldsymbol{E}\mathrm{d}\boldsymbol{A} = \frac{\sigma_\mathrm{f} A}{\varepsilon_0}$. The electric field $\boldsymbol{E}^\mathrm{l}$ inside the liquid induces the free surface charge: $\frac{\mathrm{d}\sigma_\mathrm{f}}{\mathrm{d}t} = \kappa E^\mathrm{l}_\mathrm{n}$.

with the electric field through the disk inside the liquid E^l_n reduced by the factor of the relative dielectric permittivity ε of the liquid. $\boldsymbol{E}^\mathrm{l}$ induces the carrier transport to the surface in order to build free surface charges:

$$\frac{\mathrm{d}\sigma_\mathrm{f}}{\mathrm{d}t} = \kappa E^\mathrm{l}_\mathrm{n}, \tag{A.13}$$

with the time limiting factor of the liquid's conductivity κ. This charge accumulation in turn reduces the electric field inside the liquid according to Eq. (A.12). Combining the last two Eqs. (A.12) and (A.13) results in a differential equation to get the free surface charge density σ_f:

$$\frac{\mathrm{d}\sigma_\mathrm{f}}{\mathrm{d}t} = -\frac{1}{\tau}\sigma_\mathrm{f} + \frac{\varepsilon_0}{\tau}E_\mathrm{n}, \tag{A.14}$$

with the relaxation time $\tau = \varepsilon\varepsilon_0/\kappa$. For $E_\mathrm{n} = E_\mathrm{n}(t)$ Eq. (A.14) can be solved using the method of variation of constants:

$$\sigma_\mathrm{f}(t) = c(t)e^{-\frac{t}{\tau}}. \tag{A.15}$$

Inserting Eq. (A.15) in Eq. (A.14):

$$\left(\frac{\mathrm{d}c}{\mathrm{d}t} - \frac{c}{\tau}\right)e^{-\frac{t}{\tau}} = -\frac{c}{\tau}e^{-\frac{t}{\tau}} + \frac{\varepsilon_0}{\tau}E_\mathrm{n} \tag{A.16}$$

results in

$$\frac{\mathrm{d}c}{\mathrm{d}t} = \frac{\varepsilon_0}{\tau}E_\mathrm{n}e^{\frac{t}{\tau}}. \tag{A.17}$$

Integrating Eq. (A.17) yields

$$c(t) = c_0 + \frac{\varepsilon_0}{\tau} \int_0^t E_\mathrm{n}(t') e^{\frac{t'}{\tau}} \mathrm{d}t'. \tag{A.18}$$

Using no initial free surface charge as starting condition, $c_0 = 0$ according to Eq. (A.15), and inserting Eq. (A.18) in Eq. (A.15), we get for the free surface charge density

$$\sigma_\mathrm{f}(t) = \frac{\varepsilon_0}{\tau} \int_0^t E_\mathrm{n}(t') e^{\frac{t'-t}{\tau}} \mathrm{d}t'. \tag{A.19}$$

Equation (A.19) equals Eq. (3.1).

Electrostatic versus surface pressure

For a constant external electric field, Eq. (A.19) reduces to:

$$\sigma_\mathrm{f} = \varepsilon_0 E_\mathrm{n} (1 - e^{-t/\tau}). \tag{A.20}$$

Equation (A.20) converges to an equilibrium free surface charge density:

$$\sigma_\mathrm{f} = \varepsilon_0 E_\mathrm{n} \text{ for } t \gg \tau. \tag{A.21}$$

The electrostatic pressure p_el of the external electric field on this surface charge with a charge density $\rho_\mathrm{f} = \sigma_\mathrm{f}/l$ (l = width of the surface charge region) results in:

$$p_\mathrm{el} = \rho_\mathrm{f} \int_0^l E'_\mathrm{n} \mathrm{d}x \tag{A.22}$$

$$p_\mathrm{el} = \frac{\sigma_\mathrm{f}}{E_\mathrm{n}} \int_0^{E_\mathrm{n}} E'_\mathrm{n} \mathrm{d}E'_\mathrm{n} \tag{A.23}$$

$$p_\mathrm{el} = \frac{\sigma_\mathrm{f} E_\mathrm{n}}{2} = \frac{\varepsilon_0 E_\mathrm{n}^2}{2}. \tag{A.24}$$

This pressure leads to a protruding of the surface of the liquid which will eventually increase the external electric field and therefore even more charge will be accumulated. Subsequently the electric field will be enhanced due to the additional charge and a stronger protrusion will occur until an equilibrium state is reached as the electrostatic pressure is counteracted by the pressure related to the surface tension γ on an axisymmetric surface with the curvature $1/r_\mathrm{c}$:

$$\frac{\varepsilon_0}{2} E_\mathrm{n}^2 = \frac{2\gamma}{r_\mathrm{c}}. \tag{A.25}$$

If the electrostatic pressure exceeded the surface tension due to limiting factors such as geometrical constraints the liquid surface would become unstable, i.e. for

$$E_\mathrm{n} > 2\sqrt{\frac{\gamma}{\varepsilon_0 r_\mathrm{c}}}. \tag{A.26}$$

Such a constraint may be the inner diameter $2r_0$ of a capillary, i.e. a spherical shaped protrusion will have a maximal curvature of $1/r_0$ and the normal electric field to disrupt the spherical shape will be:

$$E_\mathrm{n} > 2\sqrt{\frac{\gamma}{\varepsilon_0 r_0}}. \tag{A.27}$$

As we investigate only capillaries in this work, the following considerations refer to spherical shaped liquid surfaces where the radius r_c of curvature equals the radius r_0 of the capillary.

Instability of a near-spherical shape

In prolate spheroidal coordinates ξ, η, and θ a protruded liquid surface can be represented by a hyperboloid of revolution which is expressed by a constant value of $\eta = \eta_0$ as depicted in Fig. A.3. Both the expressions of Cartesian coordinates in prolate spheroidal coordinates and vice versa are:

$$\xi = \frac{1}{a}\left[\sqrt{x^2+y^2+\left(z+\frac{a}{2}\right)^2}+\sqrt{x^2+y^2+\left(z-\frac{a}{2}\right)^2}\right] \tag{A.28}$$

$$\eta = \frac{1}{a}\left[\sqrt{x^2+y^2+\left(z+\frac{a}{2}\right)^2}-\sqrt{x^2+y^2+\left(z-\frac{a}{2}\right)^2}\right] \tag{A.29}$$

$$\theta = \arctan\left(\frac{y}{x}\right) \tag{A.30}$$

$$\tag{A.31}$$

$$x = \frac{a}{2}\sqrt{(\xi^2-1)(1-\eta^2)}\cos\eta \tag{A.32}$$

$$y = \frac{a}{2}\sqrt{(\xi^2-1)(1-\eta^2)}\sin\eta \tag{A.33}$$

$$z = \frac{a}{2}\xi\eta. \tag{A.34}$$

Equal values of ξ ($|\xi| \in [1,\infty)$) are forming prolate spheroids with the foci located at a distance a to each other along the z axis, drawn

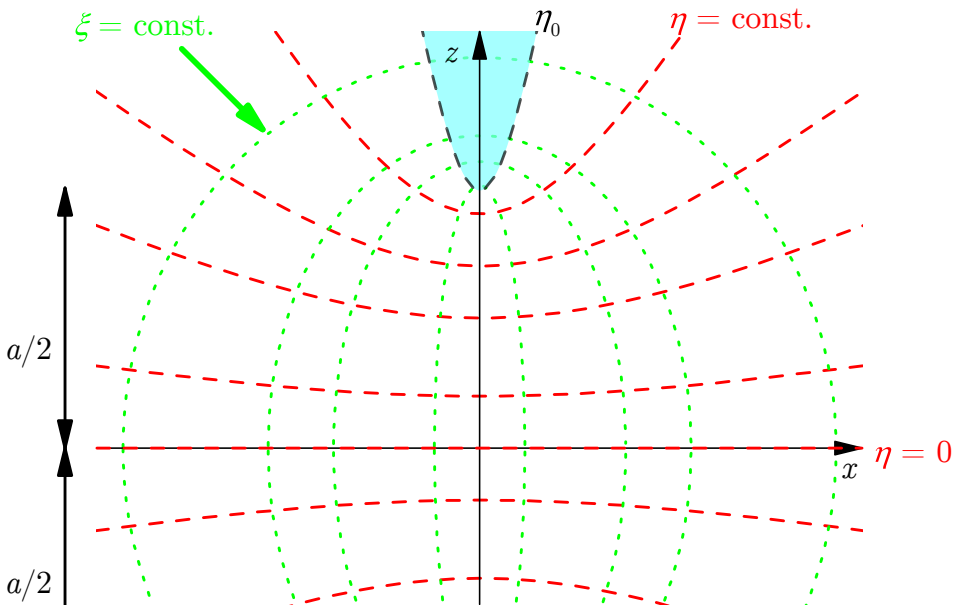

Figure A.3: Projection of lines of equal values of the prolate spheroidal coordinates ξ (green, dotted) and η (red, dashed) on the x-z plane, i.e. the third prolate spheroidal coordinate $\theta = 0$. The surfaces of constant ξ and η are obtained by rotation about the z axis and forming prolate spheroids and hyperboloids of revolution, respectively. The foci are located at a distance a from each other on the z axis. The protruding surface of an ionic liquid at a capillary tip attracted by an electric field as described in Eq. (A.27) can be approximated by a surface of constant $\eta = \eta_0$.

by green, dotted lines in Fig. A.3. Equal values of η ($\eta \in [-1, 1]$) are forming hyperboloids of revolution with the same foci, drawn by red, dashed lines in Fig. A.3. The third coordinate θ describes the rotation around the z axis and is defined in $[0, 2\pi)$.

Considering now an extraction setup as depicted in Fig. 3.1 comprising of a capillary with an inner diameter $2r_0$ and filled with an ionic liquid. When the liquid is put on a potential of $\Phi = V$ and a flat electrode placed on the opposite side on zero potential the liquid will be protruded out of the capillary as shown above. Placing the z axis on the central principal axis of inertia of the capillary the liquid surface can be approximated by a hyperboloid of revolution defined by a constant value of $\eta = \eta_0$. The flat electrode can be represented by a surface defined by $\eta = 0$.

Assuming a conductive ionic liquid in equilibrium according to Eq. (A.25) the potential within the liquid and on its surface η_0 will be at the constant value V. Outside of the liquid the equipotential surfaces are surfaces with constant η. The $\eta = 0$ surface has a potential of $\Phi = 0$. Thus, the potential depends only on η:

$$\Phi = \Phi(\eta), \text{ i.e.:} \frac{\partial \Phi}{\partial \xi} = \frac{\partial \Phi}{\partial \theta} = 0. \tag{A.35}$$

This results in the Laplacian in prolate spheroidal coordinates:

$$\Delta \Phi(\eta) = \frac{1}{h_\xi h_\eta h_\theta} \frac{\partial}{\partial \eta} \left(\frac{h_\xi h_\theta}{h_\eta} \frac{\partial \Phi}{\partial \eta} \right), \tag{A.36}$$

with the prolate spheroidal scale factors:

$$h_\xi = \frac{a}{2} \sqrt{\frac{\xi^2 - \eta^2}{\xi^2 - 1}} \tag{A.37}$$

$$h_\eta = \frac{a}{2} \sqrt{\frac{\xi^2 - \eta^2}{1 - \eta^2}} \tag{A.38}$$

$$h_\theta = \frac{a}{2} \sqrt{(\xi^2 - 1)(1 - \eta^2)} \tag{A.39}$$

yielding Laplace's equation:

$$0 = \Delta \Phi(\eta) = \frac{1}{h_\xi h_\eta h_\theta} \frac{\partial}{\partial \eta} \left(\frac{h_\xi h_\theta}{h_\eta} \frac{\partial \Phi}{\partial \eta} \right) \tag{A.40}$$

$$0 = \frac{\partial}{\partial \eta} \left(\frac{h_\xi h_\theta}{h_\eta} \frac{\partial \Phi}{\partial \eta} \right) \tag{A.41}$$

$$0 = \frac{\partial}{\partial \eta} \left[\left(1 - \eta^2\right) \frac{\partial \Phi}{\partial \eta} \right]. \tag{A.42}$$

Equation (A.42) integrates to:

$$\Phi = c \operatorname{artanh} \eta_0, \tag{A.43}$$

with a constant c. Equation (A.43) results in (using the boundary conditions stated earlier):

$$\Phi = V \frac{\operatorname{artanh} \eta}{\operatorname{artanh} \eta_0}. \tag{A.44}$$

The electric field E is then normal to the $\eta =$ const. surfaces and exhibits rotational symmetry around the z axis (with Eq. (A.38)):

$$\boldsymbol{E} = \boldsymbol{E}(\xi, \eta) = \nabla \Phi = -\frac{\boldsymbol{e}_\eta}{h_\eta} \frac{\partial \Phi}{\partial \eta} = -\frac{2V}{a} \frac{\boldsymbol{e}_\eta}{\sqrt{(\xi^2 - \eta^2)(1 - \eta^2)} \operatorname{artanh} \eta_0}. \tag{A.45}$$

Thus the maximum of the electric field on a $\eta =$ const. surface is always at $\xi = 1$. As the liquid's surface is represented by $\eta = \eta_0$, the normal field at the liquid's surface tip ($\xi = 1$) is then obviously:

$$E_\mathrm{n}^\mathrm{tip} = E_\mathrm{n}(1, \eta_0) = -\frac{2V}{a} \frac{1}{(1 - \eta^2) \operatorname{artanh} \eta_0}. \tag{A.46}$$

If $R = \sqrt{x^2 + y^2} = \frac{a}{2}\sqrt{(\xi^2 - 1)(1 - \eta^2)}$ is the distance of a point to the z axis, then the $\eta = \eta_0$ surface will be expressed as $z(R, \eta_0)$:

$$z(R, \eta_0) = \pm \sqrt{\frac{R^2}{1 - \eta_0^2} + \frac{a^2}{4}} \eta_0. \tag{A.47}$$

The radius of curvature r_c at the liquid tip is in Cartesian coordinates:

$$r_\mathrm{c} = \left| \frac{\left[1 + \left(\frac{\mathrm{d}z}{\mathrm{d}R}\right)^2\right]^{\frac{3}{2}}}{\frac{\mathrm{d}^2 z}{\mathrm{d}R^2}} \right| = \frac{1 - \eta_0^2}{2\eta_0} a \left[1 + \frac{4R^2}{a^2} \frac{1}{(1 - \eta_0)^2}\right]^{\frac{3}{2}}. \tag{A.48}$$

The distance d between flat electrode and liquid tip is:

$$d = \left| z(\xi = 1, \eta = \eta_0) = \frac{a}{2} \eta_0 \right|. \tag{A.49}$$

Equations (A.48) and (A.49) yield $a(d, r_\mathrm{c})$ and $\eta_0(d, r_\mathrm{c})$:

$$\eta_0 = \frac{1}{\sqrt{1 + \frac{r_\mathrm{c}}{d}}}; a = 2d\sqrt{1 + \frac{r_\mathrm{c}}{d}}, \tag{A.50}$$

which can be inserted in Eq. (A.46):

$$E_{\mathrm{n}}^{\mathrm{tip}} = -\frac{V}{r_{\mathrm{c}}} \frac{\sqrt{1+\frac{r_{\mathrm{c}}}{d}}}{\operatorname{artanh} \frac{1}{\sqrt{1+\frac{r_{\mathrm{c}}}{d}}}}. \tag{A.51}$$

If $r_{\mathrm{c}} \ll d$, Eq. (A.51) will be approximated ($E_{\mathrm{n}}^{\mathrm{tip}}(\frac{r_{\mathrm{c}}}{d})$ around $\frac{r_{\mathrm{c}}}{d} = 0$) to:

$$E_{\mathrm{n}}^{\mathrm{tip}} \approx -\frac{2V}{r_{\mathrm{c}}} \frac{1}{\ln \frac{4d}{r_{\mathrm{c}}}}. \tag{A.52}$$

Equation (A.52) is equivalent to Eq. (3.3) (as r_{c} is defined by the capillary radius r_0).

Sphere-on-cone (SOC) model for liquid in a dielectric capillary

The separation constant ν in the SOC model proposed by Lozano et al.[37] and discussed on SU-8 in section 3.2.2 is defined by the dielectric constant ε of the capillary material and the cone angle α:

$$\left(\frac{Q'_\nu(0)}{P'_\nu(0)} - \frac{Q_\nu(0)}{\varepsilon P_\nu(0)} \right) P_\nu(\cos\alpha) - \frac{\varepsilon - 1}{\varepsilon} Q_\nu(\cos\alpha) = 0. \tag{A.53}$$

$P_\nu(\cos\theta)$ and $Q_\nu(\cos\theta)$ are the ν-th order Legendre functions of first and second kind, respectively. $P'_\nu(\cos\theta) = \frac{\partial}{\partial\theta} P_\nu(\cos\theta)$ and $Q'_\nu(\cos\theta) = \frac{\partial}{\partial\theta} Q_\nu(\cos\theta)$ are their partial derivatives with respect to θ.

List of Publications

- M. Piechotka, M. T. Elm, S. Eisermann, T. Henning, B. K. Meyer, and P. J. Klar. Transport measurements on artificially structured ZnO epitaxial layers. In *MRS 2007 Fall Meeting, Boston, MA, USA*, number L5.10. MRS, 2007.

- D. Zhang, L. Giannone, O. Grulke, M. Piechotka, T. Windisch, A. Stark, and T. Klinger. Investigation of the Neutral Gas Pressure Effect on the Metal Resistive Bolometer. In *PLASMA 2007: International Conference on Research and Applications of Plasmas; 4th German-Polish Conference on Plasma Diagnostics for Fusion and Applications; 6th French-Polish Seminar on Thermal Plasma in Space and Laboratory, Greifswald, Germany*, volume 993, pages 199–202. AIP Publishing, 2008.

- M. Piechotka, M. T. Elm, S. Eisermann, A. Kronenberger, T. Wassner, T. Henning, M. Eickhoff, P. J. Klar, and B. K. Meyer. Artificially structured epitaxially grown ZnO layers investigated by transport measurements. In *Verhandlungen der Deutschen Physikalischen Gesellschaft, Berlin, Germany*, volume 43. DPG, 2008.

- S. Lautenschlaeger, J. Sann, P. J. Klar, M. Piechotka, and B. K. Meyer. Combinatorial growth of $Mg_xZn_{1-x}O$ epilayers by chemical vapor deposition. *physica status solidi (b)*, 246(2):383–386, 2009.

- G. Homm, M. Piechotka, A. Kronenberger, A. Laufer, F. Gather, D. Hartung, C. Heiliger, B. Meyer, P. Klar, S. Steinmüller, and J. Janek. Thermoelectric Measurements on Sputtered ZnO/ZnS Multilayers. *Journal of Electronic Materials*, 39:1504–1509, 2010.

- M. Piechotka, M. T. Elm, T. Henning, B. Szyszka, B. K. Meyer, and P. J. Klar. Transport properties of microstructured MF-

sputtered $Zn_{0.98}Al_{0.02}O$. *physica status solidi (c)*, 7(6):1580–1582, 2010.

- M. Piechotka, M. Fischer, T. Henning, B. K. Meyer, and P. J. Klar. Influence of ion-beam etching on the transport properties and the structural quality of microstructured zinc-oxide layers. In *Verhandlungen der Deutschen Physikalischen Gesellschaft, Regensburg, Germany*, volume 45. DPG, 2010.

- M. Piechotka, M. Fischer, T. Henning, D. Feili, and P. J. Klar. Improvement and investigation of the emission behaviour of YSZ samples using nanostructuring and thin film technology. In *Verhandlungen der Deutschen Physikalischen Gesellschaft, Dresden, Germany*, volume 46. DPG, 2011.

- M. Piechotka, K. Huhn, T. Henning, and P. J. Klar. Microfabrication of Colloid Emitters based on the Photo Resist SU-8 and Electro Plating. In *Proceedings of the 32nd IEPC, Wiesbaden, Germany*, number IEPC-2011-275. AIAA, 2011.

- M. Piechotka, F. Kuhl, T. Henning, and P. J. Klar. Reduction of the fabrication-induced stress of YSZ-membranes on Si. In *MRS 2011 Fall Meeting, Boston, MA, USA*, number B5.27. MRS, 2011.

- F. Kuhl, M. Piechotka, D. Reppin, et al. Influence of size variation on the strain distribution in ysz membranes on si substrates. In *Symposium I – Functional Materials for Solid Oxide Fuel Cells*, volume 1495 of *MRS Proceedings*, 2013.

- K. Huhn, M. Piechotka, T. Henning, and P. J. Klar. Investigation of the emission behavior of miniaturized SU-8 based colloid emitters. In *Proceedings of the 33rd IEPC, Washington, DC, USA*, number IEPC-2013-14, 2013.

- D. Reppin, F. Kuhl, M. Piechotka, T. Henning, P. J. Klar, N. Wolf, S. Kolling, Concepts for micro-thrusters based on solid state ion conductors. In *Proceedings of the 33rd IEPC, Washington, DC, USA*, number IEPC-2013-128, 2013.

Danksagung

An dieser Stelle möchte ich mich bei allen, direkt und indirekt, freiwillig und notgedrungen, beteiligten Kollegen, Freunden und Familienmitgliedern bedanken.

Im Einzelnen sind besonders zu erwähnen:

- Prof. Dr. Peter J. Klar für die Aufnahme eines ortsfremden Plasmaphysikers in seine, zu der Zeit frisch entstandene, Arbeitsgruppe Mikro- und Nanostrukturierung am I. Physikalischen Institut und insbesondere für die Betreuung und der Bereitstellung des Themas dieser Dissertation. Seine ausdauernde Unterstützung und Hilfestellung — auch und gerade in schwierigen Zeiten der Unsicherheit — gaben mir stets die nötige Motivation für die Fertigstellung dieser Arbeit. Weiterhin bedanke ich mich für die zeitnahe und konstruktive Kritik zu fachlich herausfordernden Fragestellungen.

- Prof. Dr. Jürgen Janek für die Übernahme des Zweitgutachtens und die hilfreichen Anregungen bezüglich Ionenleiter und ionischer Flüssigkeiten.

- Dr. Torsten Henning für seine Hilfe zu allen reinraumbezogenen Herausforderungen und bei typographischen Fragestellungen jeglicher Art sowie für das Korrekturlesen dieser Arbeit.

- meine Masterstudenten Katharina Huhn und Florian "Anton" Kuhl für ihre Geduld und Leidensfähigkeit, mich als ihren Betreuer ertragen zu haben. Katharina danke ich im Speziellen für die Herstellung von unzähligen SU-8-Emittern, der ewigen Suche nach perfekten Fabrikationsparametern und ihrer unermüdlichen Hilfe bei den Emissionsuntersuchungen an den Kolloidemittern. Bei Florian bedanke ich mich insbesondere für das Sputtern der YSZ-Schichten sowie für die Hilfe beim Ätzen und der Charakterisierung von YSZ-Membranen.

- Daniel Reppin für die XRD-Messungen von YSZ-Schichten und Hilfestellungen bei Fragen zum Aufbau von Festkörperionenleitern.

- Dr. Davar Feili, Dr. Benjamin Lotz, Peter Köhler und Waldemar Gärtner für anregende Diskussionen über elektrische Raumfahrtantriebe und Hilfe bei der Arbeit am BIGMAC.

- die AG Janek und insbesondere Markus Göttlicher für die Nutzung des Kontaktwinkelmessaufbaus und die Einweisung in dessen Bedienung.

- Markus Schäfer und Sabrina Darmawi für ihre Hilfe mit der EBL sowie dem BHF-Ätzen.

- Martin Fischer und Julian Benz für ihre Bemühungen beim Trockenätzen.

- die Werkstätten des I. Physikalischen Insituts für die zeitnahe Herstellung und Reparatur von mechanischen und elektronischen Bauteilen.

- Thomas Sander für seine Geduld und lehrreichen Unterhaltungen zur Ramanstreuung, zur Gruppentheorie und zum Thesis Repulsor Field.

- Dr. Gert "Bertram" Homm für seine fachlichen und persönlichen Ratschläge, seine Ausdauer und seinen Humor auf Konferenzen und seinen Wettkampfgeist in jeglichen sportlichen Disziplinen.

- Dr. Matthias "Max" Elm für endlose und lautstarke Diskussionen über die Physik und alle anderen Themen dieser Welt, welche dank seiner Hilfe mehrfach gerettet wurde.

- David Hartung als langjähriger Tischnachbar für seine anstandslose Hilfe jedweder Art.

- Florian Gather für geistreiche Unterhaltungen und programmiertechnische Ratschläge sowie seinem(s) (ideellen) Beitrag(s) zur Kasse des guten Humors.

- Dr. Jörg Teubert für anregende Abende und Einblicke in die Welt der Photographie.

- Christian “MoD” Will, Tobias Lind, Mario Fey, Steve Petznick, Christian Reindl und Osman Khalil für erheiternde Momente an und neben der Arbeit.

- Andreas “MoS” Rühl für Diskussionen um Alles und doch Nichts.

- Dr. Jens Wallys und das OK für die Organisation des Physikercups sowie alle Spieler des Teams “FK Klar” und insbesondere das Gewinnerteam aus dem Jahre 2012.

- die ehemaligen und aktuellen Mitarbeiter der AG Klar für die vergnüglichen und lehrreichen Diskussionen während und auch nach der Arbeitszeit sowie für einige Strafkästen dank des Drehstangenkugelentspannungsexperiments.

- alle anderen Mitarbeiter des I. Physikalischen Instituts.

- das hessische Ministerium für Wissenschaft und Kunst, welches im Rahmen des LOEWE-Schwerpunkts RITSAT diese Arbeit finanziell unterstützt hat.

- Lara, Julia und Artur für viele (zukünftige) Spiele- und Grillabende bis tief in die Nacht.

- meine Familie, vor allem meine Geschwister und insbesondere mein Vater, ohne deren Unterstützung und Liebe, Vertrauen und Glauben, gerade während der Endphase, diese Arbeit nie zu Stande gekommen wäre — Danke für Alles.

Eidesstattliche Erklärung

Hiermit erkläre ich, dass ich die vorgelegte Dissertation mit dem Titel

"Design and Development of Miniaturized Epoxy-Based Colloid Emitters and Solid-State Ion-Emitters"

selbständig und ohne unerlaubte fremde Hilfe und nur mit den Hilfen, die ich in der Dissertation angegeben habe, angefertigt habe. Alle Textstellen, die wörtlich oder sinngemäß aus veröffentlichten Schriften entnommen sind, und alle Angaben, die auf mündlichen Auskünften beruhen, sind als solche kenntlich gemacht. Bei den von mir durchgeführten und in der Dissertation erwähnten Untersuchungen habe ich die Grundsätze guter wissenschaftlicher Praxis, wie sie in der „Satzung der Justus-Liebig-Universität Gießen zur Sicherung guter wissenschaftlicher Praxis" niedergelegt sind, eingehalten.

Gießen, den 22. Juli 2015 Markus Piechotka